Controlling atom-photon interactions in nano-structured media

A dissertation presented
by

Darrick Edward Chang

to
The Department of Physics
in partial fulfillment of the requirements
for the degree of
Doctor of Philosophy
in the subject of

Physics

Harvard University
Cambridge, Massachusetts
May 2008

18,636

Thesis advisor
Mikhail D. Lukin

Author
Darrick Edward Chang

Controlling atom-photon interactions in nano-structured media

Abstract

Developing new techniques to control and manipulate the interaction between light and matter has been a central theme in science and engineering for many decades. These tools find wide-ranging applications in fields as diverse as spectroscopy, laser physics, and ultrafast science. Recently, there has been strong interest in extending this control down to the level of the constituent particles of light and matter, single atoms and single photons.

In this thesis, we explore several ways in which concepts from quantum optics and condensed matter physics can be combined with novel photonic systems to realize new tools for manipulating light-matter interactions. First, we theoretically and experimentally demonstrate that single quantum emitters can be strongly coupled to single surface plasmons (*i.e.*, single photons) tightly guided on conducting nanowires. The strong coupling occurs due to the sub-diffraction-limit mode confinement, and can be used as a resource to efficiently collect emission or generate single photons. We also show theoretically that such a system can give rise to strong single-photon nonlinearities. As an application, we propose a scheme to realize a single-photon transistor, where the presence or absence of a single photon in a "gate" field regulates the propagation of a stream of "signal" photons.

We then describe how one-dimensional optical waveguides with tight field confinement can be used to create many-body photon gases with strong quantum mechanical correlations. In particular, we discuss a technique to dynamically create a "crystal" of photons starting from a non-interacting optical pulse. This "self-organization" process is mediated by effectively repulsive nonlinearities in the system.

Finally, we develop techniques to treat many-body, dipole-dipole interactions between atoms in an optical lattice. Using this formalism, we show that an optical band gap can form in a near-resonant lattice, which can be used to suppress the spontaneous emission of a single defect atom in the lattice, or couple a pair of distant defects through modified dipolar interactions. This formalism is also applied to calculate the frequency shifts in a lattice-based atomic clock due to dipolar interactions.

Contents

Citations to Previously Published Work

Parts of Chapters 2 have appeared in the following papers:

> "Quantum Optics with Surface Plasmons", D.E. Chang, A.S. Sørensen, P.R. Hemmer, and M.D. Lukin, Phys. Rev. Lett. **97**, 053002 (2006);
>
> "Strong coupling of single emitters to surface plasmons", D.E. Chang, A.S. Sørensen, P.R. Hemmer, and M.D. Lukin, Phys. Rev. B **76**, 035420 (2007);
>
> "Single photon generation and non-linear optics with surface plasmons", A.S. Sørensen and D.E. Chang, in *Proceedings of the Ninth Rochester Conference on Coherence and Quantum Optics* (2007);
>
> "Quantum and nonlinear optics with surface plasmons: dependence of propagation losses on temperature", D.E. Chang and M.D. Lukin, in *Proceedings of SPIE, vol. 6904*, S.M. Shahriar, P.R. Hemmer, and J.R. Lowell, eds., North-Holland, 69040I (2008).

Parts of Chapter 3 have appeared in the following paper:

> "Generation of single optical plasmons in metallic nanowires coupled to quantum dots", A.V. Akimov, A. Mukherjee, C.L. Yu, D.E. Chang, A.S. Zibrov, P.R. Hemmer, H. Park, and M.D. Lukin, Nature **450**, 402 (2007).

Parts of Chapter 4 have appeared in the following paper:

> "A single-photon transistor using nanoscale surface plasmons", D.E. Chang, A.S. Sørensen, E.A. Demler, and M.D. Lukin, Nature Phys. **3**, 807 (2007).

Parts of Chapter 5 have appeared in the following paper:

> "Crystallization of strongly interacting photons in a nonlinear optical fiber", D.E. Chang, V. Gritsev, G. Morigi, V. Vuletic, M.D. Lukin, and E.A. Demler, submitted to Nature Phys., also see cond-mat/0712.1817.

Parts of Chapter 6 have appeared in the following paper:

> "Quantum electrodynamics of defect atoms in an optical lattice", D.E. Chang and M.D. Lukin, in preparation (2008).

Parts of Chapter 7 have appeared in the following paper:

> "Controlling dipole-dipole frequency shifts in a lattice-based optical atomic clock", D.E. Chang, Jun Ye, and M.D. Lukin, Phys. Rev. A **69**, 023810 (2004).

Acknowledgments

These past six years in graduate school have been tremendously exciting, fun, and challenging. There have been many people whom I've had the privilege to learn from and interact with, and many more who have lent me their advice, support, and encouragement.

First, I'd like to thank my advisor, Misha Lukin, for all of his support, the enthusiasm he showed for my projects, and the time he invested in guiding and teaching me. His knowledge and intuition, dedication, and scientific curiosity have continually pushed me and inspired me to become a better physicist. His passion for science will serve as an inspiration wherever I go.

During my time here I've also had the opportunity to learn from and collaborate with many others. I'd especially like to thank Anders Sørensen, who always was generous with his time and never seemed to lack a beautiful physical explanation of something. The ideas and resources of Phil Hemmer and Hongkun Park have helped tremendously in turning quantum plasmonics from some vague idea into something observable, and Eugene Demler has lent me his invaluable insight and knowledge of condensed matter physics on numerous occasions. I've also greatly benefitted from the many scientific conversations that I've had with Marko Loncar, Giovanna Morigi, Sasha Zibrov, Ron Walsworth, Jun Ye, Vladan Vuletic, and Peter Zoller. Finally, I'd like to thank the other members of my thesis committee, Federico Capasso and Bert Halperin, for all of their input.

There are many talented colleagues and friends here with whom it has been a pleasure to work and interact, play frisbee, and share an equal affection for coffee and cookies. More importantly, they have always provided plenty of advice and help. They include Brian Murphy, Mohammad Hafezi, Michael Hohensee, Aryesh Mukherjee, Alexey Akimov, Vladimir Gritsev, Axel Andre, Peter Rabl, Gurudev Dutt, Philip Walther, Frank Koppens, Qimin Quan, Michal Bajcsy, Liang Jiang, Alexey Gorshkov, Jeronimo Maze, and Emre Togan. I'd also like to thank some members of the Park and Loncar groups, Chun Yu, Mughees Khan, Irfan Bulu, and Nathalie de Leon. In addition, Sheila Ferguson and Marilyn O'Connor deserve countless thanks for their patience and for helping me, and many others, navigate through grad school.

Finally, I'm eternally grateful to my family, especially my parents, who have made countless sacrifices to give me these opportunities. I'd also like to thank Darice, Bart, Polly, and my Jojo and Amma for all of their encouragement. And Yi-Chen, I can't thank you enough for all of your love and support, and for bringing fun and humor to every moment.

Dedicated to my Amma

Chapter 1

Introduction

1.1 Motivation: controlling interactions between single atoms and single photons

Developing new techniques to control and manipulate the interaction between light and matter has been a central theme in science and engineering for many decades. These tools find wide-ranging applications in fields as diverse as spectroscopy and imaging, communications, metrology, and ultrafast science. Recently, much effort has been devoted to pushing these ideas down to the level of the constituent particles of light and matter – single atoms and single photons. This interest stems from the wide belief that quantum mechanical phenomena will play an increasingly important role in emerging fields and applications, such as quantum computing and quantum information science. Over the past decade, there has been tremendous progress in manipulating single-atom, single-photon interactions using cavity quantum electrodynamics (QED) [1, 2, 3, 4], in which single atoms are coupled to a photonic mode of a high-finesse optical microcavity. In the "strong coupling" regime of cavity QED when the coupling strength between atom and cavity mode far exceeds dissipation into the environment, such a system comprises an elegant platform for observing fundamental processes such as reversible transfer of excitation between a single atom and cavity mode (Rabi oscillations) [5]. When combined with quantum optical techniques for coherent manipulation, strong coupling also forms the basis for applications such as efficient single-photon generation [6, 7, 8] and realization of single-photon nonlinearities (*e.g.*, single-photon blockade [9]). In addition, strongly coupled atom-cavity systems constitute the building blocks for important theoretical proposals including quantum state transfer and entanglement distribution [10], controlled phase gates between photons [11], and the realization of many-body interacting Hamiltonians using photons [12, 13, 14, 15, 16]. However, despite the spectacular theoretical and experimental progress in cavity QED, it remains technically challenging and difficult to scale.

It is thus tempting to ask whether there exist alternative physical systems where individual atoms and photons can be strongly and coherently coupled. Fortunately, rapid advances in photonics over the past decade have spawned numerous candidates. Plasmonic systems [17, 18], photonic crystals [19], tapered optical nanofibers [20], and metamaterials [21] are among those that are being actively studied for their potential to manipulate light-matter interactions. These new systems have led to fascinating ideas such as band gaps for light [22, 23], extraordinary transmission of light through tiny holes [24, 25], super-lenses [26], and "invisibility" cloaks to make objects completely transparent [27]. While such ideas are important in their own right, the vast majority of them can be described by classical optics and electromagnetic theory, and the possibility of exploiting these systems at the quantum mechanical level remains relatively unexplored. Generally, this thesis explores how ideas and techniques from quantum optics and condensed matter can be applied to some of the aforementioned systems to gain new levels of control over the interactions between individual atoms and light quanta.

1.2 Novel photonic systems

1.2.1 Plasmonics

Metals that contain nearly free electrons have long been known to possess unique electromagnetic properties as compared to their normal, positive-dielectric counterparts. The frequency dependence of the electric permittivity of these metals is often well-approximated by a Drude-like model,

$$\epsilon = 1 - \frac{\omega_p^2}{\omega^2 + i\omega\gamma_p}. \tag{1.1}$$

Here ω_p is the plasma frequency of the conductor, and γ_p is a parameter that characterizes material losses. Temporarily ignoring the losses, it can be seen that at frequencies below the plasma frequency, $\omega < \omega_p$, the permittivity of these metals is negative. The negative value of ϵ leads to a number of important consequences; for example, perhaps the most basic is that electromagnetic energy cannot propagate within the bulk of such materials.

Although the propagation of electromagnetic energy within the bulk is prohibited, the broken translational invariance of a metal surface does allow for the guided propagation of energy [17]. The resulting collective excitations of the electromagnetic field and charge density waves are known as surface plasmon polaritons, or more simply, surface plasmons (SPs). The simplest example is that of a flat, infinite interface that separates bulk regions of positive permittivity ϵ_1 and negative permittivity ϵ_2, as shown in Fig. 1.1a. Guessing plane wave solutions on each side of the interface and enforcing appropriate boundary conditions for the fields, it is straightforward to show that the system supports guided modes of the form

$$\mathrm{E}_i \sim E_0 \left(\hat{z} + i\frac{k_\parallel}{\kappa_{i\perp}}\hat{x} \right) e^{ik_\parallel z - \kappa_{i\perp}|x| - i\omega t}. \tag{1.2}$$

Here $i = 1, 2$ denotes the regions of different permittivity. The wavevector $k_\parallel$ along the direction of propagation satisfies

$$k_\parallel^2 = \left(\frac{\omega}{c}\right)^2 \frac{\epsilon_1\epsilon_2}{\epsilon_1 + \epsilon_2}, \tag{1.3}$$

while the perpendicular components of the wavevector $k_{i\perp} = i\kappa_{i\perp}$ are imaginary and satisfy

$$\kappa_{i\perp}^2 = k_\parallel^2 - \epsilon_i \left(\frac{\omega}{c}\right)^2. \tag{1.4}$$

The imaginary perpendicular wavevectors indicate that the field decays exponentially away from the interface. If $\epsilon_2(\omega)$ has the Drude-model frequency dependence of Eq. (1.1), the dispersion relation $k_\parallel(\omega)$ for the SPs takes the form shown in Fig. 1.1b. It should be noted that the dispersion curve lies to the right of the light line, $k = \omega/c$, which indicates that these modes are guided. Also, at frequencies near the plasmon resonance $\omega = \omega_p/\sqrt{2}$, the wavevector $k_\parallel$ becomes very large, indicating that the SP wavelength $\lambda_{\mathrm{pl}} = 2\pi/k_{\|}$ can become much smaller than the vacuum wavelength at the same frequency. By use of Eq. (1.4) it also follows that at these frequencies, the SPs can be transversely confined near the interface to distances much smaller than the vacuum wavelength. Here, the presence of free charge plays a crucial role in the ability of SPs to circumvent the diffraction limit.

While we have considered a flat metal-dielectric interface in the above example, it turns out that the geometry of the interface can play a very important role in determining the localization of the SPs and the positions of plasmon resonances. The role of structure shape in determining the propagation, channelling, and focusing of electromagnetic energy has led to a number of dramatic observations involving SPs ranging from detection of single molecule fluorescence [28, 29] to extraordinary light transmission through sub-wavelength apertures [24, 25]. The potential applications of SPs to fields such as biosensing [30], subwavelength imaging [31, 32], and photonic nano-circuitry [33, 34] are being actively investigated.

1.2.2 Photonic crystals

Photonic crystals [19] are structures that consist of periodic arrays of diffractive scatterers of light. While the interaction of light with a single scatterer may be described simply in terms of scattering cross sections or reflection and transmission coefficients, the collective interference effects of light interacting with a periodic system can give rise to much richer phenomena. In analogy with electronic behavior in semiconductor crystals, the eigenmodes of the electromagnetic field in a photonic crystal can be described in terms of band structures, whose properties such as dis-

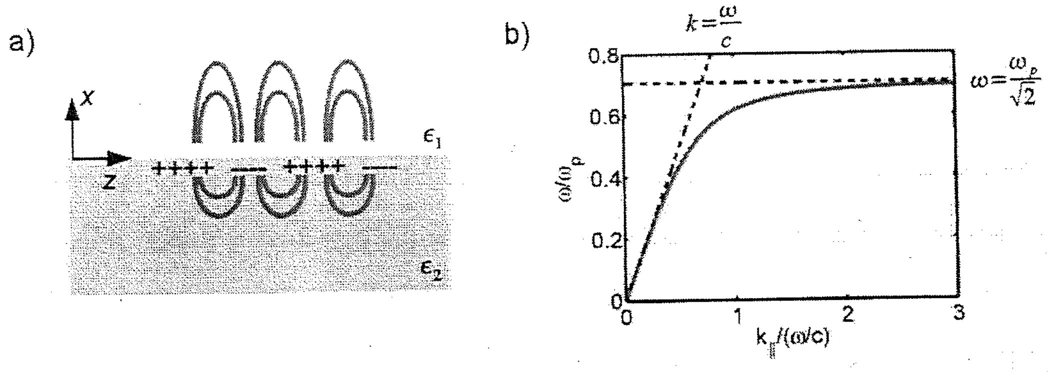

Figure 1.1: a) Schematic of guided surface plasmon mode propagating on a flat metal-dielectric interface. The red curves indicate electric field lines for these modes. b) Surface plasmon dispersion relation for a flat interface, taking $\epsilon_1 = 1$ and $\epsilon_2 = 1-(\omega_p/\omega)^2$. The dispersion curve lies to the right of the light line $k = \omega/c$, indicating that these modes are guided. The upper frequency cutoff for these modes is given by $\omega = \omega_p/\sqrt{2}$.

persion can differ greatly from those in free space. When the interference between the different scatterers comprising the photonic crystal becomes sufficiently strong, a "photonic band gap" (PBG) can appear. Here, a complete absence of photonic modes emerges over some frequency range and electromagnetic energy is prohibited from propagating through the medium [22, 23].

The physical processes leading to the emergence of band structures and band gaps can be most easily understood in a one-dimensional, periodically layered dielectric medium, as shown in Fig. 1.2a. Here, the photonic crystal is composed of alternating slabs of electric permittivity ϵ_1 and ϵ_2, and the system is periodic on a length scale a,

$$\epsilon(z + a) = \epsilon(z). \tag{1.5}$$

We consider wave solutions of the electric field that are polarized perpendicular to z, the direction of propagation. The corresponding wave equation is given by

$$\frac{c^2}{\epsilon(z)}\frac{\partial^2 E}{\partial z^2} - \frac{\partial^2 E}{\partial t^2} = 0. \tag{1.6}$$

Suppose that we would like to find the eigenmodes and eigenvalues of the system. According to Bloch's theorem [35], any eigenmode (indexed by k) can be written in the form

$$E_k(z,t) = \sum_G E_G e^{i(k+G)z - i\omega_k t}, \tag{1.7}$$

where $G = 2\pi m/a$ for all integer m constitute the set of reciprocal lattice vectors for the system, and E_G thus far are unknown coefficients. Similarly, the periodic function $1/\epsilon(z)$ can also be expanded in a Fourier series,

$$\frac{1}{\epsilon(z)} = \sum_G \alpha_G e^{iGz}. \tag{1.8}$$

In practice, one can substitute Eqs. (1.7) and (1.8) into Eq. (1.6) and numerically solve by truncating the Bloch expansions over a finite number of reciprocal lattice points G (in 1-D, the system is exactly solvable using transfer matrices [36], but the technique illustrated here is more easily generalized to higher dimensions). Truncating Eq. (1.6) at three points $G_{\pm1,0} = \pm 2\pi/a, 0$, for example, yields the set of equations

$$0 \approx \left(\frac{\omega_k^2}{c^2} - \alpha_0 k^2\right) E_0 - \alpha_{-1}\left(k + \frac{2\pi}{a}\right)^2 E_1 - \alpha_1\left(k - \frac{2\pi}{a}\right)^2 E_{-1}, \tag{1.9}$$

$$0 \approx \left(\frac{\omega_k^2}{c^2} - \alpha_0\left(k \pm \frac{2\pi}{a}\right)^2\right) E_{\pm1} - \alpha_{\pm1} k^2 E_0, \tag{1.10}$$

or in abbreviated matrix form, $M\vec{E}_G = 0$. A non-trivial solution requires that the determinant of M be zero, $\det M = 0$. While the specific nature of the dispersion relation $\omega(k)$ depends on the exact form of $\epsilon(z)$, a couple of general features can be derived. First, for low frequencies and small variations in the permittivity $|\kappa_{\pm1}| \ll \kappa_0$, the dispersion relation behaves linearly as $\omega(k){\sim}\sqrt{\alpha_0}|k|$. In other words, for wavelengths much longer than the periodicity of the material, the variation in material index has little effect on propagation. In addition, for wavevectors $k{\approx}\pi/a$ near the edge of the Brillouin zone, the dispersion relation behaves as [19]

$$\frac{\omega(k)}{c} \approx \frac{\pi}{a}\sqrt{\alpha_0 {\pm} |\alpha_1|} {\pm} \frac{a}{\pi|\alpha_1|}\left(\alpha_0^2 - |\alpha_1|^2/2\right)\left(k - \frac{\pi}{a}\right)^2. \tag{1.11}$$

In particular, a band gap or absence of modes appears in the frequency range

$$\frac{\pi}{a}\sqrt{\alpha_0 - |\alpha_1|} < \frac{\omega}{c} < \frac{\pi}{a}\sqrt{\alpha_0 + |\alpha_1|}. \tag{1.12}$$

Physically, the periodic permittivity creates a Bragg grating of wavevector $2\pi/a$ that mixes together the optical modes with wavevectors $k = \pm\pi/a$ and prevents their propagation.

While most basic aspects of photonic crystals easily emerge from considering one-dimensional systems, the ability to tailor the propagation of light, and in turn its interaction with matter, finds the most applications in two- or three-dimensional structures. Such structures can be used, *e.g.*, to realize low-threshold lasing [37], superprisms [38], optical filters [39], and optical switches [40]. Three-dimensional PBG materials in particular are predicted to dramatically modify the interactions between atoms and photons. For example, the spontaneous emission of an atom inside a photonic crystal whose resonance frequency lies within a three-dimensional PBG should be completely prohibited [22]. Physically, this inhibition is due to the complete absence of resonant modes with which the atom can interact. Thus far, however, photonic crystals in the optical range have generally been made using various micro-fabrication techniques that remain difficult to apply towards three-dimensional

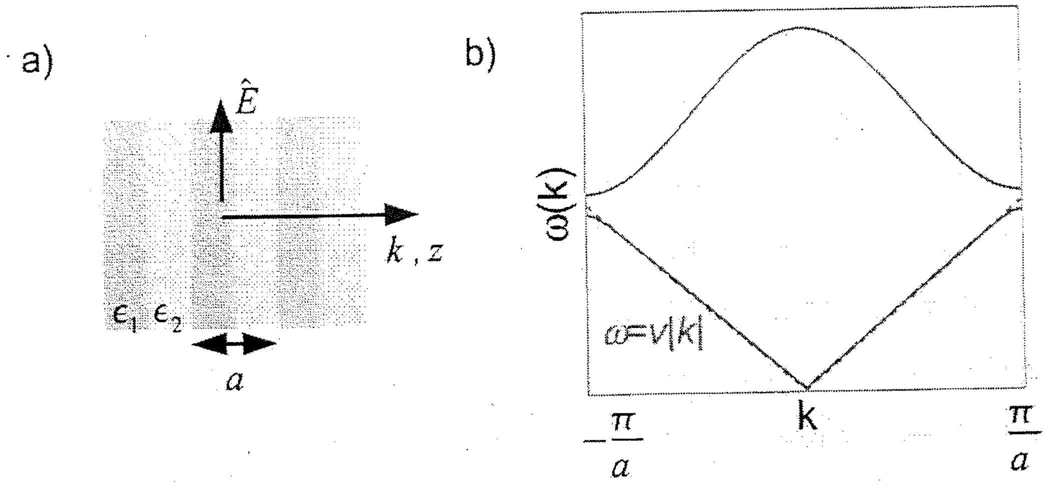

Figure 1.2: a) A one-dimensional photonic crystal formed by a periodic array of slabs of varying permittivities ϵ_1 and ϵ_2. The period of the structure is determined by the length a. Here, the horizontal arrow denotes the direction of field propagation, while the vertical area denotes the electric field polarization. b) Typical band structure $\omega(k)$ for a 1-D photonic crystal. Near the edge of the first Brillouin zone, $k \approx \pm\pi/a$, the dispersion relation splits and a band gap of forbidden energies is produced. The dashed red line $\omega = v|k|$ indicates the linear dispersion relation of low-frequency waves in the system.

structures, and consequently the suppression of spontaneous emission has only been partially observed [41].

1.2.3 Nanofibers and hollow-core photonic band gap fibers

Optical fibers and dielectric waveguides are widely used today in communications and optical sensing technologies. Typically these waveguides have diameters much larger than the optical wavelength, and their optical properties and fabrication methods are well known. In recent years, however, there has also been interest in utilizing waveguides whose transverse sizes are comparable to or smaller than the optical wavelength. Two particularly promising systems have emerged for this task:

tapered optical nanofibers [20, 42] and hollow-core photonic crystal fibers [43].

Tapered nanofibers (see Fig. 1.3a) are typically formed by heating and pulling thicker optical fibers or dielectric wires until their diameters reach tens or hundreds of nanometers [20], becoming single-mode in the process. When properly pulled, nanofibers with atomic-level surface smoothness and high uniformity can be fabricated, which in turn yields low propagation losses and high transmission coefficients through such devices [20, 44]. The guided modes of such nanofibers can be transversely confined near the diffraction limit, while simultaneously a large percentage of the total guided energy sits outside of the fiber core in the evanescent tails [42]. The tight mode confinement allows for relatively high field intensities at low powers, which has been used, for example, to enhance optical nonlinearities that lead to generation of supercontinuum light [45], while the large evanescent tails have led to the observation of strong self-coupling and interference fringes in transmission through coiled nanofibers [46].

A standard optical fiber guides light via total internal reflection in a higher refractive index fiber core that is surrounded by a lower index cladding. In contrast, as the name suggests, in hollow-core PBG fibers (see Fig. 1.3b) light is confined to an empty hole that forms the core of the fiber. The cladding generally consists of some dielectric material, such as silica, containing a periodic array of air holes that creates a photonic band gap to prevent light from escaping the core [43]. The cores can be fabricated to have diameters of several microns to yield small effective mode areas.

The possibility of coupling atoms to the guided modes of nanofibers and PBG fibers is being actively investigated [44, 47]. A primary motivation for these endeavors

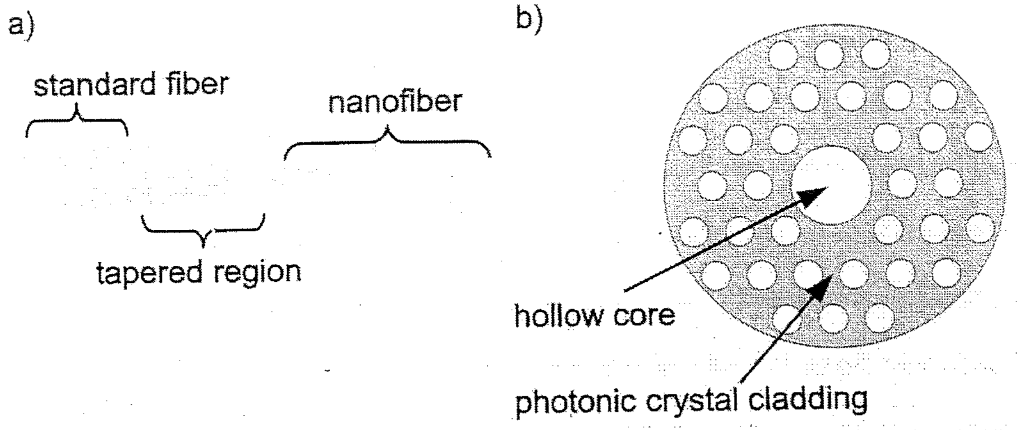

Figure 1.3: a) Illustration of a nanofiber, which is fabricated by pulling and tapering a conventional optical fiber to a radius of tens or hundreds of nanometers. b) Hollow-core photonic band gap fiber, consisting of a hollow core and a photonic crystal cladding. The presence of a band gap in the cladding prevents light in the core from escaping out.

stems from the observation that the tight field confinement allows one to reach large optical depths with relatively few atoms [47, 48], and that the strength of atom-mediated optical nonlinearities scales favorably with decreasing mode area [47, 48]. Such systems thus are promising candidates to realize few-photon nonlinearities.

1.3 Structure of thesis

This thesis explores several methods through which the unique properties of plasmonic systems, photonic crystals, and nanofibers and PBG fibers can be combined with atomic physics and quantum optics to realize new techniques to control atom-photon interactions and new strongly interacting phenomena involving photons.

Chapters 2, 3, and 4 describe techniques to realize quantum optics and single-photon nonlinear optics using nano-scale SPs. In Chapter 2, we derive the mode structure and properties of SPs propagating on conducting nanowires. For sub-wavelength wires, we show that, in analogy with optical fibers, the nanowires become single-mode systems. Unlike their dielectric counterparts, however, the presence of free charge gives rise to slow group velocities and sub-wavelength modal confinement over a large bandwidth, due purely to the geometrical effect of small wire size. This in turn gives rise to strong coupling between individual atoms (or other quantum emitters) proximal to the nanowire and single, quantized SPs (*i.e.*, single photons). The one-dimensional nanowire can thus be used to efficiently collect single emitted photons or form a nearly-ideal system to realize quantum electrodynamics in one dimension. When combined with quantum optical techniques, these systems enable applications such as efficient single-photon generation on demand or quantum state transfer between distant qubits. We also theoretically show that the lossy SP modes can be efficiently out-coupled to dielectric waveguides, which might facilitate the construction of large-scale devices. Furthermore, we derive the dependence of SP propagation losses on surface roughness of the nanowires and temperature-dependent electron-phonon scattering. The ability to decrease losses would improve the efficiency and practicality of many applications involving plasmonics. In Chapter 3 we briefly discuss an experiment in which efficient single-photon generation and collection is demonstrated, using quantum dot nanocrystals strongly coupled to chemically synthesized silver nanowires. Under certain conditions, spontaneous emission into the guided SPs is highly favored over emission into free space. The emission into SPs is observed in the far field once these excitations scatter off of the wire ends, causing them to light up. Measurements of field correlations of the scattered light allow us to deduce the coupling strength to the SPs. Chapter 4 describes how strong coupling in these nanowires can give rise to strong single-photon nonlinearities mediated by single quantum emitters. As an example, we show how a single two-level emitter naturally acts as an optical switch that distinguishes between one and two photons. Furthermore, this nonlinearity can be coherently controlled using photon storage protocols and internal state manipulation of the emitter. As an example, we demonstrate how these ideas can be used to realize a single-photon transistor, in which the propagation of a stream of "signal" photons is conditioned upon the presence of a single "gate" photon.

While schemes to generate large single-photon nonlinearities using strongly coupled systems have been heavily explored, relatively little attention has been devoted to whether such systems can be used to generate unusual interacting states involving many photons. In Chapter 5 we propose a method to realize a strongly correlated "crystal" of photons in one-dimensional systems such as conducting nanowires, tapered nanofibers, and PBG fibers that are strongly coupled to an ensemble of cold atoms. Here, we show how techniques such as electromagnetically induced transparency (EIT) and photon trapping can be used to generate significantly large optical nonlinearities that a collective many-body state of photons in the system acquires properties that are fundamentally different from those of the underlying particles. Specifically, we demonstrate that an initial overlapping state of non-interacting photons can separate and "self-organize" into a crystal in this system.

In Chapters 6 and 7 we consider the quantum electrodynamics of photon-mediated interactions between atoms in an optical lattice. Given the difficulty in creating three-dimensional PBG structures through standard micro-fabrication methods, we consider in Chapter 6 whether an ensemble of atoms regularly and periodically trapped in an optical lattice can behave as a PBG material. In particular, we show that in the absence of incoherent photon scattering, a cubic lattice of atoms supports a narrow photonic band gap near the atomic resonance frequency. Motivated by this observation, we derive the spontaneous emission rate for a "defect" atom within the lattice, taking fully into account both coherent atom-atom interactions and incoherent photon scattering. We show that the band gap can in principle suppress spontaneous emission of the defect atom relative to free-space rates by over thirty fold. The suppression of decay into free space is shown to facilitate coherent interactions between two defect atoms separated over large distances in the optical lattice.

In Chapter 7, we apply our formalism to derive the magnitudes of frequency shifts in an optical lattice-based atomic clock due to dipole-dipole interactions between atoms. Optical lattices containing many atoms have been proposed as the "ultimate" frequency standard due to their favorable signal-to-noise ratios [49], and thus minimization of this shift is crucial in developing high-accuracy clocks. We show that there exist certain lattice configurations where large frequency shifts occur due to constructive interference between pairwise atomic interactions, and that these shifts can also be minimized by properly engineering the lattice geometry.

Chapter 2

Quantum optics with surface plasmons

2.1 Introduction

In this chapter we describe a method that enables strong, coherent coupling between individual emitters and SPs tightly guided on one-dimensional conducting nanostructures. These structures are able to support SPs with transverse effective mode areas $A_{\mathrm{eff}} \ll \lambda_0^2$ that can be much smaller than the size of a diffraction-limited spot, which naturally results in a substantial increase in the emitter-field coupling constant $g \propto 1/\sqrt{A_{\mathrm{eff}}}$. We show that under realistic conditions, optical emission can be almost entirely directed into these modes, in a manner similar to the Purcell effect in cavity QED [50]. We begin by considering the case of coupling to a cylindrical nanowire, a simple geometry where the relevant physics can be understood analytically. Defining an effective Purcell factor $P = \Gamma_{\mathrm{pl}}/\Gamma_{\mathrm{other}}$ characterizing the ratio of spontaneous emission into the SPs over emission into other channels, we find that values exceeding $P{\sim}10^3$ are possible in these systems, limited only by metal losses at optical frequencies. Relative to other demonstrated methods to enhance emission via SPs [28, 29, 51, 52, 53], the technique described here is unique in two important ways. First, the enhancement is broadband in that it relies on the geometrical effect of small wire size rather than on resonances of the system. Thus, no special tuning of the nanowire to the emitter frequency is needed. Second, the enhanced emission is efficiently collected into the "nice" guided SP modes of the one-dimensional nanowire, which subsequently can facilitate, *e.g.*, efficient out-coupling to other devices.

Because of losses, the SP modes themselves are not suitable as carriers of information over long distances. In fact, the mechanism that gives rise to the strong coupling – tight field confinement near the wire – also is responsible for increased propagation losses. To circumvent this limitation, we propose a combination of two strategies. The first is to use nanostructures with optimized geometries, such as the nanotip configuration considered later, where strong coupling can be achieved with reduced losses. Second, we show that the SP excitations in these nanostructures can be efficiently converted into photons in a nearby, dielectric waveguide, as illustrated schematically in Fig. 2.1. This can be used, *e.g.*, to create a single-photon source or as part of an architecture to perform controlled interactions between distant qubits. The achievable coupling strength between the SP and dielectric waveguides can be much larger than the SP dissipation rates, and we find that single-photon generation efficiencies of ~95% are possible for the simple geometries considered here.

Finally, we take into account the effects of device imperfections, in the form of

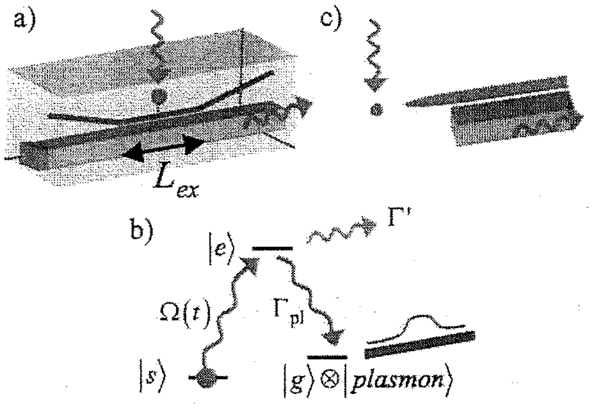

Figure 2.1: a) An emitter coupled to a nanowire is optically excited and decays with high probability into the surface plasmon modes of the nanowire. A single photon source is created by evanescently coupling the nanowire to a nearby dielectric waveguide over a length L_{ex}. The single photon source can potentially be uni-directional, *e.g.*, by capping one end of the waveguide with a reflective surface. b) An internal-level scheme that allows for shaping of the outgoing single photon pulses. An emitter that starts in state $|s\rangle$ is coupled to excited state $|e\rangle$ via a time-dependent external control field $\Omega(t)$. We assume that the excited state $|e\rangle$ is coupled to state $|g\rangle$ via the SP modes, causing $|e\rangle$ to decay into $|g\rangle$ with high probability, while simultaneously generating a single photon in the SP modes. The shape of the photon wavepacket is determined by $\Omega(t)$. c) A similar scheme for single photon generation using an emitter coupled to a nanotip instead of a nanowire. Note that this scheme is naturally uni-directional, as the generated SPs propagate in a single direction.

surface roughness of the nanowires, and the role of temperature-dependent metal losses on our previously derived results.

2.2 Surface plasmon modes on a nanowire

2.2.1 General mode structure

The general method for calculating the electromagnetic modes of a nanowire is briefly outlined here, with details of the calculation given in Appendix A.1. To be concrete, we consider a cylinder of radius R of dimensionless electric permittivity ϵ_2, which is centered along the z-axis and surrounded by a second dielectric medium ϵ_1, as shown in Fig. 2.2a. While we are particularly interested in the case of a conducting nanowire surrounded by some lossless positive dielectric ($\mathrm{Re}\,\epsilon_2 < 0, \epsilon_1 > 0$), we note that at this point the discussion is quite general. Like any other simple geometry with a high degree of symmetry, one can use separation of variables and find field solutions $\mathbf{E}, \mathbf{H}$ to Maxwell's Equations in each dielectric region [54, 55]. In cylindrical coordinates, the electric field is given by $\mathbf{E}_i(\mathrm{r}) = \mathcal{E}_{i,m}\mathbf{E}_{i,m}(k_{i\perp}\rho)e^{im\phi}e^{ik_{\parallel}z}$, where $i = 1, 2$ denotes the regions outside and inside the cylinder, respectively. Here $k_{\parallel}$ is the longitudinal component of the wavevector, which is related the vacuum wavevector $k_0 = \omega/c$, electric permittivity ϵ_i, and transverse wavevector $k_{i\perp}$ by $\epsilon_i k_0^2 = k_{\parallel}^2 + k_{i\perp}^2$, and m is an integer characterizing the winding of the mode. The functions $\mathbf{E}_{i,m}$ represent some normalized mode profiles. A similar expression holds for the magnetic field $\mathbf{H}$. For future reference, we also define the vacuum wavelength $\lambda_0 = 2\pi/k_0$, and $k_i = \sqrt{\epsilon_i}k_0$ as the wavevector in medium i. The coefficients $\mathcal{E}_{i,m}$ and $\mathcal{H}_{i,m}$ multiplying the fields are not arbitrary but instead must satisfy a set of equations that enforces the necessary boundary conditions at the dielectric interface $\rho = R$. The existence of a non-trivial solution requires that the matrix corresponding to this linear system have zero determinant ($\det M = 0$), which upon simplifying yields the mode equation for a cylinder [54, 55],

$$\begin{aligned} \frac{m^2 k_{\parallel}^2}{R^2}\left(\frac{1}{k_{2\perp}^2} - \frac{1}{k_{1\perp}^2}\right)^2 &= \left(\frac{1}{k_{2\perp}}\frac{J_m'(k_{2\perp}R)}{J_m(k_{2\perp}R)} - \frac{1}{k_{1\perp}}\frac{H_m'(k_{1\perp}R)}{H_m(k_{1\perp}R)}\right) \times \\ &\quad \left(\frac{k_2^2}{k_{2\perp}}\frac{J_m'(k_{2\perp}R)}{J_m(k_{2\perp}R)} - \frac{k_1^2}{k_{1\perp}}\frac{H_m'(k_{1\perp}R)}{H_m(k_{1\perp}R)}\right). \end{aligned} \tag{2.1}$$

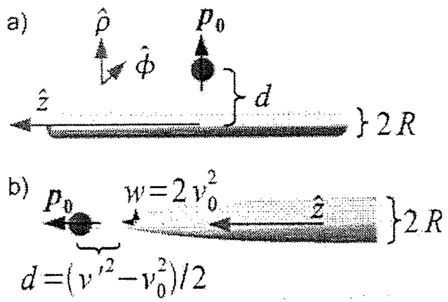

Figure 2.2: a) A dipole emitter positioned a distance d from the center of a nanowire. For the calculations presented, the orientation of the dipole moment is assumed to be along $\hat{\rho}$. b) A dipole emitter positioned near the end of a nanotip. In terms of parabolic coordinates, the physical distance d between the end of the tip and the emitter is given by $d=(v'^2-v_0^2)/2$, while the curvature parameter $w=2v_0^2$. For the nanotip, only a dipole oriented parallel to $\hat{z}$ couples to the fundamental SP mode.

The above equation, for example, determines the allowed values of $k_{\parallel}$ as functions of m, R, and ϵ_i. Here J_m and H_m are Bessel and Hankel functions of the first kind, respectively.

We now focus on the case of a sub-wavelength, conducting metal wire surrounded by a normal, positive dielectric. In Fig. 2.3 we plot the allowed wavevectors $k_{\parallel}$, as determined through Eq. (2.1), as a function of R for a few lowest-order modes in m. Unless otherwise noted, all numerical results presented in this chapter are for a silver nanowire (or later, nanotip) at room temperature, $\lambda_0 = 1\ \mu$m, and with a surrounding dielectric $\epsilon_1 = 2$, although the physical processes described are not specific to silver or to some narrow frequency range. The electric permittivity of the silver nanowire at this frequency is assumed to correspond to its measured value in thin films, $\epsilon_2 \approx -50+0.6i$ [56]. In plotting Fig. 2.3 we have temporarily ignored the dissipative imaginary part of ϵ_2, although we will address its effect later. Ignoring $\mathrm{Im}\,\epsilon_2$ results in purely real values of $k_{\parallel}$, indicating that these modes propagate without

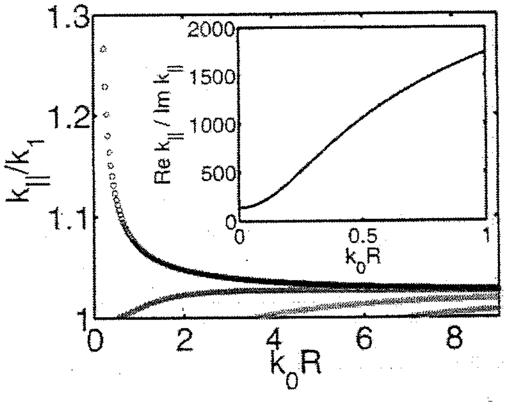

Figure 2.3: Allowed surface plasmon modes $k_{\|}$ as a function of R for a silver nanowire embedded in a surrounding dielectric $\epsilon_1 = 2$, for frequency corresponding to a vacuum wavelength $\lambda_0 = 1$ μm and room temperature. The fundamental ($m = 0$) mode, in black, exhibits a $k_{\|} \propto 1/R$ dependence, while all other modes are effectively cut off as $R \to 0$. In order of increasing cutoff radius, the other modes displayed correspond to $|m| = 1, 2$, and 3, respectively. Inset: the propagative losses for the fundamental mode, characterized by the ratio Re $k_{\|}$/Im $k_{\|}$, for the same parameters.

loss.

We first qualitatively discuss the important features of the SP modes illustrated in Fig. 2.3, before deriving them more carefully. It is clear from the figure that the longitudinal component of the wavevector exceeds the wavevector in uniform dielectric, $k_{\|} > k_1$, which in turn causes the perpendicular component $k_{i\perp} = \sqrt{k_i^2 - k_{\|}^2} \equiv i\kappa_{i\perp}$ to be purely imaginary. These conditions are similar to those for SPs on a flat interface, as derived in Sec. 1.2.1. Physically these relationships imply that the SP modes are non-radiative and are confined near the metal/dielectric interface, with the length scale of transverse confinement determined by $\sim 1/\kappa_{i\perp}$. Furthermore, these SP modes cannot couple directly to radiative fields, which have wavevectors $k_{\|} \leq k_1$. Of particular interest is the behavior of the SP modes in the nanowire limit $|k_i|R \ll 1$. In this limit, all higher-order modes ($|m| \geq 1$) exhibit a cutoff as $R \to 0$, as derived in Appendix A.2, while the $m = 0$ fundamental SP mode exhibits a unique $k_{\|}\propto 1/R$ behavior. This scaling indicates that the wavelength of these SPs can become strongly reduced relative to the free-space wavelength. Physically, in this limit, the $m = 0$ mode can be interpreted approximately as a quasi-static configuration of field and associated charge density wave on the wire. As such, R becomes the only relevant length scale, as the length scales $1/|k_i|$ associated with electrodynamic behavior become unimportant. From the $1/R$ scaling of $k_{\|}$ it also follows that $\kappa_{1\perp}\propto 1/R$. This implies that the field outside of the wire becomes tightly localized on a scale $\propto R$ around the metal surface, leading to a small effective transverse mode area that scales like $A_{\mathrm{eff}}\propto R^2$. In particular, it is possible for this mode to be confined well below the diffraction limit. This effect gives rise to a strong interaction strength with nearby emitters, as will be discussed in following sections. We note that this behavior contrasts sharply with that of, *e.g.*, a sub-wavelength normal dielectric waveguide or optical fiber, which runs into a "confinement problem" where the evanescent tails outside the device become exponentially large as $R\rightarrow 0$ [42]. This latter behavior stems from the fact that electromagnetic radiation cannot be confined below the diffraction limit.

The emergence of tight confinement of SPs due to the geometry of the wire can be further confirmed by comparing the SP dispersion relations of flat interfaces (see Sec. 1.2.1) and wires. Assuming a Drude model for the metal (Eq. (1.1)) with no losses and $\epsilon = 1$ for the dielectric medium, the dispersion relations for the two geometries are plotted in Fig. 2.4. Here we have numerically solved Eq. (2.1) for a Drude model and for $m = 0$ to obtain the fundamental modes of the wire. It can be clearly seen that the effect of small wire size is to pull the fundamental SP mode dispersion relation

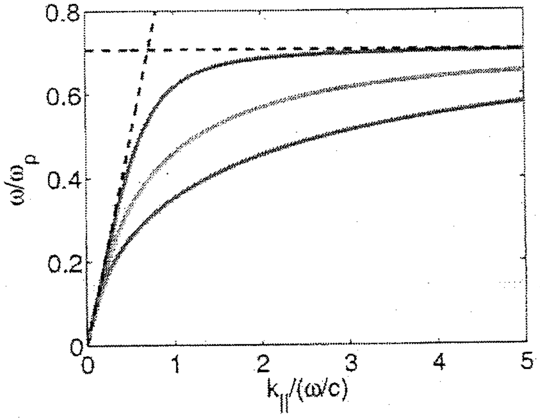

Figure 2.4: Comparison of surface plasmon dispersion relations on a flat metal-dielectric interface and a metallic wire, assuming a Drude model optical response for the metal. The blue curve represents the dispersion relation for the flat interface, while the green and red curves represent the fundamental modes of wires with radii $k_0R = 0.5$ and $k_0R = 0.2$, respectively. The dotted lines denote the light line $k_\parallel = \omega/c$ and upper frequency cutoff $\omega = \omega_p/\sqrt{2}$. The small wire size tends to pull the fundamental mode dispersion relation further away from the light line as compared to the flat interface.

further away from the light line, $k_\parallel = \omega/c$, as compared to the dispersion curve of a flat interface.

In practice ϵ_2 is not purely real but has a small imaginary part corresponding to losses in the metal (heating) at optical frequencies. Its effect is to add a small imaginary component to $k_\parallel$ corresponding to dissipation as the SP propagates along the wire. In the inset of Fig. 2.3 we plot Re $k_\parallel$/Im $k_\parallel$ for the fundamental mode as a function of R. This quantity is proportional to the decay length in units of the SP wavelength $\lambda_{\mathrm{pl}} \equiv 2\pi/\mathrm{Re}\, k_\parallel$. As R decreases, it can be seen that this ratio decreases monotonically but approaches a nonzero constant, as will be explicitly shown below. For silver at $\lambda_0 = 1$ μm and room temperature and $\epsilon_1 = 2$ this constant is approximately 140. The fact that this ratio does not approach zero even as $R \rightarrow 0$ is important for potential applications, as it implies that the SPs can still travel several times the wavelength λ_{pl} for devices of any size. We also note that while all numbers and figures presented here are for room temperature, operating at lower temperatures might somewhat reduce the value of $\mathrm{Im}\,\epsilon_2$ due to decreased losses from phonon-assisted absorption (see Sec. 2.6).

2.2.2 Analysis of fundamental mode properties

We now analyze the fundamental mode more carefully. For $m = 0$, one sees in Eq. (2.1) that one of the two terms on the right-hand side must equal zero. It can be shown that setting the first term to zero corresponds to a TE mode, while the other case corresponds to a TM mode (see Appendix A.1). The TE mode equation does not have any solutions, and thus the fundamental mode is a TM mode that satisfies the simplified equation [57, 58]

$$\frac{k_2^2}{k_{2\perp}} \frac{J_0'(k_{2\perp}R)}{J_0(k_{2\perp}R)} - \frac{k_1^2}{k_{1\perp}} \frac{H_0'(k_{1\perp}R)}{H_0(k_{1\perp}R)} = 0. \tag{2.2}$$

The fields themselves are given by (see Appendix A.1)

$$\begin{aligned}
\mathbf{E}_1 &= b_1 \left(\frac{ik_{\|}k_{1\perp}}{k_1^2} H_0'\left(k_{1\perp}\rho\right) \hat{\rho} + \frac{{k_{1\perp}}^2}{k_1^2} H_0\left(k_{1\perp}\rho\right) \hat{z} \right) e^{ik_{\|}z}, \\
\mathbf{E}_2 &= b_2 \left(\frac{ik_{\|}k_{2\perp}}{k_2^2} J_0'\left(k_{2\perp}\rho\right) \hat{\rho} + \frac{{k_{2\perp}}^2}{k_2^2} J_0\left(k_{2\perp}\rho\right) \hat{z} \right) e^{ik_{\|}z}, \\
\mathbf{H}_1 &= \frac{i}{\omega\mu_0} k_{1\perp} b_1 H_0'\left(k_{1\perp}\rho\right) e^{ik_{\|}z} \hat{\phi}, \\
\mathbf{H}_2 &= \frac{i}{\omega\mu_0} k_{2\perp} b_2 J_0'\left(k_{2\perp}\rho\right) e^{ik_{\|}z} \hat{\phi},
\end{aligned} \tag{2.3}$$

while the boundary conditions between the two dielectrics require that

$$\frac{b_1}{b_2} = \frac{k_{2\perp}}{k_{1\perp}} \frac{J_0'(k_{2\perp}R)}{H_0'(k_{1\perp}R)}. \tag{2.4}$$

The $1/R$ dependence of $k_\parallel, k_{i\perp}$ in the nanowire limit can be confirmed mathematically by considering the non-retarded limit, $c \to \infty$. In this case, $k_{i\perp} = \sqrt{k_i^2 - k_\parallel^2} \approx ik_\parallel$ and the mode equation (2.2) reduces to

$$\frac{\epsilon_2}{\epsilon_1} = \frac{K_0'(k_\parallel R) I_0(k_\parallel R)}{K_0(k_\parallel R) I_0'(k_\parallel R)}, \tag{2.5}$$

where I_m, K_m are modified Bessel functions. The solution to Eq. (2.5) requires $k_\parallel R = C$ to be constant and proves the aforementioned scaling law for $k_\parallel$. It is also straightforward to see that when ϵ_2 acquires a small imaginary component, the constant C becomes complex as well, and that $\text{Re } k_\parallel / \text{Im } k_\parallel = \text{Re } C / \text{Im } C$ takes on some fixed, non-zero value. No closed-form solution exists for the equation above, although when $|k_\parallel R| \ll 1$ (corresponding to large $|\epsilon_2/\epsilon_1|$) the equation asymptotically approaches

$$\frac{\epsilon_2}{\epsilon_1} = \frac{2}{(\gamma - \log 2 + \log C)(C)^2}, \tag{2.6}$$

where $\gamma \approx 0.577$ is Euler's constant.

Finally, it should be noted that the components of $\mathbf{E}_i$ in Eq. (2.3) are proportional to $k_\parallel k_{i\perp}$ or $k_{i\perp}^2$, while $\mathbf{H}_i$ is proportional to $k_{i\perp}$. Thus, in the nanowire limit when $k_\parallel, |k_{i\perp}| \propto 1/R$, the magnetic fields are a factor of R smaller than the electric fields, which is consistent with this mode being roughly a quasi-static configuration. More formally, one can attempt to solve for the modes via a perturbative expansion in the system size (or alternatively, the wavevector k_i). Performing this expansion, for example, on the free electrodynamic Green's function for medium i yields

$$G_i(|\mathbf{r}-\mathbf{r}'|,\omega)\sim\frac{e^{ik_i|\mathbf{r}-\mathbf{r}'|-i\omega t}}{|\mathbf{r}-\mathbf{r}'|}\sim\frac{e^{-i\omega t}}{|\mathbf{r}-\mathbf{r}'|}+\mathcal{O}(k_i). \tag{2.7}$$

To lowest order in k_i, the electrodynamic Green's function (aside from the harmonic time dependence) is identical to the electrostatic Green's function. Physically, this approximation implies that the system size is sufficiently small that the phases $e^{ik_i|\mathbf{r}-\mathbf{r}'|}$ are negligible, and thus for small systems one can understand the relevant physics just by solving electrostatic or quasi-static problems.

2.2.3 Interpretation of nanowire as a transmission line

The physical origin of the fundamental mode properties can be further understood by considering the nanowire as a transmission line. While not sufficient for quantitative predictions, this simplified model nonetheless captures the correct scaling behavior of the system.

In a typical transmission line, signals propagate at a velocity that depends simply on the inductance per unit length $\mathcal{L}$ and capacitance per unit length $\mathcal{C}$, $v=1/\sqrt{\mathcal{L}\mathcal{C}}$. For small wires, the magnetic inductance $\mathcal{L}_m$ characterizing the energy stored in the magnetic field becomes negligible. However, there is also a kinetic inductance that is associated with the kinetic energy of massive, moving electrons. We can write down the kinetic energy per unit length as

$$K=\frac{1}{2}mn\pi R^2v^2=\frac{1}{2}\frac{m}{q^2n\pi R^2}I^2=\frac{1}{2}\mathcal{L}_kI^2, \tag{2.8}$$

where m,q, and v are the electron mass, charge, and velocity, respectively, n is the density of electrons, and $I=qn\pi R^2v$ is the current. The kinetic inductance is thus identified to be

$$\mathcal{L}_k = \frac{m}{q^2 n \pi R^2} = \frac{4}{\omega_p^2 R^2}, \tag{2.9}$$

where ω_p is the plasma frequency of the metal. The total effective inductance is simply the sum of the magnetic and kinetic inductances, $\mathcal{L} = \mathcal{L}_m + \mathcal{L}_k$. One sees then that for small wire size, the kinetic inductance dominates the behavior of the system. Physically, this result reflects the fact that for small wires, there are very few electrons available to carry a current. Assuming a typical magnetic inductance $\mathcal{L}_m \sim 1/c^2$, the crossover point when the kinetic inductance starts to dominate is given by $R \sim c/\omega_p$. For small wires, it is then predicted that signals propagate at a velocity

$$v \sim 1/\sqrt{\mathcal{L}_k \mathcal{C}} \sim R\omega_p. \tag{2.10}$$

Here we have for simplicity ignored the logarithmic dependence of $\mathcal{C}$ on wire size and assumed that it is of order unity. The wavevector for the signal is then given by

$$k_{\|} = v/\omega \sim \frac{R\omega_p}{\omega}. \tag{2.11}$$

This result closely agrees with the results from the asymptotically exact expression given in Eq. (2.6). In particular, ignoring the logarithmic contribution in this equation and assuming a Drude model for ϵ_2, one again finds that the SP wavevector should scale like

$$k_{\|} = \frac{C}{R} \sim \frac{1}{R}\sqrt{\frac{1}{|\epsilon_2|}} \sim \frac{R\omega_p}{\omega}. \tag{2.12}$$

2.3 Spontaneous emission near a metal nanowire

The small mode volume associated with the fundamental SP mode of a nanowire offers a possible mechanism to achieve strong coupling with nearby optical emitters.

In this section we derive more rigorously the interaction between an emitter and an infinite, cylindrical nanowire, and show that under certain circumstances the small mode volume leads to strongly preferential spontaneous emission into the guided SP modes via a mechanism equivalent to the Purcell effect in cavity QED [50].

The spontaneous emission rate of a dipole emitter in general becomes altered from its free-space value in the presence of some dielectric body. In our system of interest, the dipole can possibly lose power radiatively to propagating photon modes, through excitation of the guided SP modes, or through non-radiative loss (heating) in the wire. The dipole in consideration can physically be formed by a single atom, a defect in a solid-state system, or any other system with a dipole-allowed transition. In Sec. 2.3.1 we calculate the radiative and non-radiative rates using a quasi-static approach, while waiting until Sec. 2.3.2 to treat the SP decay rate more thoroughly. In Sec. 2.3.3, we show how the efficiency of emission into the SP modes can be optimized to yield Purcell factors in excess of $\sim 10^3$, and discuss the physical origins of this limit.

2.3.1 Radiative and non-radiative decay rates

In this subsection we derive formulas for the decay rates of a dipole near a metal nanowire into radiative and non-radiative channels. This calculation closely follows the method of Ref. [59].

It is well-known that spontaneous emission rates can be obtained via classical calculations of the fields due to an oscillating dipole near the dielectric body [60], and this method will be employed here. Specifically, we consider a (classical) oscillating dipole $\mathbf{p}_0 e^{-i\omega t}$ positioned a distance d from the center of the wire, and wish to calculate the total fields of the system (see Fig. 2.2a). Before proceeding further, we first note that in general the solution will depend on the orientation of the dipole moment in addition to its position. Again taking $\hat{z}$ to be along the axis of the wire, we note that the fundamental SP mode will not couple to a dipole moment $\mathbf{p_0}\propto\hat{\phi}$ oriented along the azimuthal axis, due to the azimuthal symmetry of this mode. In the following calculations for the nanowire, for concreteness we will consider a dipole oriented along the radial direction ($\mathbf{p_0}\propto\hat{\rho}$), while noting that the calculation for an orientation along $\hat{z}$ yields qualitatively similar results. As argued in Sec. 2.2, for nano-structures one can make a simplification by considering the fields in the electrostatic or quasi-static limit ($\mathbf{H}\approx0$), which satisfy

$$\nabla\cdot\mathbf{D} = \rho_{\text{ext}}, \tag{2.13}$$

$$\nabla\times\mathbf{E} = 0. \tag{2.14}$$

Here $\rho_{\text{ext}}(\mathbf{r})$ is the external charge density. In the system of interest the external source is a dipole located at position $\mathbf{r}'$ outside the wire (with radial coordinate $\rho' = d$), so that

$$\rho_{\text{ext}}(\mathbf{r},\mathbf{r}') = (\mathbf{p_0}\cdot\nabla')\,\delta\left(\mathbf{r}-\mathbf{r}'\right). \tag{2.15}$$

For simplicity we omit the harmonic time dependence from our expressions for the source and all fields. Note that the $\delta(\mathbf{r}-\mathbf{r}')$ term above corresponds to a (unitless) point charge source, while the operator $(\mathbf{p_0}\cdot\nabla')$ generally converts the point charge solution to that of a dipole. It is therefore convenient to write $\mathbf{E}_i$ in similar form,

$$\mathbf{E}_i(\mathbf{r},\mathbf{r}') = -\nabla\left(\mathbf{p_0}\cdot\nabla'\right)\Phi_i\left(\mathbf{r},\mathbf{r}'\right), \tag{2.16}$$

where $\Phi_i(\mathbf{r},\mathbf{r}')$ are "pseudopotentials" that satisfy $\nabla^2\Phi_1 = -\delta(\mathbf{r}-\mathbf{r}')/\epsilon_0\epsilon_1$ and

$\nabla^2\Phi_2 = 0$. Here the indices 1, 2 again denote the regions outside and inside the cylinder, respectively. Φ physically corresponds to the potential due to a point charge at $\mathbf{r}'$, while the dipole potential follows from $\Phi_{dip} \equiv (\mathbf{p}_0 \cdot \nabla')\Phi$.

To solve for the fields, it is convenient to further separate Φ_1 into "free" and "reflected" components Φ_0 and Φ_r, respectively, where Φ_r represents a source-free contribution that ensures that boundary conditions are satisfied, and Φ_0 is the solution for a point charge in a medium of uniform electric permittivity ϵ_1. We will expand the known source term Φ_0 in a basis appropriate for the cylindrical geometry, and expand the source-free terms $\Phi_{r,2}$ in a similar basis that satisfies Laplace's Equation ($\nabla^2\Phi_{r,2} = 0$). The unknown coefficients multiplying the basis functions of $\Phi_{r,2}$ will then be determined by enforcing the proper boundary conditions at the dielectric interface. These expansions are given by

$$\begin{aligned}
\Phi_0(\mathbf{r},\mathbf{r}') &= \frac{1}{4\pi\epsilon_0\epsilon_1}\frac{1}{|\mathbf{r}-\mathbf{r}'|} \\
&= \frac{1}{2\pi^2\epsilon_0\epsilon_1}\sum_{m=0}^{\infty}(2-\delta_{m,0})\cos\left(m(\phi-\phi')\right) \\
&\quad \times \int_0^{\infty} dh\cos\left(h(z-z')\right)K_m(h\rho')I_m(h\rho) \quad (\rho<\rho'), \qquad (2.17) \\
\Phi_r(\mathbf{r},\mathbf{r}') &= \frac{1}{2\pi^2\epsilon_0}\sum_{m=0}^{\infty}(2-\delta_{m,0})\cos\left(m(\phi-\phi')\right) \\
&\quad \times \int_0^{\infty} dh\,\alpha_m(h)\cos\left(h(z-z')\right)K_m(h\rho')K_m(h\rho), \qquad (2.18) \\
\Phi_2(\mathbf{r},\mathbf{r}') &= \frac{1}{2\pi^2\epsilon_0}\sum_{m=0}^{\infty}(2-\delta_{m,0})\cos\left(m(\phi-\phi')\right) \\
&\quad \times \int_0^{\infty} dh\,\beta_m(h)\cos\left(h(z-z')\right)K_m(h\rho')I_m(h\rho), \qquad (2.19)
\end{aligned}$$

where $\alpha_m(h), \beta_m(h)$ thus far are unknown amplitude coefficients. We obtain a set of two coupled equations for $\alpha_m(h), \beta_m(h)$ by requiring continuity of Φ and $\mathbf{D}_\perp$ at the boundary, $\rho = R$. Because of the translational symmetry of the system, these equations are uncoupled in h and can easily be solved (this is in contrast to the case where translational symmetry is broken due to surface roughness, as discussed in Sec. 2.6). The solutions are given by [59]

$$\begin{aligned} \alpha_m(h) &= \frac{(\epsilon-1)\, I_m'(hR) I_m(hR)}{\epsilon_1 I_m(hR) K_m'(hR) - \epsilon_2 K_m(hR) I_m'(hR)}, \\ \beta_m(h) &= \frac{I_m(hR) K_m'(hR) - K_m(hR) I_m'(hR)}{\epsilon_1 I_m(hR) K_m'(hR) - \epsilon_2 K_m(hR) I_m'(hR)}, \end{aligned} \tag{2.20}$$

where we have defined $\epsilon \equiv \epsilon_2/\epsilon_1$. Note that Eq. (2.20) along with Eqs. (2.17)-(2.19) give the total electric field of the dipole and wire system.

To calculate the radiative emission into free space, we consider the far-field properties of the system. Physically, the presence of the emitter induces some dipole moment $\delta\mathbf{p}$ in the nanowire, which results in a total radiated power proportional to the square of the total dipole moment of the system, $P_{\text{rad}} \propto \Gamma_{\text{rad}} \propto |\mathbf{p}_0 + \delta\mathbf{p}|^2$. We can determine $\delta\mathbf{p}$ by finding the dipole-like contribution to the "reflected" potential $\Phi_{dip,r} = (\mathbf{p}_0 \cdot \nabla')\Phi_r(\mathbf{r},\mathbf{r}')$ far away from the source, which on physical grounds must behave like ρ^{-2} for large ρ. It is straightforward to show that the $m = 1$ term in Eq. (2.18) is responsible for this contribution, with all other m terms yielding faster decays in ρ. Because of the asymptotic behavior of $K_m(x) \approx \sqrt{\pi/2x}\, e^{-x}$ when $x \gg 1$, for large ρ the integrand in (2.18) is significant only over a small region $h \lesssim \rho^{-1}$. As a result, we can safely replace $K_1(h\rho')$ and $\alpha_1(h)$ by their expansions around $h = 0$. After this simplification the integral can in fact be evaluated exactly and yields

$$\Phi_r^{(m=1)} \approx -\frac{1}{4\pi\epsilon_0\epsilon_1}\frac{\epsilon-1}{\epsilon+1}\cos(\phi-\phi')\,\frac{R^2}{\rho'}\frac{\rho}{(\rho^2+(z-z')^2)^{3/2}}, \tag{2.21}$$

with a corresponding reflected potential

$$\begin{aligned}\Phi_{dip,r}^{(m=1)}(\mathbf{r},\mathbf{r}') &= (\mathbf{p}_0\cdot\nabla')\,\Phi_r^{(m=1)}(\mathbf{r},\mathbf{r}') \\ &\approx \frac{p_0}{4\pi\epsilon_0\epsilon_1}\frac{\epsilon-1}{\epsilon+1}\cos(\phi-\phi')\,\frac{R^2}{d^2}\frac{\rho}{(\rho^2+z^2)^{3/2}},\end{aligned}\tag{2.22}$$

for the choice of parameters $\rho'=d$, $z'=0$, and $\mathbf{p}_0=p_0\hat{\rho}$. Comparing Eq. (2.22) to the potential due to a dipole $\delta\mathbf{p}$ in uniform dielectric ϵ_1, $V_{\delta\mathbf{p}}=\frac{\delta\mathbf{p}\cdot\mathbf{r}}{4\pi\epsilon_0\epsilon_1 r^3}$, we can readily identify

$$\delta\mathbf{p}=p_0\frac{\epsilon-1}{\epsilon+1}\frac{R^2}{d^2}\hat{\rho}\tag{2.23}$$

as the induced dipole moment in the wire, from which it follows that the radiative spontaneous emission rate is given by [59]

$$\frac{\Gamma_{\text{rad}}}{\Gamma_0}=\left|1+\frac{\epsilon-1}{\epsilon+1}\frac{R^2}{d^2}\right|^2.\quad (d\gtrsim R)\tag{2.24}$$

Here $\Gamma_0=\sqrt{\epsilon_1}\Gamma_v$ is defined to be the spontaneous emission rate of the emitter in uniform dielectric ϵ_1, and Γ_v is the spontaneous emission rate in vacuum. Here we have ignored possible local-field corrections in defining the emission rate in a dielectric [61]. Away from the plasmon resonance ($\epsilon\approx-1$), the radiative decay rate changes slightly from Γ_0 and reflects some moderate change in the radiative density of states in the vicinity of the nanowire.

To calculate the other decay rates, one utilizes the fact that the total power loss of an oscillating dipole is proportional to the electric field in quadrature at the dipole's location, specifically, $\Gamma_{\text{total}}\propto\text{Im}\,(\mathbf{p}_0\cdot\mathbf{E}_1(\mathbf{r}',\mathbf{r}'))$. Having divided up $\mathbf{E}_1$ into free and reflected components, the contribution to $\mathbf{E}_1$ from the free field simply is associated with the decay rate in uniform dielectric ϵ_1, and thus we concentrate on the contribution from $\Phi_r(\mathbf{r},\mathbf{r}')$. First we note that the coefficient $\alpha_0(h)$ derived in Eq. (2.20) contains a pole at the point where the denominator vanishes. This pole corresponds to an excitation of a natural mode (the fundamental SP mode) of the system. This can immediately be seen by comparing the denominator of α_0 to Eq. (2.5), which gives the SP mode in the nanowire limit. The pole lies at $h = C/R$ and agrees with the SP wavevector derived in Sec. 2.2, as expected. Evaluating the contribution of this pole to $\mathbf{E}_r(\mathbf{r}', \mathbf{r}')$ gives the decay rate into the fundamental SP mode, and is discussed more carefully in the next subsection. At the same time, in the limit $d \rightarrow R$ one expects some type of divergence to occur in the non-radiative decay rate. Physically, as the emitter approaches the wire edge, the divergence results from the large currents in the wire generated by the near-field of the dipole and their resulting dissipation. We can find the leading-order term to this divergent decay rate by carefully evaluating the leading-order divergence in the reflected field.

The mathematical origin of the divergence as $d \rightarrow R$ is the significant contribution to Φ_r of an infinite number of terms in m. Specifically, in this limit, for a dipole oriented along $\hat{\rho}$,

$$\begin{aligned}
\frac{\Gamma_{\text{non-rad}}}{\Gamma_0} &\approx \frac{6\pi\epsilon_0}{k_0^3\sqrt{\epsilon_1}} \frac{\text{Im}\,\hat{\rho}\cdot\mathbf{E}_r(\mathbf{r}',\mathbf{r}')}{p_0} \\
&= -\frac{6\pi\epsilon_0}{k_0^3\sqrt{\epsilon_1}} \text{Im}\,\hat{\rho}\cdot\nabla\left(\hat{\rho}\cdot\nabla'\right)\Phi_r(\mathbf{r},\mathbf{r}')\Big|_{\mathbf{r}=\mathbf{r}'} \\
&\approx -\frac{6}{\pi k_0^3\sqrt{\epsilon_1}} \sum_{m=1}^{\infty} \int_0^{\infty} dh\, h^2 K_m'(hd)^2 \text{Im}\,\alpha_m(h) \\
&\equiv \frac{6}{\pi k_0^3\sqrt{\epsilon_1}} \sum_{m=1}^{\infty} \int_0^{\infty} dh\, f_m(h,d,R). \qquad (2.25)
\end{aligned}$$

The asymptotic behavior of the functions f_m is given by

$$f_m(h,d,R) \approx \begin{cases} \dfrac{m}{2d^2\epsilon_1}\mathrm{Im}\left(\dfrac{\epsilon-1}{\epsilon+1}\right)\left(\dfrac{R}{d}\right)^{2m} & h\to 0 \\ \dfrac{h}{2d\epsilon_1}\mathrm{Im}\left(\dfrac{\epsilon-1}{\epsilon+1}\right)e^{-2h(d-R)} & h\to\infty \end{cases} . \tag{2.26}$$

From the above expressions, we see that f_m as a function of h has a characteristic width of about $[2(d-R)]^{-1}$, yet at the same time the quantity $m(R/d)^{2m}$ reaches a maximum around $\tilde{m} \approx \frac{d}{2(R-d)}$ as $d \to R$. This confirms the non-vanishing contribution of an infinite number of terms in m to the decay rate. The exact behavior of the functions f_m is well-modelled by a Lorentzian approximation,

$$f_m(h,d,R) \approx \frac{\frac{m}{2d^2\epsilon_1}\mathrm{Im}\left(\frac{\epsilon-1}{\epsilon+1}\right)\left(\frac{R}{d}\right)^{2m}}{1+h^2(d-R)^2}, \tag{2.27}$$

which allows the integration and sum in Eq. (2.25) to be performed exactly. The resulting decay rate is given by

$$\frac{\Gamma_{\text{non-rad}}}{\Gamma_0} \approx \frac{3}{16k_0^3(d-R)^3\epsilon_1^{3/2}}\mathrm{Im}\left(\frac{\epsilon-1}{\epsilon+1}\right). \tag{2.28}$$

Note that for $|\epsilon| \gg 1$ and small $\mathrm{Im}\,\epsilon$, $\mathrm{Im}\left(\frac{\epsilon-1}{\epsilon+1}\right) \approx 2\,\mathrm{Im}\,\epsilon/(\mathrm{Re}\,\epsilon)^2$, which makes it clear that the non-radiative spontaneous emission rate is proportional to the dissipative part of the electric permittivity.

2.3.2 Decay rate into surface plasmon modes

In this subsection we quantify the spontaneous emission rate Γ_{pl} of a dipole into the surface plasmon modes on a nanowire, by evaluating the contribution of the pole in $\alpha_0(h)$ to the field seen by the dipole. Before proceeding further, we first note that in the presence of metal losses, the distinction between Γ_{pl} and $\Gamma_{\text{non-rad}}$ is not perfectly well-defined, since the SPs eventually dissipate due to heating as well. Thus, for concreteness, we will define Γ_{pl} to be the decay rate resulting from the pole in the limit that $\text{Im}\,\epsilon_2 = 0$, and take the SP wavevector $k_{\|}$ and C to be purely real in this subsection. In particular, for a dipole oriented along $\hat{\rho}$,

$$\begin{aligned}\frac{\Gamma_{\text{pl}}}{\Gamma_0} &= \frac{6\pi\epsilon_0}{k_0^3\sqrt{\epsilon_1}}\left(\frac{\text{Im}\,\hat{\rho}\cdot\mathbf{E}_r(\mathbf{r}',\mathbf{r}')}{p_0}\right)_{pole} \\ &= -\frac{6\pi\epsilon_0}{k_0^3\sqrt{\epsilon_1}}\text{Im}\left(\hat{\rho}\cdot\nabla\left(\hat{\rho}\cdot\nabla'\right)\Phi_r(\mathbf{r};\mathbf{r}')|_{\mathbf{r}=\mathbf{r}'}\right)_{pole} \\ &= -\frac{3}{\pi k_0^3\sqrt{\epsilon_1}}\text{Im}\left(\int_0^\infty dh\, h^2 K_1^2(hd)\alpha_0(h)\right)_{pole}, \end{aligned} \tag{2.29}$$

where we have explicitly indicated that we are interested in the pole contribution to the expressions above. The behavior of $\alpha_0(h)$ around the pole's vicinity is given by

$$\alpha_0(h) \approx \frac{1}{\epsilon_1}\frac{(\epsilon_2-\epsilon_1)I_1(C)I_0(C)}{(h-C/R)R\frac{d\chi(C)}{dx}}, \tag{2.30}$$

where

$$\chi(x) = \epsilon_1 I_0(x)K_0'(x) - \epsilon_2 K_0(x)I_0'(x). \tag{2.31}$$

Substituting this into Eq. (2.29) then yields the decay rate

$$\begin{aligned}\Gamma_{\text{pl}} &= \alpha_{\text{pl}}\Gamma_0\frac{K_1^2(Cd/R)}{(k_0R)^3} \\ &\approx \alpha_{\text{pl}}\Gamma_0\frac{K_1^2(\kappa_{1\perp}d)}{(k_0R)^3}, \end{aligned} \tag{2.32}$$

where we have identified $\kappa_{1\perp}{\approx}C/R$ in the nanowire limit. The coefficient α_{pl} is given by

$$\alpha_{\text{pl}} = \frac{3(\epsilon_1-\epsilon_2)}{\epsilon_1^{3/2}}\frac{C^2 I_1(C)I_0(C)}{d\chi(C)/dx} \tag{2.33}$$

and most importantly depends only on $\epsilon_{1,2}$.

The $\sim(1/R)^3$ scaling of the spontaneous emission rate into SPs indicates that this process can be strongly enhanced by using a small wire. One can gain some physical understanding of the result and its relation to the Purcell effect in cavity QED by considering the quantum mechanical derivation of the spontaneous emission rate via Fermi's Golden Rule. This rule states that, once the SP modes are quantized, the decay rate is given by

$$\Gamma_{\text{pl}} = 2\pi g^2(\mathbf{r},\omega)D(\omega), \tag{2.34}$$

where $g(\mathbf{r},\omega)$ is the position-dependent, dipole-field interaction matrix element, and $D(\omega)$ is the SP density of states on the nanowire. Here, $g(\mathbf{r},\omega) = \vec{\wp}\cdot\vec{\mathcal{E}}(\mathbf{r})/\hbar$ itself depends on the dipole matrix element $\vec{\wp} = \langle e|e\mathbf{r}|g\rangle$ of the emitter, where $|g\rangle$ ($|e\rangle$) is the ground (excited) state involved in the transition, and on the electric field per photon $\vec{\mathcal{E}}(\mathbf{r})$ for the SP modes. On dimensional grounds, the electric field per photon can be written in the form $\vec{\mathcal{E}}(\mathbf{r}) = \sqrt{\hbar\omega/\epsilon_0 V_{\text{eff}}}\,(\mathbf{E}(\mathbf{r})/E_{max})$, where V_{eff} is an effective mode volume characterizing the confinement of each mode, $\mathbf{E}(\mathbf{r})$ is the classical field profile for the SP modes given in Eq. (2.3), and $E_{max} = \max|\mathbf{E}(\mathbf{r})|$. The mode volume can be estimated by normalizing the field energy to one quantum (again, ignoring $\text{Im}\,\epsilon_2$);

$$\hbar\omega \sim L\int d^2\rho\,\epsilon_0\frac{d}{d\omega}\left(\omega\epsilon(\rho,\omega)\right)\left|\vec{\mathcal{E}}(\rho)\right|^2. \tag{2.35}$$

Here the two-dimensional integral is performed over the directions transverse to the wire axis, and L is the quantization length, set by the wire length, which is assumed to be much longer than all other relevant length scales. In the end L will disappear from the physical quantities of interest (*e.g.*, the spontaneous emission rate). The integrand appearing in Eq. (2.35) gives the correct expression for the classical electric energy density for a field in a dispersive medium [54]. Because the fields are primarily electric in the nanowire limit, we have safely ignored the magnetic field contribution to the energy density. Performing this normalization for the fundamental SP modes, one finds that $V_{\text{eff}} \propto R^2 L$, which physically implies that these modes are transversely confined to an area on the order of the wire size. The constant of proportionality depends only on the electric permittivities of the system. For a dipole oriented along $\hat{\rho}$, one then finds that $g^2(\mathbf{r}) \propto K_1^2(\kappa_{1\perp} d)/(R^2 L)$, which shows that the strong field-emitter coupling directly arises from the tight field confinement. At the same time, the density of states for the SP modes is given by $D(\omega) \sim (L/2\pi)(dk_{\parallel}/d\omega)$, and is inversely proportional to the group velocity. The group velocity for SPs is strongly reduced due to the large SP wavevector $k_{\parallel} \propto 1/R$ on a nanowire, and consequently this gives rise to a $\sim 1/R$ enhancement in the density of states. Combining all of these results into Eq. (2.34) yields

$$\Gamma_{\text{pl}} \propto \Gamma_0 \frac{K_1^2(\kappa_{1\perp} d)^2}{(k_0 R)^3}, \tag{2.36}$$

where again the constant of proportionality depends only on the electric permittivities. We emphasize that in the quantum mechanical interpretation, one achieves a factor of $\sim 1/R$ enhancement in the spontaneous emission rate due to a reduction in the SP group velocity, and a $\sim 1/R^2$ enhancement due to the small effective mode area.

2.3.3 Purcell factor of a nanowire

Comparing the spontaneous emission rates given by Eqs. (2.24), (2.28), and (2.32), we now qualitatively discuss the behavior one should expect as the position of the emitter is varied. In the limit that $d/R \gg 1$, the emitter feels no effect from the

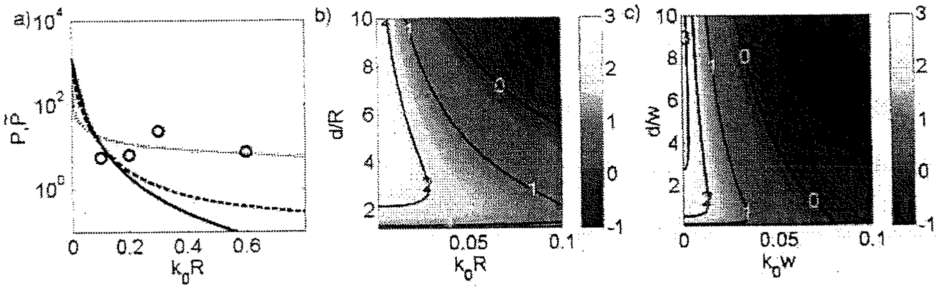

Figure 2.5: a) Solid line: Maximum Purcell factor $P = \Gamma_{\text{pl}}/\Gamma'$ for a nanowire, plotted as a function of R and optimized over the emitter position. Here P is calculated in the quasi-static approximation. Dashed line: same quantity, obtained by exact electrodynamic calculations. Dotted line: Effective Purcell factor, $\tilde{P}(R) = \tilde{\Gamma}_{\text{pl}}(R)/\tilde{\Gamma}'(R)$ for a nanotip of final radius R, optimized over nanotip shape and emitter position. Solid points: same quantity, calculated using numerical simulations (boundary element method). b) Contour plot of $\log_{10} P$ for a nanowire, as functions of R and d/R. c) Contour plot of $\log_{10} P$ for a nanotip, as functions of w and d/w.

wire and the total spontaneous emission rate is close to the radiative rate Γ_0 in a uniform dielectric medium. As one brings the emitter closer to the wire surface, the change in the electromagnetic mode structure near the wire results in some modified radiative decay rate Γ_{rad} which never exceeds approximately $4\Gamma_0$ for large $|\epsilon|$. When the emitter position d approaches $d{\sim}1/\kappa_{1\perp}{\sim}R/|C|$, the emitter starts to interact with the localized SP fields, with a corresponding rate of emission into SPs scaling with wire size like $1/R^3$. The emission rate into SPs continues to grow as the emitter is brought even closer to the wire edge, $d{\rightarrow}R$. However, the efficiency or probability of SP excitation eventually decreases due to the large non-radiative decay rate experienced by the dipole very near the wire, which diverges like $1/(d-R)^3$. We thus expect some optimal efficiency of spontaneous emission into the SP modes to occur when the emitter is positioned at a distance $\mathcal{O}(R)$ away from the wire edge, and for this optimal efficiency to improve as $R{\rightarrow}0$.

The efficiency of coupling to the SP modes can be characterized by a "Purcell factor" that is defined by the ratio $P = \Gamma_{\text{pl}}/\Gamma'$, where $\Gamma' = \Gamma_{\text{rad}} + \Gamma_{\text{non-rad}}$ denotes the total emission rate into channels other than the fundamental SP mode. Generally P depends on both the wire size and on the position d of the emitter. In Fig. 2.5a, we have numerically evaluated the spontaneous emission rates and plotted the Purcell factor as a function of wire radius R, optimized over the emitter position. As $R \rightarrow 0$, the optimized Purcell factor P exceeds $\sim 10^3$, indicating that the probability of emission into the SPs approaches almost unity. Examining this limit more carefully, it can be shown that the "error rate" in fact approaches a small quantity $\Gamma'/\Gamma_{\text{total}} \propto \text{Im}\ \epsilon/(\text{Re}\ \epsilon)^2$, which explicitly indicates that this process is ultimately limited by material losses. Again, we emphasize that these properties are specifically a result of the conducting properties of the nanowire. This can be contrasted with emission into the guided modes of a sub-wavelength optical fiber, which drops exponentially as $R \rightarrow 0$ due to the weak confinement of these guided modes [59].

Finally, we note that while the decay rates obtained in the quasi-static approximation provide a simple understanding of the system, the quantitative predictions may begin to break down even for moderate-sized wires (when $|k_1|R \gtrsim 1$). Physically, the effective mode area A_{eff} and group velocity $d\omega/dk_{\parallel}$ start to scale more slowly than $\sim R^2$ and $\sim R$, respectively, for moderate-sized wires. The quasi-static approximation can then significantly underestimate the decay rate into SPs, Γ_{pl}, and the corresponding Purcell factors. This may be important experimentally, for example, since it implies that one need not resort to very small wires to achieve moderate Purcell factors. Thus, using the electrodynamic Green's function methods of Refs .[59, 62], we have also obtained exact electrodynamic solutions of the fields created by an oscillating dipole near a cylinder, and used these solutions to find the corresponding decay rates. While technically more difficult, as one must now solve vector field equations, the general principles such as field expansion in a basis and determination of field amplitudes based on boundary conditions remain similar. The details of the calculation are given in Appendix B.2. In Fig. 2.5a, we have plotted the numerically optimized Purcell factors using these exact electrodynamic results. It can be seen that the quasi-static and exact results agree well in the nanowire limit, but for larger wires, the exact results predict significantly larger values of P. In Fig. 2.5b, we plot the Purcell factor as functions of both wire size and emitter position (using the exact results). Here it can be seen that achieving a large Purcell factor does not depend too sensitively on the placement of the emitter, which indicates that the strong coupling is a robust effect.

2.4 Spontaneous emission near a nanotip

In Sections 2.2 and 2.3 we derived and discussed the physics of SP modes on a nanowire and spontaneous emission of a nearby dipole emitter. It was seen that the tight transverse confinement of the SP modes leads to a large Purcell factor for an optimally positioned dipole emitter as the wire size decreases. At the same time, however, it is evident that the tighter confinement is accompanied by enhanced losses as the SP propagates, and also a large reduction in the SP wavelength λ_{pl} that could make out-coupling more difficult. Such factors could clearly impose limits for applications such as quantum information, but can be circumvented with simple design improvements. In this section, we investigate one specific design, a metallic nanotip (see Fig. 2.2b). As in the nanowire case, one expects a sub-wavelength SP mode volume, determined in this case by the tip curvature, and an associated enhancement of emission into the SP modes. Here, however, one expects propagative losses to be less severe, because the SPs will become less tightly confined as they propagate along the expanding tip. This expansion also results in a gradual increase in the SP wavelength along the nanotip. For the nanotip, we are not able to obtain full electrodynamic solutions for the SP modes, as the electrodynamic problem is not separable. However, in a manner similar to that described in Sec. 2.3, we will calculate all of the relevant decay rates in the quasi-static limit (which is separable) and describe an approximate method to calculate the propagative losses along the nanotip. We will also compare these results to those obtained via fully electrodynamic numerical simulations, and we find that these two approaches agree closely.

In the following we will consider a nanotip whose surface can be parameterized as a paraboloid of revolution with symmetry along the z-axis (see Fig. 2.2b). Specifically, we suppose that the surface of the nanotip is described by

$$z = \frac{1}{2}\left(\frac{x^2+y^2}{v_0^2} - v_0^2\right), \tag{2.37}$$

a paraboloid of revolution with apex at $z = -v_0^2/2$ (the reason for the offset of the apex will become apparent below). We now introduce a transformation to parabolic coordinates,

$$\begin{aligned} x &= uv\cos\phi, \\ y &= uv\sin\phi, \end{aligned}$$

$$z = \frac{1}{2}\left(u^2 - v^2\right). \tag{2.38}$$

While these coordinates may seem awkward (note, for example, that u, v have units of $\sqrt{length}$), they are convenient for deriving expressions for the fields and spontaneous emission rates, which we will then express in more "natural" coordinates at the end of the calculation. In parabolic coordinates, the nanotip profile of Eq. (2.37) is defined by a surface of constant $v = v_0$. More generally, any constant v defines some paraboloid of revolution in this system, while the unit vectors $\hat{u}$ and $\hat{v}$ run normally and tangentially to these surfaces, respectively.

Now, as in the nanowire case, we are interested in finding the quasistatic field solution for a point charge source in the vicinity of the nanotip, from which we can obtain the field due to a dipole $\mathbf{p}_0$. In particular, we seek solutions of the total field of the form (2.16) with appropriate boundary conditions. Like before, we separate the pseudopotential Φ_1 outside the nanotip into its free and reflected components $\Phi_{0,r}$, and use an integral representation of the free pseudopotential suitable for parabolic coordinates,

$$\begin{aligned}\Phi_0(\mathbf{r}, \mathbf{r}') &= \frac{1}{2\pi\epsilon_0\epsilon_1}\sum_{m=0}^{\infty}(2 - \delta_{m,0}) \cos m(\phi - \phi') \times \\ &\int_0^{\infty} dq\, q J_m(qu) J_m(qu') I_m(qv) K_m(qv'). \quad (v < v')\end{aligned} \tag{2.39}$$

Here the primed coordinates denote the position of the dipole. Because Φ_0 fully accounts for the point source, $\Phi_{r,2}$ then satisfy Laplace's Equation. Using separation of variables, it is straightforward to show that the solutions to Laplace's Equation are given in parabolic coordinates by $\sim J_m(qu) G_{i,m}(qv) e^{im\phi}$, where $G_{1,m}(qv) = K_m(qv)$ and $G_{2,m}(qv) = I_m(qv)$ are non-divergent functions in their regions of applicability.

We then define the following expansions,

$$\begin{aligned}\Phi_r(\mathbf{r},\mathbf{r}') &= \frac{1}{2\pi\epsilon_0\epsilon_1}\sum_{m=0}^{\infty}(2-\delta_{m,0})\cos m(\phi-\phi')\times \\ &\quad \int_0^\infty dq\, q\alpha_m(q)J_m(qu')K_m(qv')J_m(qu)K_m(qv), \qquad (2.40)\\ \Phi_2(\mathbf{r},\mathbf{r}') &= \frac{1}{2\pi\epsilon_0\epsilon_1}\sum_{m=0}^{\infty}(2-\delta_{m,0})\cos m(\phi-\phi')\times \\ &\quad \int_0^\infty dq\, q\beta_m(q)J_m(qu')K_m(qv')J_m(qu)I_m(qv), \qquad (2.41)\end{aligned}$$

where the coefficients α, β are determined by imposing boundary conditions at the nanotip surface $v = v_0$. Enforcing the continuity of Φ and $\mathbf{D}_\perp$ yields

$$\begin{aligned}\alpha_m(q) &= \frac{(\epsilon_1-\epsilon_2)I'_m(qv_0)I_m(qv_0)}{\epsilon_2 I'_m(qv_0)K_m(qv_0)-\epsilon_1 I_m(qv_0)K'_m(qv_0)}, \qquad (2.42)\\ \beta_m(q) &= \frac{-\epsilon_1\left(I_m(qv_0)K'_m(qv_0)-I'_m(qv_0)K_m(qv_0)\right)}{\epsilon_2 I'_m(qv_0)K_m(qv_0)-\epsilon_1 I_m(qv_0)K'_m(qv_0)}. \qquad (2.43)\end{aligned}$$

Note that the coefficients $\alpha_m(q)$, along with Eq. (2.40), completely determine the reflected field.

The calculation of the radiative and non-radiative spontaneous emission rates proceeds in the same manner as the nanowire case. To calculate Γ_{rad}, we again look for a dipole term in the far-field (large v) that corresponds to an induced dipole moment $\delta\mathbf{p}$ in the nanotip, and then use the relationship $\Gamma_{\text{rad}}\propto|\mathbf{p}_0+\delta\mathbf{p}|^2$. At the same time, we look for a divergent contribution to the reflected field at the dipole location as its position v' approaches v_0, which yields the leading term of the non-radiative decay rate through $\Gamma_{\text{non-rad}}\propto\text{Im}(\mathbf{p}_0\cdot\mathbf{E}_r(\mathbf{r}',\mathbf{r}'))$. For concreteness we will consider a dipole that is located along the z-axis ($u'=0$, also see Fig. 2.2b), which yields

$$\mathbf{p}_0\cdot\mathbf{E}_r(\mathbf{r}',\mathbf{r}') = -\frac{p_0^2}{4\pi\epsilon_0\epsilon_1}\int_0^\infty dq\,\frac{q^3}{v'^2}\alpha_1(q)K_1^2(qv'), \qquad (\mathbf{p}_0\perp\hat{z})$$

$$\mathbf{p}_0 \cdot \mathbf{E}_r(\mathbf{r}', \mathbf{r}') = -\frac{p_0^2}{2\pi\epsilon_0\epsilon_1}\int_0^\infty dq\, \frac{q^3}{v'^2}\alpha_0(q)K_1^2(qv'), \qquad (\mathbf{p}_0 \parallel \hat{z}) \qquad (2.44)$$

as shown in Appendix B. Because of the similarity of the decay rate calculations with those in Sec. 2.3, we simply state the results here, while providing more details in Appendix B. For a dipole positioned along the z-axis at $v = v'$, the radiative and non-radiative spontaneous emission rates are given by

$$\begin{aligned}\frac{\Gamma_{\text{rad}}}{\Gamma_0} &= \left|1 - \frac{v_0^2}{v'^2}\left(1 - \frac{\epsilon_2}{\epsilon_1}\right)\right|^2, \qquad (\mathbf{p}_0 \parallel \hat{z}) \\ \frac{\Gamma_{\text{rad}}}{\Gamma_0} &= \left|1 + \frac{\epsilon_1 - \epsilon_2}{\epsilon_1 + \epsilon_2}\frac{v_0^2}{v'^2}\right|^2, \qquad (\mathbf{p}_0 \perp \hat{z}) \qquad (2.45)\end{aligned}$$

and

$$\begin{aligned}\Gamma_{\text{non-rad}}/\Gamma_0 &\approx \frac{3}{16k_0^3\epsilon_1^{3/2}}\frac{1}{v'^3(v'-v_0)^3}\text{Im}\left(\frac{\epsilon_2-\epsilon_1}{\epsilon_2+\epsilon_1}\right), \qquad (\mathbf{p}_0 \perp \hat{z}) \\ \Gamma_{\text{non-rad}}/\Gamma_0 &\approx \frac{3}{8k_0^3\epsilon_1^{3/2}}\frac{1}{v'^3(v'-v_0)^3}\text{Im}\left(\frac{\epsilon_2-\epsilon_1}{\epsilon_2+\epsilon_1}\right). \qquad (\mathbf{p}_0 \parallel \hat{z}) \qquad (2.46)\end{aligned}$$

Finally we consider the decay rate into the fundamental SP mode of the nanotip, which is associated with the contribution of the poles in the integrand of Eq. (2.44) to $\text{Im}\,(\mathbf{p}_0 \cdot \mathbf{E}_r(\mathbf{r}', \mathbf{r}'))$. Examining the solutions to $\alpha_{0,1}$ given in Eq. (2.42), one finds that α_1 has no pole in the range $0 \leq q \leq \infty$. Physically, the absence of a pole means that a dipole simultaneously oriented perpendicular to $\hat{z}$ and located along the z-axis does not excite the fundamental SP mode of the nanotip. This is easily understood since a dipole oriented this way is anti-symmetric with respect to 180° rotations about $\hat{z}$, while the SP mode is symmetric. On the other hand, α_0 does have a pole corresponding to SP excitation. This pole is located at $q_0 = C/v_0$, where C happens to be the solution to Eq. (2.5). q_0 can be considered to be the "wavevector" of the fundamental mode (albeit in parabolic coordinates). Evaluating the contribution of this pole to the field is straightforward and yields a SP decay rate

$$\frac{\Gamma_{\text{pl}}}{\Gamma_0} = \frac{3\pi}{k_0^3\epsilon_1^{3/2}}\frac{C^3}{v_0^4 v'^2}K_1^2(q_0 v')\frac{(\epsilon_1-\epsilon_2)I_1(C)I_0(C)}{d\chi(C)/dx}, \qquad (\mathbf{p_0}\parallel\hat{z}) \tag{2.47}$$

$$\frac{\Gamma_{\text{pl}}}{\Gamma_0} = 0, \qquad (\mathbf{p_0}\perp\hat{z}) \tag{2.48}$$

where $\chi(x)$ is defined in Eq. (2.31). As in the nanowire case, the decay rate Γ_{pl} into the SP mode given by Eq. (2.47) is evaluated in the limit that $\text{Im}\,\epsilon_2 = 0$, such that q_0 and C in Eq. (2.47) are considered to be purely real.

Having derived the decay rates in parabolic coordinates, we now define a more natural set of parameters to describe the system (see Fig. 2.2b). Let us introduce a length scale w that characterizes the curvature of the nanotip via $\rho(z) = \sqrt{wz}$ $(z \geq 0)$, where ρ is the radius of the nanotip at position z (note also the corresponding shift in the apex of the tip from $z = -v_0^2/2$ to $z = 0$). Furthermore, let $z = -d < 0$ be the position of the emitter ($d = (v'^2 - v_0^2)/2$ is the distance between the emitter and end of the nanotip). In terms of these parameters, the spontaneous emission rates derived above for a dipole $\mathbf{p_0} \propto \hat{z}$ positioned along the z-axis can be re-written as

$$\frac{\Gamma_{\text{rad}}}{\Gamma_0} = \left|1+(1+4d/w)^{-1}\left(\frac{\epsilon_2}{\epsilon_1}-1\right)\right|^2, \tag{2.49}$$

$$\frac{\Gamma_{\text{non-rad}}}{\Gamma_0} = \frac{3}{8\epsilon_1^{3/2}}\frac{1}{(k_0 d)^3}\text{Im}\left(\frac{\epsilon_2-\epsilon_1}{\epsilon_2+\epsilon_1}\right), \tag{2.50}$$

$$\frac{\Gamma_{\text{pl}}}{\Gamma_0} = \tilde{\alpha}_{\text{pl}}\frac{1}{(k_0 w)^3(1+4d/w)}K_1^2(C\sqrt{1+4d/w}), \tag{2.51}$$

where $\tilde{\alpha}_{\text{pl}}$ only depends on $\epsilon_{1,2}$ and is given by

$$\tilde{\alpha}_{\text{pl}} = \frac{24\pi}{\epsilon_1^{3/2}}C^3\frac{(\epsilon_1-\epsilon_2)I_1(C)I_0(C)}{d\chi(C)/dx}. \tag{2.52}$$

As in the nanowire case, one can define a Purcell factor $P = \Gamma_{\text{pl}}/\Gamma'$ for the nanotip, which depends on the curvature parameter w and emitter position d. Optimization of the Purcell factor over the emitter position yields a large enhancement of $P{\approx}2.5\times10^3$ as $w{\rightarrow}0$, which is limited ultimately by dissipation in the metal. In Fig. 2.5c, we plot P as functions of w and d. Once again, it can be seen that achieving large Purcell factors does not depend too sensitively on the emitter position.

To compare the benefits of the nanotip over the nanowire, the relevant quantity is not just the Purcell factor but how efficiently the generated SPs can propagate from the end to some larger radius R further down the tip (see Fig. 2.2b). Because the SP modes here were obtained through a quasistatic approximation, this calculation yields no information about dissipative losses as the SP propagates along the nanotip. For example, in this limit $\mathbf{H}{\approx}0$ so one cannot obtain the Poynting vector for the system. To estimate the effect of propagative losses, however, we can make an eikonal approximation [63], assuming that the SPs are emitted completely into the end of the tip ($z=0$), and that the propagative losses thereafter at any position z are identical locally to those of a nanowire of radius $\rho(z)$. Specifically, the fraction of the total SP emission that successfully propagates from the end to some larger radius R is estimated to be

$$\frac{\tilde{\Gamma}_{\text{pl}}(R)}{\Gamma_{\text{pl}}}=\exp\left(-2\int_{0}^{z(R)}\text{Im}\,k_{\|}(\rho(z))dz\right). \tag{2.53}$$

Whereas Γ_{pl} is the spontaneous emission rate into the SPs, $\tilde{\Gamma}_{\text{pl}}(R)$ is the rate that these emitted SPs successfully propagate to radius R. It is also convenient to define an effective decay into other channels, $\tilde{\Gamma}'(R)=\Gamma'+(\Gamma_{\text{pl}}-\tilde{\Gamma}_{\text{pl}}(R))$, which includes the rate at which emitted SPs are dissipated before reaching R. Similarly, we define an effective Purcell factor for the nanotip, given by $\tilde{P}(R)=\tilde{\Gamma}_{\text{pl}}(R)/\tilde{\Gamma}'(R)$, which characterizes the efficiency that SPs are generated and propagate successfully to R.

In general this quantity depends both on the emitter position and the curvature of the nanotip. In Fig. 2.5a we plot $\tilde{P}(R)$, when optimized over w and d. It can be seen that the effective Purcell factor for the nanotip compares favorably to the Purcell factor of a nanowire when $k_0 R \gtrsim 0.05$. In other words, the nanotip makes it possible to use these larger sizes to reduce dissipation, without as steep a tradeoff in the efficiency of coupling to the SPs. We note that the nanotip system also has the added benefit of generating guided SPs along a single direction of propagation away from the end of the tip, whereas the emission in a wire is bi-directional.

We now discuss the limits of validity of the equations derived above for the nanotip. First, as discussed in Sec. 2.3.1, the quasistatic calculation of the decay rates is valid only when one is considering length scales where the electrodynamic Green's function can be approximated by its electrostatic equivalent. For the nanotip, this restricts the regimes of validity to $|k_i|w, |k_i|d \ll 1$. An additional set of assumptions is made in using the eikonal approximation to arrive at Eq. (2.53). Specifically, we have assumed that the change in the radius $\rho(z)$ of the nanotip occurs slowly enough that the wavevector $k_{\|}(\rho)$ of the surface plasmon modes can adiabatically follow the nanowire solution at each position z. The adiabaticity condition can be quantified by a parameter $\beta = d(1/\mathrm{Re}\, k_{\|}(\rho))/dz$, which must remain small at all positions z. Assuming, for example, that we are considering sufficiently small length scales that the wavevector $k_{\|}(\rho(z)) \approx C/\rho(z)$ follows quasi-static behavior, the condition $\beta \ll 1$ is satisfied only in the region $z \gg z_c$, where $z_c \equiv w/|C^2|$ represents some crossover point between adiabatic and non-adiabatic propagation. Thus, at first glance, the accumulated losses predicted by Eq. (2.53) in propagating from the end of the tip ($z = 0$) to

$z \sim z_c$ appear invalid. We now argue, however, that as long as the upper limit of integration $z(R)$ satisfies $z(R) \gg z_c$, Eq. (2.53) remains a good approximation for finding the total losses. In particular, we argue that the actual losses from $z = 0$ to $z \sim z_c$ are quite small, compared to the losses accumulated in going from $z \sim z_c$ to $z \gg z_c$. In the latter region, the integrand of Eq. (2.53) is a good approximation, as previously discussed. Then, in the region $z = 0$ to $z \sim z_c$, the specific form of the integrand does not matter, as long as it provides a small overall contribution to the total losses. First, it is straightforward to show that the predicted loss in this region, while incorrect, is small for realistic systems, $\tilde{\Gamma}_{\text{pl}}(R(z_c))/\Gamma_{\text{pl}} \sim \exp(-\text{Im}\, C/|C|)$. Next, we argue that the actual losses in this region should be small. Physically, the quantity $|q_0|^{-2} = v_0^2/|C|^2 \sim z_c$ determines the fundamental length scale for the nanotip SPs, since q_0 is the "wavevector" for the SPs in parabolic coordinates. Because dissipation can be treated as a small perturbation for realistic systems, the losses should be significant only on length scales much larger than this, just as losses are only relevant on scales much longer than the inverse SP wavevector, $1/|k_{\parallel}|$, for the nanowire.

To check the analytical results derived above for the nanotip, we have also performed detailed numerical simulations using boundary element method (BEM) [64]. Details of our implementation are given in Appendix C. BEM simulations are fully electrodynamic solvers of Maxwell's Equations, and they were used to obtain the classical electromagnetic field solutions of an oscillating dipole emitter $\mathbf{p}_0 e^{-i\omega t}$ near a nanotip. The results of a few sample simulations are shown in Fig. 2.6, for a tip curvature parameter $k_0 w = 0.022$, final radius $k_0 R = 0.3$, and varying emitter positions $k_0 d = 0.002, 0.2, 0.7$. In Fig. 2.6a, we plot the quantity $|\text{Re}(\mathbf{E} \times \mathbf{H}^*)|$,

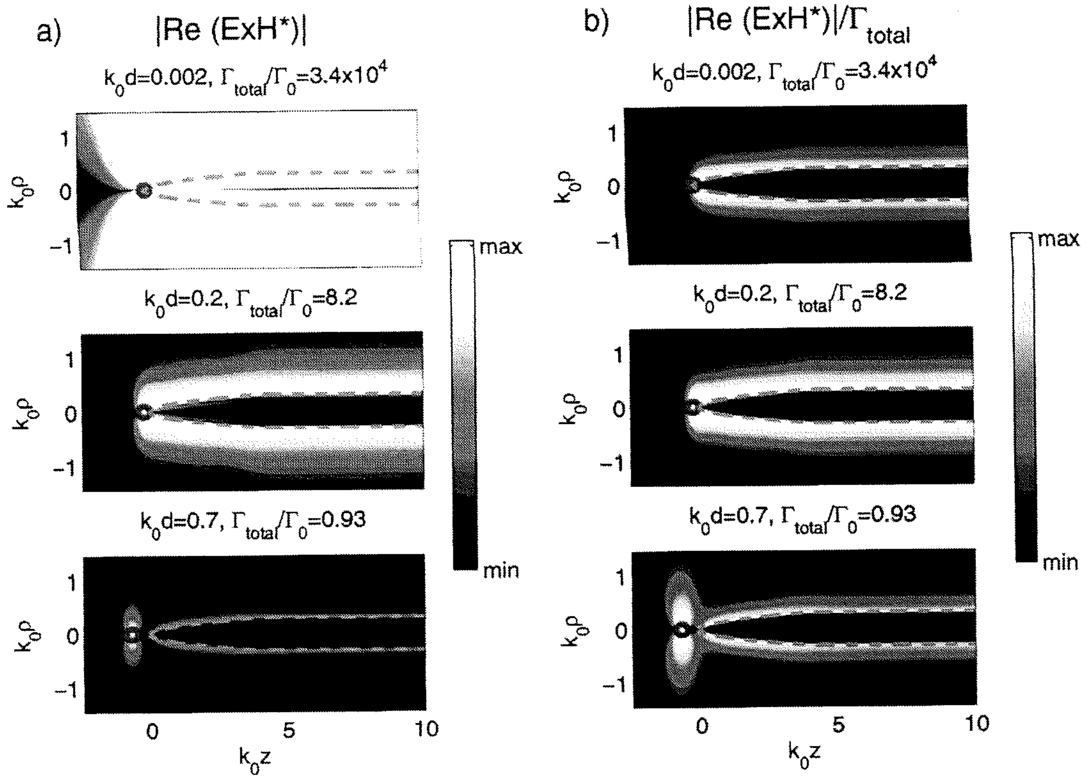

Figure 2.6: Numerically calculated fields due to a dipole emitter near a conducting nanotip, obtained by boundary element method. a) The energy flux $|\mathrm{Re}(\mathbf{E}\times\mathbf{H}^*)|$, in arbitrary units. The position of the emitter is denoted by the blue circles, while the boundary of the nanotip is given by the dotted lines . The plots shown are for a final nanotip radius of $k_0R = 0.3$, curvature parameter $k_0w = 0.022$, and emitter positions $k_0d = 0.002, 0.2, 0.7$. It can be seen that both the total spontaneous emission rate Γ_{total} and the emission rate into surface plasmons increase as the emitter is brought closer to the nanotip. b) The quantity $|\mathrm{Re}(\mathbf{E}\times\mathbf{H}^*)|/\Gamma_{\text{total}}$, for the same parameters. This quantity is proportional to the energy flux normalized by the total power output of the emitter. The $k_0d = 0.002$ plot is mostly dark, indicating that most of the decay is into non-radiative channels. The $k_0d = 0.2$ case is characterized by bright spots along the entire edge of the nanotip, which indicates efficient SP excitation. The $k_0d = 0.7$ case exhibits the typical lobe pattern associated with radiative decay of a dipole.

which is proportional to the Poynting vector and corresponds to the total energy flux of the system. The nanotip is assumed to be composed of silver in a surrounding dielectric $\epsilon_1 = 2$, and its boundary is given by the dotted line, while the emitter positions are denoted by the circles. The total spontaneous emission rate is given via $\Gamma_{\mathrm{total}} = (\Gamma_{\mathrm{pl}} + \Gamma')\propto \mathrm{Im}\,(\mathbf{p_0} \cdot \mathbf{E}_1(\mathbf{r}', \mathbf{r}'))$ and is determined numerically for each configuration by finding the total field at the dipole location. On the other hand, the effective emission rate $\tilde{\Gamma}_{\mathrm{pl}}(R)$ into the SPs is determined by a best fit of the fields in the region of constant R to the known SP solution on a nanowire given in Eq. (2.3), and then calculating the total energy transport of this best-fit mode through the integrated Poynting vector. This total power is directly proportional to $\tilde{\Gamma}_{\mathrm{pl}}(R)$. The figure confirms the qualitative behavior that we expect and have described previously. In particular, the generated SP field and total spontaneous emission rate are largest for very small separations and decrease as the emitter is placed further away from the end of the nanotip. In Fig. 2.6b, we plot $|\mathrm{Re}(\mathbf{E} \times \mathbf{H}^*)|/\Gamma_{\mathrm{total}}$, which is proportional to the energy flux normalized by the total power output of the emitter. This quantity yields information about the efficiency of decay into the various channels. For small separations ($k_0 d = 0.002$), the plot is mostly dark, which indicates that the decay of the dipole is predominantly non-radiative. For $k_0 d = 0.2$, the maximum (corresponding to bright spots in the plot) is located along the entire surface of the nanotip, which indicates highly efficient SP excitation. Here, although the total emission rate into SPs decreases from the $k_0 d = 0.002$ case (as seen in Fig. 2.6a), the efficiency increases dramatically due to less competition from non-radiative decay. Finally, for $k_0 d = 0.7$, the maximum appears as the typical lobe pattern associated with radiative decay.

In Fig. 2.5a, we have plotted the numerically optimized values of $\tilde{P}(R)$ for a few values of R. It can be seen that the values obtained through analytical approximations and numerical BEM closely agree. Unlike the theoretical predictions, however, the numerically calculated error probability does not increase monotonically with R. We believe that the origin of this is that for the numerically optimized parameters, the condition $R \gg \rho(z_c)$ under which the theoretical predictions hold is only weakly satisfied, and the excitation region for the SPs cannot strictly be thought of as a single point at the end of the tip ($z = 0$).

2.5 Single photon generation via coupling to dielectric waveguide

We have shown in previous sections that a single emitter can spontaneously emit into the guided SP modes of a nearby nano-structure with high probability. This prospect of efficient conversion between an excitation of the emitter and a single photon has a number of applications in the fields of quantum computing and quantum information. In this section, we consider one particular application, involving the use of such a system as an efficient single-photon source. The concepts behind single-photon generation on demand with an individual emitter in a cavity have been discussed elsewhere [6, 7, 8] and will not be presented in detail here. We note also that the ideas behind single-photon sources can be extended to create long-distance entanglement between emitters, as detailed, *e.g.*, in Ref. [65].

Because of dissipative losses in metals, the SP modes are not directly suitable as carriers of information over long distances. We show, however, that plasmonic devices can serve as an effective intermediate step, and in particular can be efficiently out-coupled to the modes of a co-propagating dielectric waveguide. The single photon device is illustrated schematically in Fig. 2.1. In Fig. 2.1a, an optically addressable emitter with multiple internal levels sits in the vicinity of a conducting nanowire. The emitter is strongly coupled to the nanowire, such that single photons on demand can be generated with high efficiency in the SP modes by external manipulation of the emitter. The addressability of the emitter along with the internal levels allows for shaping of this single-photon pulse [10], as illustrated in Fig. 2.1b. Here, a three-level emitter is shown with two ground or metastable states $|s\rangle, |g\rangle$. We assume that the transition between $|s\rangle$ and excited state $|e\rangle$ is decoupled from the SP modes, due to, *e.g.*, the orientation of its dipole moment, but that the states are coupled via some classical control field with Rabi frequency $\Omega(t)$. We also assume that the transition $|e\rangle - |g\rangle$ is coupled via the SP modes of the nanowire, *i.e.*, the state $|e\rangle$ can decay at a rate Γ_{pl} into $|g\rangle$ by emitting a photon into the SP modes. In addition, there is a small rate Γ' at which the excited state can decay without emitting a SP. A single photon in the SP modes of the nanowire is generated with high probability by initializing the emitter in $|s\rangle$ and exciting the transition $|s\rangle - |e\rangle$ with the control field $\Omega(t)$. The decay of $|e\rangle$ into $|g\rangle$ and the generation of an outgoing single SP then occurs with high probability, with the shape of the single photon wavepacket determined by the shape of $\Omega(t)$. We further assume that the SP is then evanescently coupled to the nearby dielectric waveguide (see Fig. 2.1a), which co-propagates with the nanowire over some distance L_{ex} during which this coupling is non-negligible. The coupling is a reversible process, and the distance L_{ex} is optimized to maximize efficiency of ending up with a single photon in the waveguide (*i.e.*, to prevent further Rabi oscillations back into the nanowire). A similar setup with a nanotip is illustrated in Fig. 2.1c. Here the nanotip radius $\rho(z)$ expands to some final radius R at which point coupling with the waveguide starts to occur. Initiating the coupling once the nanotip has reached a constant radius allows the two systems to be easily mode-matched, as discussed below. When optimized, we estimate that single-photon generation efficiencies of around 95% are possible in this tiered configuration.

To treat the problem analytically, we consider the simple situation of our nanostructure coupled to a cylindrical dielectric waveguide (*e.g.*, an optical fiber) of radius R_g, such that the modes can be calculated analytically using the methods described in Appendix A. It can be shown that the fundamental modes of the waveguide are degenerate $m = \pm 1$ modes that are not cut off as $R_g \rightarrow 0$. The dependence of their wavevector $k_\parallel$ on R_g is shown in Fig. 2.7, for a core permittivity $\epsilon_g = 13$ and surrounding permittivity $\epsilon_1 = 2$. These parameters correspond closely to that of a Si/SiO$_2$ guide at $\lambda_0 = 1$ μm. To simplify the calculation, we also assume that coupling between the wire and higher-order waveguide modes is negligible. This can be achieved, for example, by operating below the cutoff radius of higher-order modes or by operating with sufficiently large wavevector mismatch between the SP and higher-order guide modes.

We make the ansatz that the total field of the system is given by a superposition of the unperturbed modes of the nano-structure and waveguide. While this cannot

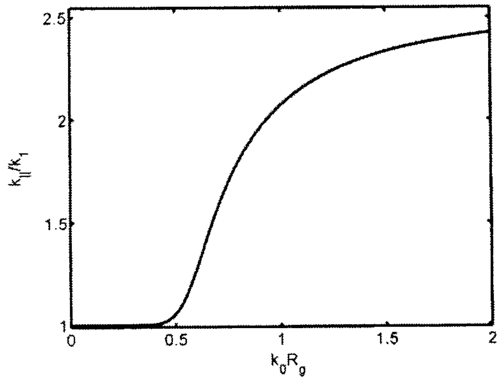

Figure 2.7: Wavevector $k_{\|}$ of the fundamental guided modes of a cylindrical dielectric waveguide with core permittivity $\epsilon_c = 13$ and surrounding permittivity $\epsilon_1 = 2$, plotted as a function of core radius R_g.

strictly be correct, as such a solution violates boundary conditions at each interface, we rely on such an assumption to give us the correct qualitative behavior without resorting to more complex numerical calculations. Specifically, we assume that the total electric field for the system takes the form

$$\mathbf{E}_T(\mathbf{r}) = \sum_{\mu=w,g} \sum_{i=1}^{N_\mu} C_{\mu,i}(z)\mathbf{E}_{\mu,i}(\mathbf{r}), \tag{2.54}$$

where μ indexes the nano-structure (w) and waveguide (g) systems, and $i = 1, \cdots, N_\mu$ runs over the modes of system μ. In the following we will explicitly treat the nanotip case, where the SPs propagate in a single direction, although this argument can easily be extended to the nanowire. We emphasize that we are considering coupling of the SP mode to the waveguide once the nanotip has already expanded to its final radius R, at which point the SP mode solution becomes identical to that of a nanowire. In our case, $N_w = 1$ as we only consider the fundamental SP mode of the nanotip, while $N_g = 2$ as we take into account the two degenerate, co-propagating fundamental modes of the waveguide. $\mathbf{E}_{\mu,i}(\mathbf{r})$ here represents the unperturbed solution of mode i

in system μ (without the presence of the other system). A similar expression holds for the total magnetic field.

With the ansatz of Eq. (2.54) for the total field of the combined waveguide and nanotip system, one can derive exact equations of evolution [66] based on Lorentz reciprocity for the coefficients $C_{\mu,i}$. Explicitly separating out the plane-wave dependence of the unperturbed fields, $\mathbf{E}_{\mu,i}(\mathbf{r}) = \mathbf{E}_{\mu,i}(\boldsymbol{\rho})e^{ik_{\|\mu,i}z}$, the $N_w + N_g$ coupled-mode equations take the form

$$\sum_{\nu=w,g}\sum_{j=1}^{N_\nu} P_{\mu,i;\nu,j}(z)\frac{dC_{\nu,j}}{dz} = i\omega\epsilon_0 \sum_{\nu=w,g}\sum_{j=1}^{N_\nu} K_{\mu,i;\nu,j}(z)C_{\nu,j}(z), \tag{2.55}$$

as derived in detail in Appendix D. The coefficients to the system of equations above are given by

$$\begin{aligned} P_{\mu,i;\nu,j}(z) &= e^{i(k_{\|\nu,j}-k_{\|\mu,i}^{*})z} \times \\ &\int d\boldsymbol{\rho}\, \left(\mathbf{E}_{\nu,j}(\boldsymbol{\rho}) \times \mathbf{H}^{*}_{\mu,i}(\boldsymbol{\rho}) + \mathbf{E}^{*}_{\mu,i}(\boldsymbol{\rho}) \times \mathbf{H}_{\nu,j}(\boldsymbol{\rho})\right) \cdot \hat{z}, \qquad (2.56) \\ K_{\mu,i;\nu,j}(z) &= e^{i(k_{\|\nu,j}-k_{\|\mu,i}^{*})z} \int d\boldsymbol{\rho}\, \mathbf{E}_{\nu,j}(\boldsymbol{\rho}) \cdot \mathbf{E}^{*}_{\mu,i}(\boldsymbol{\rho}) \left(\epsilon_T(\boldsymbol{\rho}) - \epsilon_\nu(\boldsymbol{\rho})\right), \qquad (2.57) \end{aligned}$$

where $\epsilon_T(\boldsymbol{\rho})$ is the electric permittivity of the combined system. Clearly, the presence of the phase factors $e^{i(k_{\|\nu,j}-k_{\|\mu,i}^{*})z}$ in the equations above indicate that, at least under weak coupling, significant power transfer between the two systems will not take place unless the two systems are approximately mode-matched with respect to $k_{\|}$. In practice, this implies that for a final tip radius R, there is some ideal waveguide size R_g that allows for maximum transfer efficiency between the two systems. A similar optimization of the waveguide parameters exists in the case of arbitrary coupling strength between the two systems, although this problem is more complex because one must account for factors such as the phase shift of one system due to the other.

We emphasize that the coupled-mode equations above are exact within the ansatz of Eq. (2.54). For example, for two lossless systems these equations conserve power, and for a lossy system (such as a nanotip) the effects of losses are treated exactly. By convention, the normalization of fields is such that the integrals appearing in the diagonal matrix elements $P_{\mu,i;\mu,i}$ are set to 1.

For the waveguide and nanotip systems coupled over a length L_{ex}, the exact single-photon generation efficiency will depend on the details of how the two systems are brought together and separated apart. In practice, for example, the two systems should be brought together slowly enough that the introduction of the waveguide does not cause significant back-scattering of the SP, yet quickly enough that this introduction length is small compared to the SP decay length. Furthermore, in reality the coupling region will not be a step of length L_{ex} but will be characterized by some smooth transition. To avoid the many details associated with this introduction and separation and to approximately calculate the efficiency, we will consider an idealized system and make three assumptions:

(i) The decay rates of the emitter are not affected by the presence of the nearby dielectric waveguide. In particular, the Purcell factors calculated earlier for the nanotip are unchanged.

(ii) The radius of the nanotip is given by $\rho(z) = \sqrt{wz}$ for $z < z_0$ and becomes constant, $R \equiv \rho(z_0) = \sqrt{wz_0}$, for $z \geq z_0$. For $z \geq z_0$ the SP mode solution becomes identical to the nanowire solution, and in particular has well-defined $k_{\parallel}$ which allows it to be easily mode-matched with the waveguide. It is assumed that coupling between the nanotip and waveguide begins at $z = z_0$, with the initial field amplitudes of the coupled system given by

$$C_w(z_0) = \left(\frac{\tilde{P}(R)}{1+\tilde{P}(R)}\right)^{1/2}, \tag{2.58}$$

$$C_{g,i}(z_0) = 0, \tag{2.59}$$

where the probability $\tilde{P}(R)/(1+\tilde{P}(R))$ of finding a SP excitation at R is already optimized over the nanotip curvature and emitter position.

(iii) Eq. (2.55) exactly describes the coupling between the two systems in the region $z_0 \leq z \leq z_0 + L_{ex}$. To estimate the probability of transfer from nanowire to waveguide after distance L_{ex} when the two systems are once again separated, we project the total field of Eq. (2.54) at $z = z_0 + L_{ex}$ into the waveguide mode. Specifically, the projected field amplitude in the waveguide in either of the degenerate modes i is given by

$$C_{\mathrm{proj},i}(z_0 + L_{ex}) = 2\int d\boldsymbol{\rho}\, \left(\mathbf{E}_T(\mathbf{r}) \times \mathbf{H}^*_{g,i}(\mathbf{r})\right) \cdot \hat{z}, \tag{2.60}$$

where the factor of 2 arises due to the normalization convention for the unperturbed modes.

Because of the symmetry, the projected field strengths $|C_{\mathrm{proj},i}|^2$ calculated above are equal for the two degenerate waveguide modes, and the quantity $2|C_{\mathrm{proj},i}|^2$ then corresponds to the efficiency of single photon generation. Here the additional factor of 2 accounts for the mode degeneracy. This quantity takes completely into account the propagative losses of the SPs, imperfect coupling between the nanotip and waveguide, and the Purcell factor of the nanotip.

In Fig. 2.8a we plot the efficiency of single photon generation as a function of R, for both the nanowire and nanotip systems. For each R the plotted efficiencies have

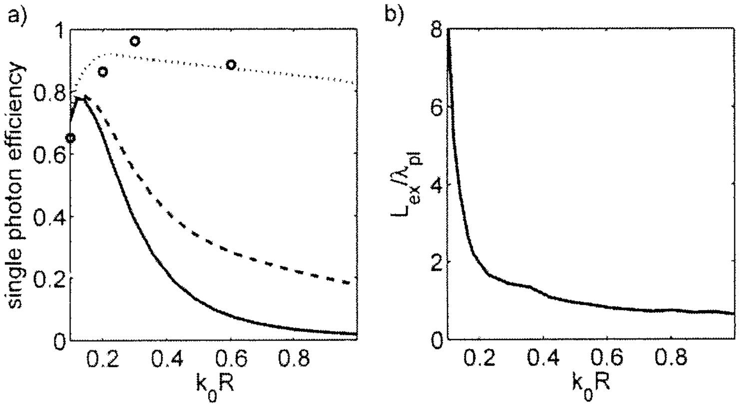

Figure 2.8: a) Optimized efficiencies of single photon generation vs. R. We have assumed that coupling to waveguide modes other than the fundamental mode is negligible, *i.e.*, the waveguide is effectively in the single-mode regime. Solid (dashed) line: theoretical efficiency using a nanowire, using spontaneous emission rates obtained by quasistatic (fully electrodynamic) calculations. Dotted line: theoretical efficiency using a nanotip. Solid points: nanotip efficiency based on boundary element method simulations, combined with coupled-mode equations. b) Optimal coupling length L_{ex} for a nanotip as a function of R. Here L_{ex} is given in units of the surface plasmon wavelength λ_{pl} at that particular value of R.

been optimized over all other possible parameters of the system. For the nanowire configuration, we have assumed that the resulting forward- and backward-propagating waves in the waveguide can be perfectly combined. In the figure we have also included points obtained by our BEM simulations of a nanotip. Here, we have taken the numerically optimized values of $\tilde{P}(R)$ and plugged them in as initial values for the coupled-mode theory above. It can be seen that the numerical simulations agree well with our theoretical predictions. We find that photon efficiencies of nearly 80% are possible for the nanowire, while efficiencies around 95% are possible for the nanotip. In Fig. 2.8b we plot the optimal coupling length L_{ex}, in units of λ_{pl}, as a function of R for the nanotip (L_{ex} for the nanowire should be twice that of the nanotip, to account for the transfer of the forward- and backward-propagating components of the emitted SP). It can be seen that the out-coupling to the waveguide can in principle occur quite rapidly, over length scales of a few λ_{pl}.

The existence of an optimum R for photon generation can be intuitively understood. For smaller R the coupling between the emitter and SP modes can be quite large. However, these tightly-confined SP modes are accompanied by higher propagative losses and cannot be as efficiently coupled to the waveguide system. The coupling efficiency between SPs and waveguide modes improves for larger R. For the nanowire, however, the larger radius results in weaker coupling between the SP and emitter, while for the nanotip the accumulated propagative loss increases as the final radius grows.

2.6 Influence of surface roughness and temperature on surface plasmon propagation losses

The effectiveness of many plasmonic devices, such as those described in this chapter, depend sensitively on the degree of losses that are present in these systems. We have shown that material losses determine the propagation length of SPs, for example, and also the effective Purcell factor that can be achieved for single emitters coupled to SPs. Thus far, our theoretical predictions were made based on the optical properties of a metal at room temperatures, and have assumed that the devices are perfectly free of defects. In this section, we calculate from first principles the effects that temperature and surface roughness have on our system.

2.6.1 Effects of surface roughness

In Section 2.2, we have treated the problem of SP propagation on a smooth nanowire, taking into account inherent dissipative losses of the metal characterized by $\operatorname{Im} \epsilon_2$. In practice, however, a nanowire may not be perfectly smooth, and the surface roughness can give rise to new scattering mechanisms for the SPs. While the general solution for the fields in the presence of arbitrary roughness is a complicated problem, we calculate the effects in two limits. First we calculate the losses on a nanowire due to radiative scattering in the limit of small roughness and zero heating ($\operatorname{Im} \epsilon_2 = 0$). Here the plasmons experience no inherent loss due to the metal but can receive momentum kicks from the roughness that cause them to scatter radiatively. Then, we calculate the effects of small roughness for a nanowire in the quasi-static limit, where radiative effects are ignored but the effects of increased dissipative losses are treated.

Radiative losses

For simplicity we consider a wire with axial symmetry, but with a surface profile given by $\rho_0(z) = R + p\zeta(z)$, where R is the average radius of the wire, $\zeta(z)$ is some random function describing the roughness, and p is an expansion parameter that will be taken to equal 1 at the end. We will calculate in perturbation theory the radiated field scattered from the roughness, from an initial field corresponding to the fundamental SP mode for a perfectly smooth wire. Because of the symmetry, the only non-zero components of the fields remain E_ρ, E_z, and H_ϕ, which will also have axial symmetry (see Eq. (2.3) for fundamental mode profile for a smooth wire). As will be seen later, it suffices for now to consider only E_z, as the other components depend on

E_z in a simple way through Maxwell's Equations. Following previous convention, we denote the metal wire and its surroundings by the indices $i = 1, 2$ respectively. We proceed by breaking up the total field along z in region i into incident and scattered fields

$$E_{i,z}^{\text{total}} = E_{i,z}^{0} + E_{i,z}^{s}, \tag{2.61}$$

where $E_{i,z}^{0}$ is the z-component of the fundamental SP mode given by Eqs. (2.3) and (2.4), and further assume that the scattered field can be expanded in a power series

$$E_{i,z}^{s} = \sum_{n=1}^{\infty} p^{n} E_{i,z}^{(n)}. \tag{2.62}$$

In the following we will calculate the first-order scattered field $E_{i,z}^{(1)}$. We make the ansatz that $E_{i,z}^{(1)}$ can be expanded in the form

$$\begin{aligned} E_{1,z}^{(1)} &= \int_{-\infty}^{\infty} dh_{\|}\, H_0(h_{1\perp}\rho)\frac{h_{1\perp}^2}{k_1^2}A(h_{\|})e^{ih_{\|}z} \\ E_{2,z}^{(1)} &= \int_{-\infty}^{\infty} dh_{\|}\, J_0(h_{2\perp}\rho)\frac{h_{2\perp}^2}{k_2^2}B(h_{\|})e^{ih_{\|}z}, \end{aligned} \tag{2.63}$$

where each Fourier component is an outgoing solution of the wave equation with appropriate boundary conditions at $\rho = 0$ and $\rho = \infty$, as derived in Eq. (A.4). The assumption that this outgoing field expansion can be continued all the way to the surface even in the presence of roughness is known as the Rayleigh hypothesis [67]. From Eq. (A.4) one also sees that E_ρ, H_ϕ are determined completely once E_z is known. Using these relations, the total (incident plus scattered) fields $\mathbf{E}^{\text{total}}$ and $\mathbf{H}^{\text{total}}$ are straightforward but lengthy to write down, and are given to order p in Eq. (I.1) in Appendix I.1.

The coefficients $A(h_{\|}), B(h_{\|})$ are determined by enforcing continuity of the tangential fields at the boundary $\rho_0(z)$. Specifically, we require that

$$\begin{aligned}
(\hat{t}\cdot\mathbf{E}_1^{\text{total}})|_{\rho=R+p\zeta(z)} &= (\hat{t}\cdot\mathbf{E}_2^{\text{total}})|_{\rho=R+p\zeta(z)}, \hat{t}=\frac{\hat{z}+p\frac{d\zeta}{dz}\hat{\rho}}{\sqrt{1+p^2\left(\frac{d\zeta}{dz}\right)^2}} \\
H_{\phi,1}^{\text{total}}|_{\rho=R+p\zeta(z)} &= H_{\phi,2}^{\text{total}}|_{\rho=R+p\zeta(z)},
\end{aligned} \tag{2.64}$$

where $\hat{t}(z)$ is the unit tangent vector to the rough interface. These equations can be solved perturbatively by expanding them in p and solving at each order. The $\mathcal{O}(p^0)$ equation is trivially satisfied by the fundamental SP mode for a smooth nanowire. To solve to $\mathcal{O}(p)$, it is useful to first introduce the Fourier transform of the surface roughness,

$$\zeta(z)=\int_{-\infty}^{\infty}\frac{dh_{\|}}{2\pi}e^{ih_{\|}z}\tilde{\zeta}(h_{\|}). \tag{2.65}$$

Using the Fourier transform $\tilde{\zeta}(h_{\|})$, the $\mathcal{O}(p)$ equations become algebraic in Fourier space and have solutions (see Appendix I.1)

$$\begin{aligned}
A(h_{\|}) &= \frac{\tilde{\zeta}(h_{\|}-k_{\|})}{2\pi}\frac{k_1^2}{h_{1\perp}}f(h_{\|}) \\
B(h_{\|}) &= \frac{\tilde{\zeta}(h_{\|}-k_{\|})}{2\pi}\frac{k_2^2}{h_{2\perp}}g(h_{\|}),
\end{aligned} \tag{2.66}$$

where $k_{\|}$ denotes the unperturbed SP wavevector (in this section we take $\text{Im}\,\epsilon_2=0$ so that $k_{\|}$ is purely real). The scattering coefficients $f(h_{\|}), g(h_{\|})$ are complicated functions of $h_{\|}$ and R and are given in Appendix I.1. Physically, the equations above state that, to first order, the surface roughness contributes single momentum kicks to the unperturbed SP fields with a strength determined by the Fourier components of the roughness. From this point forward we set $p=1$.

We now consider some random surface profile such that

$$\langle\zeta(z)\rangle = 0$$

$$\langle\zeta(z)\zeta(z')\rangle = \delta^2 e^{-(z-z')^2/a^2}, \tag{2.67}$$

with corresponding correlations

$$\begin{aligned}\langle\tilde{\zeta}(k)\rangle &= 0\\ \langle\tilde{\zeta}(k)\tilde{\zeta}^*(k')\rangle &= 2\pi^{3/2}\delta^2 a e^{-\frac{1}{4}a^2k^2}\delta(k-k')\end{aligned} \tag{2.68}$$

for the Fourier components. Physically δ and a correspond respectively to the typical amplitude and length of a rough patch on the surface of the wire. It is also useful to define $s = \delta/a$ as a typical "slope" to the roughness. To calculate the power radiated due to the surface roughness we find the ensemble-averaged Poynting vector far from the wire. It is sufficient to consider just the component of $\langle\mathbf{S}\rangle$ oriented along $\hat{\rho}$, given outside the wire by

$$S_\rho = -\frac{1}{2}\langle E_{1,z}^{\text{total}} H_{1,\phi}^{*\,\text{total}}\rangle, \tag{2.69}$$

where the fields $E_{1,z}^{\text{total}}, H_{1,\phi}^{\text{total}}$ are given to first order by Eq. (I.1). The calculation of S_ρ simplifies further because the incident SP field decays exponentially away from the wire, and thus to lowest order only the first-order scattered fields will contribute to the Poynting vector at large ρ, which physically corresponds to the power radiated away to infinity. Specifically, the radiated power per unit area is given by

$$\begin{aligned}S_\rho &= -\frac{1}{2}\langle E_{1,z}^{(1)} H_{1,\phi}^{(1)*}\rangle \qquad (\rho\rightarrow\infty) && (2.70)\\ &= \frac{1}{2\omega\mu_0}\int_{-\infty}^{\infty} dh_\parallel dh'_\parallel \frac{i{h_{1\perp}}^2 h'^*_{1\perp}}{k_1^2} H_0(h_{1\perp}\rho) H'^*_0(h'_{1\perp}\rho)\times\\ &\quad \langle A(h_\parallel)A^*(h'_\parallel)\rangle e^{i(h_\parallel-h'_\parallel)z}. && (2.71)\end{aligned}$$

Substituting the solution for $A(h_\parallel)$ derived in Eq. (2.66) and using the correlations

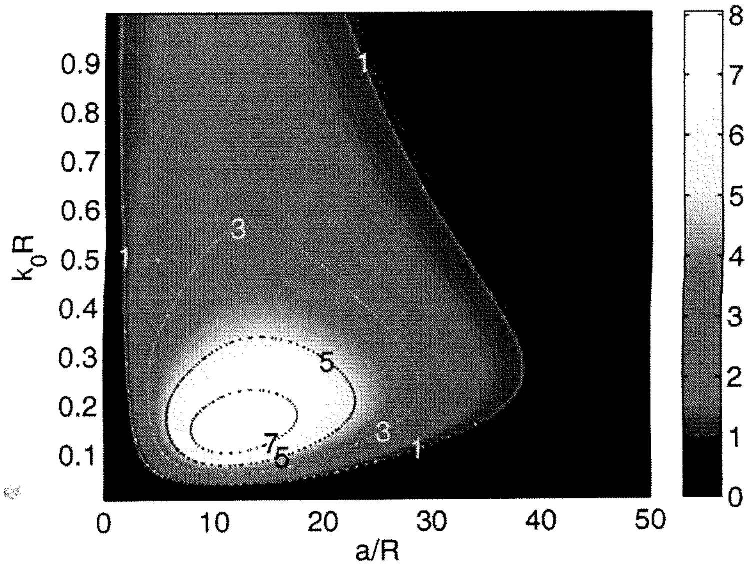

Figure 2.9: The SP dissipation rate due to radiative scattering off of surface roughness, $\Gamma_{\text{rad,rough}}/s^2\omega$, as functions of wire radius R and correlation length a/R. The numbers are calculated for a silver nanowire at $\lambda_0 = 1\,\mu$m and $\epsilon_1 = 2$.

in Eq. (2.68), it is straightforward to evaluate the integral over $h'_\parallel$ and arrive at

$$S_\rho = \frac{i\epsilon_0\epsilon_1\omega}{4\sqrt{\pi}} s^2 a^3 \int_{-k_1}^{k_1} dh_\parallel e^{-\frac{1}{4}a^2(h_\parallel - k_\parallel)^2} h_{1\perp} H_0(h_{1\perp}\rho) H_0'^*(h_{1\perp}\rho) \left|f(h_\parallel)\right|^2 . \tag{2.72}$$

In the expression above we have truncated the bounds of the integral to $\pm k_1$ because we are interested in the Poynting vector far away from the wire, where only radiative fields $|h_\parallel| \leq k_1$ contribute. With knowledge of the Poynting vector it is then possible to find the dissipation rate of the SPs due to radiative scattering, given by

$$\Gamma_{\text{rad,rough}} = \lim_{\rho\to\infty} \frac{2\pi\rho S_\rho}{\frac{1}{4}\int d\boldsymbol{\rho}\, \epsilon_0 \frac{d}{d\omega}\left(\epsilon(\boldsymbol{\rho},\omega)\omega\right) \left|\mathbf{E}(\boldsymbol{\rho})\right|^2 + \mu_0 \left|\mathbf{H}(\boldsymbol{\rho})\right|^2} . \tag{2.73}$$

The denominator on the right-hand side of the equation above can be identified with the SP energy per unit length.

We first qualitatively discuss the behavior of $\Gamma_{\text{rad,rough}}$ before deriving various limits more quantitatively. From Eq. (2.72) it is clear that $\Gamma_{\text{rad,rough}}$ scales explicitly like δ^2 or s^2. Physically, this occurs because the lowest-order contribution to the Poynting vector far away from the wire is due to the combination of a first-order scattered electric field and first-order scattered magnetic field. In Fig. 2.9 the quantity $\Gamma_{\text{rad,rough}}/s^2\omega$ is evaluated numerically as a function of wire radius R and correlation length a/R, for a silver nanowire at $\lambda_0 = 1\,\mu\text{m}$ and $\epsilon_1 = 2$. We are particularly interested in the nanowire limit, when the SP wavevector $k_{\|}\approx C/R$. We see that for fixed R, the scattering reaches a peak for some particular value of a/R. More careful inspection reveals that the maximum occurs when $a\propto R/C \propto \lambda_{\text{pl}}$. This result makes intuitive sense, since the characteristic momentum kick $\sim 1/a$ that the SP wavevector $k_{\|}$ receives due to roughness must be on the order of C/R in order for the resulting wavevector to lie in the radiative range between $-k_1$ and k_1. In the limit $a/R\gg C$, one observes an exponential suppression of scattering, due to the fact that the roughness has a very narrow momentum distribution and cannot possibly contribute a large kick to $k_{\|}$. In fact, in this regime one physically expects for the SP wavevector to adiabatically vary with the changing wire radius. In the other limit $a/R\ll C$, the scattering also decreases, but with a polynomial dependence on R, as will be proven below. Here, the momentum distribution of the roughness becomes very wide, and thus the probability of receiving a kick that results in a final momentum between $\pm k_1$ becomes quite small. Finally, for fixed slope s, it can be seen that the scattering decreases as $R\to 0$ at any correlation length a. This result is also easily understood, as the SP wavevector $k_{\|}$ becomes increasingly far-removed from the range

Roughness parameters	$k_0R = 0.1$ ($R\approx 16$ nm)	$k_0R = 0.2$	$k_0R = 0.3$
$a = 0.1R$, $\delta = 0.05R$ ($s = 0.5$)	0.09%	0.5%	1.4%
$a = 0.1R$, $\delta = 0.1R$ ($s = 1$)	0.4%	1.9%	5.6%
$a = R$, $\delta = 0.05R$ ($s = 0.05$)	0.9%	4.5%	12%
$a = 5R$, $\delta = 0.05R$ ($s = 0.01$)	2.8%	8.0%	10%
$a = 10R$, $\delta = 0.1R$ ($s = 0.01$)	7.0%	14%	16%
$a = 20R$, $\delta = 0.1R$ ($s = 0.005$)	0.9%	2.9%	3.8%
$a = 25R$, $\delta = 0.1R$ ($s = 0.004$)	0.3%	1.3%	1.8%

Table 2.1: Losses due to radiative scattering off of surface roughness for nanowires of varying sizes and roughness parameters. The scattering rates are given in terms of the percentage increase in Im $k_{\|}$ that one would expect over the values for a smooth nanowire.

of radiative wavevectors. In Table 2.1, we calculate the scattering rates for wire sizes $k_0R = 0.1, 0.2, 0.3$ (or $R\approx 16, 32, 48$ nm), for a few chosen roughness parameters. The scattering rates are given as a percentage increase in Im $k_{\|}$ over the values for a smooth nanowire. It can be seen that strong suppression of radiative scattering occurs both for smaller R and when a is either much larger or much smaller than R, which confirms our earlier observations. Furthermore, it is evident that under reasonable parameters, the losses in the system are increased only slightly due to radiative scattering.

We now analyze more carefully the behavior of the radiative scattering in the nanowire regime. To simplify the expression further, we first note that since we are interested in the far field ($\rho \to \infty$), we can take the asymptotic limits of the Hankel functions in Eq. (2.72), $H_0(h_{1\perp}\rho)H_0^{\prime *}(h_{1\perp}\rho)\approx -2i/(\pi h_{1\perp}\rho)$. One can also derive an asymptotic relationship of $f(h_{\|})$ as $R\to 0$ (see Appendix I.1), which upon substitution yields

$$\begin{aligned} \Gamma_{\mathrm{rad,rough}} &\approx \pi^{3/2}\frac{|\phi|^2}{\tilde{V}}\omega\epsilon_1 s^2 a^3 \int_{-k_1}^{k_1} dh_{\parallel}\, h_{1\perp}^2 e^{-(1/4)a^2(k_{\parallel}-h_{\parallel})^2}, \quad (R\rightarrow 0) \quad (2.74) \\ \phi &\equiv \frac{H_0'(iC)}{J_0'(iC)}J_0''(iC) - H_0''(iC). \quad (2.75) \end{aligned}$$

Here $\tilde{V}$ is a complicated dimensionless parameter, but most importantly only depends on $\epsilon_{1,2}$.

From the equation above, it is clear that there are three distinct regimes of interest defined by the quantity $\alpha{\equiv}k_{\parallel}a = 2\pi a/\lambda_{\mathrm{pl}}{\approx}Ca/R$, which characterizes the typical extent of a rough patch compared to the SP wavelength. In the limit $\alpha{\ll}1$, one can approximate the exponential in the integrand of Eq. (2.74) as a constant, which leads to straightforward evaluation of the integral,

$$\Gamma_{\mathrm{rad,rough}}{\approx}\frac{4}{3}\pi^{3/2}\frac{|\phi|^2}{\tilde{V}}\omega\epsilon_1^{5/2}s^2\left(\frac{k_0R}{C}\right)^3\alpha^3. \quad (\alpha{\ll}1) \quad (2.76)$$

Here, the noise spectrum of Eq. (2.68) becomes very wide and leads to an α^3 scaling of the dissipation rate. In the opposite limit $\alpha{\gg}1$, the value of the exponential term becomes exponentially small, with a corresponding exponential suppression of the scattering rate. A more careful evaluation of the integrand yields

$$\Gamma_{\mathrm{rad,rough}}{\approx}8\pi^{3/2}\frac{|\phi|^2}{\tilde{V}}\omega\epsilon_1^{3/2}s^2\frac{k_0R}{C\alpha}e^{-(1/4)a^2(k_{\parallel}-k_1)^2}. \quad (\alpha{\gg}1) \quad (2.77)$$

Finally, one can show that for fixed, sub-wavelength R the radiative scattering is most significant when $\alpha{\sim}\mathcal{O}(1)$. In this case, the exponential appearing in Eq. (2.74) is neither exponentially small nor constant. However, one can make the rough approximation $e^{-(1/4)a^2(k_{\parallel}-h_{\parallel})^2}{\approx}1-(1/4)a^2(k_{\parallel}-h_{\parallel})^2$ to get an idea of the scaling in this regime. It is straightforward to show that the scattering rate has a maximum with respect to α at $\alpha\approx(12/5)^{1/2}$, with a corresponding maximum decay rate

$$\max_{a}\left\{\Gamma_{\mathrm{rad,rough}}\right\}\propto\frac{|\phi|^2}{\tilde{V}}\omega\epsilon_1^{5/2}s^2\left(\frac{k_0R}{C}\right)^3. \tag{2.78}$$

Again, the radiative scattering is most significant when the length scale a of the roughness is on the order of the SP wavelength, and the maximum scattering (for fixed s) decreases as $R\rightarrow 0$ due to the increasing mismatch between $k_{\|}$ and radiative wavevectors. The conditions of validity of these perturbative calculations are discussed in further detail in Appendix I.1.

We finally note that while the radiative scattering goes like δ^2 or s^2, the relevant quantity for dissipative (heating) losses due to roughness becomes $\mathbf{S}$ inside the wire. For this quantity the lowest-order correction to the smooth wire solution will come from a combination of a first-order and zeroth-order field. Thus one expects roughness-induced dissipative losses to contribute a decay term proportional to δ or s, which for small roughness will dominate over radiative scattering. This correction will be treated in the next subsection.

Non-radiative losses

To study the effects of surface roughness on non-radiative losses, we will make one simplifying assumption and calculate these losses in the quasi-static limit. To do this we will proceed in a manner similar to that in Sec. 2.3.1, where we found the quasi-static fields associated with a smooth nanowire. Here the calculations for the fields yielded the presence of poles whose positions and widths give the real and imaginary parts of the wavevector $k_{\|}$. The case of a smooth nanowire was particularly easy to treat because of the translational symmetry of the system. A system containing surface roughness lacks such translational symmetry and therefore must be considered more carefully, but the calculation proceeds in much the same way. In particular, we will find expressions for the pseudopotentials $\Phi_1 = \Phi_0 + \Phi_r$ and Φ_2 that satisfy the necessary boundary conditions in the presence of surface roughness. We can once again find the positions and widths of the poles associated with the system, which are now altered by the roughness.

We first write down appropriate expansions for $\Phi_{0,r,2}(\mathbf{r},\mathbf{r}')$. The expansion for the incident component Φ_0, given originally in Eq. (2.17), is slightly re-written here,

$$\begin{aligned}\Phi_0(\mathbf{r},\mathbf{r}') &= \frac{1}{4\pi\epsilon_0\epsilon_1}\frac{1}{|\mathbf{r}-\mathbf{r}'|} \\ &= \frac{1}{2\pi^2\epsilon_0\epsilon_1}\sum_{m=0}^{\infty}(2-\delta_{m,0})\cos\left(m(\phi-\phi')\right)\times \\ &\quad \int_0^{\infty} dh\cos\left(h(z-z')\right)K_m(h\rho')I_m(h\rho)\quad(\rho<\rho') \\ &= \frac{1}{4\pi^2\epsilon_0\epsilon_1}\sum_{m=-\infty}^{\infty}e^{im(\phi-\phi')}\times \\ &\quad \int_{-\infty}^{\infty} dh\, e^{ih(z-z')}\tilde{K}_m(h\rho')\tilde{I}_m(h\rho)\quad(\rho<\rho'). \end{aligned} \tag{2.79}$$

The functions $\tilde{K}_m(x), \tilde{I}_m(x)$ are defined by

$$\tilde{K}_m, \tilde{I}_m(x) = K_m, I_m(|x|). \tag{2.80}$$

We also break up $\Phi_{r,2}$ into Fourier components that satisfy Laplace's equation, and assume that these expressions hold up to the interface:

$$\Phi_r(\mathbf{r},\mathbf{r}') = \frac{1}{4\pi^2\epsilon_0\epsilon_1}\sum_{m=-\infty}^{\infty}e^{im(\phi-\phi')}\int_{-\infty}^{\infty}dh\, e^{ih(z-z')}\tilde{K}_m(h\rho)\alpha_m(h), \tag{2.81}$$

$$\Phi_2(\mathbf{r},\mathbf{r}') = \frac{1}{4\pi^2\epsilon_0\epsilon_1}\sum_{m=-\infty}^{\infty}e^{im(\phi-\phi')}\int_{-\infty}^{\infty}dh\, e^{ih(z-z')}\tilde{I}_m(h\rho)\beta_m(h). \tag{2.82}$$

To describe the surface roughness, we assume an interface with axial symmetry as before, $\rho_0(z) = R+p\zeta(z)$, where the roughness profile ζ satisfies the correlations given in Eqs. (2.67) and (2.68). The coefficients α_m, β_m are determined by the boundary conditions, namely that Φ and $\mathbf{D}_\perp$ must be continuous at the interface:

$$\begin{aligned} \Phi_1(\mathbf{r},\mathbf{r}')\big|_{\rho=R+p\zeta(z)} &= \Phi_2(\mathbf{r},\mathbf{r}')\big|_{\rho=R+p\zeta(z)}, \\ \epsilon_1 \hat{n}\cdot\nabla\Phi_1(\mathbf{r},\mathbf{r}')\big|_{\rho=R+p\zeta(z)} &= \epsilon_2 \hat{n}\cdot\nabla\Phi_2(\mathbf{r},\mathbf{r}')\big|_{\rho=R+p\zeta(z)}, \qquad (2.83) \\ \hat{n} &\equiv \frac{\hat{\rho}-p\frac{d\zeta}{dz}\hat{z}}{\sqrt{1+p^2\left(\frac{d\zeta}{dz}\right)^2}}. \qquad (2.84) \end{aligned}$$

Plugging in the expressions for Φ_i given by Eqs. (2.79), (2.81), and (2.82), one can expand both boundary condition equations to $\mathcal{O}(p^2)$. Then, replacing $\zeta(z)$ in these equations with its Fourier transform given in Eq. (2.65), one obtains a set of coupled equations for $\alpha_m, \beta_m(h)$ completely in Fourier space, which, unlike the case of a smooth nanowire, is not de-coupled in h. It is tedious but straightforward to show that, to $\mathcal{O}(p^2)$, this set of equations is given by the matrix integral equation

$$\begin{aligned} &M_0(h)\begin{pmatrix}\alpha_m(h)\\ \beta_m(h)\end{pmatrix} + p\int\frac{dq}{2\pi}\tilde{\zeta}(h-q)M_1(h,q)\begin{pmatrix}\alpha_m(q)\\ \beta_m(q)\end{pmatrix} \\ &+p^2\int\frac{dq\,dq'}{(2\pi)^2}\tilde{\zeta}(h-q-q')\tilde{\zeta}(q')M_2(h,q,q')\begin{pmatrix}\alpha_m(q)\\ \beta_m(q)\end{pmatrix} + \mathcal{O}(p^3) = \\ &\quad \mathbf{v}_0(h) + p\int\frac{dq}{2\pi}\tilde{\zeta}(h-q)\mathbf{v}_1(h,q) + p^2\int\frac{dq\,dq'}{(2\pi)^2}\tilde{\zeta}(h-q-q')\tilde{\zeta}(q')\mathbf{v}_2(h,q,q') \\ &\quad +\mathcal{O}(p^3). \qquad (2.85) \end{aligned}$$

The matrices M_i and vectors $\mathbf{v}_i$ are complicated expressions and are given in Appendix I.2. We note, however, that in the case of no surface roughness ($\tilde{\zeta} = 0$), the solution to the resulting equation $M_0(h) \cdot (\alpha_m(h)\ \beta_m(h))^T = \mathbf{v}_0(h)$ reduces to that of a smooth nanowire.

We now discuss how to solve Eq. (2.85) in the presence of surface roughness, using the methods detailed in Ref. [68]. One might first consider expanding α_m, β_m in a power series of p, in a manner similar to the field expansion in Eq. (2.62) for the case of radiative scattering, and then solving the $\mathcal{O}(p^{n+1})$ equations based on the $\mathcal{O}(p^n)$ solutions. However, such a perturbative solution simply yields poles for each higher-order correction with the same location as that of the unperturbed solutions $\alpha_m^{(0)}, \beta_m^{(0)}$. Mathematically, this occurs because each calculation of the next correction involves an inversion $M_0^{-1}(h)$. On the other hand, physically we expect for the surface roughness to result in some shift of the pole that is not predicted by such a perturbative method [68]. We thus consider an alternate approach, in which we symbolically sum the perturbation series in Eq. (2.85) to all orders and then only keep the lowest order result in p. Let us symbolically write Eq. (2.85) in the form

$$(\mathcal{M}_0 + \delta\mathcal{M})\mathbf{x} = \mathbf{f}_0 + \delta\mathbf{f}, \tag{2.86}$$

where $\mathcal{M}_0$ and $\mathbf{f}_0$ are non-random matrices and vectors, respectively, $\delta\mathcal{M}$ is a random 2×2 matrix integral operator, $\delta\mathbf{f}$ is a random vector, and $\mathbf{x}$ is a column vector with components α_m, β_m. We now define the averaging operator

$$Px = \langle x \rangle, \tag{2.87}$$

and the operator $Q = 1 - P$. We can apply P, Q to Eq. (2.86) to get

$$\begin{aligned} P\mathcal{M}_0\mathbf{x} + P\delta\mathcal{M}\mathbf{x} &= P(\mathbf{f}_0 + \delta\mathbf{f}), & (2.88)\\ Q\mathcal{M}_0\mathbf{x} + Q\delta\mathcal{M}\mathbf{x} &= Q(\mathbf{f}_0 + \delta\mathbf{f}), & (2.89) \end{aligned}$$

which after some manipulation results in the set of equations

$$(\mathcal{M}_0 + P\delta\mathcal{M})\,\langle\mathbf{x}\rangle + P\delta\mathcal{M}Q\mathbf{x} = P(\mathbf{f}_0 + \delta\mathbf{f}), \tag{2.90}$$

$$\begin{aligned} Q\mathbf{x} &= (1 + \mathcal{M}_0^{-1}Q\delta\mathcal{M})^{-1}\mathcal{M}_0^{-1}Q(\mathbf{f}_0 + \delta\mathbf{f}) \\ &\quad -(1 + \mathcal{M}_0^{-1}Q\delta\mathcal{M})^{-1}\mathcal{M}_0^{-1}Q\delta\mathcal{M}\langle\mathbf{x}\rangle. \end{aligned} \tag{2.91}$$

One can then substitute Eq. (2.91) into Eq. (2.90) and solve for $\langle\mathbf{x}\rangle$, in which case one obtains

$$\left(\mathcal{M}_0 + \langle(1 + \delta\mathcal{M}\mathcal{M}_0^{-1}Q)^{-1}\delta\mathcal{M}\rangle\right)\langle\mathbf{x}\rangle = \langle(1 + \delta\mathcal{M}\mathcal{M}_0^{-1}Q)^{-1}(\mathbf{f}_0 + \delta\mathbf{f})\rangle. \tag{2.92}$$

We note that, unlike a perturbative expansion and solution for α_m, β_m, the equation above is thus far exact. Now, we assume that $\delta\mathcal{M}$ and $\delta\mathbf{f}$ can be expanded in powers of p in the form

$$\begin{aligned} \delta\mathcal{M} &= p\delta\mathcal{M}_1 + p^2\delta\mathcal{M}_2 + \cdots, \\ \delta\mathbf{f} &= p\delta\mathbf{f}_1 + p^2\delta\mathbf{f}_2 + \cdots. \end{aligned} \tag{2.93}$$

Comparing Eqs. (2.85) and (2.93), we see that $\langle\delta\mathcal{M}_1\rangle = \langle\delta\mathbf{f}_1\rangle = 0$ since $\langle\tilde{\zeta}\rangle = 0$. With this result, and utilizing the definition $Q = 1 - P$, one can proceed to expand Eq. (2.92) up to $\mathcal{O}(p^2)$, which yields (after setting $p = 1$)

$$\left(\mathcal{M}_0 + \langle\delta\mathcal{M}_2\rangle - \langle\delta\mathcal{M}_1\mathcal{M}_0^{-1}\delta\mathcal{M}_1\rangle\right)\langle\mathbf{x}\rangle = \langle\mathbf{f}_0\rangle + \langle\delta\mathbf{f}_2\rangle - \langle\delta\mathcal{M}_1\mathcal{M}_0^{-1}\delta\mathbf{f}_1\rangle. \tag{2.94}$$

Substituting the corresponding terms of Eq. (2.85) into the equation above and using the second-order correlations given by Eq. (2.68), we find after simplifying that

$$\left[M_0(h) + \frac{s^2a^3}{2\sqrt{\pi}}\int dq\,F(q)\right]\left\langle \begin{array}{c} \alpha_m(h) \\ \beta_m(h) \end{array}\right\rangle = \left[\mathrm{v}_0(h) + \frac{s^2a^3}{2\sqrt{\pi}}\int dq\,G(q)\right], \tag{2.95}$$

Roughness parameters	$\Delta(\mathrm{Re}\,\tilde{C})$	$\Delta(\mathrm{Im}\,\tilde{C}/\mathrm{Re}\,\tilde{C})$
$a = 0.1R$, $\delta = 0.01R$ $(s = 0.1)$	0.2%	0.2%
$a = 0.1R$, $\delta = 0.05R$ $(s = 0.5)$	7.5%	6.8%
$a = R$, $\delta = 0.01R$ $(s = 0.01)$	0.03%	1.0%
$a = R$, $\delta = 0.05R$ $(s = 0.05)$	0.9%	26%
$a = R$, $\delta = 0.1R$ $(s = 0.1)$	3.5%	110%
$a = 10R$, $\delta = 0.01R$ $(s = 0.001)$	$> 0.01\%$	2.7%
$a = 10R$, $\delta = 0.05R$ $(s = 0.005)$	0.2%	67%
$a = 10R$, $\delta = 0.1R$ $(s = 0.01)$	0.8%	270%

Table 2.2: Losses and wavevector shifts due to non-radiative scattering off of surface roughness for nanowires with varying roughness parameters. The shifts in $\mathrm{Re}\,\tilde{C}$ and changes in loss parameters $\mathrm{Im}\,\tilde{C}/\mathrm{Re}\,\tilde{C}$ are given in terms of percentage increase over the corresponding values for a smooth nanowire.

$$F(q) \equiv e^{-a^2q^2/4}M_2(h,h,q) - e^{-a^2(h-q)^2/4}M_1(h,q)M_0^{-1}(q)M_1(q,h), \qquad (2.96)$$

$$G(q) \equiv e^{-a^2q^2/4}\mathbf{v}_2(h,h,q) - e^{-a^2(h-q)^2/4}M_1(h,q)M_0^{-1}(q)\mathbf{v}_1(q,h), \qquad (2.97)$$

where $s = \delta/a$.

We now discuss the solution to $\alpha_0(h)$, which contains a pole corresponding to the fundamental SP mode ($m = 0$). When ϵ_2 is a negative real number, α_0 has a pole on the real h-axis whose position gives the new, shifted SP wavevector $\tilde{k}_\parallel$. When ϵ_2 has a non-zero imaginary component, α_0 will have a resonance feature along this axis whose peak corresponds $\mathrm{Re}\,\tilde{k}_\parallel$ and whose width corresponds to $\mathrm{Im}\,\tilde{k}_\parallel$. A quick inspection of the equation above reveals that $\tilde{k}_\parallel R = \tilde{C}(\epsilon_i, s, a/R)$ is a constant that depends only on the quantities ϵ_i,s, and a/R. Unfortunately, because of the complexity of Eq. (2.95) it is difficult to derive other scaling results for $\tilde{k}_\parallel$ even in limiting cases. However, Eq. (2.95) can be solved numerically. In practice, for known parameters, the matrices M and vectors $\mathbf{v}$ can be readily evaluated over some range of h, from which the solutions to the system $\alpha_0, \beta_0(h)$ in that range immediately follow. The resulting resonance in $\mathrm{Im}\,\alpha_0(h)$ as a function of h is then fitted to a Lorentzian, with its peak giving the shifted wavevector $\mathrm{Re}\,\tilde{k}_{\|}$ and its half-width giving $\mathrm{Im}\,\tilde{k}_{\|}$. In Table 2.2, we give the resulting losses and wavevector shifts for a few roughness parameters, as calculated through Eq. (2.95). Again the numbers that we have used are for a silver nanowire at $\lambda_0 = 1\,\mu\mathrm{m}$ and $\epsilon_1 = 2$. The shifts in $\mathrm{Re}\,\tilde{k}_{\|}$ (or equivalently, $\mathrm{Re}\,\tilde{C}$) and increases in the loss parameter $\mathrm{Im}\,\tilde{k}_{\|}/\mathrm{Re}\,\tilde{k}_{\|}$ (or $\mathrm{Im}\,\tilde{C}/\mathrm{Re}\,\tilde{C}$) are given in terms of the percentage increase over their values for a smooth nanowire. It can be seen that for reasonable parameters, surface roughness adds only a moderate amount of loss to the system.

2.6.2 Dependence of metal losses on temperature and frequency

The inherent losses of a metal, characterized by the imaginary part of its electric permittivity $\epsilon(\omega)$, plays a detrimental or limiting role in both the maximum achievable Purcell factor and propagation losses. To reduce its effect on propagation losses, for example, we have suggested techniques such as integration of plasmonics with conventional microphotonics (see Sec. 2.5). Another approach that has been suggested is operating plasmonic devices at lower temperatures, with the expectation that the losses can be "frozen out" [69].

To determine if such an approach is feasible, it is important to understand the physical processes that lead to dissipation and how they depend on temperature. Here, we investigate a major dissipation mechanism, involving absorption of a surface plasmon (*i.e.*, a photon) of energy $\hbar\omega$ accompanied by an electron-phonon scattering event. We note that electron-impurity scattering and electron-surface scattering can be important processes as well [70], although in principle their effects can be reduced simply by using better samples, and thus they are not considered here. Before proceeding further, we also note that the problem of metal losses at optical frequencies due to electron-phonon scattering was first addressed by Holstein in Ref. [71], and a quite comprehensive theory of electron transport in metals was further developed by him in Ref. [72]. Discussions of his results also appear in, *e.g.*, Refs. [70, 73, 74], but to our knowledge, a concise, complete derivation has not previously appeared in literature, nor have the implications for plasmonics been considered.

We begin by deriving the rate of photon absorption due to electron-phonon scattering as functions of frequency and temperature. We then apply these results towards SP propagation and discuss the implications for plasmonic devices.

Photon absorption rate via electron-phonon scattering

The process that we wish to analyze is the absorption of a single photon accompanied by electron scattering. This electron scattering event simultaneously must be accompanied by the emission or absorption of a single phonon in order to conserve momentum and energy of the total process. To proceed, we split up the total interaction Hamiltonian $\hat{V} = H_{el-ph} + H_{el-field}$ into terms separately describing the electron interactions with phonon modes and the electromagnetic field. The electron-phonon interaction Hamiltonian, as derived in Appendix I.3, is given by

$$H_{el-ph} \approx \sum_{\mathbf{k}\mathbf{q}\sigma} \sqrt{\frac{2\hbar}{M N \omega_{\mathbf{q}}}} \left(\mathbf{Q}_{\mathbf{k}+\mathbf{q},\mathbf{k}} \cdot \hat{\epsilon}_{\mathbf{q}}\right) \hat{c}^{\dagger}_{\mathbf{k}+\mathbf{q},\sigma} \left(\hat{a}_{\mathbf{q}} + \hat{a}^{\dagger}_{-\mathbf{q}}\right) \hat{c}_{\mathbf{k}\sigma}. \tag{2.98}$$

Here M is the mass of an underlying ion in the lattice, N is the total number of ions, $\hbar\omega_{\mathbf{q}}$ and $\hat{\epsilon}_{\mathbf{q}}$ are the energy and polarization of phonon mode $\mathbf{q}$, $\hat{a}_{\mathbf{q}}$ is the annihilation operator for a phonon in mode $\mathbf{q}$, and $\hat{c}_{\mathbf{k}\sigma}$ is the annihilation operator for an electron with Bloch wavevector $\mathbf{k}$ and spin σ. Here, the subscript $\mathbf{q}$ appearing in the summations above and in $\omega_{\mathbf{q}}, \hat{a}_{\mathbf{q}}$ are understood to cover the polarization degrees of freedom as well. One can typically to good approximation make the simplification $\mathbf{Q}_{\mathbf{k}+\mathbf{q},\mathbf{k}} = C\mathbf{q}$ [72], where C is the phenomenological Sommerfeld-Wilson interaction constant [75]. Note that this result implies that the interaction of electrons with vibrations of the underlying crystal is mainly via longitudinal phonons. In other words, the electrons are sensitive to changes in the local density of the crystal (as opposed to transverse phonons that do not change the local density). We now consider the form of the electron-field Hamiltonian. In the following we will assume that the electrons are interacting with a uniform classical plane-wave field,

$$\mathbf{E} = \mathbf{E}_0 \left(e^{i\mathbf{h}\cdot\mathbf{r} - i\omega t} + c.c. \right). \tag{2.99}$$

In this case, as derived in Appendix I.3, the electron-field interaction Hamiltonian is given approximately by

$$H_{el-field} \approx e\mathbf{E}_0 \cdot \left(\sum_{\mathbf{k}} \mathbf{v}_{\mathbf{k}} \hat{c}^{\dagger}_{\mathbf{k}+\mathbf{h}/2} \hat{c}_{\mathbf{k}-\mathbf{h}/2} \frac{e^{-i\omega t}}{i\omega} + h.c. \right), \tag{2.100}$$

where $\mathbf{v}_{\mathbf{k}} \approx \nabla_{\mathbf{k}} \mathcal{E}(\mathbf{k})/\hbar$ is the electron velocity in state $\mathbf{k}$.

The process of photon absorption, accompanied by scattering of an electron and absorption/emission of a phonon is a second-order process. The corresponding transition rate from some initial system state $|i\rangle$ to final state $|f\rangle$ can be obtained from second-order perturbation theory:

$$\Gamma(i \rightarrow f) = \frac{2\pi}{\hbar^3} \left| \sum_n \frac{\langle f|\hat{V}|n\rangle\langle n|\hat{V}|i\rangle}{\omega_n - \omega_i} \right|^2 \delta(\mathcal{E}_f - \mathcal{E}_i), \tag{2.101}$$

where $\hat{V} = H_{el-ph} + H_{el-field}$. We first consider the situation when a photon is absorbed while scattering an electron from $\mathbf{k}$ to $\mathbf{k}'$, and accompanied by the emission of a phonon of wavevector $\mathbf{q}$ (*i.e.*, the number of phonons in mode $\mathbf{q}$ increases from $n_\mathbf{q}$ to $n_\mathbf{q}+1$). We denote this rate by $R^+_-(\mathbf{k} \rightarrow \mathbf{k}')$, where the superscript $+(-)$ refers to creation (annihilation) of a phonon, and the subscript $+(-)$ refers to creation (annihilation) of a photon. Starting from Eq. (2.101),

$$\begin{aligned}
R^+_-(\mathbf{k} \rightarrow \mathbf{k}') &= \frac{2\pi}{\hbar^3} f_\mathbf{k}(1-f_{\mathbf{k}'}) \left| \sum_n \frac{\langle f|H_{el-field}|n\rangle\langle n|H_{el-ph}|i\rangle}{\omega_n - \omega_i} \right. \\
&\quad \left. + \frac{\langle f|H_{el-ph}|n\rangle\langle n|H_{el-field}|i\rangle}{\omega_n - \omega_i} \right|^2 \times \\
&\quad \delta(\mathcal{E}_{\mathbf{k}-\mathbf{q}+\mathbf{h}} + \hbar\omega_\mathbf{q} - \mathcal{E}_\mathbf{k} - \hbar\omega) \qquad (2.102) \\
&\approx f_\mathbf{k}(1-f_{\mathbf{k}'}) \frac{4\pi e^2 (n_\mathbf{q}+1)}{MN\hbar^2\omega^2\omega_\mathbf{q}} \left| \frac{(\mathbf{E}_0 \cdot \mathbf{v}_{\mathbf{k}-\mathbf{q}+\mathbf{h}/2})(\mathbf{Q}_{\mathbf{k}-\mathbf{q},\mathbf{k}} \cdot \hat{\epsilon}_\mathbf{q})}{(\mathcal{E}_{\mathbf{k}-\mathbf{q}}/\hbar + \omega_\mathbf{q}) - \mathcal{E}_\mathbf{k}/\hbar} \right. \\
&\quad \left. + \frac{(\mathbf{E}_0 \cdot \mathbf{v}_{\mathbf{k}+\mathbf{h}/2})(\mathbf{Q}_{\mathbf{k}-\mathbf{q}+\mathbf{h},\mathbf{k}+\mathbf{h}} \cdot \hat{\epsilon}_\mathbf{q})}{(\mathcal{E}_{\mathbf{k}+\mathbf{h}}/\hbar) - (\mathcal{E}_\mathbf{k}/\hbar + \omega)} \right|^2 \times \\
&\quad \delta(\mathcal{E}_{\mathbf{k}-\mathbf{q}+\mathbf{h}} + \hbar\omega_\mathbf{q} - \mathcal{E}_\mathbf{k} - \hbar\omega). \qquad (2.103)
\end{aligned}$$

Here we have assumed that $\omega_\mathbf{q} = \omega_{-\mathbf{q}}$ and $\hat{\epsilon}_\mathbf{q} = \hat{\epsilon}_{-\mathbf{q}}$. $f_\mathbf{k}$ denotes the probability of occupation of electron state $\mathbf{k}$ (as determined by a Fermi distribution), and $\mathcal{E}_\mathbf{k}$ denotes the energy of electron $\mathbf{k}$. Under realistic parameters the photon momentum $\hbar\mathbf{h}$ can be considered negligible, and we can approximate $\mathcal{E}_{\mathbf{k}-\mathbf{q}+\mathbf{h}} \approx \mathcal{E}_{\mathbf{k}-\mathbf{q}}$, $\mathcal{E}_{\mathbf{k}+\mathbf{h}} \approx \mathcal{E}_\mathbf{k}$, and $\mathbf{k}' = \mathbf{k} - \mathbf{q} + \mathbf{h} \approx \mathbf{k} - \mathbf{q}$. We further will assume a dispersion relation for nearly free electrons, $\mathcal{E}_k = \hbar^2 k^2/2m$ and $\mathbf{v}_\mathbf{k} = \hbar\mathbf{k}/m$, where m is the effective electron mass.

With these assumptions, we finally arrive at

$$R_-^+(\mathbf{k}\to\mathbf{k}-\mathbf{q}) \approx f_\mathbf{k}(1-f_{\mathbf{k}'})\frac{4\pi e^2(n_\mathbf{q}+1)}{MNm^2\omega^4\omega_\mathbf{q}}|C\mathbf{q}\cdot\hat{\epsilon}_\mathbf{q}|^2\,|\mathbf{E}_0\cdot\mathbf{q}|^2\,\delta(\mathcal{E}_{\mathbf{k}-\mathbf{q}}+\hbar\omega_\mathbf{q}-\mathcal{E}_\mathbf{k}-\hbar\omega). \tag{2.104}$$

Similar calculations hold for various combinations of phonon and photon absorption/emission. We can write the result compactly as

$$\begin{aligned} R_{j'=\pm1}^{j=\pm1}(\mathbf{k}\to\mathbf{k}'=\mathbf{k}-j\mathbf{q}) \quad &\approx \quad f_\mathbf{k}(1-f_{\mathbf{k}'})\frac{4\pi e^2}{MNm^2\omega^4\omega_\mathbf{q}}\left(n_\mathbf{q}+\frac{1+j}{2}\right)|C\mathbf{q}\cdot\hat{\epsilon}_\mathbf{q}|^2\times \\ &\quad |\mathbf{E}_0\cdot\mathbf{q}|^2\,\delta(\mathcal{E}_{\mathbf{k}-j\mathbf{q}}+j\hbar\omega_\mathbf{q}-\mathcal{E}_\mathbf{k}+j'\hbar\omega). \end{aligned} \tag{2.105}$$

From Eq. (2.105) it is evident that only longitudinal phonons are involved in the scattering process. To describe the phonons in the system, we take a simple Debye model in three dimensions, and furthermore assume that the dispersion relation for phonons is isotropic and given by $\omega_q = vq$. The density of states for the longitudinal acoustic phonons in the Debye model is given by

$$D(q) = \frac{V}{(2\pi)^3}\theta(\omega_D-\omega_q), \tag{2.106}$$

where ω_D is the Debye frequency, which is defined by $N/V = \omega_D^3/(6\pi^2v^3)$, and $\theta(x)$ is the step function. For convenience we also define the Debye temperature $\Theta_D = \hbar\omega_D/k_B$ and the Debye wavevector $q_D = \omega_D/v$.

We first consider the total scattering rate for electrons with initial wavevector amplitude k. We can obtain this rate by summing the expressions in Eq. (2.105) over all final states $\mathbf{k}'$ (or equivalently $\mathbf{q}$) and averaging over all possible orientations of $\mathbf{k}$. We thus define the quantity

$$R_{j'=\pm1}^{j=\pm1}(k) \equiv \sum_\mathbf{q}\frac{\int d\Omega_0\, R_{j'}^j(\mathbf{k}\to\mathbf{k}-j\mathbf{q})}{\int d\Omega_0}, \tag{2.107}$$

where the angular integrals yield the average over all possible orientations (θ_0, ϕ_0) of $\mathbf{k}$. Converting the sum over $\mathbf{q}$ into an integral $\int dq \int d\Omega_{\mathbf{q}}$ and integrating over all angles $d\Omega_{\mathbf{q}}\, d\Omega_0$ yields

$$R^{j=\pm 1}_{j'=\pm 1}(k) = f(\mathcal{E}_k)\frac{8\pi^2 e^2 C^2 E_0^2}{3Mm\omega^4\hbar k}\frac{V}{N}\int_0^{q_D} dq\,\frac{q^5}{\omega_q}\left(n_q + \frac{1+j}{2}\right)\left(1 - f(\mathcal{E}_k - j\hbar\omega_q - j'\hbar\omega)\right). \tag{2.108}$$

The overall rate for photon emission/absorption is subsequently obtained by averaging over all initial magnitudes k. For an isotropic electron dispersion relation and when the Fermi energy is the largest energy scale, the overall rate can be approximated by

$$R^{j=\pm 1}_{j'=\pm 1} \equiv \frac{\sum_k R^j_{j'}(k)}{\sum_k f(\mathcal{E}_k)} \approx \frac{3}{2\mathcal{E}_F}\int_0^{\infty} d\mathcal{E}_k\, R^j_{j'}(k). \tag{2.109}$$

Simplifying the integral above yields

$$R^{j=\pm 1}_{j'=\pm 1} \approx \alpha\frac{e^2 E_0^2}{2m\omega^4}\int_0^{q_D} dq\,\frac{q^5}{\omega_q}\left(n_q + \frac{1+j}{2}\right)\frac{j\hbar\omega_q + j'\hbar\omega}{e^{\beta(j\hbar\omega_q + j'\hbar\omega)} - 1}, \tag{2.110}$$

where $\alpha = (C^2 V)/(\pi M N\hbar k_F \mathcal{E}_F)$. The net rate of energy transfer from the electromagnetic field is given by

$$\begin{aligned} W &= \hbar\omega\sum_{j=\pm 1}(R^j_- - R^j_+) && (2.111)\\ &\equiv \frac{e^2 E_0^2}{2m\omega^2}\frac{1}{\tau}, && (2.112)\end{aligned}$$

which in general can be evaluated numerically. Here the quantity τ can be identified as the frequency and temperature dependent net relaxation time for the conductor. While τ can always be obtained by numerically evaluating Eqs. (2.110) and (2.111), it is beneficial to consider a couple of limiting cases to understand the relevant physics:

- **Low-frequency limit** $\hbar\omega \ll k_B\Theta_D, k_B T$. In this limit, we can expand the integrand of Eq. (2.110) to first order in ω. Upon substituting into Eq. (2.111),

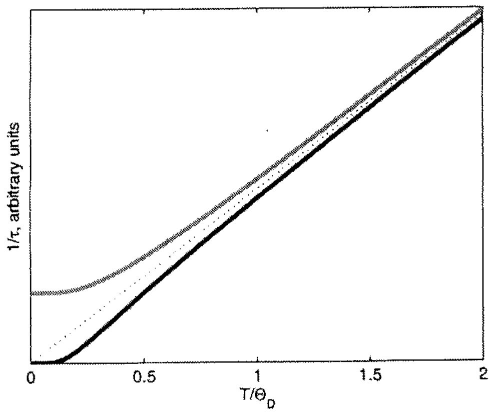

Figure 2.10: The relaxation rate $1/\tau$ as a function of temperature T. The black and red curves indicate the low and high frequency results, respectively, which are defined by $\hbar\omega \ll k_B\Theta_D, k_BT$ and $\hbar\omega \gg k_B\Theta_D, k_BT$. The dashed line indicates the high-temperature asymptotic result, $1/\tau \propto T$. The crossover between low- and high-temperature behavior occurs at a temperature $T \sim \Theta_D$.

one obtains

$$\frac{1}{\tau} = \frac{1}{\tau_0}\left(\frac{T}{\Theta_D}\right)^5 \int_0^{\Theta_D/T} dz \, \frac{z^5}{-1+\cosh z}. \tag{2.113}$$

Here, the constant $\tau_0 = (\hbar C^2 V \omega_D^5)/(\pi v^6 M N k_F \mathcal{E}_F)$ depends only on the physical properties of the crystal. In the limits $\Theta_D \gg T$ and $\Theta_D \ll T$, the integral appearing above can be approximately evaluated to yield

$$\frac{1}{\tau} \approx \frac{1}{\tau_0} \begin{cases} \frac{T}{2\Theta_D} & \Theta_D \ll T \\ 240\zeta(5)\left(\frac{T}{\Theta_D}\right)^5 & \Theta_D \gg T \end{cases}. \tag{2.114}$$

Note in particular that in the low-temperature limit, the relaxation rate goes to zero as the phonon degrees of freedom get frozen out. In the high-temperature limit, the scattering rate increases linearly with T.

- **High-frequency limit $\hbar\omega \gg k_B\Theta_D, k_BT$.** In this limit, the probability of a thermal photon being created is negligible, so

$$W \approx \hbar\omega \sum_{j=\pm} R_-^j, \tag{2.115}$$

and

$$\frac{1}{\tau} = \frac{1}{\tau_0}\left(\frac{1}{5} + 2\left(\frac{T}{\Theta_D}\right)^5 \int_0^{\Theta_D/T} dz\, \frac{z^4}{e^z - 1}\right). \tag{2.116}$$

Again the integral can be approximately evaluated in the limits of low and high temperature,

$$\frac{1}{\tau} \approx \frac{1}{\tau_0}\begin{cases} \frac{T}{2\Theta_D} & \Theta_D \ll T \\ \frac{1}{5} & \Theta_D \gg T \end{cases}. \tag{2.117}$$

For high temperatures, note that the low- and high-frequency results of Eqs. (2.114) and (2.117) are identical. In the low-temperature limit, however, the relaxation rate at high frequencies approaches a constant $1/(5\tau_0)$ instead of going to zero. Physically, the first term in parentheses in Eq. (2.116) corresponds to the spontaneous creation of the phonon needed to conserve momentum from some of the initial photon energy. Because the photon energy is large, this process persists even at zero temperature and cannot be frozen out.

A comparison of the low- and high-frequency results as a function of T is plotted in Fig. 2.10.

Discussion of results

We now consider the derived results derived in the context of plasmonics. We suppose that SPs propagate on a conductor whose electric permittivity is given by a Drude model,

$$\epsilon(\omega, T) = 1 - \frac{\omega_p^2}{\omega^2 - i\omega/\tau(\omega, T)}, \tag{2.118}$$

where ω_p is the plasma frequency and $\tau(\omega, T)$ is the relaxation time as determined by Eq. (2.112). For concreteness, in the following we choose the material parameters ω_p, τ_0, and Θ_D to closely correspond to those of silver (the constant τ_0 for silver is taken from Ref. [70]).

In Fig. 2.11a we plot the normalized relaxation rate τ_0/τ, as functions of temperature and the vacuum wavelength $\lambda_0 = 2\pi c/\omega$ corresponding to the frequency of the electromagnetic field. It is evident that the temperature $T{\sim}\Theta_D$ and frequency $\omega{\sim}\omega_D$ (denoted by blue lines in the plot) distinguish different regimes of behavior, as discussed previously. In particular, for frequencies $\omega{\gg}\omega_D$, the scattering rate decreases only moderately between room and cryogenic temperatures. Physically, the photon energy is so large that its absorption allows for the spontaneous creation of phonons needed to conserve momentum in a scattering process. For high temperatures $T{\gtrsim}\Theta_D$, one observes the expected linear increase in relaxation rate, independent of frequency. Finally, at low temperatures $T{\ll}\Theta_D$ and low frequencies $\omega{\ll}\omega_D$, lowering the temperature does allow for a significant decrease in the relaxation rate. Here, the photon energy is small compared to the characteristic phonon energy, which allows for the phonon degrees of freedom to be frozen out. This phenomenon is related to the well-known behavior of dc current transport in silver, where low temperatures can significantly reduce the electric resistivity.

In Fig. 2.11b, we plot the quantity $\omega\tau$ as functions of temperature and wavelength. In order for our relaxation rates derived from second-order perturbation theory to be valid and consistent, $\omega\tau{\gg}1$ must be satisfied. Physically, this requirement states that the electron-phonon interaction is sufficiently weak that the effects of higher-

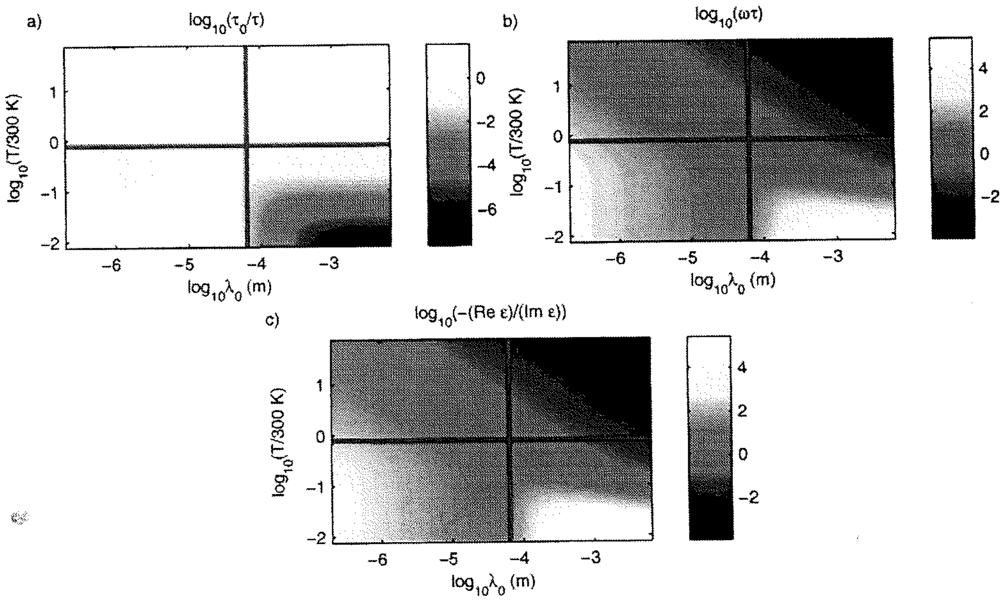

Figure 2.11: a) The normalized relaxation rate τ_0/τ of silver, plotted on a logarithmic scale, as functions of temperature and vacuum wavelength $\lambda_0 = 2\pi c/\omega$ of the electromagnetic field. The horizontal and vertical blue lines indicate the Debye temperature Θ_D and the wavelength $\lambda_D = 2\pi c/\omega_D$ corresponding to the Debye frequency, respectively, which separate different regimes of behavior. b) Logarithmic plot of $\omega\tau$ for silver. Regions where $\omega\tau \gg 1$ indicate that the electron-phonon coupling is weak and that the perturbative calculation of the relaxation time τ carried out here is valid. c) Logarithmic plot of $-\mathrm{Re}\,\epsilon/\mathrm{Im}\,\epsilon$ for silver.

order scattering processes do not need to be taken into account. For silver, it can be seen that $\omega\tau \gg 1$ is satisfied over a large range of operating parameters, and thus the perturbative calculations presented here are indeed sufficient. In Fig. 2.11c, we have plotted the ratio of the real to imaginary parts of the electric permittivity ϵ for silver, as obtained by the model of Eq. (2.118).

We now consider the properties of the fundamental SP mode of a silver wire as functions of temperature and frequency, in the limit that the wire radius is smaller than the skin depth. As discussed in Sec. 2.2, in this limit the wavevector characterizing propagation of the SPs along the wire axis must behave like $k_{\|} = C/R$. In general C is complex, and the ratio Re C/Im C determines how many SP wavelengths a SP excitation can travel before being dissipated. The propagation constant depends on the electric permittivity $\epsilon(\omega, T)$ of the wire via Eq. (2.5),

$$\frac{\epsilon(\omega, T)}{\epsilon_1} = \frac{K_0'(C)I_0(C)}{K_0(C)I_0'(C)}, \tag{2.119}$$

where ϵ_1 is the permittivity of the material surrounding the wire and K_m, I_m are modified Bessel functions. In the following we will take the surrounding material to be vacuum, such that $\epsilon_1 = 1$. In Fig. 2.12 we plot the quantity Re C/Im C as functions of frequency and temperature. For room temperatures and below, there is a broad range of frequencies from the near infrared to the optical where this ratio is large, and the SPs can propagate with low losses. The upper bound of this allowed frequency range is given by $\omega \sim \omega_p/\sqrt{2}$, which is the cutoff for the existence of SP modes on the silver wire. The lower bound is set by the condition $\omega \sim 1/\tau$, when the real and imaginary parts of the dielectric constant $\epsilon(\omega, T)$ become comparable. For silver, this entire frequency range lies above the Debye frequency ω_D, which implies that losses can only be moderately reduced by going from room temperature to cryogenic temperatures. Furthermore, one sees that the mid- to far-infrared frequency range is extremely lossy for any temperature. For these frequencies, it is then expected that it is not possible to confine SPs to dimensions smaller than the skin depth without severe losses. When the frequency of operation is further reduced such that $\omega < \omega_D$ ($\lambda_0 \gtrsim 100$ μm), going to low temperatures does have a positive effect, and the silver wire can once again support tightly confined fundamental SP modes with long propagation lengths. It is significant to note that the THz frequency range lies

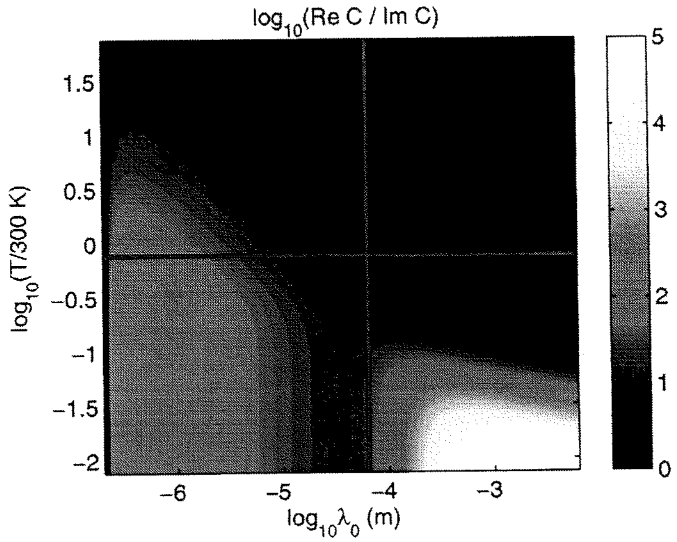

Figure 2.12: Logarithmic plot of the ratio $(\mathrm{Re}\, C)/(\mathrm{Im}\, C)$, where $C \equiv k_{\|} R$ is the propagation constant in the electrostatic limit. The horizontal and vertical blue lines indicate the Debye temperature Θ_D and the wavelength $\lambda_D = 2\pi c/\omega_D$ corresponding to the Debye frequency, respectively, which separate different regimes of behavior.

within this regime, since the development of THz technology is becoming increasingly important to many fields.

In conclusion, the benefits of going to low temperature to improve surface plasmon propagation are heavily dependent on the frequency of operation. The relevant parameter is the photon energy $\hbar\omega$ as compared to the characteristic energy of phonons, $\hbar\omega_D$. When the photon energy is small, this situation closely resembles that of dc current transport in conducting wires, and a lowering of the temperature can dramatically improve propagation lengths. When the photon energy is much larger, the phonons needed to conserve momentum in scattering events can be spontaneously created, and this process cannot be efficiently frozen out. Even so, it may turn out that the moderate improvement in propagation lengths at low temperatures for these frequencies can be combined with other techniques (*e.g.*, optimization of nano-structures and integration with microphotonics) to enable efficient, large-scale quantum plasmonic devices and applications.

Chapter 3

Efficient generation of single surface plasmons in metallic nanowires coupled to quantum dots

3.1 Introduction

In this chapter, we report on the experimental observation of strong coupling between an individual quantum emitter and single SPs on a conducting nanowire, confirming some of the theoretical ideas developed in Chapter 2. In particular, we investigate experimentally the nature of emitter-SP coupling in simple systems consisting of individual CdSe quantum dot (QD) nanocrystals coupled to proximal, chemically synthesized silver nanowires. We find that when a single QD is positioned well within the evanescent tails of the SP modes of the nanowire, its spontaneous emission rate is significantly enhanced due to coupling with single SPs. The emission into SPs can be observed in the far field when the guided SPs scatter radiatively off of the wire ends (see Fig. 3.1a), causing the ends to light up. Measuring the field correlations of the scattered light allows us to deduce that these are single spontaneously emitted photons originating from the QD. Furthermore, they also allow us to extract the total spontaneous emission rates and Purcell factors for these systems. For the best coupled systems, values of $P > 1$ are observed, indicating that the strong coupling regime is reached.

3.2 Experimental setup

The nanowire and CdSe quantum dot nanocrystal systems were prepared by spinning QD nanocrystals (with diameters ~15 nm) onto a glass substrate, covering them with a thin layer of PMMA [76] of controlled thickness, and then depositing nanowires on top via a "stamping" process, as described below. Finally the sample was overcoated with a thick layer of PMMA. It should be noted that this method of sample preparation results in a system of randomly positioned nanowires and QDs. However, the minimum allowed distance between a nanowire and QD, which is given by the sum of the thickness of the thin, separating PMMA layer and the nanocrystal radius, can be controlled.

Crystalline, chemically synthesized silver nanowires were chosen for this experiment because they have significantly reduced SP propagation losses compared to amorphous, lithographically defined wires [77]. The chemical process used here was based, with some modifications, on the solution-phase polyol method developed in Ref. [78], which results in bi-crystalline wires with relatively uniform sizes. The syn-

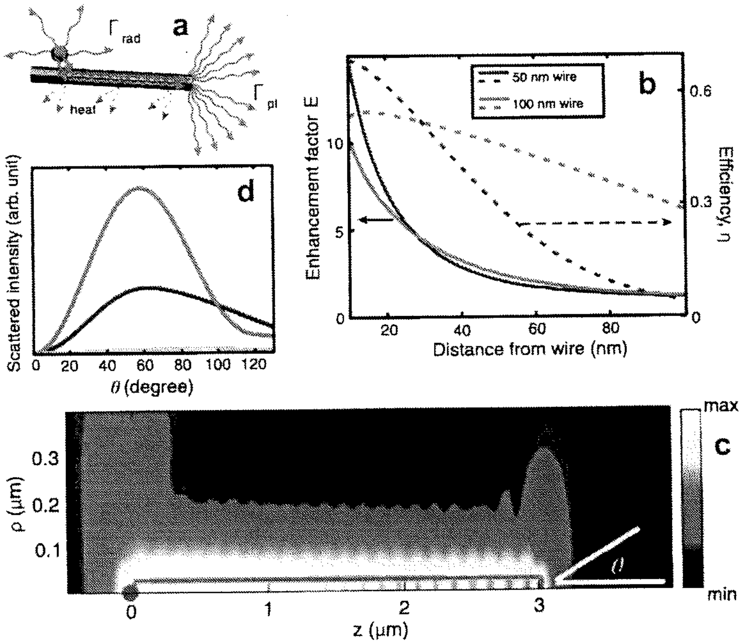

Figure 3.1: a) Illustration of coupling between a QD and conducting nanowire. The QD can either spontaneously emit into free space or into the SPs. For a finite-length wire, the guided SPs can be scattered off of the wire ends into free space. b) Theoretical dependence of the total spontaneous emission rate enhancement factor E (solid line) and efficiency of emission into SPs (dashed line) on the distance of the emitter from the nanowire edge. The red and blue curves correspond to wires with diameters 100 nm and 50 nm, respectively. c) Simulations of the electric field amplitude (arbitrary units) emitted by a dipole (blue point) positioned 25 nm from one end of a conducting nanowire (whose surface is outlined). Note that the vertical scale is enlarged compared to the horizontal in order to clearly show the near field of the SPs. The wire is $3\,\mu$m in length and $50\,$nm in diameter. The field profile indicates strong emission into the guided SPs of the nanowire. Upon hitting the far end of the nanowire, some of the SP energy is clearly scattered into the far-field with some angular dependence θ, while the remaining is either lost to dissipation or to back-reflection. The interference of the back-reflected and forward-propagating SPs is clearly visible as oscillations of the field along the nanowire. d) Amplitude of the Poynting vector of the light scattered from the far end of the nanowire, as a function of emission angle θ (see Fig. 3.1c), for wires of diameter 100 nm (red curve), 50 nm (blue), 25 nm (green).

thesis process was tuned to yield nanowire radii of approximately $R = 50\pm10$ nm and lengths of ~5 μm [79]. As discussed further below, this wire radius was chosen as a balance between achieving large Purcell factors and efficient SP scattering to free space at the wire ends. The silver nanowires in solution were subsequently dried onto a stamp that could be applied to the QD/PMMA layers.

In general, as discussed in Chapter 2, the coupling between an optical emitter and single SPs should be stronger for thinner wires. This can be seen in Fig. 3.1b, which shows the total spontaneous emission rates and coupling efficiencies $\eta = \Gamma_{\text{pl}}/\Gamma_{\text{total}}$ for wires of diameters 50 and 100 nm. However, for thinner wires, the out-coupling efficiency of SPs to far-field optical modes at the wire end decreases due to a large wavevector mismatch. In this case, significant SP reflection at the nanowire ends causes standing SP wave formation within the nanowire [80] and eventual energy loss due to heating (Ohmic losses). Both effects of SP to far-field scattering at the wire ends and SP standing wave formation can be seen in the boundary element method simulation (see Appendix C) shown in Fig. 3.1c. The effect of nanowire diameter on out-coupling efficiency, as obtained from these BEM simulations, is illustrated in Fig. 3.1d. Here, the intensity of the scattered radiation from the wire end is plotted for different wire diameters. For a thin, 25 nm nanowire hardly any scattering is seen from the end despite the stronger coupling between the emitter and SPs, but the scattering is significant for a 100 nm wire. Nanowires with $d{\sim}100$ nm exhibit both reasonable emitter-SP couplings and SP to far-field scattering, and thus were chosen for the experiments. The large bandwidth of the SP-emitter coupling enables the experiments to be performed at room temperature, where a single QD spectral width exceeds 15 nm.

The experimental setup for studying the QD-nanowire system is based on a modified confocal microscope with three scanning channels, as illustrated in Fig. 3.2a. The excitation source is a cw, 532 nm laser. One channel (Ch I) was used to image nanowires by detecting reflected green light from the sample, and the second channel (Ch II) was used for imaging QDs via fluorescence at 655 nm. The third channel (Ch III) includes an independent galvanometer which can separately image any diffraction-limited spot within the field of view of the objective lens. This channel was used to detect the scattered SPs from the nanowire ends at 655 nm.

3.3 Observation of strong coupling

A typical image of the sample is given in Fig. 3.2c, which demonstrates directed emission of a QD into SPs. The first figure in the series shows a confocal reflection image of a silver nanowire recorded with Ch I. The second corresponds to a fluorescence image of QDs detected at 655 nm with Ch II. These two images were used to determine the positions of the nanowire and QD relative to each other. Due to the resolution limit of our optical system, the actual distance between a QD and the nanowire could not be determined, and only QDs that appear directly on the top of a nanowire were chosen for the experiment. The third figure shows a coupled wire-dot system imaged with Ch III. When the proximal QD (circled in red) was excited by the laser, the nanowire ends literally lit up. The large spot in the center of the figure corresponds to emission from the QD itself, whereas the two other points coincide with the ends of the wire. Significantly, a high degree of correlation was seen between

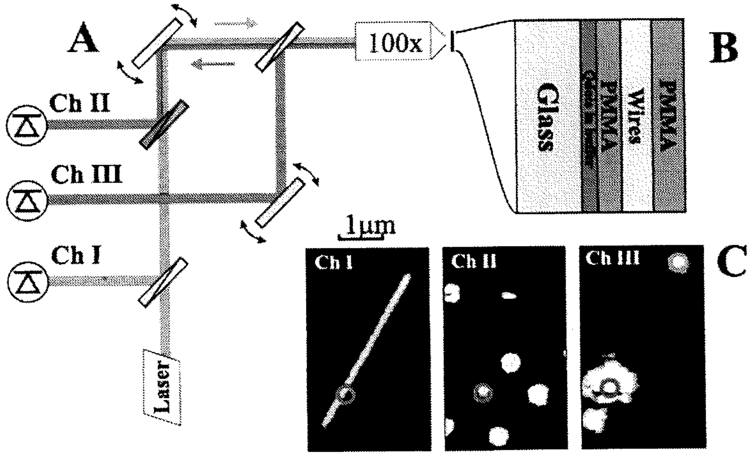

Figure 3.2: Experimental setup. a) Three-channel confocal microscope. A 532 nm laser serves as the excitation source, and collection is through a high numerical aperture objective lens (NA 1.3). b) Layout of sample containing QDs and nanowires. c) Images taken with channels I,II,III, showing coupling of QD radiation to SPs. The first image is of a nanowire taken with Ch I. The second is an image of QDs taken with Ch II. The red circle in the second figure corresponds to the position of the coupled QD, and the same point is also denoted in the first image. The third image was taken with Ch III. The excitation laser was focused on the QD (marked by red circle). The largest bright spot corresponds to the QD fluorescence, while two smaller spots correspond to SPs scattered from the nanowire ends. The blue circle indicates the furthest end of the nanowire, used for photon cross-correlation measurements (see Fig. 3.3).

the time traces of the fluorescence counts from the QD and from the end of the wire to which the QD was coupled, as shown in Fig. 3.3a. These observations indicate that the source of the fluorescence from the end of the wire is the QD.

Photon coincidence measurements [82] of the QDs, shown in Fig. 3.3b, demonstrate that the QDs used in these experiments can only emit a single photon at a time. In these measurements, the free-space fluorescence from the QD was equally split into two channels using a beam splitter and detected by avalanche photo-diodes. The coincidences between two channels were recorded as a function of time delay.

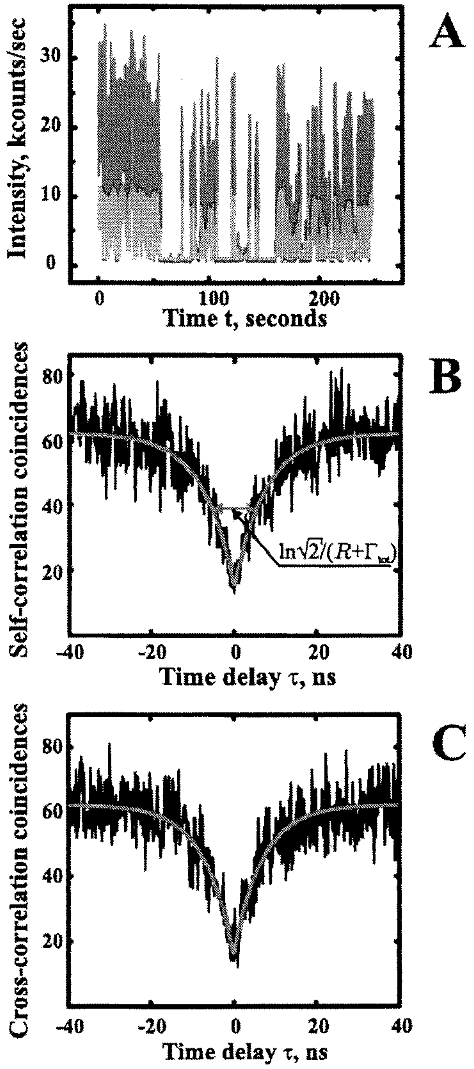

Figure 3.3: a) Time trace of fluorescence counts (red curve) from a coupled QD and scattered light (blue) from the end of the nanowire to which it is coupled. Fluctuations are due to QD blinking [81]. b) Second-order correlation function $G^{(2)}(\tau)$ (corresponding to the number of coincidences between the two channels) of QD fluorescence. The number of coincidences at $\tau = 0$ goes almost to zero, confirming that the QD is a single-photon source. The width of the dip depends on the total decay rate Γ_{total} and the pumping rate R. c) Second-order cross-correlation function between fluorescence of the QD and scattering from the nanowire end. This data was taken by looking at coincidences between Ch II (QD) and Ch III (wire end) in our setup.

If the QD emits only one photon at a time it can only be recorded at one of the channels, and therefore zero coincidences are expected between two channels at zero time delay as seen in Fig. 3.3b. The slight offset from zero can be attributed to stray light, dark counts of the detectors and the resolution limit of the electronics [79].

The light emission at the nanowire end is a result of single, quantized SPs scattering off the ends of the nanowire. This is demonstrated in Fig. 3.3c by the dip at $\tau = 0$ in the photon coincidence measurements between the free-space fluorescence of the QD and the emission from the wire end. This near-zero coincidence is a consequence of the fact that the single photon emitted from a QD can either radiate into free space or into the SP modes but never both simultaneously.

Data presented in Fig. 3.3c can be used to quantify the coupling strength of the QD to the SP modes. Since the QD-SP coupling creates a new decay channel for the QD, its decay rate is expected to increase. To study this enhancement, observed coincidence data was fitted to a simple two-level model of QD emission [83], as shown in Fig. 3.3b. Specifically, the dynamics of the QD is assumed to consist of some incoherent pumping rate R (which is proportional to laser power) from the ground to excited state, and a decay rate Γ_{total} back to the ground state. After the detection of an initially emitted photon, the QD is projected back into the ground state, and the evolution of the excited-state population following the projection is given by

$$P_{ee} = \frac{R}{R + \Gamma_{\text{total}}} \left(1 - e^{-(R+\Gamma_{\text{total}})t}\right). \tag{3.1}$$

The probability of detecting another photon at time t following the initial detection is simply proportional to the excited state population. In particular, the temporal width of the anti-bunching dip will be given by $\Delta\tau = \left(\ln\sqrt{2}\right)/(R + \Gamma_{\text{total}})$. Therefore, by extracting $\Delta\tau$ from coincidence measurements as a function of incident laser power and by extrapolating it to $R = 0$, the total decay rate Γ_{total} can be obtained (see Fig. 3.4a).

The natural lifetimes of individual dots (20-30 ns) vary from dot to dot due to the heterogeneity in their structures. However, the comparison of the lifetime distributions of 30 coupled and 100 uncoupled QDs shown in Fig. 3.4b clearly demonstrates that statistically the lifetime (decay rate) of the exciton in coupled QDs is shortened (enhanced). For a separating PMMA layer thickness of ~30 nm (which, including the QD shell radius, corresponds to a ~35 nm separation between QD and wire), the average lifetime of the coupled (uncoupled) QDs was found to be 12 ns±4 ns (21 ns±6 ns). At the same time, the distribution for coupled QDs has a larger weight towards shorter lifetimes. We found that certain coupled and uncoupled QDs exhibited lifetimes as short as 6 ns and 15 ns, respectively, indicating that a spontaneous emission enhancement of $E \equiv \Gamma_{\text{total}}/\Gamma_0 > 2.5$ is achieved for some coupled QD-nanowire systems. The apparent efficiency of emission into the SPs can be estimated by comparing the ratio of photon counts obtained directly from the dot and from the wire ends, $\eta_m \approx n_{ends}/(n_{dot} + n_{ends})$, and is found to be ~25% for the best coupled QD-nanowire system (see Fig. 3.4d). Note that this value does not account for the SPs that are dissipated before they reach the wire ends. Correcting for the measured average absorption lengths in the nanowires allows us to deduce that the actual efficiency approaches $\eta \sim 60 \pm 10\%$, with a corresponding Purcell factor of $P \sim 1.5$. Thus the strong coupling regime is reached in these systems.

The broadband nature of strong coupling is demonstrated by comparing the optical spectra associated with direct emission from the QD and from the wire end. For individual dots randomly drawn from an inhomogeneous ensemble with $\lambda = 655 \pm 15$ nm we find that both the QD and wire-end emission exhibit identical ~15 nm wide spectra. This is consistent with the ability of metallic wires to guide a broad range of optical frequencies [84] and with the predictions of Chapter 2 that strong coupling can be obtained for a broad continuum of frequencies away from the peak of the observed plasmon resonances [85].

Further insight into the QD-SP coupling can be obtained by comparing our experimental observations with fully electrodynamic theoretical calculations using the techniques of Chapter 2. Fig. 3.1b shows the theoretical total spontaneous emission rates and the efficiency $\eta = \Gamma_{\mathrm{pl}}/\Gamma_{\mathrm{total}}$ for single SP generation as a function of QD distance from the wire (d = 50 and 100 nm). Here the polarization of the QD transition was selected to be radially oriented, because this direction is expected to yield the dominant contribution to enhancement. For QDs positioned 35 nm from the wire and for a 100 nm wire, the calculation yields a Purcell factor $P{\sim}3.7$. The lower enhancement observed experimentally can be attributed to the contributions from other polarization directions and the random positioning of the QDs away from the wire. For this distance of separation, the non-radiative decay rate ($\Gamma_{\text{non-rad}} < 0.05\Gamma_0$) is predicted to be negligible. In addition to enhanced emission into guided SP modes, our theory also predicts a moderate increase in the radiative emission rate, as given in Eq. (2.24), a well-known phenomenon for dipoles oriented perpendicularly to a metallic surface [86]. For the 100 nm wires and 35-40 nm nanowire-QD distances, the efficiency η is theoretically estimated to be ~ 50%, which is consistent with our observations as well.

Further comparison with theoretical predictions is obtained by repeating our observations with thicker PMMA layers (see Figs. 3.4c,d). These measurements demonstrate that both enhancement and estimated coupling efficiency rapidly decrease as the minimum QD-nanowire spacing increases, and become very small for PMMA thicknesses above 100 nm. These observations are also in good agreement with the above theoretical predictions.

3.4 Conclusion

The unique properties of nanoscale SPs have recently been explored in a variety of fascinating systems, ranging from transmission and waveguiding through sub-wavelength structures [87] to biomedical devices [88] and proposals for realizing "perfect" lenses and invisibility cloaks [88]. Enhancement of fluorescence [52], polarization-dependent coupling [53] and normal mode splitting [89] near the subwavelength structures have also recently been observed. The present work extends these developments in two principal directions. First, we have shown experimentally and theoretically that the present approach results simultaneously in significant enhancement of SP emission and efficient collection into guided modes propagating along a well-defined direction. Second, it establishes direct coupling between individual emitters and individual, quantized SPs. It thus bridges the fields of nanoscale plasmonics and quantum optics [90], and opens up the possibility of using quantum optical techniques to achieve new levels of control over the interaction of single SPs and to realize novel quantum plasmonic devices. In the current setup, the benefits of using smaller wires must be balanced against poor out-coupling to free-space modes. However, this trade-off can be circumvented by using optimized geometries (*e.g.*, SPs on conducting nanotips) and evanescent out-coupling to mode-matched optical fibers [91, 92, 93]. The excellent coupling expected from these integrated systems can be uniquely used, *e.g.*, for efficient single-photon sources, high resolution microscopy [94] and sensing [95], or long-range quantum bit coupling [10]. Furthermore, in such systems an individual emitter can be made optically opaque to incident, localized single SPs, which can be used to produce large optical nonlinearities for realization of single-photon switches and photonic transistors [96]. Beyond these specific applications, the ability to create and control individual quanta of radiation with sub-wavelength localization may open up intriguing possibilities on the interface of several areas of optics and electronics.

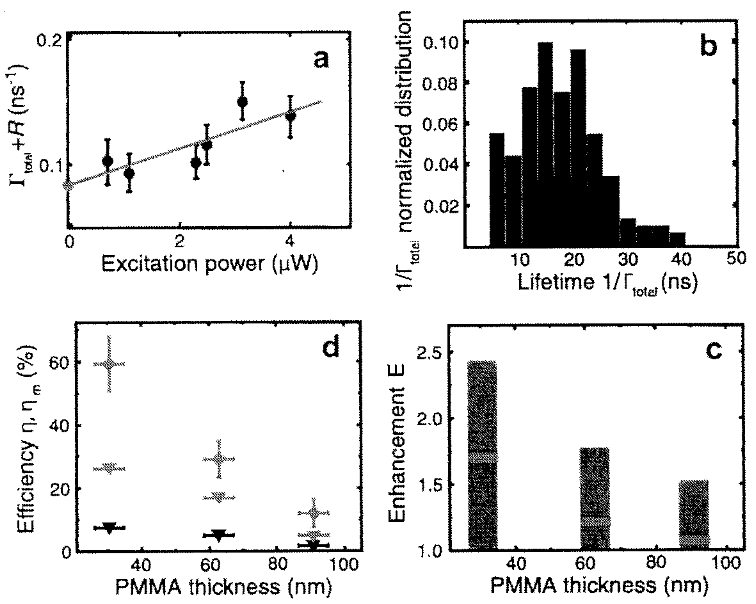

Figure 3.4: a) The linear dependence of the width of the $G^{(2)}$ dip on laser excitation power can be extrapolated to zero power, yielding the total spontaneous emission rate of a QD. b) Normalized histograms of QD lifetimes. The black curve corresponds to the distribution of uncoupled QDs (100 data points) and grey to coupled QDs (30 points). The mean lifetimes for uncoupled and coupled dots are 21 ns± 6ns and 12 ns± 4ns respectively. c) Average enhancement of coupled systems as a function of PMMA thickness. The gray columns indicate the standard deviations of the obtained distributions. The red rectangle indicates the average value observed. d) Measured maximum and average efficiencies of emission into the SPs as a function of PMMA thickness, as determined from count rates obtained from the QD and wire ends. The black (red) triangles indicate average (maximum) apparent efficiencies η_m of the coupled systems, without compensating for SP losses. The red diamonds give the maximum actual efficiency η, after compensating for the measured dissipation losses of the nanowires.

Chapter 4

Nonlinear optics using surface plasmons: a single-photon transistor

4.1 Introduction

In analogy with the electronic transistor, a photonic transistor is a device where a small optical "gate" field is used to control the propagation of another optical "signal" field via a nonlinear optical interaction [97, 98]. Its fundamental limit is the single-photon transistor, where the propagation of the signal field is controlled by the presence or absence of a single photon in the gate field. Such a nonlinear device has many interesting applications from optical communication and computation [98] to quantum information processing [99]. However, its practical realization is challenging because the requisite single-photon nonlinearities are generally very weak [97]. Several schemes for producing nonlinearities at the single-photon level are currently being explored, ranging from resonantly enhanced nonlinearities of atomic ensembles [100, 101, 102, 103] to individual atoms coupled to photons in cavity quantum electrodynamics (QED) [1, 2, 3, 4, 9, 11, 104], and possibilities of single-photon switching in these contexts have been proposed as well [101, 105]. However, a robust, practical approach has yet to emerge.

In Chapters 2 and 3, it was shown that strong coupling between individual emitters and single SPs on conducting nanowires could be achieved based on the tight confinement of the SP modes. The strong coupling was demonstrated to give rise to strongly preferential spontaneous emission into the SP modes. Whereas spontaneous emission can be thought of as a linear optical effect, here we show that such a system allows for the realization of remarkable nonlinear optical phenomena as well, where individual photons strongly interact with each other. As an example, we describe how this nonlinearity may be controlled and manipulated to implement a single-photon transistor. While ideas for developing plasmonic analogues of electronic devices by combining SPs with electronics are already being explored [88, 106], the process we describe here opens up fundamentally new possibilities, in that it combines the ideas of plasmonics with the tools of quantum optics [1, 2, 3, 102, 103] to achieve unprecedented control over the interactions of individual light quanta.

4.2 Nanowire surface plasmons: interaction with matter

Quite generally, a conducting nanowire can be thought of as a single-mode waveguide that supports a set of one-dimensional, travelling electromagnetic modes (see Chapter 2). We now describe a general model for such a system interacting with an individual, proximal optical emitter (see Figs. 4.1a, b). We first consider a simple two-level configuration for the emitter, consisting of ground and excited states ($|g\rangle, |e\rangle$) separated by frequency ω_{eg}. The corresponding Hamiltonian is

$$H = \hbar(\omega_{eg} - i\Gamma'/2)\sigma_{ee} + \int dk\, \hbar v|k|\hat{a}_k^\dagger \hat{a}_k - \hbar g \int dk\, \left(\sigma_{eg}\hat{a}_k e^{ikz_a} + h.c.\right), \qquad (4.1)$$

where $\sigma_{ij} = |i\rangle\langle j|$, $\hat{a}_k$ is the annihilation operator for the mode with wavevector k, and z_a is the emitter position. We have assumed that a linear dispersion relation holds over the relevant frequency range, $\nu_k = v|k|$, where v is the group velocity of the SPs, and similarly that g is frequency-independent. In the spirit of the "quantum jump" description of an open system [107], we have also included a non-Hermitian term in H due to the decay of state $|e\rangle$ at a rate Γ' into the other channels (*e.g.*, radiative and non-radiative emission). This effective Hamiltonian accurately describes the dynamics provided that the probability of a quantum jump remains small. As discussed in previous chapters, $g \propto 1/\sqrt{A_{\text{eff}}}$ scales favorably with decreasing mode area, which allows this interaction strength to be very large in conducting nanowires that support tightly confined SP modes.

In what follows we will only be interested in the dynamics of SP modes near the optical frequency ω_{eg}, and thus we can effectively treat left- and right-propagating

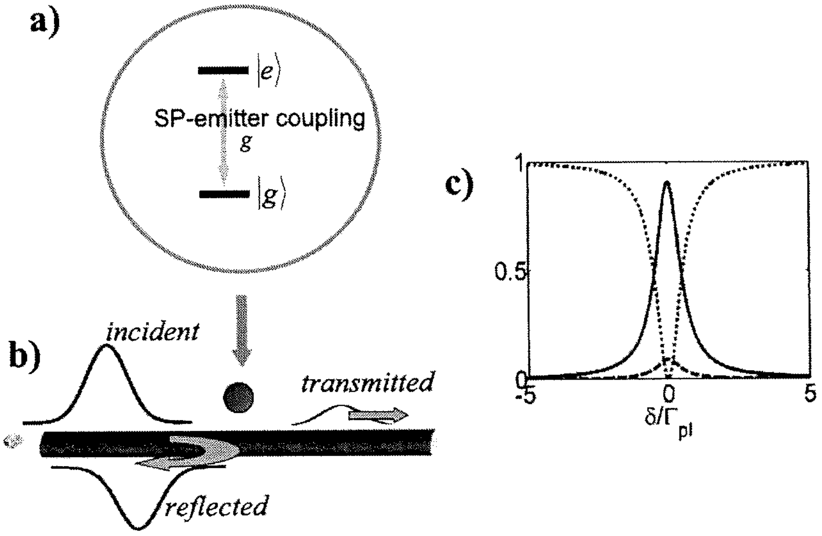

Figure 4.1: a) Two-level emitter interacting with the nanowire. States $|g\rangle, |e\rangle$ are coupled via the SP modes with a strength g. b) Schematic of a single incident photon scattered off of a near-resonant emitter. The interaction leads to reflected and transmitted fields whose amplitudes can be calculated exactly. c) Probabilities of reflection (solid line), transmission (dotted line), and loss (dashed line) for a single photon incident upon a single emitter, as a function of detuning. The Purcell factor for this system is taken to be $P = 20$.

SPs as completely separate fields. We define operators that annihilate a left (right)-propagating photon at position z, $\hat{E}_{L(R)}(z) = (1/\sqrt{2\pi}) \int dk\, e^{ikz} \hat{a}_{L(R),k}$, where operators acting on the left and right branches are assumed to have vanishing commutation relations with the other branch. The commutation relations for a single branch are given by the usual field relations, $\left[\hat{E}_j(z), \hat{E}_j^{\dagger}(z')\right] = \delta(z - z')$, where $j = L, R$. In principle this approximation allows for the existence of negative-energy modes (as the index k runs over the range $\pm\infty$), but this is unimportant if we are only considering near-resonant dynamics. Under this approximation, the relevant terms in Eq. (4.1) are transformed via

$$\int dk\, \hbar v|k|\hat{a}_k^\dagger \hat{a}_k \quad \longrightarrow \quad \int dk\, \hbar v k \left(\hat{a}_{R,k}^\dagger \hat{a}_{R,k} + \hat{a}_{L,-k}^\dagger \hat{a}_{L,-k}\right), \tag{4.2}$$

$$\sigma_{eg}\hat{a}_k e^{ikz_a} \quad \longrightarrow \quad \sigma_{eg}\left(\hat{a}_{R,k} + \hat{a}_{L,k}\right) e^{ikz_a}. \tag{4.3}$$

4.3 Single emitter as a saturable mirror

The propagation of SPs can be dramatically altered by interaction with the single two-level emitter. In particular, for low incident powers, the interaction occurs with near-unit probability, and each photon can be reflected with very high efficiency. However, for higher powers the emitter response rapidly saturates, as it is not able to scatter more than one photon at a time.

The low-power behavior can be understood by first considering the scattering of a single photon, as illustrated schematically in Fig. 4.1b. An exact solution to the scattering from the right to left branches in the limit of infinite Purcell factor ($P \to \infty$) was derived in Ref. [108] by solving for the scattering eigenstates of the system, and the approach can be generalized to finite P. In particular, to solve for the reflection and transmission coefficients of single-photon scattering, we write the general wave function for a system containing one (either photonic or atomic) excitation in the following way,

$$|\psi_k\rangle = \int dz\, \left(\phi_L(z)\hat{E}_L^\dagger(z) + \phi_R(z)\hat{E}_R^\dagger(z)\right)|g, vac\rangle + c_e|e, vac\rangle. \tag{4.4}$$

The field amplitudes are chosen to correspond to photons of well-defined momenta in the limits $z \to \pm\infty$, *i.e.*,

$$\phi_R(z) \quad = \quad e^{ikz}\left(\Theta(-z+z_a) + t_k\Theta(z-z_a)\right), \tag{4.5}$$

$$\phi_L(z) \;=\; e^{-ikz} r_k \Theta(-z+z_a) \tag{4.6}$$

for a photon propagating initially to the right. Here t_k (r_k) is the transmission (reflection) coefficient, and $\Theta(z)$ is the step function. Following Ref. [108], we consider the time-independent Schrodinger equation $H|\psi_k\rangle = E_k|\psi_k\rangle$, and project this equation into the various basis states to get a set of equations that can be readily solved for E_k, r_k, t_k and c_e.

The resulting reflection coefficient for an incoming photon of wavevector k is found to be

$$r(\delta_k) = -\frac{1}{1+\Gamma'/\Gamma_{\mathrm{pl}} - 2i\delta_k/\Gamma_{\mathrm{pl}}}, \tag{4.7}$$

where $\delta_k \equiv vk - \omega_{eg}$ is the photon detuning, while the transmission coefficient is given by $t(\delta_k) = 1 + r(\delta_k)$. Here $\Gamma_{\mathrm{pl}} = 4\pi g^2/v$ is the decay rate into the SPs, as obtained by application of Fermi's Golden Rule to the Hamiltonian in Eq. (4.1). On resonance, $r \approx -(1-1/P)$, and thus for large Purcell factors the emitter in state $|g\rangle$ acts as a nearly perfect mirror, which simultaneously imparts a π-phase shift upon reflection. The bandwidth $\Delta\omega$ of this process is determined by the total spontaneous emission rate, $\Gamma = \Gamma_{\mathrm{pl}} + \Gamma'$, which can be quite large. Furthermore, the probability κ of losing the photon to the environment is strongly suppressed, $\kappa \equiv 1 - \mathcal{R} - \mathcal{T} = 2\mathcal{R}/P$, where $\mathcal{R}\,(\mathcal{T}) \equiv |r|^2\,(|t|^2)$ is the reflectance (transmittance). These results are illustrated in Fig. 4.1c, where $\mathcal{R}, \mathcal{T}, \kappa$ are plotted as a function of detuning δ_k, taking a conservative value of $P = 20$.

The nonlinear response of the system can be seen by considering the interaction of a single emitter not just with a single photon, but with multi-photon input states. To be specific, we consider the case when the incident field consists of a coherent state, the quantum mechanical state that most closely corresponds to a classical field [107] (note also similar work in Refs. [109, 110] where scattering of two-photon states is considered). We assume that the incident field propagates to the right, with $\langle \hat{E}_R \rangle = \mathcal{E}_c(z,t)$, and that the emitter is initially in the ground state. As shown in Appendix E, by transformation the initial coherent state can be formally mapped to an external Rabi frequency (given by $\Omega_c = \sqrt{2\pi} g \mathcal{E}_c$) in the Hamiltonian, which allows all quantities of interest (*e.g.*, field correlation functions) to be calculated exactly. For a narrow bandwidth ($\delta\omega \ll \Gamma$), resonant ($\delta_k = 0$) input field, the steady-state transmittance and reflectance are found to be (see Appendix E)

$$\begin{aligned} \mathcal{T} &= \frac{1+8(1+P)^2(\Omega_c/\Gamma)^2}{(1+P)^2(1+8(\Omega_c/\Gamma)^2)}, \\ \mathcal{R} &= \left(1+\frac{1}{P}\right)^{-2} \frac{1}{1+8(\Omega_c/\Gamma)^2}. \end{aligned} \tag{4.8}$$

At low powers ($\Omega_c/\Gamma \ll 1$), the emitter has scattering properties identical to the single-photon case, $\mathcal{R} \approx (1+1/P)^{-2}, \mathcal{T} \approx (1+P)^{-2}$, and for large Purcell factors the single emitter again acts as a perfect mirror. At high incident powers ($\Omega_c/\Gamma \gg 1$), however, the emitter saturates and most of the incoming photons are transmitted past with no effect, $\mathcal{T} \to 1, \mathcal{R} \sim \mathcal{O}((\Gamma/\Omega_c)^2)$. The significance of these results can be understood by noting that saturation is achieved at a Rabi frequency $\Omega_c \sim \Gamma$ that, in the limit of large P, corresponds to a switching energy of a single quantum ($\sim \hbar\nu$) within a pulse of duration $\sim 1/\Gamma$.

4.4 Photon correlations

The strongly nonlinear atomic response at the single-photon level leads to dramatic modification of photon statistics that cannot be captured by only considering average intensities, but which appear in higher-order correlations of the transmitted and reflected fields. Specifically, we focus on the normalized second-order correlation functions, $g^{(2)}_{R,L}(t)$, which for a stationary process are defined as

$$g^{(2)}_{\beta=R,L}(z,t) \equiv \langle \hat{E}^{\dagger}_{\beta}(z,\tau)\hat{E}^{\dagger}_{\beta}(z,\tau+t)\hat{E}_{\beta}(z,\tau+t)\hat{E}_{\beta}(z,\tau)\rangle / \langle \hat{E}^{\dagger}_{\beta}(z,\tau)\hat{E}_{\beta}(z,\tau)\rangle^{2}, \quad (4.9)$$

where t denotes the difference between the two observation times τ and $\tau+t$.

The statistics of the reflected field are identical to the well-known result for resonance fluorescence [107] in three dimensions (see Fig. 4.2) because it is a purely scattered field. It follows that the field is strongly anti-bunched, $g^{(2)}(0) = 0$, since the emitter can only absorb and re-emit one photon at a time. The transmitted field, however, has unique properties because it is a sum of the incident and scattered fields. For near-resonant excitation and low powers (see Appendix E),

$$g^{(2)}(t) = e^{-\Gamma t}\left(P^2 - e^{\Gamma t/2}\right)^2 + \mathcal{O}(\Omega_c^2/\Gamma^2), \quad (4.10)$$

while for high powers $g^{(2)}(t)$ approaches unity for all times due to saturation of the atomic response. The low-power behavior reflects that of an efficient single-photon switch. Specifically, for $P \gg 1$, individual photons have a large reflection probability, but when two photons are incident simultaneously the transition saturates, so that pairs have a much larger probability of transmission (for $P \ll 1$ the emitter has little influence and the transmitted statistics are almost unchanged). This phenomenon yields a strong bunching effect at $t = 0$ that behaves like $g^{(2)}(0) \approx P^4$. Furthermore,

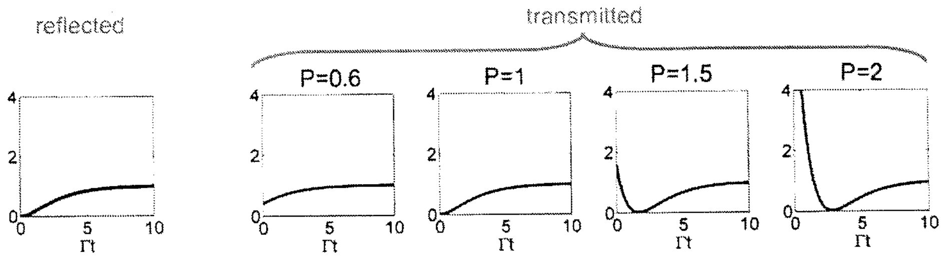

Figure 4.2: Second-order correlation function $g^{(2)}(t)$ for the reflected and transmitted fields at low incident power ($\Omega_c/\Gamma = 0.01$). $g^{(2)}(t)$ for the reflected field is independent of P at low powers. For the transmitted field, going from left to right, the Purcell factors are $P = 0.6, 1, 1.5, 2$, respectively. A rise in $g^{(2)}(0)$ for large Purcell factors indicates a strong initial bunching of photons at the transmitted end. This initial bunching is accompanied by an anti-bunching effect, $g^{(2)}(t_0)\approx 0$, at some later time $t_0 = (4 \log P)/\Gamma$ for $P \geq 1$. For high incident powers (not shown), $g^{(2)}(t)$ approaches unity for all times due to a saturation of the atomic response.

at time $t_0 = (4 \log P)/\Gamma$ there is a subsequent anti-bunching and perfect vanishing of $g^{(2)}(t)$ for weak input fields. A more detailed analysis of these features is presented in Appendix E (also see Ref. [111] for a similar phenomenon in cavity QED).

4.5 Ideal single-photon transistor

A greater degree of coherent control over the field interaction can be gained by considering a multi-level emitter, such as the three-level configuration shown in Fig. 4.3. Here, a metastable state $|s\rangle$ is decoupled from the SPs due to, *e.g.*, a different orientation of its associated dipole moment, but is resonantly coupled to $|e\rangle$ via some classical, optical control field with Rabi frequency $\Omega(t)$. States $|g\rangle, |e\rangle$ remain coupled via the SP modes as discussed earlier. Using this system, we now describe a process in which a single "gate" photon can completely control the propagation of subsequent "signal" pulses consisting of either individual or multiple photons, whose timing can

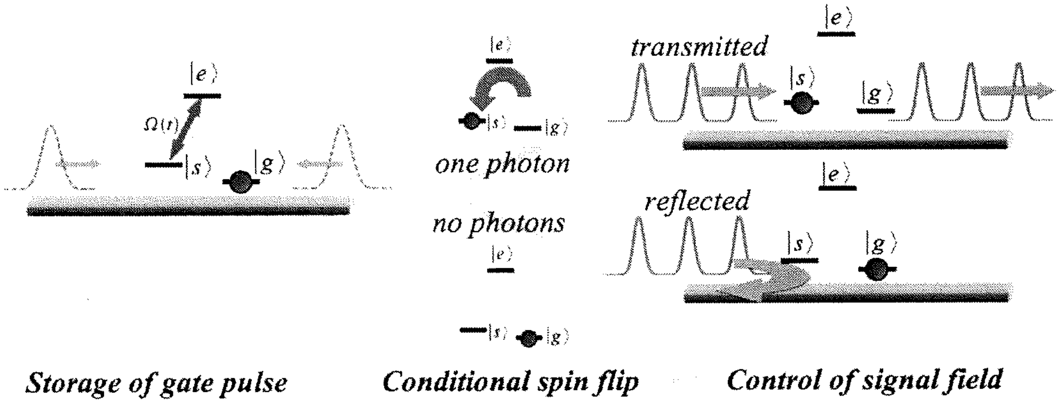

Storage of gate pulse **Conditional spin flip** **Control of signal field**

Figure 4.3: Schematic of transistor operation involving a three-level emitter. In the storage step, a gate pulse consisting of zero or one photon is split equally in counter-propagating directions and coherently stored using an impedance-matched control field $\Omega(t)$. The storage results in a spin flip conditioned on the photon number. A subsequent incident signal field is either transmitted or reflected depending on the photon number of the gate pulse, due to the sensitivity of the propagation to the internal state of the emitter.

be arbitrary. In analogy to the electronic counterpart, this corresponds to an ideal single-photon transistor.

We first describe how one can achieve coherent storage of a single photon, which is an important ingredient as it provides an atomic memory of the gate field and thus allows the gate to interact with the subsequent signal. We initialize the emitter in $|g\rangle$ and apply the control field $\Omega(t)$ simultaneous with the arrival of a single photon in the SP modes. The control field, if properly chosen (or "impedance-matched") [10], will result in capture of the incoming single photon while inducing a spin flip from $|g\rangle$ to $|s\rangle$. Generally, by time reversal symmetry [112], the optimal storage strategy is the time-reversed process of single-photon generation, where the emitter is driven from $|s\rangle$ to $|g\rangle$ by the external field while emitting a single photon whose wavepacket depends on $\Omega(t)$. By this argument, it is evident that optimal storage is obtained by splitting the incoming pulse and having it incident from both sides of the emitter simultaneously (see Fig. 4.3), and that there is a one-to-one correspondence between the incoming pulse shape and the optimal field $\Omega(t)$. The storage efficiency is identical to that of single photon generation and is thus given by $\sim 1 - 1/P$ for large P (see Chapter 2, also see Appendix E.3 for an exact solution of the system dynamics). A detailed analysis reveals that this optimum is achievable for any input pulse of duration $T \gg 1/\Gamma$ and for a certain class of pulses of duration $T \sim 1/\Gamma$ [112]. Finally, if no photon impinges upon the emitter, the pulse $\Omega(t)$ has no effect and the emitter remains in $|g\rangle$ for the entire process. The result is more generally described as a mapping between single SP states and metastable atomic states, $(\alpha|0\rangle + \beta|1\rangle)|g\rangle \rightarrow |0\rangle(\alpha|g\rangle + \beta|s\rangle)$.

We next consider the reflection properties of the emitter when the control field $\Omega(t)$ is turned off. If the emitter is in $|g\rangle$, the reflectance and transmittance derived above for the two-level emitter remain valid. On the other hand, if the emitter is in $|s\rangle$, any incident fields will simply be transmitted with no effect since $|s\rangle$ is decoupled from the SPs. Therefore, with $\Omega(t)$ turned off, the three-level system effectively behaves as a conditional mirror whose properties depend sensitively on its internal state.

The techniques of state-dependent conditional reflection and single-photon storage can be combined to create a single-photon transistor, whose operation is illustrated in Fig. 4.3. The key principle is to utilize the presence or absence of a photon in an initial "gate" pulse to conditionally flip the internal state of the emitter during the storage process, and to then use this conditional flip to control the flow of subsequent "signal" photons arriving at the emitter. Specifically, we first initialize the emitter in $|g\rangle$ and apply the storage protocol for the gate pulse, which consists of either zero or one photon. The presence (absence) of a photon causes the emitter to flip to (remain in) state $|s\rangle$ ($|g\rangle$). Now, the interaction of each signal pulse arriving at the emitter depends on the internal state following storage. The storage and conditional spin flip causes the emitter to be either highly reflecting or completely transparent depending on the gate, and the system therefore acts as an efficient switch or transistor for the subsequent signal field.

The ideal operation of the transistor is limited only by the characteristic time over which an undesired spin flip can occur. In particular, if the emitter remains in $|g\rangle$ after storage of the gate pulse, the emitter can eventually be optically pumped to $|s\rangle$ upon the arrival of a sufficiently large number of photons in the signal field. For strong coupling, the number of incident photons n that can be scattered before pumping occurs is given by the branching ratio of decay rates from $|e\rangle$ to these states, $n{\sim}\Gamma_{e\to g}/\Gamma_{e\to s}$, which can be large due to the large decay rate $\Gamma_{e\to g} \geq \Gamma_{\text{pl}}$. Thus $n{\gtrsim}P$ and the emitter can reflect $\mathcal{O}(P)$ photons before an undesired spin flip occurs. This number corresponds to the effective "gain" of the single-photon transistor.

Finally, we note that there exist other possible realizations of a single-photon transistor as well. The "impedance-matching" condition and need to split a pulse for optimal storage, for example, can be relaxed using a small ensemble of emitters and photon storage techniques based on electromagnetically induced transparency (EIT) [113]. Here, storage also results in a spin flip within the ensemble that sensitively alters the propagation of subsequent photons.

4.6 Integrated systems

Inevitably, SPs experience losses as they propagate along the nanowire, which could potentially limit their feasibility as long-distance carriers of information and in large-scale devices. For the nanowire, one must consider the trade-off between the larger Purcell factors obtainable with smaller diameters and a commensurate increase in dissipation due to the tighter field confinement. However, these limitations are not fundamental, if one can integrate SP devices with low-loss dielectric waveguides, *e.g.*, using the techniques of Sec. 2.5. Here, the SPs can be used to achieve strong nonlinear interactions over very short distances, but are rapidly in- and out-coupled to conventional waveguides for long-distance transport. Such a conductor/dielectric interface would provide convenient integration with conventional optical elements, enable many nonlinear operations without loss, and make large-scale, integrated photonic devices feasible.

Another key feature of nano-scale SPs is that the strong interaction is very robust. Because the large coupling occurs over a very large bandwidth and requires no special tuning of either the emitter or nanowire, SPs are promising candidates for use with solid-state emitters such as quantum dot nanocrystals [114] or color centers [115], where the spectral properties can vary over individual emitters. Color centers in diamond [115], for instance, are especially promising because they offer sharp optical lines and three-level internal configurations. At the same time, guided SPs might be used for trapping isolated neutral atoms in the vicinity of suspended wires, thereby creating an effective interface for isolated atomic systems.

4.7 Outlook

A single-photon transistor can be used for many important applications such as efficient single-photon detection, where the large gain in the signal field provides for efficient detection of the gate pulse. This system also finds applications in quantum information science. One can prepare Schrodinger cat states of photons, for example, if the gate pulse contains a superposition of zero and one photon, since this initial pulse becomes entangled with the propagation direction of potentially many subsequent signal photons. The controlled-phase gate for photons proposed in Ref. [11] for cavity QED is also directly extendable to our system. In particular, this scheme relies on conditional phase shifts acquired as photons are reflected from a resonant cavity containing a single atom, which are analogous to the reflection dynamics derived for single SPs here. In addition, by using SPs it is possible to achieve very large optical depths with just a few emitters, which makes this system effective for realizing EIT-based nonlinear schemes [100, 101, 102, 103]. Finally, the present system is an intriguing candidate to observe phenomena associated with strongly interacting, one-dimensional many-body systems. For example, non-perturbative effects such as dynamical cross-overs [116] involving photons can be explored. Higher-order correlations created in the transmitted field can become a useful tool to study and probe the non-equilibrium quantum dynamics of these strongly interacting photonic systems.

Chapter 5

Crystallization of strongly interacting photons in an optical fiber

5.1 Introduction

The idea of using nonlinear effects to create optical systems with unusual properties has been pursued for several decades, and fascinating advances have been made in recent years [1, 2, 3, 97, 103]. The focus of such work has mostly been on systems containing a small number of photons, such as the single-photon transistor proposed in Chapter 4. At the same time, the effects of strong correlations manifest themselves most dramatically in many-body systems, often resulting in new states of matter with properties that are very different from those of the underlying particles. One famous example is the Tonks-Girardeau (TG) regime of interacting bosons in one dimension, in which strong interactions between particles lead to an effective "fermionization" of bosons [117, 118]. This unusual regime has been explored in several condensed matter systems and in recent experiments with ultracold atoms in one dimensional traps [119, 120]. In this article we investigate the feasibility of creating and detecting a TG gas of photons. This system would correspond to nonlinear quantum optics in its extreme, in which individual photons behave as impenetrable particles. In this limit, an optical pulse separates into non-overlapping wavepackets of individual photons, and a "crystal of photons" can be created.

Several papers have recently considered the possibility of phase transitions involving photons, focusing on large systems of coupled optical cavities [12, 13, 14, 15, 16, 121]. The present study differs from this previous work in several ways. First, while dramatic progress has been achieved in controlling individual atoms and photons in single cavities [1, 2, 3], the complex architecture of coupled cavities proposed in Refs. [12, 13, 14, 15, 16, 121] represents a considerable experimental challenge. In contrast, the approach described here to realize a TG gas of photons involves currently available experimental techniques [44, 122]. Second, we show that a strongly correlated photonic state can be created dynamically, without the need to assume that a thermodynamic equilibrium for photons must be achieved as in previous work. Finally, we provide a method for the strongly interacting photon gas to be read out of our system without disturbing any of the quantum correlations that were previously formed, and show that these correlations can be detected using standard quantum optical measurements. This potentially enables many new applications and allows one to study even more exotic phenomena involving interacting particles using readily controlled photons with tunable interactions.

5.2 Strongly interacting photons in one dimension: the system

Recently, much effort has been directed toward realizing single-mode optical waveguides where the guided photons can be tightly confined in the transverse directions to an area A_{eff} near or below the diffraction limit. Such confinement is desirable in part because it allows for a large interaction strength between single photons and nearby coupled atoms. Specific systems that have recently been explored in this context include tapered optical fibers [44], hollow-core photonic crystal fibers [43, 122], and surface plasmons on conducting nanowires [79, 92].

The propagation and interaction of photons in such a medium can be controlled by interfacing them with atoms using quantum optical techniques such as Electromagnetically Induced Transparency (EIT) [103]. In particular, our scheme relies on resonantly enhanced optical nonlinearities with low losses [100] using EIT and the creation and trapping of stationary pulses of light in the medium using spatially modulated control fields [123] (see Fig. 5.1a). As will be shown, the dynamical evolution of the photonic system is governed by an equation that has the form of the Nonlinear Schrödinger Equation (NLSE), where the signs and strengths of the effective mass and interaction can be controlled using external fields. Under conditions where the nonlinear interaction is large and effectively *repulsive*, the TG regime of photons can be achieved.

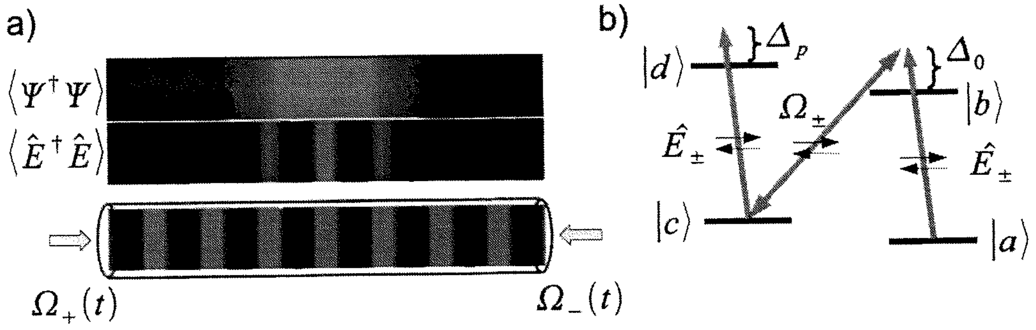

Figure 5.1: a) Schematic of fields inside the waveguide, whose axis of propagation corresponds to the horizontal axis. The control beams $\Omega_\pm(t)$ (shown in blue) create a standing wave inside the waveguide, which forms a Bragg grating that traps a quantum optical field inside the medium (intensity $\langle\hat{E}^\dagger\hat{E}\rangle$ shown in red). The optical field couples to spin-wave excitations in the medium, resulting in collective polariton excitations whose density $\langle\Psi^\dagger\Psi\rangle$ is also plotted. b) Schematic of the four-level atomic configuration and coupling between levels and fields used in our system.

Specifically, we consider the propagation of counter-propagating quantum fields, characterized by operators $\hat{E}_\pm$, inside a single-transverse mode optical waveguide and interacting with cold atoms in the four-level configuration shown in Fig. 5.1b. The fields $\hat{E}_\pm$ couple the ground state $|a\rangle$ (in which the system is initialized) to excited state $|b\rangle$ with a strength given by g, while metastable state $|c\rangle$ and $|b\rangle$ are coupled by classical, counter-propagating control fields $\Omega_\pm(t)$ (we assume these fields are also guided). Here, the lambda configuration consisting of states $|a, b, c\rangle$ comprise the typical EIT setup. In particular, in the case where the quantum and classical fields propagate only in one direction, the quantum field can be dynamically and reversibly mapped into a stationary spin-wave excitation by turning the control field $\Omega(t)$ to zero adiabatically. On the other hand, as shown in Ref. [123], by creating a standing wave formation with the control fields ($\Omega_+(t) = \Omega_-(t)$), the quantum fields can be effectively stopped while simultaneously maintaining a non-zero photonic component of the excitation (see Fig. 5.1a). Intuitively, the standing wave pattern forms a set of reflection gratings that traps the photonic excitations through multiple scattering. The nonlinear response is introduced via an additional state $|d\rangle$ that is coupled to $|c\rangle$ by the quantum fields (for simplicity we assume that this coupling strength is also given by g). When these fields are far off resonance, this coupling results in an ac Stark shift of state $|c\rangle$ whose magnitude is proportional to the intensity of the quantum field [100]. This gives rise to an intensity-dependent refractive index, or nonlinear susceptibility, that in turn influences the evolution of the quantum fields. While similar schemes for realizing nonlinear optics in atomic media have been previously explored [124], their implementation in waveguides with tight confinement is unique because they can constitute a true one-dimensional system, and because the strong transverse localization enables large nonlinear interactions.

5.3 The Lieb-Liniger model with stationary pulses of light

Considerable theoretical literature exists that discusses the connection between Maxwell's equations for a nonlinear medium in one dimension and the Lieb-Liniger Model (LLM) describing interacting massive particles [125, 126]. However, most of this work has focused on the regime of attractive interactions. Interest in this regime stems from the observation that interaction with basic two-level atomic systems leads to photon bunching, since it is easier for many photons to pass through an atom without being absorbed [96]. The main feature of the attractive regime is the formation of solitons [125]. This regime of the LLM has few quantum mechanical features and can be described by classical equations of motion. Indeed, typical optical solitons contain on the order of a million photons, and therefore a quasi-classical description is very appropriate [127]. On the other hand, the *repulsive* case is intrinsically "quantum mechanical", as one needs to keep track of correlations at the level of individual particles. Solutions based on perturbation theory or classical equations of motion break down and one needs to use non-perturbative approaches such as the Bethe ansatz solution [128, 129, 130, 131] or the Luttinger liquid formalism [132]. Thus, formation of a TG gas of photons is fundamentally a collective *many-body* effect.

We now derive an evolution equation for the fields of the system illustrated in Figure 5.1. Following the methods of Refs. [113, 123, 124], we define dark-state polariton operators $\Psi_\pm$ describing the coupled photonic and spin-wave excitations, which in the slow-light limit are given approximately by $\Psi_\pm = g\sqrt{2\pi n_z}\hat{E}_\pm/\Omega_\pm$, where n_z is the density of atoms coupled to the waveguide (the density is assumed to be uniform). We specialize to the case when $\Omega_\pm(t) = \Omega(t)$. We further assume that the quantum and control fields vary slowly in time, such that the fast-varying atomic operators can be adiabatically eliminated, while the remaining slowly-varying operators are solved in the adiabatic limit. Subsequently inserting these solutions into the Maxwell-Bloch equations describing evolution of the quantum fields yields an effective NLSE for the polaritons (see Appendix F.1),

$$i\partial_t\Psi(z,t) = -\frac{1}{2m_{\text{eff}}}\partial_z^2\Psi(z,t) + 2\tilde{g}\Psi^\dagger(z,t)\Psi^2(z,t), \tag{5.1}$$

where

$$\Psi = \frac{(\Psi_+ + \Psi_-)}{2}, \qquad m_{\text{eff}} = -\frac{\Gamma_{1D} n_z}{4\Delta_0 v_g}, \qquad 2\tilde{g} = \frac{\Gamma_{1D} v_g}{\Delta_p}. \tag{5.2}$$

Here $\Gamma_{1D} = 4\pi g^2/v$ is the spontaneous emission rate of a single atom into the waveguide modes, where v is the velocity of these modes at the atomic resonance frequency in an empty waveguide, while $v_g \approx v\Omega^2/(\pi g^2 n_z)$ is the group velocity of untrapped pulses under EIT conditions. Δ_0 and Δ_p are the one-photon detunings of the fields $\hat{E}_\pm$ from the transitions $|a\rangle$-$|b\rangle$ and $|c\rangle$-$|d\rangle$, respectively (see Fig. 5.1b), and $g \sim 1/\sqrt{A_{\text{eff}}}$ is the single-photon, single-dipole interaction matrix element. In principle the full dynamics of the field will also include losses and higher-order terms, and the conditions under which such terms can be neglected are described in Appendix F. One should also note that even with the standing wave control field, the evolution of Eq. (5.1) remains smooth and in particular does not contain features determined by the standing wave period.

Eq. (5.1) determines the evolution of a quantum field $\Psi(z,t)$ as derived from the Hamiltonian of the Lieb-Liniger model,

$$H = \hbar \int dz [\frac{1}{2m_{\text{eff}}} \partial_z \Psi^\dagger(z) \partial_z \Psi(z) + \tilde{g} \Psi^\dagger(z) \Psi^\dagger(z) \Psi(z) \Psi(z)]. \tag{5.3}$$

The first term on the right describes the kinetic energy in one dimension of bosons with mass m_{eff}, while the second term describes a contact interaction potential. The quantum field $\Psi(z,t)$ satisfies the usual equal-time bosonic commutation relations, $[\Psi(z,t), \Psi^\dagger(z',t)] = \delta(z-z')$. The behavior and properties of this system can be effectively characterized by a single dimensionless parameter

$$\gamma = \frac{m_{\text{eff}} \tilde{g}}{n_{ph}} = -\frac{\Gamma_{1D}^2}{8\Delta_0 \Delta_p} \frac{n_z}{n_{ph}}, \tag{5.4}$$

which physically corresponds to the ratio of the interaction and kinetic energies. Here n_{ph} is the density of photons at the center of the pulse. When $\gamma < 0$, the interaction with the atoms induces an effective attraction between photons. As discussed above, this is responsible, *e.g.*, for the formation of bound states (solitons) when a large number of photons are present. On the other hand, for $\gamma > 0$ the regime of effective *repulsion* between photons is realized. From Eq. (5.2), one finds that the regime of repulsion can be achieved if exactly *one* of the detuning parameters Δ_0 or Δ_p is negative. It is also clear that only the attractive regime can be reached using a two-level system, since $\Delta_0 \equiv \Delta_p$ in this situation. The special limit $\gamma \to \infty$ is called the Tonks-Girardeau (TG) regime [117, 118]. In this regime, it can be said that the strongly interacting Bose gas "fermionizes", in that all of its properties can be derived from those of a noninteracting Fermi gas (and likewise, the bosonic system can be described by effective "Fermi" momenta and energies) [118]. Finally, we note that $\gamma \propto \Gamma_{1D}^2 \propto A_{\text{eff}}^{-1}$, which underscores the importance of tight mode confinement in reaching the strongly interacting regime.

One useful feature of this realization of the NLSE is that the parameters m_{eff} and $\tilde{g}$ can be dynamically tuned by varying different parameters of the system. Specifically, both are functions of detuning, and thus γ can be altered by changing either the control field frequencies or by externally manipulating the energies of the atomic levels. As described below, this tunability facilitates the creation of novel photonic states.

5.4 Preparation and detection of strongly correlated photon gas

The process by which novel photonic states can be prepared and detected consists of three basic steps – loading of the pulse, controlled evolution under the NLSE, and readout of the final photonic state – each of which we now describe. During the initial loading process, a resonant optical pulse, given by, *e.g.*, a coherent state, is incident from one direction. It is injected into the waveguide at the same time that the co-propagating control field (say $\Omega_+(t)$) is turned on. During the loading procedure the counter-propagating control field $\Omega_-(t)$ is off. This describes the usual situation in EIT, where the input field is mapped into a spatially compressed polariton pulse upon entering the medium, which propagates with a variable group velocity $v_g \sim v\Omega_+^2(t)/(g^2 n_z)$. Once the pulse completely enters the medium, $\Omega_+(t)$ is adiabatically turned to zero, reversibly converting the excitations into pure spin-wave form [113]. Under certain conditions this input pulse can be stored with minimal distortion relative to the initial field [113], such that all relevant properties (*e.g.*, field correlations) remain constant during the loading. Following the initial storage, both control fields are then adiabatically switched on, with $\Omega_\pm = \Omega(t)$, during which the pulse becomes trapped and evolves under Eq. (5.1). The parameters m_{eff} and $\tilde{g}$ can be changed in time during the evolution to reach the final state of interest. Here, we propose to create a TG gas of polaritons through adiabatic transformation by varying these parameters such that $\gamma(t)$ adiabatically increases from zero to a large value. During this process the initial coherent state (an eigenstate of the initial noninteracting Hamiltonian) remains an eigenstate of the instantaneous Hamiltonian so that it finally reaches the TG regime. It should be noted that this method differs from the proposals of Refs. [12, 13, 14, 15, 16, 121], where only thermodynamic equilibrium of photons was considered. Once this state has been achieved, the pulse is released by turning one of the control fields (say Ω_-) off, thereby allowing the pulse to propagate undistorted until it exits the waveguide [123]. During this readout, any spatial correlations that formed in the polaritons while evolving under the NLSE are directly mapped into temporal correlations (at a common point in space) of purely outgoing photons, which can be measured using standard quantum optical techniques. An appealing feature of this approach is that the pulse velocity as it exits the waveguide is determined by the control field. In particular, one is able to specify the timing and bandwidth of the outgoing pulse without affecting the underlying spatial correlations, which allows one to efficiently probe local properties of the system upon exit.

A characteristic signature of a strongly interacting gas is the appearance of Friedel oscillations [133] in the normalized second-order correlation function, $g^{(2)}(z,z') = \langle I(z)I(z')\rangle/(\langle I(z)\rangle\langle I(z')\rangle)$, where $I(z) = \Psi^{\dagger}(z)\Psi(z)$ is the stationary pulse intensity prior to release. In particular, if the photonic state remains close to the ground state of the LLM, $g^{(2)}(z,z')$ contains an oscillating part that behaves as $\sim \cos(2k_F(z-z'))$ (see Appendix F). Here $k_F = \pi n_{ph}$ is the "Fermi momentum" in the TG limit. In the TG limit, the ground-state correlation function takes on a simple form given by Lenard's formula [134],

$$g^{(2)}_{TG}(z,z') = 1 - \left(\frac{\sin k_F(z-z')}{k_F(z-z')}\right)^2. \tag{5.5}$$

The $2k_F$-oscillations are a direct manifestation of "fermionization" of bosons. We note that Friedel oscillations are more than simple anti-bunching in that they indicate real crystal correlations. In particular, one cannot predict the position of an individual photon, but knowing the position of one photon, other photons are likely to follow at well-defined distances determined by the average photon density. These correlations are predicted to decay relatively slowly in space. It should be emphasized that the oscillation period depends on the density of photons n_{ph} inside the medium and not on the standing wave period ($\sim\lambda/2$) formed by the control fields. These two length scales can be dramatically different and thus the observation of Friedel oscillations indicates a true "self-organization" process instead of an inherent periodicity of the system.

The usual definition of the TG regime of the LLM is given with respect to the equilibrium state. However, in our system the evolution of the initial coherent state under the NLSE inherently involves non-equilibrium quantum dynamics, and hence one must specify the conditions under which one can obtain a strongly interacting state of photons that remains close to the ground state of the LLM and exhibits its characteristic features, such as Friedel oscillations. To be concrete, we consider the evolution of a pulse under Eq. (5.1), where the atomic parameters are varied such that the effective mass m_{eff} is constant in time, while the interaction strength $\tilde{g}(t)$ increases exponentially. From Eq. (5.4), the resulting time-dependent interaction parameter can be written in the form $\gamma = \gamma_0 e^{\beta\omega_F t}$, where β is a dimensionless parameter characterizing the rate of increase, and $\omega_F \sim n_{ph}^2/m_{\text{eff}}$ corresponds to the "Fermi energy" at the center of the pulse before expansion. We assume that $\gamma_0 \ll 1$, so that the system initially consists of non-interacting photons, and interactions are gradually switched on to reach the regime of $\gamma \gg 1$. Here we will not discuss the effect of a time-dependent mass, although it can be included using a similar analysis.

The non-equilibrium dynamics of the LLM has previously been studied in the context of ultracold atoms and has focused either on changing the interaction strength in a system with uniform, constant density [135, 136], or on the expansion of particles in a system with constant interaction [137, 138]. In our system both processes take place, but in the experimentally relevant regime of a large photon number there is a separation of time scales that simplifies the analysis. We consider an initial pulse containing $N_{ph} \sim n_{ph} z_0$ photons with spatial extent z_0 at $t = 0$. Our discussion applies for a general pulse shape and thus we need not specify it.

There are three distinct regimes in the time evolution of the pulse: i) Interactions are weak and the photons expand freely due to dispersion; ii) Interactions begin to dominate over the kinetic energy. However, the system is still in the weakly interacting regime with $\gamma < 1$, in which case the expansion is hydrodynamic [139, 140]; iii) The system reaches the strongly interacting regime with $\gamma > 1$, and the expansion resembles that of fermionized bosons [137, 138]. A simple analysis (see Appendix F) shows that by the time the system reaches regime iii), the relative change in the photon density at the center of the pulse is only of the order of $\frac{1}{\beta^2 N_{ph}^2}$. Hence for $\beta N_{ph} \gg 1$ one can assume that the turning on of interactions takes place at a constant density and any subsequent expansion takes place in the TG regime.

We now consider the effect of non-adiabaticity on correlation functions such as $g^{(2)}(z, z')$. By analogy with ultracold atoms, we introduce a chemical potential, which in regimes i) and ii) is given by $\mu(t) \approx \tilde{g}(t) n_{ph}$. We can approximately separate the turning on of interactions into two stages, which both take place during the regimes i) or ii). In the first stage, $\dot{\mu} > \mu^2$ and the adiabatic transformation is inefficient. In the second stage, $\dot{\mu} < \mu^2$ and the evolution is essentially adiabatic. At the time t_{adiab} separating the two regimes, the interaction parameter is given by $\gamma(t_{adiab}) \sim \beta$. The first stage can be thought of as an instantaneous projection of the wavefunction, which gives rise to a finite density of excitations characterized by an effective healing length $\xi_{neq} \sim (\mu(t) m_{\text{eff}})^{-1/2}$ at time t_{adiab}. During the second stage, the number of excitations does not change. Hence, we find that the finite rate of change in the interaction strength leads to a finite correlation length in our system, $\xi_{neq} \sim \beta^{-1/2} n_{ph}^{-1}$. For length scales shorter than ξ_{neq}, all correlation functions are essentially the same as in the ground state, whereas for length scales longer than ξ_{neq}, correlation functions rapidly decay. To observe Friedel oscillations over length scales on the order of the inter-photon distance, for example, requires that $\beta \lesssim 1$. The argument presented above can be turned into a quantitative calculation for the correlation functions following a time-dependent change in the interaction strength [136]. This analysis uses bosonization to treat the LLM and the conclusions agree with the qualitative picture presented here.

At the end of regime ii) we have a system of "fermionized" hard-core photons that should exhibit Friedel oscillations. In regime iii), the pulse of hard-core photons expands, but such spreading does not lead to the suppression of the Friedel oscillations [137, 138]. The problem of expansion of hard-core photons starting from a general pulse shape has to be analyzed numerically. However, an explicit analytic solution is available for the case of a parabolic pulse shape. Under realistic conditions this solution, which is discussed in detail in Appendix F, yields the correlation function shown in Fig. 5.2.

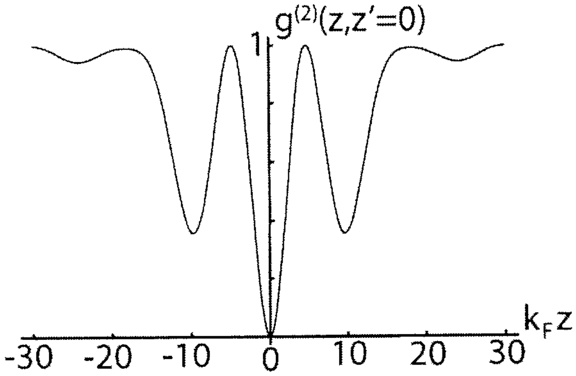

Figure 5.2: Density-density correlation function $g^{(2)}(z, z' = 0)$ for an expanding Tonks-Girardeau gas of photons with initial density profile $n_{ph}(z) = n_0(1 - z^2/z_0^2)^{1/2}$. This expansion is equivalent to the problem of a TG gas released from an initial parabolic confining potential. $z' = 0$ denotes the center of the pulse, and distances are indicated in units of k_F^{-1}. The density-density correlation function shown here is for a system of $N_{ph} = 10$ photons, $z_0 \approx 5k_F^{-1}$, and at a time $t = 10\omega_F^{-1}$ following the initial release.

During the evolution one must also consider the effects of incoherent photon scattering or absorption, which set a maximum evolution time t_{max} and interaction parameter γ_{max} that can be achieved before a substantial fraction of the initial pulse is lost. The number of photons scattered during the evolution has been fully calculated in the Supplementary Information (SI), and requiring that this quantity be small yields the following limit on the maximum achievable interaction parameter,

$$\gamma_{max} \sim \min\left(\gamma_0 \exp\left(\frac{\beta|\Delta_0|}{\Gamma}\right), \eta\beta\frac{\Gamma}{|\Delta_0|}\frac{OD}{N_{ph}}\right). \tag{5.6}$$

Here Γ is the total spontaneous emission rate of states $|b\rangle$ and $|d\rangle$ (assumed to be equal for simplicity), which includes the emission rate into the waveguide modes (Γ_{1D})

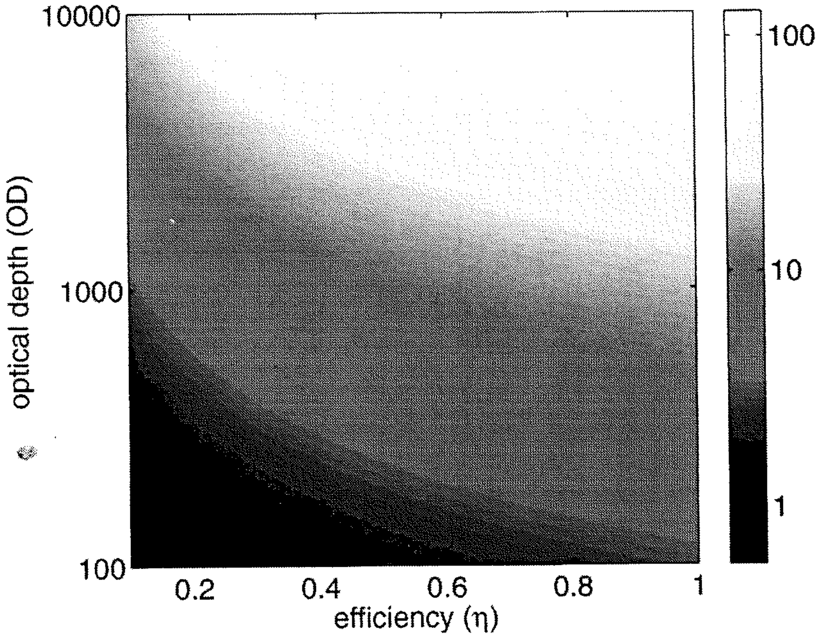

Figure 5.3: γ_{max} as functions of optical depth and single-atom cooperativity, optimized over the detuning Δ_0. γ_{max} is plotted for fixed values of $\beta = 1$, $\gamma_0 = 0.1$, and $N_{ph} = 10$. It is evident that the TG regime for photons can be approached by increasing either the cooperativity or optical depth.

as well as emission into non-guided modes (*e.g.*, into free space). We have also defined an efficiency $\eta = \Gamma_{1D}/\Gamma$ ($\eta \leq 1$) which describes the rate of emission into the waveguide compared to the total emission, and defined the optical depth of the medium, $OD = \eta z_0 n_z$. We note that γ_{max} can be improved by increasing the optical depth or efficiency and optimized by adjusting the detuning $|\Delta_0|$. The optimal values of γ_{max}, as functions of optical depth and efficiency, are plotted in Fig. 5.3, for parameters $\beta = 1, \gamma_0 = 0.1$, and $N_{ph} = 10$. One sees that with realistic values of $OD{\sim}2000$ and $\eta{\sim}0.2$, for example, an interaction parameter of $\gamma_{max}{\sim}10$ is possible. While photon losses limit the maximum evolution time, somewhat surprisingly, the nonlinear losses may also help in bringing the system closer to the ground state of the LLM. Specifically, these losses predominantly remove states in which two photons are close to each other, which correspond to high energy states of the LLM. Deep in the TG regime we can estimate the rate for the system to lose the high energy states, $t_{en}^{-1} \approx \frac{\Gamma}{\Delta_p} \tilde{g} n_{ph}$. On the other hand, the photon loss rate is $t_{los}^{-1} \approx \frac{\Gamma}{\Delta_p} \omega_F$. Thus $t_{en}/t_{los} \approx \gamma^{-1}$ and for large γ there is a sufficient time window for the high-energy states to decay before too many photons are lost.

5.5 Outlook

The above analysis indicates that strongly correlated states of photons can be controllably prepared and observed in one-dimensional waveguides. These techniques are made possible through strong coupling between the photons and nearby atoms and the use of quantum optical techniques such as EIT, which allow the system to be widely tunable. Such photonic states should find numerous applications in various areas of physics. Crystal correlations that arise in the fermionized state make it a promising candidate for applications in metrology and quantum information. In particular, TG states feature strongly suppressed photon number fluctuations within a given detection interval. Such states therefore could be used as an input for sub-shot noise interferometers [141, 142], or in extension to schemes for quantum computing [143] or quantum cryptography [144] that rely on single photons. Another exciting direction is quantum simulation of matter Hamiltonians using optical systems. In the discussion so far, we have considered photons with only one polarization. Including photons of different polarizations should be equivalent to adding a spin degree of freedom to effective matter Hamiltonians. This opens up exciting prospects for exploring spin charge separation (see, *e.g.*, Ref. [145]) and modelling exotic spin systems [121]. It is also interesting to note that the level structure of the atoms comprising the medium can vary considerably. This fact can be used for the study of strongly-correlated systems with non-Abelian symmetry, similar to the ones realized in multi-channel Kondo models and quantum chromodynamics. Possible phases and phase transitions in these models are difficult, if possible at all, to realize in matter systems. Furthermore, it would be interesting to consider a situation where interactions between the cold atoms create non-trivial correlations [146] and their effect on the resulting photonic states. Using light to simulate matter Hamiltonians will give a new meaning to the old idea of the particle-wave duality.

Chapter 6

Quantum electrodynamics of defects in an optical lattice

6.1 Introduction

Advances in atom cooling and trapping now make it possible to create "crystals" of atoms (known as optical lattices) with a period determined by the wavelength of the trapping light [147]. In an optical lattice, atoms can be trapped in any number of dimensions by the periodic variation in the ac Stark shift potential created by a set of interfering laser beams. A near-resonant light field propagating through such an optical lattice will generally experience multiple reflections off of the trapped atoms, which can dramatically modify the propagation properties [148]. Recently, techniques to prepare an optical lattice with a well-defined number of atoms per lattice site have been experimentally demonstrated [149].

At the same time, artificial photonic crystals have been actively studied in recent years because of their remarkable ability to control the propagation of electromagnetic radiation [19]. Photonic crystals are generally composed of periodic arrays of dielectric materials, and thus the eigenmodes of the electromagnetic field can be described by band structures and band gaps, much like electronic states in solid-state crystals. An atom whose resonance frequency sits inside a band gap is predicted to exhibit novel properties, due to the absence of resonant optical modes with which it can interact. Phenomena such as suppressed spontaneous emission in a band gap [22, 41] and photon-atom bound states near a band gap edge [150, 151] are predicted to occur. Thus far, photonic crystals in the optical range have generally been made using various microfabrication techniques, which are difficult to apply towards three-dimensional structures. This in part motivates a closer examination of three-dimensional optical lattices, which can be more easily realized, in terms of their potential to act as a photonic crystal. One important distinguishing feature of photonic crystals based on optical lattices is that they are most effective at frequencies near atomic resonance, where each atom experiences the largest optical response, but where incoherent photon scattering plays an important role as well and cannot be neglected.

In this chapter, we investigate the effect of an optical lattice on the radiative interactions of trapped atoms. Of particular interest are atoms that are trapped away from the potential minima of the background periodic lattice. These extra "defect" atoms, which exist in addition to the atoms forming the optical lattice, might be controllably introduced into the system using, *e.g.*, multiple laser beams to create a superlattice with a very large period [152]. Specifically, we investigate theoretically the radiative properties of a defect atom in the lattice taking fully into account the relevant absorptive and dispersive effects of the surrounding lattice atoms. We show that even in the presence of absorption, the spontaneous emission rate can be reduced significantly from the free-space value, and the formation of a localized field around the defect can be observed due to the effect of multiple reflections of its emitted field off the lattice atoms. We also study the interactions between multiple defects in the lattice. When the distance of separation between a pair of defects is on the order of the field localization length or less, they are able to exchange excitations coherently through dipole-dipole interactions before the excitation is lost to decay. Such long-range coherent interactions between defect atoms can be used, for example, to facilitate quantum logic gate operations in optical lattice quantum computers [153, 154]. We derive an effective interaction Hamiltonian between defects and study the fidelity of an exchange quantum gate.

6.2 Band structure of an optical lattice

The physical system of interest consists of an optical lattice of atoms in a simple cubic configuration, with one atom per lattice site. We further assume for simplicity that each lattice atom is trapped in the Lamb-Dicke regime, such that the characteristic trap width at each site $\Delta x \ll \lambda_0$ is much smaller than the resonant optical wavelength. A resulting simplification is that to lowest order, each atom can effectively be treated as a point scatterer of light, although in principle the following calculations can be extended to treat corrections as well. To illustrate the unique optical properties that such a system might have, we first simplify the dynamics somewhat and consider each atom to be a non-absorptive, classical point scatterer with a purely real Lorentzian polarizability $\alpha(\omega)$,

$$\alpha(\omega) \propto \frac{1}{(\Gamma_0/2)^2 + (\omega - \omega_0)^2}. \tag{6.1}$$

The polarizability above describes a scatterer of resonant frequency ω_0 and linewidth Γ_0. Note that a single atom has a significant optical response only within a narrow bandwidth $\sim\Gamma_0$ near the resonance frequency. It is also convenient to define a "quality factor" for the scatterers, given by $Q = \omega_0/\Gamma_0$. In reality, the atomic polarizability will contain an imaginary part as well, which describes absorption, but we momentarily neglect it here. Ignoring the imaginary part makes it possible to calculate the photonic band structure of the system using techniques originally developed in Refs. [155, 156, 157]. While technically more complicated, the idea is similar to that presented in Sec. 1.2.2 for the calculation of a 1-D band structure. In particular, for each Bloch wave, we derive a determinantal condition that must be satisfied for a non-trivial solution to exist. This condition, as derived in Appendix G, is given by

$$\left\| \frac{1}{\Omega k_0^3} \left\{ \sum_{\mathbf{G}} \Upsilon(\mathbf{G}, \mathbf{k}, \omega(\mathbf{k})) \right\} + \frac{Q}{6\pi} \left(\left(\frac{\omega_0}{\omega(\mathbf{k})} \right)^2 - 1 \right) \right\| = 0, \tag{6.2}$$

$$\Upsilon(\mathbf{G}, \mathbf{k}, \omega(\mathbf{k})) \equiv \frac{1}{\left(\frac{\omega(\mathbf{k})}{\omega_0}\right)^2 I - \left|\frac{\mathbf{k}-\mathbf{G}}{k_0}\right|^2 \Delta_{\mathbf{k}-\mathbf{G}}} + \frac{2}{3}\frac{1 - \delta_{G,0}}{(G/k_0)^2} I - \frac{1}{3\left(\omega(\mathbf{k})/\omega_0\right)^2} I, \tag{6.3}$$

which can be used to find the allowed frequencies $\omega(\mathbf{k})$ for a photon with Bloch vector $\mathbf{k}$. Here Ω is the volume of a unit cell of the lattice, $k_0 = \omega_0/c$, I is the identity matrix, $\{\mathbf{G}\}$ is the set of reciprocal lattice vectors, and $\Delta_{\mathbf{p}} = I - \hat{\mathbf{p}}\hat{\mathbf{p}}$ is the operator that projects onto the subspace orthogonal to $\mathbf{p}$. Numerically, Eq. (6.2) can be evaluated by truncating the sum over $\mathbf{G}$ to a finite set of points.

We solve Eq. (6.2) for an optical lattice in a simple cubic configuration, where nearest neighbors are separated by a distance corresponding to half a resonant wavelength, $d = \lambda_0/2$. The numerically evaluated band structure for such a lattice is shown in Fig. 6.1, where we have plotted $\omega(\mathbf{k})$ as a function of $\mathbf{k}$ along lines connecting points of high symmetry in the first Brillouin zone. The mode frequencies $\omega(\mathbf{k})$ are plotted in units of δ/Γ_0, where $\delta = \omega(\mathbf{k}) - \omega_0$, and the letters O, X, M, and R denote the points $(0,0,0)$, $(0,0,\pi/d)$, $(\pi/d,\pi/d,0)$, and $(\pi/d,\pi/d,\pi/d)$, respectively. In this calculation, the sum over $\mathbf{G}$ has been truncated to approximately 3500 points, and we have chosen a quality factor $Q = 3000$. It should be noted that for optical transitions of atoms, Q can be much larger, perhaps around 10^8, but for such large values evaluation of Eq. (6.2) is not straightforward. The dependence of the band structure on Q within the range that Eq. (6.2) can be evaluated is discussed later. It can be seen that the dispersion relation around the atomic resonance ω_0 is dramatically altered from the free-space behavior, $\omega(\mathbf{k}) = ck$, due to the interaction of the photons with the scatterers. More specifically, the calculation predicts an absence of propagating states, or a photonic band gap, just below resonance. The width Δ_{gap} of this gap is on the order of Γ_0, the bandwidth of the response of the scatterers.

It can be noted that the range of forbidden frequencies along the line OX is much larger than in the other directions. Within the range of Q where we are able to evaluate Eq. (6.2), we find that the gap width $\Delta_{\text{gap},OX}/\Gamma_0$ along OX scales like $Q^{1/2}$, while in other directions $\Delta_{\text{gap}}/\Gamma_0$ is roughly independent of Q. Physically, a near-resonant plane wave of light incident on the optical lattice along the direction OX scatters off of planes of atoms normal to OX that are separated by a distance $\lambda_0/2$. The Bragg reflections off of consecutive planes therefore constructively interfere with each other, giving rise to strongly inhibited propagation and a large gap in that

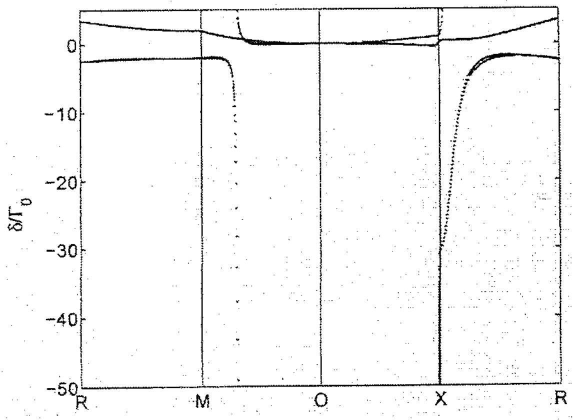

Figure 6.1: The band structure near resonance for a simple cubic optical lattice, with nearest neighbor spacing $d = \lambda_0/2$ and atomic quality factor $Q = 3000$.

direction [36].

The band structure calculation suggests that near-resonant light will propagate and behave very differently in an optical lattice. In particular, if a large photonic band gap appears, one would expect a complete suppression of spontaneous emission for a "defect" atom sitting inside the lattice, whose resonant frequency happens to sit within the gap. Here, however, the width of the gap is very narrow, on the order of Γ_0, so simple exponential decay dynamics (*e.g.*, as predicted through Fermi's Golden Rule) might not apply here. In addition, the band structure calculation assumed a purely real polarizability and thus neglected the absorption or spontaneous emission of the lattice atoms themselves, which might be expected to be significant around the resonance frequency ω_0. These factors motivate a quantum-mechanical treatment where the interactions between photons and all atoms in the system are fully taken into account.

6.3 Dynamics of atomic excitations in a lattice

6.3.1 Derivation of effective atom-atom Hamiltonian

In the band structure calculation of Sec. 6.2 we have ignored the absorptive part of the atomic susceptibility, yet near resonance one does not expect absorption to be negligible. Therefore, to fully treat the problem of a defect in a lattice, we now introduce quantum equations of evolution for the system. These equations will include both coherent interaction terms and absorption.

Specifically, we consider a simplified level system and the problem of N isotropic ($J_g = 0 \rightarrow J_e = 1$) atoms in an optical lattice arranged in a simple cubic configuration. From this point we will refer to these atoms as the "lattice" atoms. We assume an occupation of one lattice atom per lattice site, and assume that the atoms are well within the Lamb-Dicke regime, *i.e.*, they can be treated as point particles. Generalization of these results to the case when one or more "defect" atoms, atoms not located at lattice sites, are introduced into the system will be straightforward. The atoms are coupled to and can interact through electromagnetic field modes. In principle, to solve exactly the problem of interacting atoms, one would have to start from the full atom-field Hamiltonian and take into account not only all the atomic degrees of freedom but the continuum of electromagnetic field modes, which is quite a daunting task. To simplify the treatment, we effectively eliminate the photon degrees of freedom using the Born-Markov approximation and arrive at an effective (non-Hermitian) atom-atom interaction Hamiltonian, which can be interpreted as a description of excited atoms interacting through their dipole fields. This standard technique has been used before in a variety of contexts, such as in the study of superradiance [158] and the effects of atom interactions on laser cooling [159, 160].

First, we define the generalized raising, lowering, and excited state population operators for multi-level atoms,

$$\begin{aligned}
\sigma^j_{ee} &= \sigma^j_{eg} \cdot \sigma^j_{ge}, && (6.4)\\
\sigma^j_{ge} &= \left(\sigma^j_{eg}\right)^\dagger, && (6.5)\\
\sigma^j_{eg} &= \sum_{q=-1}^{1} \sigma^j_{eg}(q)\hat{\epsilon}^*_q, && (6.6)\\
\sigma^j_{eg}(q) &= \sum_{m_e,m_g} \langle J_g m_g, 1q | J_e m_e \rangle |J_e m_e\rangle_j \langle J_g m_g|_j, && (6.7)
\end{aligned}$$

where the polarization vectors are given by

$$\hat{\epsilon}_{\pm 1} = \mp \frac{1}{\sqrt{2}} (\hat{\mathbf{x}} \pm i\hat{\mathbf{y}}), \hat{\epsilon}_0 = \hat{\mathbf{z}}. \tag{6.8}$$

Here j indexes the atoms, e and g denote excited and ground states, respectively, m_e and m_g the magnetic quantum numbers of the excited and ground states, and q the polarization of the transition. We note that for isotropic ($J_g = 0 \rightarrow J_e = 1$) atoms, evaluation of the sum in Eq. (6.7) is trivial since $m_g = 0$ and $m_e = \pm 1, 0$. As derived in Appendix H, the effective Hamiltonian for our system is given by

$$H_{\text{eff}} = -i\frac{\hbar\Gamma_0}{2}\sum_{j=1}^{N} \sigma^j_{ee} - \frac{\hbar\Gamma_0}{2}\sum_{j\neq j'} \sigma^j_{eg} \cdot [i\alpha(k_0\mathbf{r}_{jj'}) + \beta(k_0\mathbf{r}_{jj'})] \cdot \sigma^{j'}_{ge}. \tag{6.9}$$

Here $\Gamma_0 = k_0^3 d_{eg}^2/[3\pi\epsilon_0\hbar(2J_e+1)]$ is the free-space spontaneous emission rate of a single lattice atom, $k_0 = \omega_0/c$ is the resonant wavevector, and $\mathbf{r}_{jj'} = \mathbf{r}_j - \mathbf{r}_{j'}$ is the relative position vector between atoms j and j'. The tensor $i\alpha(k_0\mathbf{r}) + \beta(k_0\mathbf{r})$ has a simple physical meaning, as it is proportional to the emission tensor at a location $\mathbf{r}$

from an oscillating classical point dipole [54]. Writing out these tensors in detail,

$$\alpha(\rho) = \frac{3}{2}(I - \hat{\rho}\hat{\rho})\frac{\sin\rho}{\rho} + \frac{3}{2}(I - 3\hat{\rho}\hat{\rho})\left(\frac{\cos\rho}{\rho^2} - \frac{\sin\rho}{\rho^3}\right), \tag{6.10}$$

$$\beta(\rho) = \frac{3}{2}(I - \hat{\rho}\hat{\rho})\frac{\cos\rho}{\rho} - \frac{3}{2}(I - 3\hat{\rho}\hat{\rho})\left(\frac{\sin\rho}{\rho^2} + \frac{\cos\rho}{\rho^3}\right). \tag{6.11}$$

6.3.2 Effective Hamiltonian for a system with defects

Eq. (6.9) gives the effective Hamiltonian for a set of N identical, interacting lattice atoms. Ultimately, we will want to study the problem of a system of lattice atoms interacting with one or more defect atoms, which do not sit at the lattice sites. In principle, these defect atoms can have a resonance frequency ω_d different from that of the lattice atoms, as well as a different free-space linewidth Γ_d. We will assume, however, that the defect atoms also can be treated as point particles, and are effectively two-level atoms with polarizability along $\hat{z}$. We furthermore assume that we are dealing with atomic systems whose characteristic length scale L satisfies

$$|(k_d - k_0)|\, L \ll 1, \tag{6.12}$$

i.e., the phase error incurred over a length L by replacing $k_d = \omega_d/c$ with k_0 is negligible. Physically this assumption implies that over a length L, one is not able to distinguish between the spatial emission patterns of dipoles at frequencies ω_0 and ω_d.

With these assumptions, the effective Hamiltonian of the system of lattice and defect atoms becomes a straightforward generalization of Eq. (6.9). Defining the parameters $\eta = \Gamma_d/\Gamma_0$ and $\delta = \omega_d - \omega_0$, the effective Hamiltonian H_s for the entire atomic system with N_d defects in the rotating frame becomes

$$H_s = -i\frac{\hbar\Gamma_0}{2}\sum_{j=1}^{N}\sigma_{ee}^{j} + \left(\hbar\delta - i\frac{\hbar\eta\Gamma_0}{2}\right)\sum_{m=1}^{N_d}\sigma_{ee}^{m}$$

$$
\begin{aligned}
&-\frac{\hbar\Gamma_0}{2}\sum_{j\neq j'}\sigma^{j}_{eg}\cdot\left[i\alpha(k_0\mathbf{r}_{jj'})+\beta(k_0\mathbf{r}_{jj'})\right]\cdot\sigma^{j'}_{ge}\\
&-\frac{\hbar\sqrt{\eta}\Gamma_0}{2}\sum_{j,m}\sigma^{j}_{eg}\cdot\left[i\alpha(k_0\mathbf{r}_{jm})+\beta(k_0\mathbf{r}_{jm})\right]\cdot\sigma^{m}_{ge}\\
&-\frac{\hbar\sqrt{\eta}\Gamma_0}{2}\sum_{j,m}\sigma^{m}_{eg}\cdot\left[i\alpha(k_0\mathbf{r}_{mj})+\beta(k_0\mathbf{r}_{mj})\right]\cdot\sigma^{j}_{ge}\\
&-\frac{\hbar\eta\Gamma_0}{2}\sum_{m\neq m'}\sigma^{m}_{eg}\cdot\left[i\alpha(k_0\mathbf{r}_{mm'})+\beta(k_0\mathbf{r}_{mm'})\right]\cdot\sigma^{m'}_{ge},
\end{aligned}
\qquad (6.13)
$$

where m, m' and j, j' are indices for the defect and lattice atoms, respectively. For the two-level defects, the raising operator is defined as

$$\sigma^{m}_{eg}=\sigma^{m}_{eg}(q=0)\hat{\epsilon}^{*}_{0}, \qquad (6.14)$$

while the excited state operator σ^{m}_{ee} is defined in the obvious way.

Eq. (6.13) gives us a starting point for studying the properties of a defect inside an optical lattice, taking fully into account decay mechanisms.

6.3.3 Reconstructing photon states from atomic dynamics

Although we have eliminated the photon degrees of freedom to arrive at the effective atom-atom interaction Hamiltonian of Eq. (6.13), in principle it is possible to reconstruct the photonic state from the atomic variables. The motivations for calculation of the photonic state include finding the field emitted by a defect atom, calculating the emission pattern outside the lattice, and deriving an effective interaction between pairs of defects. We thus now derive the single-photon wave function for a system that begins with just a single excitation.

The wave function of an atom/field system that begins with a single excitation can be written as a superposition of states consisting of a single excited lattice atom ($|e_j^q\rangle \equiv \sigma_{eg}^j(q)|G\rangle$), a single excited defect ($|e_m\rangle \equiv \sigma_{eg}^m|G\rangle$), and a single photon in mode $\mathbf{k},\mu$ ($|1_{\mathbf{k},\mu}\rangle \equiv a_{\mathbf{k},\mu}^\dagger|G\rangle$), where the state $|G\rangle$ consists of all atoms in their ground states and the vacuum state for photons. We can then write

$$|\psi(t)\rangle = \sum_{j,q} c_j^q(t)|e_j^q\rangle + \sum_m c_m(t)|e_m\rangle + \sum_{\mathbf{k},\mu} c_{\mathbf{k},\mu}(t)|1_{\mathbf{k},\mu}\rangle. \tag{6.15}$$

The evolution of the amplitudes $c_{\mathbf{k},\mu}(t)$ is governed by an atom/field interaction Hamiltonian given by

$$H_{\text{af}} = -\sum_{j=1}^{N}\sum_{\mathbf{k},\mu}\hbar g_k^0 \left(\sigma_{eg}^j \cdot \hat{\epsilon}_{\mathbf{k},\mu}\right) a_{\mathbf{k},\mu} e^{i\mathbf{k}\cdot\mathbf{r}_j} - \sum_{m=1}^{N_d}\sum_{\mathbf{k},\mu}\hbar g_k^d \left(\sigma_{eg}^m \cdot \hat{\epsilon}_{\mathbf{k},\mu}\right) a_{\mathbf{k},\mu} e^{i\mathbf{k}\cdot\mathbf{r}_m} + h.c., \tag{6.16}$$

where g_k^0 and g_k^d denote the field coupling constants to the lattice and defect atoms, respectively. In a frame rotating at frequency ω_0, Eq. (6.16) yields the evolution equations

$$\begin{aligned}\frac{\partial}{\partial t}c_{\mathbf{k},\mu}(t) &= -i(\omega_k-\omega_0)c_{\mathbf{k},\mu}(t) + ig_k^0\sum_{j,q}\left(\hat{\epsilon}_q\cdot\hat{\epsilon}_{\mathbf{k},\mu}^*\right)c_j^q(t)e^{-i\mathbf{k}\cdot\mathbf{r}_j} + \\ &\quad ig_k^d\sum_m\left(\hat{\epsilon}_0\cdot\hat{\epsilon}_{\mathbf{k},\mu}^*\right)c_m(t)e^{-i\mathbf{k}\cdot\mathbf{r}_m}.\end{aligned} \tag{6.17}$$

If the photon states are initially unexcited at $t=0$, Eq. (6.17) can be formally integrated to give

$$\begin{aligned}c_{\mathbf{k},\mu}(t) &= i\int_0^t d\tau e^{-i(\omega_k-\omega_0)(t-\tau)}\left[g_k^0\sum_{j,q}\left(\hat{\epsilon}_q\cdot\hat{\epsilon}_{\mathbf{k},\mu}^*\right)c_j^q(\tau)e^{-i\mathbf{k}\cdot\mathbf{r}_j} + \right.\\ &\quad \left. g_k^d\sum_m\left(\hat{\epsilon}_0\cdot\hat{\epsilon}_{\mathbf{k},\mu}^*\right)c_m(\tau)e^{-i\mathbf{k}\cdot\mathbf{r}_m}\right].\end{aligned} \tag{6.18}$$

The single-photon wave function is defined as

$$\Psi(\mathbf{r},t) = \sum_{\mathbf{k},\mu}\langle 0|\mathcal{E}_{\mathbf{k},\mu}\hat{\epsilon}_{\mathbf{k},\mu}a_{\mathbf{k},\mu}e^{i\mathbf{k}\cdot\mathbf{r}}|\psi(t)\rangle, \tag{6.19}$$

where $\mathcal{E}_{\mathbf{k},\mu} = \sqrt{\hbar\omega_0/2\epsilon_0 V}$ is the "electric field per photon". Substituting in the results of Eqs. (6.15) and (6.18) into Eq. (6.19) readily yields

$$\begin{aligned}\Psi(\mathbf{r},t) \;=\; & \sum_{\mathbf{k},\mu} \mathcal{E}_{\mathbf{k},\mu}\hat{\epsilon}_{\mathbf{k},\mu} e^{i\mathbf{k}\cdot\mathbf{r}} i \int_0^t d\tau e^{-i(\omega_k-\omega_0)(t-\tau)} \left[g_k^0 \sum_{j,q} \left(\hat{\epsilon}_q \cdot \hat{\epsilon}^*_{\mathbf{k},\mu}\right) c_j^q(\tau) e^{-i\mathbf{k}\cdot\mathbf{r}_j} + \right. \\ & \left. g_k^d \sum_m \left(\hat{\epsilon}_0 \cdot \hat{\epsilon}^*_{\mathbf{k},\mu}\right) c_m(\tau) e^{-i\mathbf{k}\cdot\mathbf{r}_m} \right]. \qquad (6.20)\end{aligned}$$

Eq. (6.20) is formally an exact expression for the photon wave function, but can be difficult to evaluate under arbitrary conditions. On the other hand, when the atomic amplitudes vary slowly in time, they can approximately be pulled out of the integral. In this case, the sum and time integral are similar to those used in the derivation of Eq. (6.9), and one finds that the single-photon wave function (in dimensionless units) is

$$\begin{aligned}\Psi(\mathbf{r},t) \;=\; & \sum_{j,q} c_j^q(t) \left[i\alpha\left(k_0(\mathbf{r}-\mathbf{r}_j)\right) + \beta\left(k_0(\mathbf{r}-\mathbf{r}_j)\right) \right] \cdot \hat{\epsilon}_q + \\ & \sqrt{\eta} \sum_m c_m(t) \left[i\alpha\left(k_0(\mathbf{r}-\mathbf{r}_m)\right) + \beta\left(k_0(\mathbf{r}-\mathbf{r}_m)\right) \right] \cdot \hat{\epsilon}_0, \qquad (6.21)\end{aligned}$$

where we have used the fact that $g^d_{k_0}/g^0_{k_0} = \sqrt{\eta}$.

6.4 Properties of a single defect

6.4.1 Decay dynamics

We now consider the properties of a single defect atom initially excited in the optical lattice, with all the lattice atoms initially in the ground state. We are particularly interested in the case where the detuning $\delta = \omega_d - \omega_0$ is chosen such that the defect frequency lies within the band gap, and $\eta = \Gamma_d/\Gamma_0 \ll 1$, so that the free-space linewidth of the defect is much narrower than the gap width. Furthermore we restrict ourselves to studying defects that occupy points of high symmetry in the lattice, as shown in Fig. 6.2. Having derived in Eq. (6.13) an effective Hamiltonian that describes both coherent interactions and decay in the lattice/defect system, there are now two possible approaches to obtaining the defect properties. The first approach is rather intuitive and involves numerical integration of the system evolving under H_s, which we will briefly discuss in this subsection. Another approach is to find the resonant modes of the system under H_s, which we will discuss in the following subsection. The results obtained by each approach closely agree, although in practice the method of resonant modes involves less computation time and is used more extensively here. We thus defer a more detailed discussion of the physical results until the next subsection, while illustrating the results of numerical integration here.

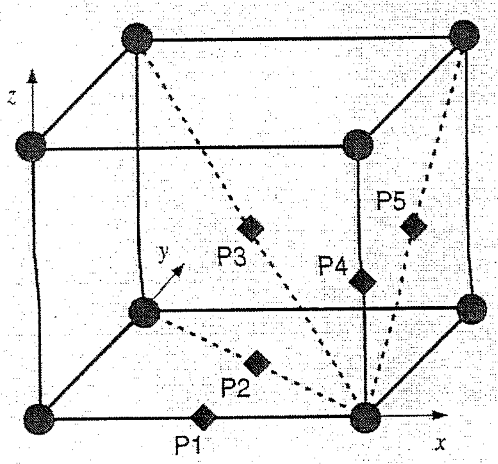

Figure 6.2: We consider the properties of defect atoms sitting at several points of high symmetry inside the lattice. The circles denote lattice atoms, while the diamonds denote the different positions of defects that we consider.

It is at least in principle straightforward to directly obtain the time evolution of the system by numerically integrating

$$\frac{\partial}{\partial t}|\psi(t)\rangle = -\frac{i}{\hbar}H_s|\psi(t)\rangle. \tag{6.22}$$

We will consider the case when the defect is initially excited while the lattice atoms are initially in the ground state. Because such a system contains at most one excitation, the atomic wave function can be written as

$$|\psi(t)\rangle = \sum_{j,q} c_j^q(t)|e_j^q\rangle + c_d(t)|e_d\rangle, \tag{6.23}$$

with $c_d(0) = 1$ and $c_j^q(0) = 0$, and the evolution equations for the state amplitudes under H_s are readily found to be

$$\begin{aligned}
\dot{c}_j^q(t) &= -\frac{\Gamma_0}{2}c_j^q(t) + \sum_{j'\neq j,q'} \hat{\epsilon}_q^* \cdot [i\beta(k_0\mathbf{r}_{jj'}) - \alpha(k_0\mathbf{r}_{jj'})] \cdot \hat{\epsilon}_{q'} c_{j'}^{q'}(t) + \\
&\quad \sqrt{\eta}\hat{\epsilon}_q^* \cdot [i\beta(k_0\mathbf{r}_{jd}) - \alpha(k_0\mathbf{r}_{jd})] \cdot \hat{\epsilon}_0 c_d(t), \\
\dot{c}_d(t) &= -\left(\frac{\eta\Gamma_0}{2} + i\delta\right) c_d(t) + \sqrt{\eta}\sum_{j,q} \hat{\epsilon}_0^* \cdot [i\beta(k_0\mathbf{r}_{dj}) - \alpha(k_0\mathbf{r}_{dj})] \cdot \hat{\epsilon}_q c_j^q(t).
\end{aligned} \tag{6.24}$$

To illustrate the dynamics of the equations above, we consider a system consisting of a single defect occupying the symmetry point $P1$, as illustrated in Fig. 6.2, in a finite-size lattice of $N{\approx}8000$ atoms, with a chosen detuning of $\delta = -0.5\Gamma_0$ and $\eta = 2{\times}10^{-4}$. The population of the excited state of the defect, $|c_d(t)|^2$, is plotted in Fig. 6.3a as a function of time (solid line), with the decay rate in free space plotted as well (dotted line) for comparison. It can be seen that spontaneous emission is significantly suppressed for the defect whose frequency resides inside the band gap, even though the dynamics have a dissipative component. Fitting the decay to an exponential yields a suppression factor of approximately 31.5 relative to free space. The suppression factor does not appear to improve significantly with smaller η or

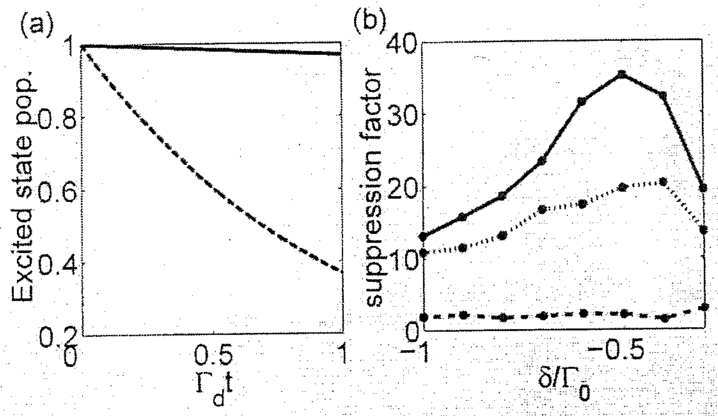

Figure 6.3: a) Population decay of an initially excited defect in the lattice (solid line) vs. free space (dotted line). The lattice is composed of approximately 8000 atoms, with defect parameters $\eta = 2\times10^{-4}$ and $\delta/\Gamma_0 = -0.5$. b) Suppression of spontaneous emission in lattice relative to free space, as a function of defect position and detuning. The defect positions correspond to points of high symmetry, as shown in Fig. 6.2. The solid line corresponds to a defect at $P1$, the dotted line to $P2$, and the dashed line to $P3$. The suppression at points $P4$ and $P5$ are negligible and are omitted from the plot.

larger system size, and thus is apparently limited by absorption in the system. While this example clearly illustrates that the dynamics can be obtained by straightforward numerical integration, in practice this method can be time exhaustive if η is small, which creates a very large separation of time scales between the lattice and defect atom dynamics.

6.4.2 System resonances

It is also possible to numerically calculate the spontaneous decay rate without integrating Eq. (6.22), by finding the eigenmodes of the differential equation. In particular, we are interested in solutions of Eq. (6.24) of the form

$$\begin{aligned} c_{j,n}^{q}(t) &= e^{-(\gamma_n+i\omega_n)t}c_{j,n}^{q}(t), \\ c_{d,n}(t) &= e^{-(\gamma_n+i\omega_n)t}c_{d,n}(t), \end{aligned} \tag{6.25}$$

where n labels the different eigenmode solutions. For a system of N lattice atoms and one defect, there will in general be $3N+1$ solutions to the equation. γ_n and ω_n give the decay rates and energies of mode n, respectively.

We still focus on the regime where $\eta = \Gamma_d/\Gamma_0 \ll 1$. In this regime, the characteristic time scale of the defect is much longer than that of the lattice atoms. As a result, relative to the time scale of the defect, the lattice atoms will respond and equilibrate almost instantaneously to the defect's dynamics. Equivalently, one expects the lattice atoms to adiabatically follow the dynamics of the defect in this limit. Moreover, the response of the lattice atoms should be proportional to the field emitted by the defect, *i.e.*, proportional to $\sqrt{\eta}$. Mathematically, we are thus interested in finding resonances of the form

$$c_j^q(t) \approx \alpha_j^q \sqrt{\eta}\, c_d(t), \tag{6.26}$$

which correspond physically to the situation described above. In general, only one of the eigenmodes corresponds to a solution of the form of Eq. (6.26), while the others can be viewed as perturbations of the eigenmodes of a lattice without the defect. The eigenvalue corresponding to this eigenmode gives us the decay rate of the defect in the lattice. The results obtained by this method agree well with those obtained by numerical integration of the dynamical equations. In Fig. 6.3b we plot the suppression factor $\tilde{\Gamma}_d/\Gamma_d$ of spontaneous emission rates in the lattice ($\tilde{\Gamma}_d$) relative to free space (Γ_d), as a function of both detuning and defect position. In these numerical simulations the lattice contains approximately 10^4 atoms. It can be seen that the optimal suppression occurs at point $P1$ (see Fig. 6.2) around a detuning $\delta \approx -0.5\Gamma_0$, for which the suppression factor is calculated to be 35.2. The suppression factor does not appear to change significantly by choosing larger system sizes. Nor does it change significantly by choosing smaller η, which is to be expected if the lattice response indeed scales like Eq. (6.26). Thus the limits to suppression are likely a result of absorption. That absorption from the surrounding lattice imposes a limit on inhibition of spontaneous emission can be understood from a classical standpoint. Classically, spontaneous emission (or power loss) from a dipole can be interpreted as the result of interaction between the dipole and the in-quadrature part of the electric field at the dipole's location [161]. In the presence of the lattice, the total field consists of both the self-field of the defect and a field reflected from the lattice. Complete inhibition would occur if the contributions from the self- and reflected fields cancelled perfectly. If the lattice were purely dispersive, the reflectivity of the lattice could approach unity within the band gap. When absorption is present, however, the reflectivity can saturate at values below unity even when the dispersive part of the susceptibility provides a band gap.

In our system, absorption by the lattice only occurs when there is some field intensity at the lattice sites. One then expects that the adverse effects of absorption can be minimized when nodes of the field emitted by the defect tend to form around these sites. We can confirm this by using the calculated resonance amplitudes $\{c_j^q(t), c_m(t)\}$ and Eq. (6.21) to find the emission pattern. In Fig. 6.4 we plot the field intensities $I(\mathbf{r})$ in the x-y plane caused by an excited defect at points $P1$ and $P2$. In each case,

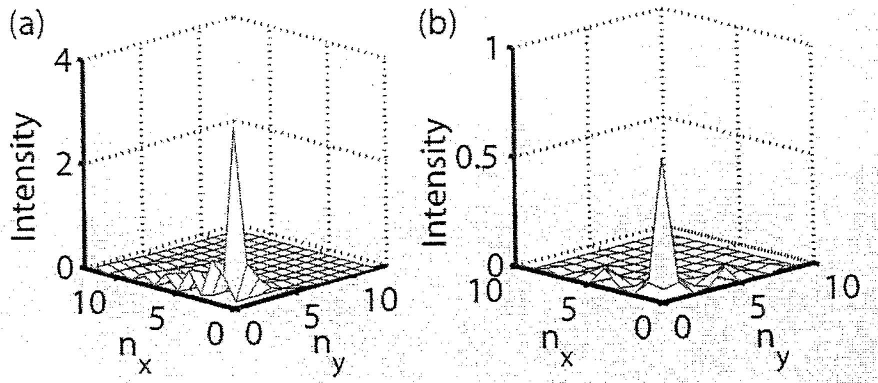

Figure 6.4: a) The field intensity $I(\mathbf{r})$ (in arbitrary units) in the x-y plane created by an excited defect at point $P1$ in an optical lattice. The origin is defined as the location of the defect. The field intensity is calculated at points $\frac{\lambda_0}{4}(n_x, n_y, 0)$. In this case lattice sites coincide with odd n_x and even n_y. The positioning of field nodes around lattice sites minimizes the effect of absorption by the lattice. b) Same quantity for an excited defect at point $P2$. Here lattice sites coincide with odd n_x and odd n_y.

the defect is chosen to lie at the origin. Because the field diverges as one approaches a point dipole, numerical calculation of the field is restricted to points $P \in \frac{\lambda_0}{4}(n_x, n_y, 0)$ where n_i are integers. Furthermore, we do not include the divergent self-field of an atom whose location coincides with P. It is also helpful to consider the quantity $r^2 I(\mathbf{r})$ for each configuration, which we note approaches a constant for a dipole in free space as $r \to \infty$. Plots of $r^2 I(\mathbf{r})$ in the x-y plane for defect locations $P1$ and $P2$ are plotted in Fig. 6.5. It is clear from the figures that the field appears to be localized around the defect. Furthermore, nodes in the field tend to be located around lattice sites for a $P1$ defect, which explains how spontaneous emission can be strongly suppressed despite absorption from the lattice atoms. It is also clear that the field is highly anisotropic in the x-y plane, unlike the free-space case. This suggests that the emission pattern outside the lattice will be anisotropic as well. In Fig. 6.6 we

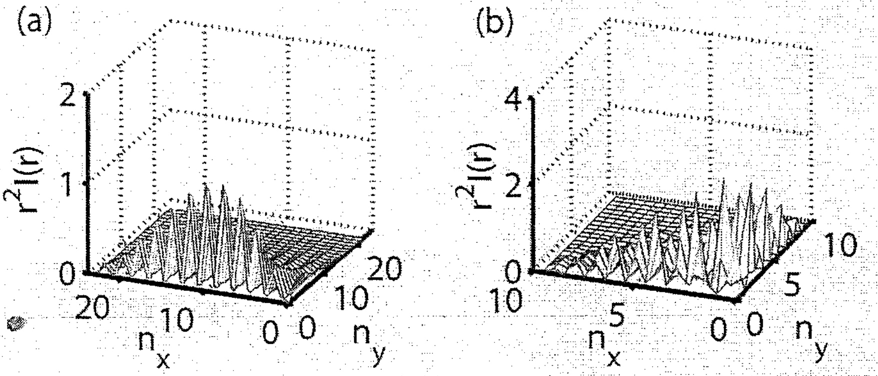

Figure 6.5: a) The quantity $r^2 I(\mathbf{r})$ (in arbitrary units) in the x-y plane for a defect located at $P1$. b) The same quantity for a defect located at $P2$.

evaluate Eq. (6.21) for a $P1$ defect to find the field intensity outside the lattice. The intensity is highly focused along the x-axis, as we find a directivity of approximately 50 as compared to an isotropic oscillator.

6.5 Long-range coupling of multiple defects

It is well-known that two atoms in free space can coherently exchange excitations with each other through resonant dipole-dipole interactions [162]. However, in free space the population oscillations are destroyed by spontaneous emission except at distances much smaller than a resonant wavelength λ_0.

In an optical lattice, however, spontaneous emission of a defect atom can be strongly suppressed while a field localized to several λ_0 forms around it. This raises the possibility that an excited defect atom may be able to coherently exchange excitations

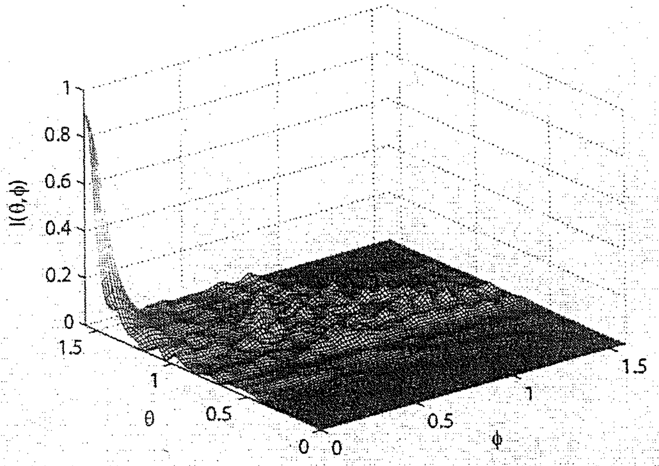

Figure 6.6: The field intensity (in arbitrary units) seen outside the lattice for an excited $P1$ defect. θ and ϕ refer respectively to the polar and azimuthal angles in spherical coordinates. The intensity is concentrated along $\theta = \pi/2$, $\phi = 0$ (the x-axis).

with a second defect provided that they are located within a localization length of each other. In this section we seek to quantify the interaction and decay mechanisms of a pair of defects, deriving an effective Hamiltonian involving only the defect degrees of freedom and calculating the fidelity of the excitation transfer process.

Specifically, we are interested in the dynamics of two defects in a lattice, with at most one excitation in the entire system. These conditions are quite similar to those of the single defect problem studied in Sec. 6.4, and those methods could be extended to study the problem of two defects. One expects that there will be two eigenmodes corresponding not to individual excitations $|e_a\rangle$ or $|e_b\rangle$ of the defects but to symmetric and anti-symmetric superpositions:

$$|S\rangle \equiv (|e_a\rangle + |e_b\rangle)/\sqrt{2}, \tag{6.27}$$

$$|A\rangle \equiv (|e_a\rangle - |e_b\rangle)/\sqrt{2}. \tag{6.28}$$

Because of the computational resources required for these methods, we instead introduce another method for calculating the energies and decay rates of the states $|S\rangle$ and $|A\rangle$. This method utilizes the well-known result that level shifts and emission rates can be calculated classically based on the interaction of a dipole with the total field [161]. Specifically, when a single oscillating dipole $\mathbf{d}e^{-i\omega_0 t}$ at position $\mathbf{r}_0$ is in the vicinity of some passive medium, the total electric field $\mathbf{E}(\mathbf{r})e^{-i\omega_0 t}$ can in general be written as the sum of the dipole's free field plus some reflected field:

$$\mathbf{E}(\mathbf{r}) = \mathbf{E}_f(\mathbf{r}) + \mathbf{E}_r(\mathbf{r}). \tag{6.29}$$

The in-phase component of the reflected field causes a shift $\Delta\omega$ in the resonance frequency of the dipole, where

$$\Delta\omega \propto -\mathrm{Re}\left\{\mathbf{d}\cdot\mathbf{E}_r^*(\mathbf{r}_0)\right\}. \tag{6.30}$$

The decay rate Γ of the dipole is affected by the in-quadrature component and is given by

$$\begin{aligned} \Gamma &\propto -\mathrm{Im}\left\{\mathbf{d}\cdot\mathbf{E}^*(\mathbf{r}_0)\right\} && (6.31) \\ &= -\mathrm{Im}\left\{\mathbf{d}\cdot\left(\mathbf{E}_f^*(\mathbf{r}_0)+\mathbf{E}_r^*(\mathbf{r}_0)\right)\right\}. && (6.32) \end{aligned}$$

It should be noted that the term $\mathrm{Im}\left\{\mathbf{d}\cdot\mathbf{E}_f^*(\mathbf{r}_0)\right\}$ is responsible for the free-space decay.

These results can easily be extended to find the energies and decay rates of a pair of defect atoms in states $|S\rangle$ and $|A\rangle$ sitting inside an optical lattice. We suppose that the defects are located at $\mathbf{r}_a$ and $\mathbf{r}_b$, and we continue to assume that $\eta \ll 1$. When only

a is present in the lattice, the lattice atoms adiabatically follow the state amplitude $c_a(t)$:

$$c_j^q(t) \approx \alpha_{j,a}^q \sqrt{\eta} c_a(t). \tag{6.33}$$

Similarly, when only b is present,

$$c_j^q(t) \approx \alpha_{j,b}^q \sqrt{\eta} c_b(t). \tag{6.34}$$

When both atoms are present in the limit $\eta \ll 1$, the total lattice response is just a sum of the individual responses,

$$c_j^q(t) = \alpha_{j,a}^q \sqrt{\eta} c_a(t) + \alpha_{j,b}^q \sqrt{\eta} c_b(t). \tag{6.35}$$

We note that the quantities α_j^q have been numerically calculated in Sec. 6.4.2. $\alpha_{j,a}^q$ and $\alpha_{j,b}^q$ can be obtained by translation, and errors due to finite lattice and boundary effects should be negligible for sufficiently large simulated system size.

Having obtained an approximate solution (6.35) to the response of the lattice due to a pair of defects, we can use Eq. (6.21) to calculate the total field of the system. Substitution of Eq. (6.35) immediately yields

$$\begin{aligned}
\Psi(\mathbf{r},t) \;=\;& \sqrt{\eta}\Big\{ \sum_{j,q} \alpha_{j,a}^q c_a(t) \left[i\boldsymbol{\alpha}\left(k_0(\mathbf{r}-\mathbf{r}_j)\right) + \boldsymbol{\beta}\left(k_0(\mathbf{r}-\mathbf{r}_j)\right)\right] \cdot \hat{\epsilon}_q \\
& + \sum_{j,q} \alpha_{j,b}^q c_b(t) \left[i\boldsymbol{\alpha}\left(k_0(\mathbf{r}-\mathbf{r}_j)\right) + \boldsymbol{\beta}\left(k_0(\mathbf{r}-\mathbf{r}_j)\right)\right] \cdot \hat{\epsilon}_q \\
& + c_a(t) \left[i\boldsymbol{\alpha}\left(k_0(\mathbf{r}-\mathbf{r}_a)\right) + \boldsymbol{\beta}\left(k_0(\mathbf{r}-\mathbf{r}_a)\right)\right] \cdot \hat{\epsilon}_0 \\
& + c_b(t) \left[i\boldsymbol{\alpha}\left(k_0(\mathbf{r}-\mathbf{r}_b)\right) + \boldsymbol{\beta}\left(k_0(\mathbf{r}-\mathbf{r}_b)\right)\right] \cdot \hat{\epsilon}_0 \Big\} && (6.36) \\
\equiv\;& \sqrt{\eta}\left\{ c_a(t)\Psi_{r,a}(\mathbf{r},t) + c_b(t)\Psi_{r,b}(\mathbf{r},t) \right. \\
& \left. + c_a(t)\Psi_{f,a}(\mathbf{r},t) + c_b(t)\Psi_{f,b}(\mathbf{r},t) \right\}, && (6.37)
\end{aligned}$$

where in the last line we have separated $\Psi(\mathbf{r},t)$ into the reflected and free fields due to a, b. Having found the total field, it is now possible to calculate the shifts and decay rates of $|S\rangle$ and $|A\rangle$. In the symmetric state, $c_a(t) = c_b(t)$, while in the antisymmetric state, $c_a(t) = -c_b(t)$. Application of Eqs. (6.30) and (6.31) then gives

$$\frac{\Delta\omega_{S,A}}{\Gamma_d} = -\mathrm{Re}\left\{\Psi_{r,a}(\mathbf{r}_a,t) \pm \Psi_{r,b}(\mathbf{r}_a,t) \pm \Psi_{f,b}(\mathbf{r}_a,t)\right\}^* \cdot \hat{\epsilon}_0, \tag{6.38}$$

$$\frac{\Gamma_{S,A}}{\Gamma_d} = -\mathrm{Im}\left\{\Psi_{f,a}(\mathbf{r}_a,t) + \Psi_{r,a}(\mathbf{r}_a,t) \pm \Psi_{r,b}(\mathbf{r}_a,t) \pm \Psi_{f,b}(\mathbf{r}_a,t)\right\}^* \cdot \hat{\epsilon}_0, \tag{6.39}$$

where we have scaled the energy shifts and decay rates in terms of the free-space defect decay rate Γ_d.

It is convenient to group all of these effects into a single effective interaction Hamiltonian involving only the defect degrees of freedom, which takes the form

$$H_d = -i\frac{\hbar\tilde{\Gamma}_d}{2}\sum_{j=1}^{m}\sigma_{ee}^{m} - \frac{\hbar\tilde{\Gamma}_d}{2}\sum_{m\neq m'}\left[i\alpha_{mm'} + \beta_{mm'}\right]\sigma_m^{+}\sigma_{m'}^{-}, \tag{6.40}$$

where $\tilde{\Gamma}_d$ is the decay rate of a single defect inside the lattice, while $\alpha_{mm'}$ and $\beta_{mm'}$ describe the pairwise interaction strengths between two defects m and m'. The former accounts for cooperative decay, while the latter accounts for the energy splitting between $|S\rangle$ and $|A\rangle$.

In Fig. 6.7 we plot β_{0m} and $|\beta_{0m}|$ as a function of the spacing m between defects. Here the individual defects are assumed to have detunings $\delta = -0.5\Gamma_0$ and are located at points $P1$ in the lattice along the x-axis (see Fig. 6.2). The distance between two defects is thus $m\lambda_0/2$. It is evident that $|\beta_{0m}|$ decays exponentially as a function of the separation m, unlike in free space, where $|\beta(\mathbf{r})|{\sim}r^{-1}$. At separations on the order of a few λ_0, the coherent coupling strengths are several times larger than the decay rates in the medium, which implies that an excitation can be transferred coherently between

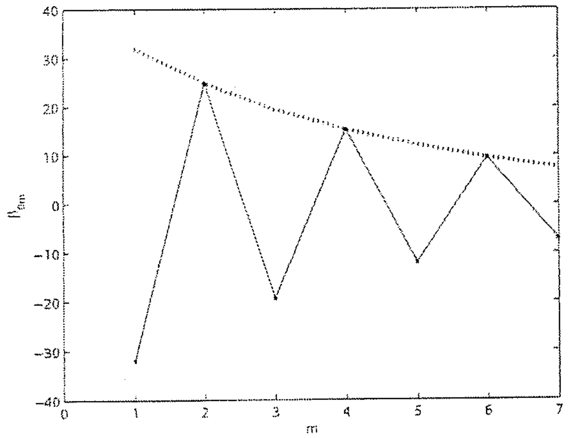

Figure 6.7: β_{0m} (solid line) and $|\beta_{0m}|$ (dotted line) as a function of defect separation m. The defects are assumed to have detunings $\delta = -0.5\Gamma_0$ and sit along the x-axis at points of the type $P1$.

defects several times before it is lost to decay. It can be verified that the coupling strengths at this separation are not much larger than those in free space; in other words, this coherent transfer is made possible by strongly suppressed spontaneous emission. In Fig. 6.8 we plot α_{0m} as a function of m. One can see that cooperative decay does not play a significant role beyond a separation $\sim \lambda_0$.

We next numerically calculate the fidelity of the coherent transfer process. In particular, we assume that a pair of defects a, b sit at a separation $m\lambda_0/2$, with a initially excited. Under evolution of Eq. (6.40), population between the excited states $|e_a\rangle$ and $|e_b\rangle$ are imperfectly exchanged back and forth until the system completely loses its excitation. In Fig. 6.9 we plot the maximum population that is transferred to defect b as a function of the spacing m. For $m = 1$, the probability of successful transfer to b is over 90%, and the fidelity remains quite high even at a spacing of several λ_0.

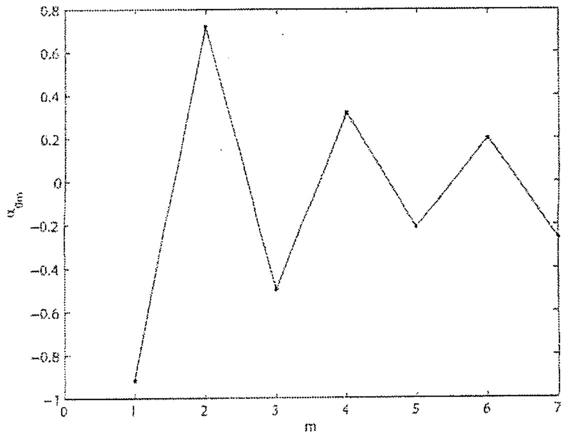

Figure 6.8: α_{0m} as a function of defect separation m. The defects are assumed to have detunings $\delta = -0.5\Gamma_0$ and sit along the x-axis at points of the type $P1$.

6.6 Discussion

We have shown that under certain conditions, an optical lattice can act as an effective photonic crystal medium that strongly suppresses propagation of light and spontaneous emission of defect atoms inside, even when operating near the resonance frequency of the background lattice atoms where absorption cannot be neglected. The suppression of spontaneous emission is accompanied by the formation of a localized field around the defect and allows the possibility of coherent coupling of defects separated by many lattice constants.

In the theory presented above, we have relied on introducing defect atoms whose coupling to the electromagnetic field modes is much smaller than that of the lattice atoms (*e.g.*, small η). In practice, instead of introducing some different atomic species with a small natural linewidth, one could simply use a Raman process to reduce the effective linewidth of the excited state $|e\rangle$. This can be accomplished, for example, by

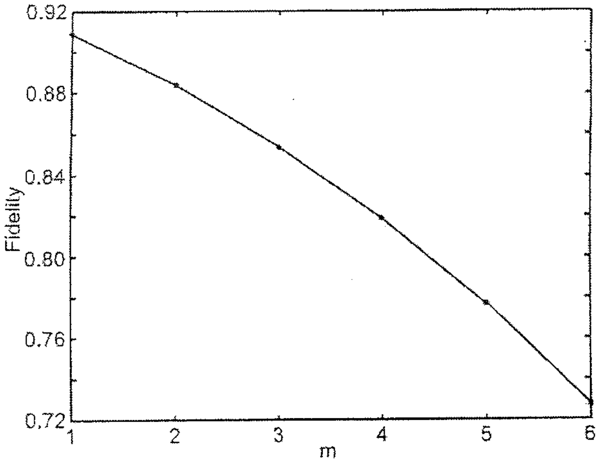

Figure 6.9: Maximum population transfer from an excited defect to an initially unexcited defect, as a function of distance $m\lambda_0/2$ separating the two defects.

initializing the defect atom in some metastable or other ground state $|s\rangle$, and using a weak external field to slowly couple it to $|e\rangle$. Furthermore, while we have considered theoretically a two-level defect atom for simplicity, in reality these atoms could also be defined by some different magnetic quantum number from the lattice atoms, which would allow the use of fields with spatially varying polarizations to trap the lattice and defect atoms in different locations. Examples of such field geometries can be found, for instance, in Refs. [163, 164]. Finally, we note that advances in areas such as patterned loading [152] and loading of lattices with reduced site occupation number defects [165] may put the creation of a lattice and defect system within experimental reach.

Chapter 7

Controlling frequency shifts in an optical-lattice based atomic clock

7.1 Introduction

The development of increasingly accurate atomic clocks has led to many advances in technology and tests of fundamental physics. In the search for the next generation of clocks and frequency standards, there has been considerable interest in using alkaline earth species because of their narrow intercombination lines in the optical spectrum [166]. In order to achieve a high level of short-term stability and long-term reproducibility and accuracy on the clock transition, it is desirable to have a large number of cold atoms located in a trap for an improved signal-to-noise ratio (S/N) and for a reduction in resolution limitations and systematic errors caused by atomic motion. Although with a limited S/N, single ion-based systems do effectively eliminate Doppler and other motion related systematic errors when the single ions are confined in the Lamb-Dicke regime [167]. For neutral atoms it is important that level structure changes due to the trapping potential do not alter the relevant clock transition frequency. Such a scheme has been proposed by trapping alkaline earth atoms in three-dimensional optical lattices tuned to a magic wavelength where the relevant states for the clock transition experience exactly the same level shift [49]. The ${}^1S_0(F = 9/2) - {}^3P_0(F = 9/2)$ forbidden transition ($\lambda_0 = 700$ nm) in ^{87}Sr is in particular a promising candidate for a lattice-based optical clock transition because of the long lifetime of the excited state ($\sim$160 s) and the insensitivity of the $J = 0$ states to the polarization of the trapping light [49]. Already there have been efforts towards the cooling and trapping of ^{87}Sr [168, 169, 170], and recently this transition was directly observed and measured for the first time [171]. Calcium, another alkaline earth atom that has been studied extensively as a frequency standard [172, 173], may be a candidate for optical lattice clocks as well.

In the case of N independent atoms, one benefits from a $\sqrt{N}$ improvement in S/N in spectroscopy. However, atoms trapped in an optical lattice can interact through dipole-dipole interactions and cannot truly be considered independent. These interactions can manifest themselves as shifts in the observed transition frequencies. Because of the spatial ordering of atoms in a lattice and the potentially high atomic density, it is possible that the interactions may add constructively to produce very large frequency shifts. One might expect then that dipole-dipole interactions can be much more severe here than in, for example, atomic fountains, and thus place serious limits on the accuracy of an optical lattice clock if not accounted for. On the other hand, it might be possible to design lattice geometries where this shift is reduced or cancelled. In ^{87}Sr one chooses a magic wavelength for the trapping lasers such that the shift on the clock transition due to the first-order ac Stark shift is cancelled [49]. However, one does retain some control over the lattice geometry. Here, we show that by varying the lattice geometry relative to the actual wavelength of the clock transition we can quantitatively control the clock frequency shift and even reduce the shift to zero.

This chapter is organized as follows. In Sec. 7.2 we derive equations describing the evolution of an atomic system with dipole-dipole interactions. These equations are derived assuming that the atoms are in the Lamb-Dicke regime, with one atom or less per lattice site. In Sec. 7.3 we give a brief review of Ramsey spectroscopy and solve for the dipole-dipole line shift using perturbation theory. We find that the shift can be partially understood in terms of the classical interaction energies between oscillating dipoles. There is a contribution to the shift that is zeroth order in the interrogation time t, which is due to imperfections in the Ramsey pulses. Even with perfect pulses, one finds a shift that is first order in t that results from spontaneous decay of the atoms. Sec. 7.4 discusses how our result for the line shift can be generalized for systems with imperfect filling of the lattice sites and for multilevel atoms. In Sec. 7.5, we analyze how the line shift can be reduced by choosing an appropriate lattice design. Experimentally, one has control of the orientations of the trapping lasers, whose degrees of freedom are characterized by a set of variables $\{\alpha\}$. We give an analytical equation that can be solved giving solutions $\{\alpha_0\}$ where constructive interference causes the line shift to be very large. In these "bad" lattice configurations, the magnitude of the shift scales approximately like $N^{2/3}$. Quite generally we propose that by tuning the parameter space $\{\alpha\}$ to lie in between two of these bad configurations, one can find "good" configurations where the shift is nearly zero. We illustrate this result numerically for one particular lattice design.

7.2 Equations of motion

To treat the problem of interacting atoms in a lattice, we consider N two-level atoms in the Lamb-Dicke limit with polarizability along the $\hat{z}$-axis. A simple model of the system consists of treating the atoms as point dipoles, and we further assume that there is one or less atom per lattice site. This corresponds to a Mott-insulator state for bosons and an insulating state for fermions. Starting from the full atom-field Hamiltonian, we eliminate the field in the standard way using the Born-Markov approximation (see Appendix H). This is valid provided that the atomic system evolves slowly on timescales of the correlation time τ_c, which is of the order L/c where L is the linear size of the system. As a result of eliminating the field, one finds an effective equation of motion for the density matrix ρ of the atomic system. Atom-atom interactions then appear through an effective Hamiltonian H_{eff} as well as through a non-Hermitian operator $\mathcal{L}$:

$$\frac{\partial \rho}{\partial t} = \frac{1}{i\hbar}\left[H_0 + H_{\text{eff}}, \rho\right] + \mathcal{L}[\rho]. \tag{7.1}$$

Here, H_0 is the atomic Hamiltonian for a non-interacting system. Writing out all the terms in detail,

$$\frac{\partial \rho}{\partial t} = \frac{1}{i}\sum_{a}\left[\frac{\omega_0}{2}\sigma^z_a, \rho\right] - \frac{i\Gamma}{2}\sum_{a\neq b} g(k\mathbf{r}_{ab})\left[\sigma^+_a\sigma^-_b, \rho\right]$$

$$
\begin{aligned}
&-\frac{\Gamma}{2}\sum_{a,b} f(k\mathrm{r}_{ab})\left(\{\sigma_a^+\sigma_b^-,\rho\} - 2\sigma_b^-\rho\sigma_a^+\right) \\
&-\frac{1}{8}\sum_{a,b}\gamma_{ab}\left(\{\sigma_a^z\sigma_b^z,\rho\} - 2\sigma_b^z\rho\sigma_a^z\right),
\end{aligned}
\tag{7.2}
$$

where

$$
\begin{aligned}
f(\mathrm{v}) &= \frac{3}{2}\left(\sin^2\theta\frac{\sin v}{v} + (3\cos^2\theta - 1)\left(\frac{\sin v}{v^3} - \frac{\cos v}{v^2}\right)\right), \\
g(\mathrm{v}) &= -\frac{3}{2}\left(\sin^2\theta\frac{\cos v}{v} + (3\cos^2\theta - 1)\left(\frac{\cos v}{v^3} + \frac{\sin v}{v^2}\right)\right),
\end{aligned}
\tag{7.3}
$$

and θ is the angle that v makes with the z-axis. Aside from the γ_{ab} term, Eqs. (7.2) and (7.3) are the results derived in Appendix H when applied to the simple case of a collection of two-level atoms.

The first term on the right-hand side of Eq. (7.2) corresponds to H_0. σ_a^z is the population inversion operator of atom a measuring the population difference between the excited and ground states, and ω_0 is the resonance frequency of the dipole transition. The second term corresponds to H_{eff}. Here, $\Gamma = k_0^3 d^2/3\pi\epsilon_0\hbar$ is the spontaneous decay rate of a single atom, where $k_0 = 2\pi/\lambda_0$ and d is the dipole moment between the ground and excited states. σ_a^+ is the atomic raising operator on atom a, and σ_b^- is the lowering operator on atom b. One then sees that the effect of dipole-dipole interactions is an exchange of excitation between pairs of atoms. One can also see that the strength of interaction is modified by a function $g(k\mathrm{r}_{ab})$ depending on the distance and orientation between two dipoles. It is to be understood that $k = k_0$ in the functions f and g. The third term on the right corresponds to $\mathcal{L}$ and also is due to dipole-dipole interactions. It too depends on Γ and has a position dependence described by $f(k\mathrm{r}_{ab})$. Physically $\mathcal{L}$ describes the processes of both independent and cooperative decay. Finally, we have also added phenomenological dephasing through the γ_{ab} terms. We allow this damping to be quite general, requiring only that $\gamma_{ab} = \gamma_{ba}$ and that $\gamma_{aa} = \gamma_{bb} \equiv \gamma$. This term captures the effects of a finite laser linewidth, for example.

From Eq. (7.2), one can derive equations of motion for any atomic operators. For our particular application of Ramsey spectroscopy, we find it necessary to solve for the coherence $\langle\sigma_a^+\rangle$ and the two-atom correlation $\langle\sigma_a^z\sigma_b^+\rangle$. Furthermore, to remove the rapid oscillations due to ω_0, it is convenient to work in the frame rotating with the probe laser frequency ν, where

$$\begin{aligned}
\frac{\partial\langle\sigma_a^+\rangle}{\partial t} &= -i\delta\langle\sigma_a^+\rangle - \frac{\Gamma+\gamma}{2}\langle\sigma_a^+\rangle + \frac{\Gamma}{2}\sum_{b\neq a}\left(f(k\mathbf{r}_{ab}) - ig(k\mathbf{r}_{ab})\right)\langle\sigma_a^z\sigma_b^+\rangle, \qquad (7.4)\\
\frac{\partial\langle\sigma_a^z\sigma_b^+\rangle}{\partial t} &= -\left(i\delta + \frac{3\Gamma+\gamma}{2}\right)\langle\sigma_a^z\sigma_b^+\rangle - \Gamma\langle\sigma_b^+\rangle - \frac{\Gamma}{2}\left(f(k\mathbf{r}_{ab}) + ig(k\mathbf{r}_{ab})\right)\langle\sigma_a^+\rangle\\
&\quad -\Gamma f(k\mathbf{r}_{ab})\langle\sigma_a^+\sigma_b^z\rangle + \frac{\Gamma}{2}\sum_{j\neq a,b}\left(f(k\mathbf{r}_{bj}) - ig(k\mathbf{r}_{bj})\right)\langle\sigma_a^z\sigma_b^z\sigma_j^+\rangle\\
&\quad -\Gamma\sum_{j\neq a,b}\left(f(k\mathbf{r}_{aj}) + ig(k\mathbf{r}_{aj})\right)\langle\sigma_a^+\sigma_b^+\sigma_j^-\rangle\\
&\quad -\Gamma\sum_{j\neq a,b}\left(f(k\mathbf{r}_{aj}) - ig(k\mathbf{r}_{aj})\right)\langle\sigma_a^-\sigma_b^+\sigma_j^+\rangle, \qquad (7.5)
\end{aligned}$$

and $\delta = \nu - \omega_0$.

7.3 Ramsey spectroscopy

7.3.1 Basic principles

We now analyze the effects of atom-atom interactions on Ramsey spectroscopy. Starting from the ground state of the system, suppose that one applies a strong probe pulse to the system, given in the rotating frame by the Hamiltonian

$$H = \sum_a i\hbar\Omega \left(\sigma_a^+ e^{i\mathbf{k}\cdot\mathbf{r}_a} - \sigma_a^- e^{-i\mathbf{k}\cdot\mathbf{r}_a}\right), \tag{7.6}$$

where Ω is the Rabi frequency. For simplicity, we have made a plane-wave assumption about the probing laser, taking $\mathbf{k}$ to be in the positive x direction. We also assume that $k \approx k_0$, and suppress the subscript in future calculations. We can do this if the phase error $e^{i\delta L/c}$ over the length of the sample incurred by making this assumption is small. Applying this pulse for a time τ evolves the system through the unitary operator

$$U = \prod_a^{\otimes} \begin{pmatrix} \cos\Omega\tau & e^{ikx_a}\sin\Omega\tau \\ -e^{-ikx_a}\sin\Omega\tau & \cos\Omega\tau \end{pmatrix} \tag{7.7}$$

to the state

$$|\psi_i\rangle = \prod_a^{\otimes} \left(\cos\Omega\tau|g\rangle + e^{ikx_a}\sin\Omega\tau|e\rangle\right). \tag{7.8}$$

In Ramsey spectroscopy, one lets $|\psi_i\rangle$ evolve for an interrogation time t to $\rho(t)$, applies the inverse unitary operation $U^\dagger$, and then measures the signal $\tilde{S} = \langle\sum_a \sigma_a^z\rangle$ on the final system ρ_f. $\tilde{S}$ corresponds to the total population inversion. We can rewrite $\tilde{S}$ as

$$\begin{aligned} \tilde{S} &= \mathrm{Tr}\left(\sum_a \sigma_a^z U^\dagger \rho(t) U\right) \\ &= \mathrm{Tr}\left(\sum_a U\sigma_a^z U^\dagger \rho(t)\right) \\ &= \cos 2\Omega\tau\langle\textstyle\sum_a \sigma_a^z\rangle - 2\sin 2\Omega\tau \,\mathrm{Re}\langle\textstyle\sum_a e^{ikx_a}\sigma_a^+\rangle, \end{aligned} \tag{7.9}$$

where the averages denoted above now apply to the system $\rho(t)$.

In the case of N non-interacting, independently decaying atoms,

$$\langle\sigma_a^z\rangle = -1 + e^{-\Gamma t}\left(1 - \cos 2\Omega\tau\right), \tag{7.10}$$

$$\langle e^{ikx_a}\sigma_a^+\rangle = \frac{1}{2}\sin 2\Omega\tau e^{-(i\delta+\Gamma/2)t}, \tag{7.11}$$

which gives a corresponding signal

$$\tilde{S} = -N\left(\cos 2\Omega\tau\left(1-e^{-\Gamma t}\right) + e^{-\Gamma t}\cos^2 2\Omega\tau + e^{-\Gamma t/2}\sin^2 2\Omega\tau\cos\delta t\right). \tag{7.12}$$

One can see that there is a peak in the signal around $\delta = 0$. Determination of this peak allows one to find the frequency of the transition. One can note two important points about $\tilde{S}$. The contrast in $\tilde{S}$ with respect to δ is maximized when a "perfect" $\pi/2$ pulse is applied, *i.e.*, when $\Omega\tau = \pi/4$. Furthermore, the contribution to $\tilde{S}$ due to $\langle\sigma_a^z\rangle$ in Eq. (7.9) is independent of δ and thus plays no role in determination of the resonance line. Thus, one is motivated to define an effective signal S that consists of the part of $\tilde{S}$ that is actually used to determine the line:

$$S = -2\sin 2\Omega\tau \mathrm{Re}\langle\textstyle\sum_a e^{ikx_a}\sigma_a^+\rangle. \tag{7.13}$$

The equation above states that from a theoretical standpoint, determination of the resonance line by measuring the population inversion after the second Ramsey pulse is equivalent to measuring the real part of $\langle e^{ikx_a}\sigma_a^+\rangle$ directly before the second pulse.

7.3.2 Effect of interactions

Solving for S exactly in the presence of dipole-dipole interactions appears to be quite a difficult task. Our approach then is to solve for S as a perturbative expansion in Γ. In particular, we use the expansions

$$\langle\sigma_a^+\rangle = \langle\sigma_a^+\rangle^{(0)} + \Gamma\langle\sigma_a^+\rangle^{(1)} + \Gamma^2\langle\sigma_a^+\rangle^{(2)} + O(\Gamma^3), \tag{7.14}$$

$$\langle\sigma_a^z\sigma_b^+\rangle = \langle\sigma_a^z\sigma_b^+\rangle^{(0)} + \Gamma\langle\sigma_a^z\sigma_b^+\rangle^{(1)} + O(\Gamma^2), \tag{7.15}$$

and equate terms of equal powers of Γ in Eqs. (7.4) and (7.5). Here, we have solved for $\langle\sigma_a^+\rangle$ to second order in Γ, which requires us to solve for $\langle\sigma_a^z\sigma_b^+\rangle$ to first order in Γ. The solution with appropriate initial conditions is

$$\begin{aligned}\langle\sigma_a^+\rangle &= \frac{1}{2}e^{-ikx_a}\sin(2\Omega\tau)e^{-(i\delta+\gamma/2)t}\left[1-\frac{\Gamma t}{2}(1+C_a)+\frac{(\Gamma t)^2}{8}(1+C_a)+\right.\\ &\left.\frac{\Gamma^2}{2\gamma^2}\sum_{b\neq a}\left(f(k\mathbf{r}_{ab})-ig(k\mathbf{r}_{ab})\right)\left(A_{ab}\gamma^2t^2-2B_{ab}\left(e^{-\gamma t}+\gamma t-1\right)\right)\right], \qquad (7.16)\end{aligned}$$

where

$$\begin{aligned}A_{ab} &= -\frac{3}{4}e^{ik(x_a-x_b)}\cos(2\Omega\tau)+\frac{1}{2}e^{ik(x_a-x_b)}\\ &+\frac{1}{4}\left(f(k\mathbf{r}_{ab})+ig(k\mathbf{r}_{ab})\right)-\frac{1}{2}f(k\mathbf{r}_{ab})\cos(2\Omega\tau)\\ &-\frac{1}{4}\sum_{j\neq a,b}\left(f(k\mathbf{r}_{bj})-ig(k\mathbf{r}_{bj})\right)e^{ik(x_a-x_j)}\cos^2(2\Omega\tau), \qquad (7.17)\\ B_{ab} &= \frac{1}{4}e^{ik(x_a-x_b)}\sin^2(2\Omega\tau)\sum_{j\neq a,b}\left(f(k\mathbf{r}_{aj})\cos kx_{aj}+g(k\mathbf{r}_{aj})\sin kx_{aj}\right), \qquad (7.18)\\ C_a &= \sum_{b\neq a}\left(f(k\mathbf{r}_{ab})-ig(k\mathbf{r}_{ab})\right)e^{ik(x_a-x_b)}\cos 2\Omega\tau. \qquad (7.19)\end{aligned}$$

Eq. (7.16) is correct to every order of γ. Eqs. (7.13) and (7.16) can be evaluated numerically for a given lattice configuration and number of atoms. To illustrate the general features of the shift, however, we now make the following simplifications. We expand Eq. (7.16) to lowest order in γ. We also assume that the Ramsey pulses are nearly perfect $\pi/2$ pulses, *i.e.*, $\cos 2\Omega\tau = \epsilon \ll 1$. We then keep terms like $\epsilon\Gamma t$ but ignore terms like $\epsilon\Gamma^2t^2$. With these simplifications,

$$\langle\sigma_a^+\rangle \approx \frac{1}{2}e^{-ikx_a}\sin(2\Omega\tau)e^{-i\delta t}\left(1-\frac{\Gamma t}{2}+\frac{(\Gamma t)^2}{8}-\phi_a\right), \qquad (7.20)$$

where

$$\phi_a = \sum_{b\neq a}\left(f(k\mathbf{r}_{ab})-ig(k\mathbf{r}_{ab})\right)e^{ik(x_a-x_b)}\left(\frac{\Gamma t}{2}\cos(2\Omega\tau)+\frac{(\Gamma t)^2}{4}\right(1+$$

$$\frac{1}{2}\left(f(k\mathrm{r}_{ab})+ig(k\mathrm{r}_{ab})\right)e^{-ik(x_a-x_b)}$$
$$+\frac{1}{2}\sum_{j\neq a,b}\left(f(k\mathrm{r}_{aj})\cos kx_{aj}+g(k\mathrm{r}_{aj})\sin kx_{aj}\right)\Bigg)\Bigg) \tag{7.21}$$

The first three terms in the parentheses of Eq. (7.20) are a result of expanding the $e^{-\Gamma t/2}$ term that appears in the result for independent atoms, given in Eq. (7.12). This is just the decay of the signal one would get from independent spontaneous emission. The last term in the parentheses is a correction due to atom-atom interactions. Plugging this result into Eq. (7.13), we find that

$$S \approx -\sin^2 2\Omega\tau\left((\cos\delta t)\left(N-\frac{N\Gamma t}{2}+\frac{N(\Gamma t)^2}{8}-\sum_a \mathrm{Re}\phi_a\right)-(\sin\delta t)\sum_a \mathrm{Im}\phi_a\right). \tag{7.22}$$

Because of the asymmetric $\sin\delta t$ term now appearing in S, one immediately sees that dipole-dipole interactions introduce a shift δ_p in the Ramsey fringes, which can be found by solving $\partial S/\partial\delta=0$. Suppose that the inequalities $\delta_p t \ll 1, \Gamma t \ll 1$ are satisfied. Under these conditions, a simple expression for δ_p results:

$$\frac{\delta_p}{\Gamma} \approx \frac{1}{N}\sum_a\sum_{b\neq a}\left(g(k\mathrm{r}_{ab})\cos kx_{ab}-f(k\mathrm{r}_{ab})\sin kx_{ab}\right)\times\left(\frac{1}{2}\cos 2\Omega\tau+\right.$$
$$\left.\frac{\Gamma t}{4}\left(1+\frac{1}{2}\sum_{j\neq a,b}\left(f(k\mathrm{r}_{aj})\cos kx_{aj}+g(k\mathrm{r}_{aj})\sin kx_{aj}\right)\right)\right). \tag{7.23}$$

7.3.3 Interpretation of shift

The shift given by Eq. (7.23) yields a simple interpretation. In anticipation of future analysis, we write δ_p as

$$\frac{\delta_p}{\Gamma}=\frac{1}{N}\sum_a\sum_{b\neq a}\bar{U}_{ab}\times\left(\frac{1}{2}\epsilon+\frac{\Gamma t}{4}\tilde{\Gamma}_a\right), \tag{7.24}$$

where

$$\begin{aligned}
\tilde{U}_{ab} &= g(k\mathbf{r}_{ab})\cos kx_{ab} - f(k\mathbf{r}_{ab})\sin kx_{ab}, && (7.25)\\
\epsilon &= \cos 2\Omega\tau, && (7.26)\\
\tilde{\Gamma}_a &= 1 + \frac{1}{2}\sum_{j\neq a,b}\left(f(k\mathbf{r}_{aj})\cos kx_{aj} + g(k\mathbf{r}_{aj})\sin kx_{aj}\right). && (7.27)
\end{aligned}$$

We will see that $\tilde{U}_{ab}$ is a dimensionless quantity proportional to the classical interaction energy between two oscillating dipoles, ϵ is a parameter characterizing the error in the Ramsey pulses, and $\tilde{\Gamma}_a$ is a dimensionless quantity characterizing cooperative decay of the system.

To show the meaning of the $\tilde{U}_{ab}$ term in Eq. (7.24), consider the interaction between a classical, oscillating dipole at $\mathbf{r}_a$ excited with phase $e^{i(kx_a-\omega t)}$ and the field incident on it due to a classical, oscillating dipole at $\mathbf{r}_b$ excited with phase $e^{i(kx_b-\omega t)}$. We assume that both dipoles are oriented along the z-axis and that their magnitudes d are given by $\Gamma = k_0^3 d^2/3\pi\epsilon_0\hbar$. The classical interaction energy between dipole a and the incident field is given by $U_{ab} = -(1/2)\mathrm{Re}(\mathbf{d}_a\cdot\mathbf{E}_b^*(\mathbf{r}_a))$. The field at $\mathbf{r}_a$ due to dipole b is [54]:

$$E_z(\mathbf{r}_a) = e^{i(kx_b-\omega t)}\frac{k^3 d}{4\pi\epsilon_0}e^{ikr}\left(\frac{\sin^2\theta}{kr} + (3\cos^2\theta - 1)\left(\frac{1}{(kr)^3} - \frac{i}{(kr)^2}\right)\right), \qquad (7.28)$$

where $r = |\mathbf{r}_b - \mathbf{r}_a|$. Now using the definitions in Eq. (7.3), the interaction energy can readily be rewritten as:

$$\begin{aligned}
U_{ab} &= -\frac{1}{2}\mathrm{Re}(\mathbf{d}_a\cdot\mathbf{E}_b^*(\mathbf{r}_a)) = \frac{\hbar\Gamma}{4}\left(g(k\mathbf{r}_{ab})\cos kx_{ab} - f(k\mathbf{r}_{ab})\sin kx_{ab}\right) && (7.29)\\
&= \frac{\hbar\Gamma}{4}\tilde{U}_{ab}. && (7.30)
\end{aligned}$$

One then sees that this indeed corresponds to the first term of Eq. (7.24).

Although the $\tilde{U}_{ab}$ term in Eq. (7.24) resembles a classical interaction energy, the terms in parentheses reflect the quantum mechanical nature of the system. There is a contribution to the shift that is zeroth order in the interrogation time t and proportional to ϵ. One notes that for perfect $\pi/2$ Ramsey pulses, $\epsilon = 0$. Thus, the zeroth order is due to error in the Ramsey pulse. This can be understood by considering Eq. (7.4). One sees that the interaction terms only influence evolution of the coherence through the term $\langle \sigma_a^z \sigma_b^+ \rangle$. For a perfect $\pi/2$ pulse, this term is initially zero, and in this case, interactions cannot affect the measurement at short times.

Even if a perfect $\pi/2$ pulse is applied, there is an additional contribution to the shift that is first order in t and whose strength is given by $\tilde{\Gamma}_a$. The intuition behind this is also straightforward. Even if $\langle \sigma_a^z \sigma_b^+ \rangle$ is initially zero, decay of the excited state will eventually evolve $\langle \sigma_a^z \rangle$ away from zero and back towards its equilibrium value of -1. Once $\langle \sigma_a^z \sigma_b^+ \rangle$ is nonzero, interactions can influence evolution of $\langle \sigma_a^+ \rangle$. The rate of decay is characterized by $\tilde{\Gamma}_a$. The first term in $\tilde{\Gamma}_a$ is the contribution from independent decay of the atoms back to the ground state. The second contribution involves a sum over other atoms and represents a correction due to the fact that the decay process may in fact be cooperative (e.g., superradiance). One can easily verify that the contribution from atom j is proportional to $\mathrm{Im}(\mathbf{d}_a \cdot \mathbf{E}_j^*(\mathbf{r}_a))$:

$$\mathrm{Im}(\mathbf{d}_a \cdot \mathbf{E}_j^*(\mathbf{r}_a)) \propto f(k\mathbf{r}_{aj}) \cos(k x_{aj}) + g(k\mathbf{r}_{aj}) \sin(k x_{aj}). \tag{7.31}$$

This reflects the well-known result that the atomic inversion $\langle \sigma_a^z \rangle$ is driven by the dipole component in quadrature with the incident field.

7.4 Generalization of results

7.4.1 Imperfect filling of lattice sites

Experimentally, knowing the exact number of atoms in the lattice and achieving a filling factor of one atom per lattice site are difficult tasks. Most likely, one can experimentally determine the density $\rho(\mathbf{r})$ of atoms in the lattice, such that the probability of occupation at any particular site a is $P(\mathbf{r}_a) = \rho(\mathbf{r}_a)V$, where V is the volume of a unit cell. It is straightforward to modify Eq. (7.23) to the case of imperfect filling. For simplicity, we only consider the shift that is zeroth order in t. This shift can be written

$$\begin{aligned} \frac{\delta_p}{\Gamma} &= \frac{1}{N}\sum_{a}\sum_{b\neq a}\frac{1}{2}\cos 2\Omega\tau\left(g(k\mathbf{r}_{ab})\cos kx_{ab} - f(k\mathbf{r}_{ab})\sin kx_{ab}\right) && (7.32)\\ &= \frac{2}{N}\sum_{\text{pairs}}\frac{1}{2}\cos 2\Omega\tau\; g(k\mathbf{r}_{ab})\cos kx_{ab} && (7.33)\\ &= \frac{1}{2}\cos 2\Omega\tau\sum_{\mathbf{R}\neq 0}U(\mathbf{R})\frac{N(\mathbf{R})}{N}, && (7.34) \end{aligned}$$

where $U(\mathbf{R}) = g(k\mathbf{R})\cos kR_x$, $\{\mathbf{R}\}$ denotes the set of direct lattice vectors, and $N(\mathbf{R})$ is the number of pairs of atoms separated by $\mathbf{R}$. In the derivation above we have utilized the fact that $\sin kx_{ab} = -\sin kx_{ba}$ to cancel the sum of $f(k\mathbf{r}_{ab})\sin kx_{ab}$. In a realistic scenario, one neither knows $N(\mathbf{R})$ nor N exactly. In this case, one must solve instead for the ensemble average $\langle\delta_p\rangle$ and the variance $\Delta\delta_p$. For large N, one can safely pull the factor of N out of the ensemble average:

$$\langle\tfrac{N(\mathbf{R})}{N}\rangle \approx \frac{\langle N(\mathbf{R})\rangle}{\langle N\rangle}. \tag{7.35}$$

With this simplification,

$$\begin{aligned}
\frac{\langle\delta_p\rangle}{\Gamma} &= \frac{1}{2\langle N\rangle}\cos 2\Omega\tau \sum_{\mathbf{R}\neq 0} U(\mathbf{R})\langle N(\mathbf{R})\rangle && (7.36)\\
&= \frac{1}{2\langle N\rangle}\cos 2\Omega\tau \sum_{\mathbf{R}\neq 0} U(\mathbf{R}) \int d\mathbf{r}\rho(\mathbf{r})\rho(\mathbf{r}+\mathbf{R})V, && (7.37)\\
\frac{(\Delta\delta_p)^2}{\Gamma^2} &= \left(\frac{1}{2\langle N\rangle}\cos 2\Omega\tau\right)^2 \sum_{\mathbf{R},\mathbf{R}'\neq 0} U(\mathbf{R})U(\mathbf{R}')\langle N(\mathbf{R})N(\mathbf{R}')\rangle \\
&\quad - \left(\frac{1}{2\langle N\rangle}\cos 2\Omega\tau \sum_{\mathbf{R}\neq 0} U(\mathbf{R})\langle N(\mathbf{R})\rangle\right)^2 && (7.38)\\
&= \left(\frac{1}{2\langle N\rangle}\cos 2\Omega\tau\right)^2 \Bigg[\sum_{\mathbf{R},\mathbf{R}'\neq 0} U(\mathbf{R})U(\mathbf{R}') \int d\mathbf{r}\rho(\mathbf{r})\rho(\mathbf{r}+\mathbf{R})V^2 \times \\
&\quad \Big((1-\rho(\mathbf{r})V)\rho(\mathbf{r}+\mathbf{R}') + (1-\rho(\mathbf{r}+\mathbf{R})V)\rho(\mathbf{r}+\mathbf{R}+\mathbf{R}') \\
&\quad + (1-\rho(\mathbf{r})V)\rho(\mathbf{r}-\mathbf{R}') + (1-\rho(\mathbf{r}+\mathbf{R})V)\rho(\mathbf{r}+\mathbf{R}-\mathbf{R}')\Big) \\
&\quad +2\sum_{\mathbf{R}\neq 0} U(\mathbf{R})^2 \int d\mathbf{r}\rho(\mathbf{r})\rho(\mathbf{r}+\mathbf{R})V\Big((1-\rho(\mathbf{r})\rho(\mathbf{r}+\mathbf{R})V^2) \\
&\quad -(1-\rho(\mathbf{r})V)\rho(\mathbf{r}+\mathbf{R})V - \rho(\mathbf{r})(1-\rho(\mathbf{r}+\mathbf{R})V)V\Big)\Bigg]. && (7.39)
\end{aligned}$$

Eq. (7.39) appears complicated, but the meaning of each term is quite simple. To calculate the average shift in Eq. (7.37), one must evaluate $\langle N(\mathbf{R})\rangle$. To do this, one must perform a sum over $\mathbf{r}_i$ of the probability that the sites $\mathbf{r}_i$ and $\mathbf{r}_i + \mathbf{R}$ are both occupied. To find the variance, one must calculate quantities like $\langle N(\mathbf{R})N(\mathbf{R}')\rangle$, and thus the probability that the sites $\mathbf{r}_i$, $\mathbf{r}_i + \mathbf{R}$, $\mathbf{r}_j$, and $\mathbf{r}_j + \mathbf{R}'$ are all occupied. When these four points are distinct, the probability is simply a product of the probabilities of each point being occupied. This is untrue when one or more of the points overlap. The terms in Eq. (7.39) represent corrections due to these overlaps. The product $\rho(\mathbf{r})\rho(\mathbf{r}+\mathbf{R})V^2((1-\rho(\mathbf{r})V)\rho(\mathbf{r}+\mathbf{R}')$, for example, is due to the overlap of $\mathbf{r}_i$ and $\mathbf{r}_j$.

7.4.2 Generalization to multilevel atoms

Our results derived thus far are for the specific case of two-level atoms. One might consider more complicated level structures, such as the case of an atom with a single ground and multiple excited states. A simple argument shows that Eq. (7.23) remains correct to the lowest nontrivial order in t. If multiple excited states are present in addition to the one that is initially excited, the equation of motion for $\langle \sigma^+_{a\,\text{clock}} \rangle$ will contain additional terms like $\langle \sigma^z_a \sigma^+_{b\,\text{other}} \rangle$, where the subscript "clock" refers to the clock transition and "other" refers to other excited state levels. Initially, $\langle \sigma^+_{b\,\text{other}} \rangle = 0$ and increases at a rate proportional to Γt. At short times then $\langle \sigma^z_a \sigma^+_{b\,\text{other}} \rangle$ is smaller than $\langle \sigma^z_a \sigma^+_{b\,\text{clock}} \rangle$ by an amount proportional to Γt, and the evolution of $\langle \sigma^+_{a\,\text{clock}} \rangle$ will be dominated by the clock transition. Thus, if imperfections in the Ramsey pulse constitute the major source of shift, the multiple excited states will contribute an additional source of shift that is first order in Γt. If decay of the clock excited state constitutes the major source, the multiple excited states will contribute a shift that is of order $\Gamma^2 t^2$.

7.5 Analysis of results

Eq. (7.23) or Eqs. (7.37) and (7.39) can be evaluated numerically for a given lattice configuration and number of atoms. To extract the salient features of the shift, we note that the zeroth-order shift in t in Eq. (7.23) essentially consists of adding together the classical dipole interaction energies $\tilde{U}_{ab} \propto -\mathrm{Re}(\mathbf{d}_a \cdot \mathbf{E}^*_b(\mathbf{r}_a))$. For a generic configuration of atoms, the phases of the dipole fields incident on a given dipole a tend to interfere. For certain configurations though, it is possible that the fields will add constructively along some direction of propagation $\mathbf{k}$. Near these configurations one will expect large shifts to result. The condition for constructive interference between radiated dipole fields is similar to that of Bragg scattering in a crystal, and is readily found to occur when

$$|\tilde{\mathrm{G}}| = k_0, \tag{7.40}$$

where $\tilde{\mathrm{G}} = (G_x - k_0, G_y, G_z)$ and G is a reciprocal lattice vector. This condition can be rewritten as

$$|\mathrm{G}|^2 = 2k_0 G_x. \tag{7.41}$$

Numerical results indicate that peaks in the line shift do indeed occur when condition (7.41) is nearly satisfied.

One can easily derive the scaling laws for the line shift in these resonant configurations. Define a dimensionless parameter β related to the density of atoms by $n = 1/(\beta\lambda)^3$. β characterizes the spacing between neighbors in the lattice. In a resonant configuration, the electric fields add constructively, and the total electric field experienced by an atom is approximately

$$E \sim \int d^3\mathrm{r}\frac{n}{kr} \sim \int_0^L dr\frac{nr}{k} \sim \frac{L^2}{k(\beta\lambda)^3}, \tag{7.42}$$

where L is the linear size of the system. For N total atoms, $L \sim \beta\lambda N^{1/3}$. Then

$$\frac{\delta_p}{\Gamma} \sim \frac{N^{2/3}}{\beta}. \tag{7.43}$$

Experimentally, one has freedom to choose the orientation of the trapping lasers. The control parameters can be parameterized by a set of variables $\{\alpha\}$, which will also determine the reciprocal lattice vectors $\mathrm{G}(\{\alpha\})$. One can then find solutions $\{\alpha_0\}$

of Eq. (7.41) corresponding to configurations with large line shifts. In the parameter space between two sets of solutions $\{\alpha_0\}$, one can numerically find configurations where the shift is significantly reduced.

7.6 Numerical example

As an illustration of our results, we consider ^{87}Sr atoms trapped in a lattice formed by six interfering beams, as shown in Fig. 7.1. For ^{87}Sr, the magic wavelength of the trapping lasers is roughly $\lambda_L = 1.07\lambda_0$ [49], and one can vary the angle θ between the propagation vectors of the trapping beams. The resulting lattice is tetragonal, with lattice constants of $a_x = \pi/k_L \sin\theta$, $a_y = \pi/k_L \cos\theta$, and $a_z = \pi/k_L$ along the x, y, and z, respectively. The lattice constants are plotted in Fig. 7.2. The basis of the reciprocal lattice then has lengths $G_x = 2k_L \sin\theta$, $G_y = 2k_L \cos\theta$, and $G_z = 2k_L$. We have ignored the effect of atomic back-action [36, 174] on the trapping fields, whereby scattering of light by the atoms introduces phases that might modify the lattice constants. Such effects are expected to be more severe in red-detuned lattices, where atoms lie in the antinodes of the potential, and with increasing atomic density. Taking into account this back-action does not modify our results, except that now the lattice constants must be solved self-consistently.

Using Eq. (7.41) we can find values of θ where constructive interference causes the shifts to be large. We focus on two specific solutions, $\theta_0/\pi = 0.116$ and $\theta_0/\pi = 0.180$. For our system we take $\langle N \rangle = 10^5$ atoms and a uniform filling factor of $P = \rho(\mathrm{r})V = 0.05$ for $r < r_0$, and zero density for $r > r_0$. The critical value r_0 is determined by

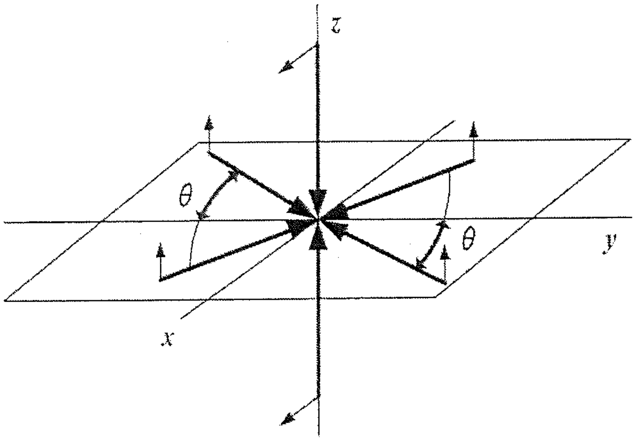

Figure 7.1: The lattice studied in our numerical example is formed by the interference of six laser beams. Four beams are oriented along the x-y plane, each making an angle $\pm\theta$ with the y-axis and polarized along z. Two additional beams run parallel to z and are polarized along x.

the equation

$$r_0 = \left(\frac{3\langle N\rangle V}{4\pi P}\right)^{1/3}. \tag{7.44}$$

Fig. 7.3 gives the quantity $2\langle\delta_p\rangle/\Gamma\cos(2\Omega\tau)$ as a function of θ. Peaks in the shift are clearly visible at the points θ_0 that were calculated analytically. One also finds that there is a value of θ in between those two peaks where the average shift $\langle\delta_p\rangle$ vanishes, which occurs around $\theta/\pi = 0.125$. At this good point, one can use Eq. (7.39) to calculate the variance in the expected shift. For large numbers of atoms, Eq. (7.39) cannot be evaluated exactly without extensive computational resources. With a small filling factor $\rho V \ll 1$, however, we can estimate that the major contribution to the variance results from the ρ^2 terms, while the ρ^3 terms remain negligible. With this approximation, we find that the variance

$$\frac{\Delta\delta_p}{\Gamma} \approx \frac{1}{2}\cos(2\Omega\tau)\times 3.1\times 10^{-3}. \tag{7.45}$$

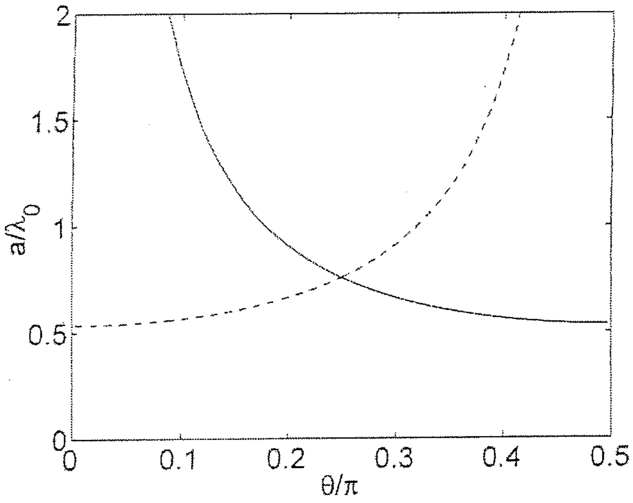

Figure 7.2: The lattice constants for the six-beam lattice are plotted in units of λ_0 as functions of θ. We assume that the ratio of the resonant wavevector to that of the trapping lasers is $k_0/k_L = 1.07$, consistent with the magic wavelength of ^{87}Sr. The solid line represents the lattice constant along x, the dashed line along y, and the constant dotted line along z.

Experimentally, there will be additional sources of error that result from not knowing $\rho(\mathrm{r})$ perfectly, errors in the configuration of the trapping lasers, and from the effects of atomic back-action on the lattice constants. Nonetheless, it appears that the error due to dipole-dipole interactions can be made quite small by appropriately designing the lattice.

It should also be noted that the line shift can be very large in the constructive interference configurations. This is perhaps a surprising result, and occurs because the spatial ordering of the atoms allows the interactions to behave constructively. In *Fig. 7.4, we plot the line shift to zeroth order in t as a function of θ, for a system* of $\langle N \rangle = 10^6$ atoms and a filling factor of one. Even in the limit $t \to 0$, one can see that it is possible to achieve shifts of order $\langle \delta_p \rangle \sim 10\Gamma$ at one of the bad configurations.

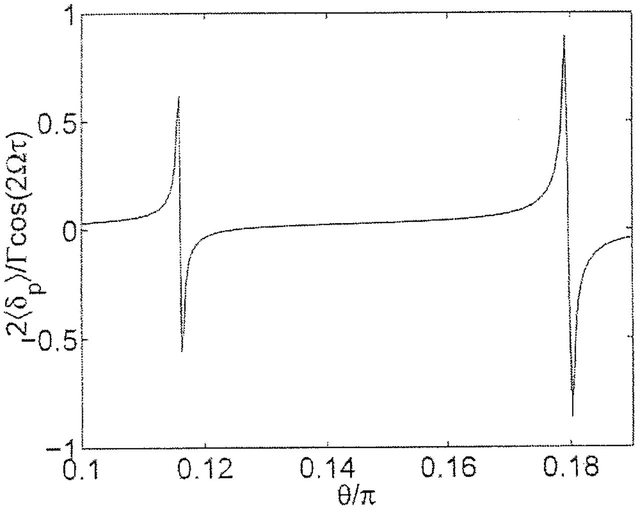

Figure 7.3: The calculated shifts for the six-beam lattice as a function of θ. The system consists of $\langle N \rangle = 10^5$ atoms with a filling factor of 0.05.

For extended interrogation times, one expects this line shift to become much larger, since the constructive interference also leads to superradiant decay, and thus a large contribution to the shift that is first order in t.

7.7 Conclusion

We have derived an equation for the line shift measured in Ramsey spectroscopy due to dipole-dipole interactions. We find that the lattice geometry strongly affects the magnitude of the shift, and is peaked in lattice configurations where the interactions between atoms add constructively. Because of the spatial ordering in the lattice, the shift can be quite large in these resonant configurations. By tuning the lattice between two of these configurations, one can significantly reduce the errors due to interactions.

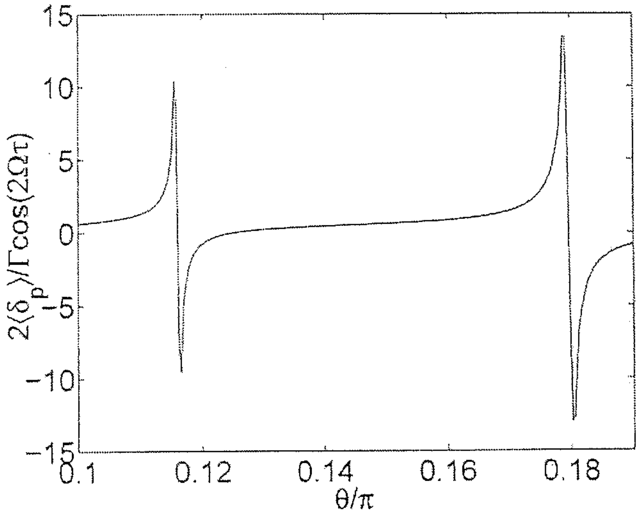

Figure 7.4: The calculated shifts for the six-beam lattice as a function of θ. The system consists of $\langle N \rangle = 10^6$ atoms with a filling factor of 1.

While the resonant configurations might be bad for clock applications, it might be worthwhile to study these configurations further. The strong, constructive interactions and the possibility of dynamically tuning the lattice geometry might be useful for other applications such as quantum information processing.

Bibliography

[1] Miller, R. *et al.* Trapped atoms in cavity QED: Coupling quantized light and matter. *J. Phys. B* **38**, S551–S565 (2005).

[2] Walther, H., Varcoe, B. T. H., Englert, B.-G. & Becker, T. Cavity quantum electrodynamics. *Rep. Prog. Phys.* **69**, 1325–1382 (2006).

[3] Haroche, S. & Raimond, J. M. *Exploring the quantum: atoms, cavities, and photons* (Oxford University Press, New York, 2006).

[4] Vahala, K. (ed.) *Optical Microcavities* (World Scientific, Singapore, 2004).

[5] Brune, M. *et al.* Quantum Rabi Oscillation: A Direct Test of Field Quantization in a Cavity. *Phys. Rev. Lett.* **76**, 1800–1803 (1996).

[6] Michler, P. *et al.* A Quantum Dot Single-Photon Turnstile Device. *Science* **290**, 2282–2285 (2000).

[7] Pelton, M. *et al.* Efficient Source of Single Photons: A Single Quantum Dot in a Micropost Microcavity. *Phys. Rev. Lett.* **89**, 233602 (2002).

[8] McKeever, J. *et al.* Deterministic Generation of Single Photons from One Atom Trapped in a Cavity. *Science* **303**, 1992–1994 (2004).

[9] Birnbaum, K. M. *et al.* Photon blockade in an optical cavity with one trapped atom. *Nature* **436**, 87–90 (2005).

[10] Cirac, J. I., Zoller, P., Kimble, H. J. & Mabuchi, H. Quantum State Transfer and Entanglement Distribution among Distant Nodes in a Quantum Network. *Phys. Rev. Lett.* **78**, 3221–3224 (1997).

[11] Duan, L.-M. & Kimble, H. J. Scalable Photonic Quantum Computation through Cavity-Assisted Interactions. *Phys. Rev. Lett.* **92**, 127902 (2004).

[12] Hartmann, M. J., Brandão, F. G. S. L. & Plenio, M. B. Strongly interacting polaritons in coupled arrays of cavities. *Nature Phys.* **2**, 849–855 (2006).

[13] Greentree, A. D., Tahan, C., Cole, J. H. & Hollenberg, L. C. L. Quantum phase transitions of light. *Nature Phys.* **2**, 856–861 (2006).

[14] Angelakis, D. G., Santos, M. F. & Bose, S. Photon-blockade-induced Mott transitions and XY spin models in coupled cavity arrays. *Phys. Rev. A* **76**, 031805 (2007).

[15] Na, N., Utsunomiya, S., Tian, L. & Yamamoto, Y. Strongly correlated polaritons in a two-dimensional array of photonic crystal microcavities. *Phys. Rev. A* **77**, 031803 (2008).

[16] Hartmann, M. J. & Plenio, M. B. Strong Photon Nonlinearities and Photonic Mott Insulators. *Phys. Rev. Lett.* **99**, 103601 (2007).

[17] Zayats, A. V. & Smolyaninov, I. I. Near-field photonics: surface plasmon polaritons and localized surface plasmons. *J. Opt. A* **5**, S16–S50 (2003).

[18] Maier, S. A. *Plasmonics: fundamentals and applications* (Springer-Verlag, New York, 2006).

[19] Sakoda, K. *Optical Properties of Photonic Crystals* (Springer, New York, 2001).

[20] Tong, L. *et al.* Subwavelength-diameter silica wires for low-loss optical wave guiding. *Nature* **426**, 816–819 (2003).

[21] Smith, D. R., Pendry, J. B. & Wiltshire, M. C. K. Metamaterials and Negative Refractive Index. *Science* **305**, 788–792 (2004).

[22] Yablonovitch, E. Inhibited Spontaneous Emission in Solid-State Physics and Electronics. *Phys. Rev. Lett.* **58**, 2059–2062 (1987).

[23] John, S. Strong localization of photons in certain disordered dielectric superlattices. *Phys. Rev. Lett.* **58**, 2486–2489 (1987).

[24] Ebbesen, T. W., Lezec, H. J., Ghaemi, H. F., Thio, T. & Wolff, P. A. Extraordinary optical transmission through sub-wavelength hole arrays. *Nature* **391**, 667–669 (1998).

[25] Thio, T., Pellerin, K. M., Linke, R. A., Lezec, H. J. & Ebbesen, T. W. Enhanced light transmission through a single subwavelength aperture. *Opt. Lett.* **26**, 1972–1974 (2001).

[26] Pendry, J. B. Negative Refraction Makes a Perfect Lens. *Phys. Rev. Lett.* **85**, 3966–3969 (2000).

[27] Pendry, J. B., Schurig, D. & Smith, D. R. Controlling Electromagnetic Fields. *Science* **312**, 1780–1782 (2006).

[28] Kneipp, K. *et al.* Single Molecule Detection Using Surface-Enhanced Raman Scattering (SERS). *Phys. Rev. Lett.* **78**, 1667–1670 (1997).

[29] Nie, S. & Emory, S. R. Probing Single Molecules and Single Nanoparticles by Surface-Enhanced Raman Scattering. *Science* **275**, 1102–1106 (1997).

[30] Oldenburg, S. J., Genick, C. C., Clark, K. A. & Schultz, S. A. Base pair mismatch recognition using plasmon resonant particle labels. *Anal. Biochem.* **309**, 109–116 (2002).

[31] Smolyaninov, I. I., Elliott, J., Zayats, A. V. & Davis, C. C. Far-Field Optical Microscopy with a Nanometer-Scale Resolution Based on the In-Plane Image Magnification by Surface Plasmon Polaritons. *Phys. Rev. Lett.* **94**, 057401 (2005).

[32] Zayats, A. V., Elliott, J., Smolyaninov, I. I. & Davis, C. C. Imaging with short-wavelength surface plasmon polaritons. *Appl. Phys. Lett.* **86**, 151114 (2005).

[33] Brongersma, M. L., Hartman, J. W. & Atwater, H. A. Electromagnetic energy transfer and switching in nanoparticle chain arrays below the diffraction limit. *Phys. Rev. B* **62**, R16356–R16359 (2000).

[34] Bozhevolnyi, S. I., Volkov, V. S., Devaux, E., Laluet, J.-Y. & Ebbesen, T. W. Channel plasmon subwavelength waveguide components including interferometers and ring resonators. *Nature* **440**, 508–511 (2006).

[35] Landsberg, P. T. *Solid state theory: methods and applications* (Wiley-Interscience, New York, 1969).

[36] Deutsch, I. H., Spreeuw, R. J. C., Rolston, S. L. & Phillips, W. D. Photonic band gaps in optical lattices. *Phys. Rev. A* **52**, 1394–1410 (1995).

[37] Kopp, V. I., Fan, B., Vithana, H. K. M. & Genack, A. Z. Low-threshold lasing at the edge of a photonic stop band in cholesteric liquid crystals. *Opt. Lett.* **23**, 1707–1709 (1998).

[38] Kosaka, H. *et al.* Superprism phenomena in photonic crystals. *Phys. Rev. B* **58**, R10096–R10099 (1998).

[39] Sigalas, M. M., McCalmont, J. S., Ho, K.-M. & Tuttle, G. Theoretical and experimental study of silicon-based angular filters. *Appl. Phys. Lett.* **68**, 3525–3527 (1996).

[40] Scalora, M., Dowling, J. P., Bowden, C. M. & Bloemer, M. J. Optical Limiting and Switching of Ultrashort Pulses in Nonlinear Photonic Band Gap Materials. *Phys. Rev. Lett.* **73**, 1368–1371 (1994).

[41] Koenderink, A. F., Bechger, L., Schriemer, H. P., Lagendijk, A. & Vos, W. L. Broadband Fivefold Reduction of Vacuum Fluctuations Probed by Dyes in Photonic Crystals. *Phys. Rev. Lett.* **88**, 143903 (2002).

[42] Tong, L., Lou, J. & Mazur, E. Single-mode guiding properties of subwavelength-diameter silica and silicon wire waveguides. *Opt. Express* **12**, 1025–1035 (2004).

[43] Knight, J. C. Photonic crystal fibres. *Nature* **424**, 847–851 (2003).

[44] Nayak, K. P. *et al.* Optical nanofiber as an efficient tool for manipulating and probing atomic fluorescence. *Opt. Express* **15**, 5431–5438 (2007).

[45] Leon-Saval, S., Birks, T., Wadsworth, W., Russell, P. S. J. & Mason, M. Supercontinuum generation in submicron fibre waveguides. *Opt. Express* **12**, 2864–2869 (2004).

[46] Sumetsky, M., Dulashko, Y. & Hale, A. Fabrication and study of bent and coiled free silica nanowires: Self-coupling microloop optical interferometer. *Opt. Express* **12**, 3521–3531 (2004).

[47] Bhagwat, A. R. & Gaeta, A. L. Nonlinear optics in hollow-core photonic bandgap fibers. *Opt. Express* **16**, 5035–5047 (2008).

[48] Chang, D. E. *et al.* Crystallization of strongly interacting photons in a nonlinear optical fiber (2008). `e-print cond-mat/0712.1817`.

[49] Katori, H. Spectroscopy of strontium atoms in the Lamb-Dicke confinement. In Gill, P. (ed.) *Proceedings of the 6th Symposium on Frequency Standards and Metrology*, 323–330 (World Scientific, Singapore, 2002).

[50] Purcell, E. M. Spontaneous emission probabilities at radio frequencies. *Phys. Rev.* **69**, 681 (1946).

[51] Hecker, N. E., Höpfel, R. A., Sawaki, N., Maier, T. & Strasser, G. Surface plasmon-enhanced photoluminescence from a single quantum well. *Appl. Phys. Lett.* **75**, 1577–1579 (1999).

[52] Biteen, J. S., Lewis, N. S., Atwater, H. A., Mertens, H. & Polman, A. Spectral tuning of plasmon-enhanced silicon quantum dot luminescence. *Appl. Phys. Lett.* **88**, 131109 (2006).

[53] Mertens, H., Biteen, J. S., Atwater, H. A. & Polman, A. Polarization-Selective Plasmon-Enhanced Silicon Quantum-Dot Luminescence. *Nano Lett.* **6**, 2622–2625 (2006).

[54] Jackson, J. D. *Classical Electrodynamics, 3rd ed.* (John Wiley & Sons, New York, 1999).

[55] Stratton, J. A. *Electromagnetic theory, 1st ed.* (McGraw-Hill, New York, 1941).

[56] Johnson, P. B. & Christy, R. W. Optical Constants of the Noble Metals. *Phys. Rev. B* **6**, 4370–4379 (1972).

[57] Takahara, J., Yamagishi, S., Taki, H., Morimoto, A. & Kobayashi, T. Guiding of a one-dimensional optical beam with nanometer diameter. *Opt. Lett.* **22**, 475–477 (1997).

[58] Cao, Q. & Jahns, J. Azimuthally polarized surface plasmons as effective terahertz waveguides. *Opt. Express* **13**, 511–518 (2005).

[59] Klimov, V. V. & Ducloy, M. Spontaneous emission rate of an excited atom placed near a nanofiber. *Phys. Rev. A* **69**, 013812 (2004).

[60] Wylie, J. M. & Sipe, J. E. Quantum electrodynamics near an interface. *Phys. Rev. A* **30**, 1185–1193 (1984).

[61] Scheel, S., Knöll, L., Welsch, D.-G. & Barnett, S. M. Quantum local-field corrections and spontaneous decay. *Phys. Rev. A* **60**, 1590–1597 (1999).

[62] Lucke, W. S. Electric Dipoles in the Presence of Elliptic and Circular Cylinders. *J. Appl. Phys.* **22**, 14–19 (1951).

[63] Stockman, M. I. Nanofocusing of Optical Energy in Tapered Plasmonic Waveguides. *Phys. Rev. Lett.* **93**, 137404 (2004).

[64] García de Abajo, F. J. & Howie, A. Retarded field calculation of electron energy loss in inhomogeneous dielectrics. *Phys. Rev. B* **65**, 115418 (2002).

[65] van Enk, S. J., Cirac, J. I. & Zoller, P. Ideal Quantum Communication over Noisy Channels: A Quantum Optical Implementation. *Phys. Rev. Lett.* **78**, 4293–4296 (1997).

[66] Barclay, P. E., Srinivasan, K. & Painter, O. Design of photonic crystal waveguides for evanescent coupling to optical fiber tapers and integration with high-Q cavities. *J. Opt. Soc. Am. B* **20**, 2274–2284 (2003).

[67] Agassi, D. & George, T. F. Convergent scheme for light scattering from an arbitrary deep metallic grating. *Phys. Rev. B* **33**, 2393–2400 (1986).

[68] Rahman, T. S. & Maradudin, A. A. Effect of surface roughness on the image potential. *Phys. Rev. B* **21**, 504–521 (1980).

[69] Gong, Y. & Vučković, J. Design of plasmon cavities for solid-state cavity quantum electrodynamics applications. *Appl. Phys. Lett.* **90**, 033113 (2007).

[70] Tillin, M. D. & Sambles, J. R. Phonon assisted absorption in thin Ag films using surface plasmon-polaritons. *J. Phys.: Condens. Matter* **2**, 7055–7059 (1990).

[71] Holstein, T. Optical and Infrared Volume Absorptivity of Metals. *Phys. Rev.* **96**, 535–536 (1954).

[72] Holstein, T. Theory of transport phenomena in an electron-phonon gas. *Ann. Phys.* **29**, 410–535 (1964).

[73] Allen, P. B. Electron-Phonon Effects in the Infrared Properties of Metals. *Phys. Rev. B* **3**, 305–320 (1971).

[74] McKay, J. A. & Rayne, J. A. Temperature dependence of the infrared absorptivity of the noble metals. *Phys. Rev. B* **13**, 673–685 (1976).

[75] Wilson, A. H. *The Theory of Metals, 2nd ed.* (Cambridge University Press, London, 1953).

[76] Walsh, C. B. & Franses, E. I. Ultrathin PMMA films spin-coated from toluene solutions. *Thin Solid Films* **429**, 71–76 (2003).

[77] Ditlbacher, H. *et al.* Silver Nanowires as Surface Plasmon Resonators. *Phys. Rev. Lett.* **95**, 257403 (2005).

[78] Wiley, B., Sun, Y. & Xia, Y. Polyol Synthesis of Silver Nanostructures: Control of Product Morphology with Fe(II) or Fe(III) Species. *Langmuir* **21**, 8077–8080 (2005).

[79] Akimov, A. V. *et al.* Generation of single optical plasmons in metallic nanowires coupled to quantum dots. *Nature* **450**, 402–406 (2007).

[80] Sanders, A. W. *et al.* Observation of Plasmon Propagation, Redirection, and Fan-Out in Silver Nanowires. *Nano Lett.* **6**, 1822–1826 (2006).

[81] Chung, I., Witkoskie, J. B., Cao, J. & Bawendi, M. G. Description of the fluorescence intensity time trace of collections of CdSe nanocrystal quantum dots based on single quantum dot fluorescence blinking statistics. *Phys. Rev. E* **73**, 011106 (2006).

[82] Yamamoto, Y. & Imamoglu, A. *Mesoscopic Quantum Optics* (John Wiley & Sons, Inc., New York, 1999).

[83] Lounis, B., Bechtel, H. A., Gerion, D., Alivisatos, P. & Moerner, W. P. Photon antibunching in single CdSe/ZnS quantum dot fluorescence. *Chem. Phys. Lett.* **329**, 399–404 (2000).

[84] Dickson, R. M. & Lyon, L. A. Unidirectional Plasmon Propagation in Metallic Nanowires. *J. Phys. Chem. B* **104**, 6095–6098 (2000).

[85] Sun, Y., Gates, B., Mayers, B. & Xia, Y. Crystalline Silver Nanowires by Soft Solution Processing. *Nano Lett.* **2**, 165–168 (2002).

[86] Chance, R. R., Prock, A. & Silbey, R. Molecular fluorescence and energy transfer near interfaces. *Adv. Chem. Phys.* **37**, 1–65 (1978).

[87] Genet, C. & Ebbesen, T. W. Light in tiny holes. *Nature* **445**, 39–46 (2007).

[88] Atwater, H. A. The promise of plasmonics. *Scientific American* **296**, 56–63 (2007).

[89] Dintinger, J., Klein, S., Bustos, F., Barnes, W. L. & Ebbesen, T. W. Strong coupling between surface plasmon-polaritons and organic molecules in subwavelength hole arrays. *Phys. Rev. B* **71**, 035424 (2005).

[90] Altewischer, E., van Exter, M. P. & Woerdman, J. P. Plasmon-assisted transmission of entangled photons. *Nature* **418**, 304–306 (2002).

[91] Hochberg, M., Baehr-Jones, T., Walker, C. & Scherer, A. Integrated plasmon and dielectric waveguides. *Opt. Express* **12**, 5481–5486 (2004).

[92] Chang, D. E., Sørensen, A. S., Hemmer, P. R. & Lukin, M. D. Quantum optics with surface plasmons. *Phys. Rev. Lett.* **97**, 053002 (2006).

[93] Chang, D. E., Sørensen, A. S., Hemmer, P. R. & Lukin, M. D. Strong coupling of single emitters to surface plasmons. *Phys. Rev. B* **76**, 035420 (2007).

[94] Klimov, V. V., Ducloy, M. & Letokhov, V. S. A model of an apertureless scanning microscope with a prolate nanospheroid as a tip and an excited molecule as an object. *Chem. Phys. Lett.* **358**, 192–198 (2002).

[95] Tao, A. *et al.* Langmuir-Blodgett Silver Nanowire Monolayers for Molecular Sensing Using Surface-Enhanced Raman Spectroscopy. *Nano Lett.* **3**, 1229–1233 (2003).

[96] Chang, D. E., Sørensen, A. S., Demler, E. A. & Lukin, M. D. A single-photon transistor using nanoscale surface plasmons. *Nature Phys.* **3**, 807–812 (2007).

[97] Boyd, R. W. *Nonlinear Optics* (Academic, New York, 1992).

[98] Gibbs, H. M. *Optical bistability: Controlling light with light* (Academic Press, Inc., Orlando, FL, 1985).

[99] Bouwmeester, D., Ekert, A. & Zeilinger, A. (eds.) *The Physics of Quantum Information* (Springer, Berlin, 2000).

[100] Schmidt, H. & Imamoglu, A. Giant Kerr nonlinearities obtained by electromagnetically induced transparency. *Opt. Lett.* **21**, 1936–1938 (1996).

[101] Harris, S. E. & Yamamoto, Y. Photon Switching by Quantum Interference. *Phys. Rev. Lett.* **81**, 3611-3614 (1998).

[102] Lukin, M. D. Colloquium: Trapping and manipulating photon states in atomic ensembles. *Rev. Mod. Phys.* **75**, 457–472 (2003).

[103] Fleischhauer, M., Imamoglu, A. & Marangos, J. P. Electromagnetically induced transparency: Optics in coherent media. *Rev. Mod. Phys.* **77**, 633–673 (2005).

[104] Waks, E. & Vuckovic, J. Dipole Induced Transparency in Drop-Filter Cavity-Waveguide Systems. *Phys. Rev. Lett.* **96**, 153601 (2006).

[105] Bermel, P., Rodriguez, A., Johnson, S. G., Joannopoulos, J. D. & Soljačić, M. Single-photon all-optical switching using waveguide-cavity quantum electrodynamics. *Phys. Rev. A* **74**, 043818 (2006).

[106] Pacifici, D., Lezec, H. J. & Atwater, H. A. All-optical modulation by plasmonic excitation of CdSe quantum dots. *Nature Photonics* **1**, 402–406 (2007).

[107] Meystre, P. & Sargent III, M. *Elements of Quantum Optics, 3rd ed.* (Springer-Verlag, New York, 1999).

[108] Shen, J. T. & Fan, S. Coherent photon transport from spontaneous emission in one-dimensional waveguides. *Opt. Lett.* **30**, 2001–2003 (2005).

[109] Kojima, K., Hofmann, H. F., Takeuchi, S. & Sasaki, K. Nonlinear interaction of two photons with a one-dimensional atom: Spatiotemporal quantum coherence in the emitted field. *Phys. Rev. A* **68**, 013803 (2003).

[110] Shen, J.-T. & Fan, S. Strongly Correlated Two-Photon Transport in a One-Dimensional Waveguide Coupled to a Two-Level System. *Phys. Rev. Lett.* **98**, 153003 (2007).

[111] Carmichael, H. J., Brecha, R. J. & Rice, P. R. Quantum interference and collapse of the wavefunction in cavity QED. *Opt. Comm.* **82**, 73–79 (1991).

[112] Gorshkov, A. V., André, A., Fleischhauer, M., rensen, A. S. S. & Lukin, M. D. Universal Approach to Optimal Photon Storage in Atomic Media. *Phys. Rev. Lett.* **98**, 123601 (2007).

[113] Fleischhauer, M. & Lukin, M. D. Dark-State Polaritons in Electromagnetically Induced Transparency. *Phys. Rev. Lett.* **84**, 5094–5097 (2000).

[114] Klimov, V. I. *et al.* Optical Gain and Stimulated Emission in Nanocrystal Quantum Dots. *Science* **290**, 314–317 (2000).

[115] Brouri, R., Beveratos, A., Poizat, J.-P. & Grangier, P. Photon antibunching in the fluorescence of individual color centers in diamond. *Opt. Lett.* **25**, 1294–1296 (2000).

[116] Lesage, F. & Saleur, H. Boundary Interaction Changing Operators and Dynamical Correlations in Quantum Impurity Problems. *Phys. Rev. Lett.* **80**, 4370–4373 (1998).

[117] Tonks, L. The Complete Equation of State of One, Two and Three-Dimensional Gases of Hard Elastic Spheres. *Phys. Rev.* **50**, 955–963 (1936).

[118] Girardeau, M. Relationship between Systems of Impenetrable Bosons and Fermions in One Dimension. *J. of Math. Phys.* **1**, 516–523 (1960).

[119] Kinoshita, T., Wenger, T. & Weiss, D. S. Observation of a One-Dimensional Tonks-Girardeau Gas. *Science* **305**, 1125–1128 (2004).

[120] Paredes, B. *et al.* Tonks-Girardeau gas of ultracold atoms in an optical lattice. *Nature* **429**, 277–281 (2004).

[121] Hartmann, M. J., Brandao, F. G. S. L. & Plenio, M. B. A polaritonic two-component Bose-Hubbard model (2007). `e-print quant-ph/0706.2251`.

[122] Ghosh, S., Sharping, J. E., Ouzounov, D. G. & Gaeta, A. L. Resonant Optical Interactions with Molecules Confined in Photonic Band-Gap Fibers. *Phys. Rev. Lett.* **94**, 093902 (2005).

[123] Bajcsy, M., Zibrov, A. S. & Lukin, M. D. Stationary pulses of light in an atomic medium. *Nature* **426**, 638–641 (2003).

[124] André, A., Bajcsy, M., Zibrov, A. S. & Lukin, M. D. Nonlinear Optics with Stationary Pulses of Light. *Phys. Rev. Lett.* **94**, 063902 (2005).

[125] Lai, Y. & Haus, H. A. Quantum theory of solitons in optical fibers. II. Exact solution. *Phys. Rev. A* **40**, 854–866 (1989).

[126] Drummond, P. Quantum Theory of Nonlinear Optics (2001). URL `http://www.physics.uq.edu.au/people/drummond/notes/lecture.pdf`.

[127] Mazets, I. E. & Kurizki, G. How different are multiatom quantum solitons from mean-field solitons? *Europhys. Lett.* **76**, 196–202 (2006).

[128] Lieb, E. H. & Liniger, W. Exact Analysis of an Interacting Bose Gas. I. The General Solution and the Ground State. *Phys. Rev.* **130**, 1605–1616 (1963).

[129] Korepin, V. E., Bogoliubov, N. M. & Izergin, A. G. *Quantum Inverse Scattering Method and Correlation Functions* (Cambridge University Press, Cambridge, UK, 1993).

[130] Caux, J.-S. & Calabrese, P. Dynamical density-density correlations in the one-dimensional Bose gas. *Phys. Rev. A* **74**, 031605 (2006).

[131] Caux, J.-S., Calabrese, P. & Slavnov, N. A. One-particle dynamical correlations in the one-dimensional Bose gas. *J. Stat. Mech.* P01008 (2007).

[132] Haldane, F. D. M. Effective Harmonic-Fluid Approach to Low-Energy Properties of One-Dimensional Quantum Fluids. *Phys. Rev. Lett.* **47**, 1840–1843 (1981).

[133] Friedel, J. Metallic alloys. *Nuovo Cimento Suppl.* **7**, 287–311 (1958).

[134] Lenard, A. One-Dimensional Impenetrable Bosons in Thermal Equilibrium. *J. Math. Phys.* **7**, 1268–1272 (1966).

[135] Cazalilla, M. A. Effect of Suddenly Turning on Interactions in the Luttinger Model. *Phys. Rev. Lett.* **97**, 156403 (2006).

[136] Polkovnikov, A. & Gritsev, V. Breakdown of the adiabatic limit in low dimensional gapless systems (2007). `e-print cond-mat/0706.0212`.

[137] Rigol, M. & Muramatsu, A. Free Expansion of Impenetrable Bosons on One-Dimensional Optical Lattices. *Mod. Phys. Lett. B* **19**, 861–881 (2005).

[138] Minguzzi, A. & Gangardt, D. M. Exact Coherent States of a Harmonically Confined Tonks-Girardeau Gas. *Phys. Rev. Lett.* **94**, 240404 (2005).

[139] Castin, Y. & Dum, R. Bose-Einstein Condensates in Time Dependent Traps. *Phys. Rev. Lett.* **77**, 5315–5319 (1996).

[140] Kagan, Y., Surkov, E. L. & Shlyapnikov, G. V. Evolution of a Bose-condensed gas under variations of the confining potential. *Phys. Rev. A* **54**, R1753–R1756 (1996).

[141] Dowling, J. P. Correlated input-port, matter-wave interferometer: Quantum-noise limits to the atom-laser gyroscope. *Phys. Rev. A* **57**, 4736–4746 (1998).

[142] Bouyer, P. & Kasevich, M. A. Heisenberg-limited spectroscopy with degenerate Bose-Einstein gases. *Phys. Rev. A* **56**, R1083–R1086 (1997).

[143] Kok, P. *et al.* Linear optical quantum computing with photonic qubits. *Rev. Mod. Phys.* **79**, 135 (2007).

[144] Gisin, N., Ribordy, G., Tittel, W. & Zbinden, H. Quantum cryptography. *Rev. Mod. Phys.* **74**, 145–195 (2002).

[145] Akkermans, E., Montambaux, G., Pichard, J. & Zinn-Justin, J. (eds.). *Fermi liquids and non-Fermi liquids*, Mesocopic Quantum Physics, Proceedings of Les Houches Summer School LXI (Elsevier, Amsterdam, 1995).

[146] Mašalas, M. & Fleischhauer, M. Scattering of dark-state polaritons in optical lattices and quantum phase gate for photons. *Phys. Rev. A* **69**, 061801 (2004).

[147] Grimm, R., Weidemüller, M. & Ovchinnikov, Y. B. Optical dipole traps for neutral atoms. *Adv. At. Mol. Opt. Phys.* **42**, 95–170 (2000).

[148] Birkl, G., Gatzke, M., Deutsch, I. H., Rolston, S. L. & Phillips, W. D. Bragg Scattering from Atoms in Optical Lattices. *Phys. Rev. Lett.* **75**, 2823–2826 (1995).

[149] Greiner, M., Mandel, O., Esslinger, T., Hänsch, T. W. & Bloch, I. Quantum phase transition from a superfluid to a Mott insulator in a gas of ultracold atoms. *Nature* **415**, 39–44 (2002).

[150] John, S. & Wang, J. Quantum electrodynamics near a photonic band gap: Photon bound states and dressed atoms. *Phys. Rev. Lett.* **64**, 2418–2421 (1990).

[151] John, S. & Quang, T. Spontaneous emission near the edge of a photonic band gap. *Phys. Rev. A* **50**, 1764–1769 (1994).

[152] Peil, S. *et al.* Patterned loading of a Bose-Einstein condensate into an optical lattice. *Phys. Rev. A* **67**, 051603 (2003).

[153] Jaksch, D., Briegel, H.-J., Cirac, J. I., Gardiner, C. W. & Zoller, P. Entanglement of Atoms via Cold Controlled Collisions. *Phys. Rev. Lett.* **82**, 1975–1978 (1999).

[154] Brennen, G. K., Caves, C. M., Jessen, P. S. & Deutsch, I. H. Quantum Logic Gates in Optical Lattices. *Phys. Rev. Lett.* **82**, 1060–1063 (1999).

[155] Sprik, R., van Tiggelen, B. A. & Lagendijk, A. Optical emission in periodic dielectrics. *Europhys. Lett.* **35**, 265–270 (1996).

[156] van Coevorden, D. V., Sprik, R., Tip, A. & Lagendijk, A. Photonic Band Structure of Atomic Lattices. *Phys. Rev. Lett.* **77**, 2412–2415 (1996).

[157] de Vries, P., van Coevorden, D. V. & Lagendijk, A. Point scatterers for classical waves. *Rev. Mod. Phys.* **70**, 447–466 (1998).

[158] Gross, M. & Haroche, S. Superradiance: An essay on the theory of collective spontaneous emission. *Phys. Rep.* **93**, 301–396 (1982).

[159] Guo, J. & Cooper, J. Cooling and resonance fluorescence of two atoms in a one-dimensional optical molasses. *Phys. Rev. A* **51**, 3128–3135 (1995).

[160] Menotti, C. & Ritsch, H. Laser cooling of atoms in optical lattices including quantum statistics and dipole-dipole interactions. *Appl. Phys. B* **69**, 311–321 (1999).

[161] Meschede, D. Radiating atoms in confined space: from spontaneous emission to micromasers. *Phys. Rep.* **211**, 201–250 (1992).

[162] Beige, A., Huelga, S. F., Knight, P. L., Plenio, M. B. & Thompson, R. C. Coherent manipulation of two dipole-dipole interacting ions. *J. Mod. Opt.* **47**, 401–414 (2000).

[163] Dalibard, J. & Cohen-Tannoudji, C. Laser cooling below the Doppler limit by polarization gradients: Simple theoretical models. *J. Opt. Soc. Am. B* **6**, 2023–2045 (1989).

[164] Verkerk, P. *et al.* Designing Optical Lattices: An Investigation with Cesium Atoms. *Europhys. Lett.* **26**, 171–176 (1994).

[165] Rabl, P., Daley, A. J., Fedichev, P. O., Cirac, J. I. & Zoller, P. Defect-Suppressed Atomic Crystals in an Optical Lattice. *Phys. Rev. Lett.* **91**, 110403 (2003).

[166] Hall, J. L., Zhu, M. & Buch, P. Prospects for using laser-prepared atomic fountains for optical frequency standards applications. *J. Opt. Soc. Am. B* **6**, 2194–2205 (1989).

[167] Rafac, R. J. *et al.* Sub-dekahertz Ultraviolet Spectroscopy of $^{199}\mathrm{Hg}^+$. *Phys. Rev. Lett.* **85**, 2462–2465 (2000).

[168] Mukaiyama, T., Katori, H., Ido, T., Li, Y. & Kuwata-Gonokami, M. Recoil-Limited Laser Cooling of $^{87}\mathrm{Sr}$ Atoms near the Fermi Temperature. *Phys. Rev. Lett.* **90**, 113002 (2003).

[169] Xu, X. *et al.* Single-Stage Sub-Doppler Cooling of Alkaline Earth Atoms. *Phys. Rev. Lett.* **90**, 193002 (2003).

[170] Xu, X., Loftus, T. H., Hall, J. L., Gallagher, A. & Ye, J. Cooling and trapping of atomic strontium. *J. Opt. Soc. Am. B* **20**, 968–976 (2003).

[171] Courtillot, I. *et al.* Clock transition for a future optical frequency standard with trapped atoms. *Phys. Rev. A* **68**, 030501 (2003).

[172] Udem, T. *et al.* Absolute Frequency Measurements of the Hg^+ and Ca Optical Clock Transitions with a Femtosecond Laser. *Phys. Rev. Lett.* **86**, 4996–4999 (2001).

[173] Wilpers, G. *et al.* Optical Clock with Ultracold Neutral Atoms. *Phys. Rev. Lett.* **89**, 230801 (2002).

[174] Weidemüller, M., Görlitz, A., Hänsch, T. W. & Hemmerich, A. Local and global properties of light-bound atomic lattices investigated by Bragg diffraction. *Phys. Rev. A* **58**, 4647–4661 (1998).

[175] Mollow, B. R. Pure-state analysis of resonant light scattering: Radiative damping, saturation, and multiphoton effects. *Phys. Rev. A* **12**, 1919–1943 (1975).

[176] Harris, S. E. Electromagnetically induced transparency with matched pulses. *Phys. Rev. Lett.* **70**, 552–555 (1993).

[177] Giamarchi, T. *Quantum Physics in One Dimension* (Oxford University Press, New York, 2004).

[178] Slavnov, N. A. Nonequal-time current correlation function in a one-dimensional Bose gas. *Theor. and Math. Phys.* **82**, 273–282 (1990).

[179] Rostunov, T., Gritsev, V. & Demler, E. A. In preparation .

Appendix A

Electromagnetic modes of a cylinder: mode equation and cutoffs

A.1 Derivation of mode equation

The solution for the electromagnetic modes of a cylinder has been known for quite some time [54, 55] but for future use is briefly derived here.

We consider a cylinder of radius R of dimensionless electric permittivity ϵ_2, centered along the z-axis and surrounded by a second dielectric medium ϵ_1. For non-magnetic media the electric and magnetic fields in frequency space satisfy the wave equation

$$\nabla^2 \left\{ \begin{array}{c} \mathrm{E}(\mathbf{r}) \\ \mathrm{H}(\mathbf{r}) \end{array} \right\} + \frac{\omega^2}{c^2}\epsilon(\mathbf{r}) \left\{ \begin{array}{c} \mathrm{E}(\mathbf{r}) \\ \mathrm{H}(\mathbf{r}) \end{array} \right\} = 0. \tag{A.1}$$

The solutions to Eq. (A.1) are perhaps most easily derived by first finding scalar solutions of the equation and then constructing vector solutions. Working in cylindrical coordinates, scalar solutions of Eq. (A.1) satisfying the necessary boundary conditions take the form $\psi_1 \propto H_m\left(k_{1\perp}\rho\right) e^{im\phi+ik_\parallel z}$ and $\psi_2 \propto J_m\left(k_{2\perp}\rho\right) e^{im\phi+ik_\parallel z}$ outside and inside the cylinder, respectively. Here J_m and H_m are Bessel functions and Hankel functions of the first kind, respectively, while $k_{i\perp} = \sqrt{k_i^2 - k_\parallel^2}$ and $k_i = \omega\sqrt{\epsilon_i}/c$. J_m is well-behaved at $\rho = 0$, while $H_m(x) \sim e^{ix}$ for large x satisfies outgoing-wave conditions. It is easy to verify that two independent vector solutions to Eq. (A.1) are given by $\mathbf{v}_i = \frac{1}{k_i}\nabla \times (\hat{z}\psi_i)$ and $\mathbf{w}_i = \frac{1}{k_i}\nabla \times \mathbf{v}_i$. The curl relations of Maxwell's Equations then imply that $\mathbf{E}$ and $\mathbf{H}$ must take the form

$$\mathbf{E}_i(\mathbf{r}) = a_i\mathbf{v}_i(\mathbf{r}) + b_i\mathbf{w}_i(\mathbf{r}), \tag{A.2}$$

$$\mathbf{H}_i(\mathbf{r}) = -\frac{i}{\omega\mu_0}k_i\left(a_i\mathbf{w}_i(\mathbf{r}) + b_i\mathbf{v}_i(\mathbf{r})\right), \tag{A.3}$$

where a_i, b_i are constant coefficients. Expanding out these expressions in detail,

$$\begin{aligned}
\mathbf{E}_i(\mathbf{r}) &= \left[\left(\frac{im}{k_i\rho}a_iF_{i,m}(k_{i\perp}\rho) + \frac{ik_\parallel k_{i\perp}}{k_i^2}b_iF'_{i,m}(k_{i\perp}\rho)\right)\hat{\rho} + \right. \\
&\quad \left.\left(-\frac{k_{i\perp}}{k_i}a_iF'_{i,m}(k_{i\perp}\rho) - \frac{mk_\parallel}{k_i^2\rho}b_iF_{i,m}(k_{i\perp}\rho)\right)\hat{\phi} + \frac{k_{i\perp}^2}{k_i^2}b_iF_{i,m}(k_{i\perp}\rho)\hat{z}\right] e^{im\phi+ik_\parallel z}, \\
\mathbf{H}_i(\mathbf{r}) &= -\frac{i}{\omega\mu_0}k_i\left[\left(\frac{ik_\parallel k_{i\perp}}{k_i^2}a_iF'_{i,m}(k_{i\perp}\rho) + \frac{im}{k_i\rho}b_iF_{i,m}(k_{i\perp}\rho)\right)\hat{\rho} - \right. \\
&\quad \left.\left(\frac{mk_\parallel}{k_i^2\rho}a_iF_{i,m}(k_{i\perp}\rho) + \frac{k_{i\perp}}{k_i}b_iF'_{i,m}(k_{i\perp}\rho)\right)\hat{\phi} + \frac{k_{i\perp}^2}{k_i^2}a_iF_{i,m}(k_{i\perp}\rho)\hat{z}\right] \times \\
&\quad e^{im\phi+ik_\parallel z},
\end{aligned} \tag{A.4}$$

where $F_{1,m}(x) \equiv H_m(x)$ and $F_{2,m}(x) \equiv J_m(x)$.

Up to this point a_i, b_i are arbitrary coefficients, whose relationship becomes fixed by imposing boundary conditions between the cylinder and surrounding dielectric.

Requiring that the tangential components E_ϕ, E_z, H_ϕ, H_z of the fields be continuous at the boundary results in a linear system of four equations, which we write in abbreviated matrix form as $M(a_1\ a_2\ b_1\ b_2)^T = 0$. It can be verified that the boundary condition equations for the perpendicular field components E_ρ, H_ρ are redundant with those for the parallel field components. A non-trivial solution for the fields requires that $\det M = 0$, which after some work simplifies to the mode equation given in Eq. (2.1).

One special case of interest is that of a TM mode with no winding ($m = 0$). The component of $\mathbf{H}$ along $\hat{z}$ by definition vanishes, which implies that the coefficients a_i in Eq. (A.4) vanish. The condition $\det M = 0$ is then significantly easier to evaluate in this situation. In particular, $a_i = 0$ implies that the field components E_ϕ and H_z vanish, and continuity of the remaining tangential field components E_z and H_ϕ at the boundary requires that

$$\begin{pmatrix} \frac{k_{1\perp}^2}{k_1^2} H_0(k_{1\perp}R) & -\frac{k_{2\perp}^2}{k_2^2} J_0(k_{2\perp}R) \\ ik_{1\perp}H_0'(k_{1\perp}R) & -ik_{2\perp}J_0'(k_{2\perp}R) \end{pmatrix} \begin{pmatrix} b_1 \\ b_2 \end{pmatrix} = \begin{pmatrix} 0 \\ 0 \end{pmatrix}. \tag{A.5}$$

Setting the determinant of the above matrix equal to zero immediately yields the mode equation of Eq. (2.2), and it is also immediately seen that the ratio of the coefficients $b_{1,2}$ must be given by Eq. (2.4).

A.2 Derivation of cutoff for higher-order modes

In this section we show that to a very good approximation, a nanowire essentially supports a single, fundamental surface plasmon mode with winding number $m = 0$. In particular, for all higher-order plasmon modes $|m| \geq 2$ a cutoff wire size R_{cutoff} exists below which such modes cannot exist, while the $|m| = 1$ surface plasmon modes exhibit an exponential growth in their mode volumes as $R \to 0$. For simplicity, we will assume in this section that we are dealing with a lossless system ($\mathrm{Im}\,\epsilon_2 = 0$).

A.2.1 Behavior of $|m| \geq 2$ modes

We are interested here in the behavior of the $|m| \geq 2$ modes near cutoff, which is characterized by a small deviation of the surface plasmon wavevector $k_\parallel$ from $\sqrt{\epsilon_1}\omega/c$ (see Fig. 2.3). To simplify algebra in the derivation of R_{cutoff}, from this point *forward we make the mode equation (2.1) dimensionless by setting* $\omega/c = 1$, *and we* will assume that m is positive (the case where m is negative follows this derivation with a few minor modifications). Furthermore, it is useful to define a small quantity $\delta = k_\parallel - \sqrt{\epsilon_1}$, where we specifically consider the positive $k_\parallel$ solution. On physical grounds, any mode with positive $k_\parallel$ must satisfy $\delta \geq 0$, because if $k_\parallel < \sqrt{\epsilon_1}$ the fields outside of the wire would be radiative in nature and would imply that the system is continually radiating energy out to infinity without a source. It follows that any value of R where $\delta = 0$ becomes a solution to Eq. (2.1) for some m then corresponds to a critical point in behavior, and specifically is a cutoff beyond which modes cease to exist. To find this $R = R_{\mathrm{cutoff}}$, we expand the two sides of Eq. (2.1) in δ. Both sides have contributions to these expansions that are divergent at $\delta = 0$ (terms that behave like δ^{-n}, where $n > 0$), and we will show that, for $m \geq 2$, there exists one value of R that equates these two divergent contributions; *i.e.*, $\delta = 0$ satisfies the mode equation at this particular value $R = R_{\mathrm{cutoff}}$.

It is straightforward to show that the divergent contribution to the expansion of the left-hand side of Eq. (2.1) is given by

$$LHS = \frac{m^2}{4R^2\delta^2} - \frac{m^2(3\epsilon_1+\epsilon_2)}{4R^2\sqrt{\epsilon_1}(\epsilon_1-\epsilon_2)\delta} + \mathcal{O}(\delta^0). \tag{A.6}$$

To expand the right-hand side, we first note that the quantity

$$(1/k_{2\perp})J'_m(k_{2\perp}R)/J_m(k_{2\perp}R) = (1/\sqrt{\epsilon_2-\epsilon_1})\tilde{J}_m(\sqrt{\epsilon_2-\epsilon_1}R) + \mathcal{O}(\delta^1) \tag{A.7}$$

is well-behaved near $\delta = 0$. Here we have defined $\tilde{J}_m(x) = J'_m(x)/J_m(x)$. Then, using the identity

$$H_m(ix) = \frac{2}{\pi i^{m+1}}K_m(x), \tag{A.8}$$

where $K_m(x)$ is a modified Bessel function of the second kind, and the expansions

$$\begin{aligned} K_m(x) &= \frac{(m-1)!}{2}\left(\frac{2}{x}\right)^m - \frac{(m-2)!}{2}\left(\frac{2}{x}\right)^{m-2} + \mathcal{O}(x^{4-m}) \quad (m\geq 2), && \text{(A.9)} \\ k_{1\perp} &= i\left(\sqrt{2\delta\sqrt{\epsilon_1}} + \frac{\delta^{3/2}}{2^{3/2}\epsilon_1^{1/4}} + \mathcal{O}(\delta^{5/2})\right) && \text{(A.10)} \\ &\equiv i\kappa_{1\perp}, && \text{(A.11)} \end{aligned}$$

it is tedious but straightforward to expand the expression

$$(1/k_{1\perp})(H'_m(k_{1\perp}R)/H_m(k_{1\perp}R)) \tag{A.12}$$

as well. Performing these expansions and simplifying, one finds that

$$RHS = \frac{m^2}{4R^2\delta^2} - \frac{m^2}{4R^2\sqrt{\epsilon_1}\delta} + \frac{m\sqrt{\epsilon_1}}{2(m-1)\delta} + \frac{im(\epsilon_1+\epsilon_2)\tilde{J}_m(\sqrt{\epsilon_2-\epsilon_1}R)}{2R\sqrt{\epsilon_1(\epsilon_1-\epsilon_2)}\delta} + \mathcal{O}(\delta^0). \tag{A.13}$$

Comparing Eqs. (A.6) and (A.13), we see that $\delta = 0$ is a solution provided that these expressions are equal to $\mathcal{O}(\delta^{-1})$, *i.e.*,

$$\frac{m}{R}\frac{\epsilon_1+\epsilon_2}{\epsilon_2-\epsilon_1} = \frac{R\epsilon_1}{m-1} + \frac{i(\epsilon_1+\epsilon_2)\tilde{J}_m(\sqrt{\epsilon_2-\epsilon_1}R)}{\sqrt{\epsilon_1-\epsilon_2}}. \tag{A.14}$$

The solution $R = R_{\text{cutoff}}$ to Eq. (A.14) gives the cutoff wire size below which the mode m cannot exist. In the regime of interest ($\epsilon_1 > 0, \epsilon_2 < 0, \epsilon_1 + \epsilon_2 < 0$), the first and second terms are positive while the third term is a negative function (for $R > 0$) that behaves like $-1/R$ for small R and approaches a constant for large R. It can be seen then that a solution exists for any $m \geq 2$, which establishes that these modes are indeed cut off in the nanowire limit.

A.2.2 Behavior of $|m| = 1$ mode

For simplicity we will assume that $m = 1$, as the case of $m = -1$ follows this derivation closely. The case of $m = 1$ must be studied separately because the expansion of $K_m(x)$ given in Eq. (A.9) only holds for $m \geq 2$. The different asymptotic scaling of $K_1(x)$ leads to unique behavior of the $m = 1$ mode in the nanowire limit. In particular we will show that this mode does not strictly have a cutoff size, but that $k_\| \to \sqrt{\epsilon_1}$ exponentially in the limit $R \to 0$. In turn, the magnitude of $k_{1\perp}$ becomes exponentially small, which corresponds to an exponential growth in the spatial extent or mode volume.

Again defining $\delta = k_\| - \sqrt{\epsilon_1}$, we are interested in finding an approximate solution to Eq. (2.1) in the limit of small δ. We proceed by expanding both sides of the equation as a series in the small parameter. The expression for the left-hand side given by Eq. (A.6) remains valid for $m = 1$. For the right-hand side, we anticipate that both the quantities $k_{1\perp}R$ and $k_{1\perp}$ will be small as $R \to 0$ (these assumptions can be checked for consistency at the end of the calculation), and we thus expand around

$k_{1\perp}R = 0$ the term

$$\begin{aligned}\frac{1}{k_{1\perp}}\frac{H_1'(k_{1\perp}R)}{H_1(k_{1\perp}R)} &= \frac{1}{i\kappa_{1\perp}}\frac{H_1'(i\kappa_{1\perp}R)}{H_1(i\kappa_{1\perp}R)} && \text{(A.15)}\\ &= \frac{1}{i\kappa_{1\perp}}\left(\frac{i}{\kappa_{1\perp}R} - i\left(\gamma + \log\frac{\kappa_{1\perp}R}{2}\right)\kappa_{1\perp}R\right.\\ &\quad \left. + O(\kappa_{1\perp}^2R^2)\right), && \text{(A.16)}\end{aligned}$$

where $\gamma \approx 0.577$ is Euler's constant. Here we have used Eq. (A.8) to convert $H_m(ix)$ to $K_m(x)$ and the expansion

$$K_1(x) = \frac{1}{x} + \left(\frac{\gamma}{2} - \frac{\log 2}{2} - \frac{1}{4} + \frac{\log x}{2}\right)x + O(x^3). \tag{A.17}$$

We now assume that $\kappa_{1\perp}R$ is small enough that $\gamma \ll |\log\kappa_{1\perp}R|$, such that

$$\frac{1}{k_{1\perp}}\frac{H_1'(k_{1\perp}R)}{H_1(k_{1\perp}R)} \approx \frac{1}{i\kappa_{1\perp}}\left(\frac{i}{\kappa_{1\perp}R} - i\kappa_{1\perp}R\log\frac{\kappa_{1\perp}R}{2}\right). \tag{A.18}$$

Furthermore, having assumed that $k_{1\perp}$ (and by extension, $\kappa_{1\perp}$) is a small quantity, we can now expand the expression above in terms of δ using Eqs. (A.10) and (A.11). Making this substitution, and after a bit of algebra, one finds that the expansion of the right-hand side of Eq. (2.1) is given by

$$RHS \approx \frac{1}{4R^2\delta^2} + \frac{\epsilon_1 + 3\epsilon_2 - 2R^2\epsilon_1(\epsilon_1 - \epsilon_2)\log\left(\delta R^2\sqrt{\epsilon_1}/2\right)}{4R^2\sqrt{\epsilon_1}(\epsilon_1 - \epsilon_2)\delta}. \tag{A.19}$$

Finally, equating the left- and right-hand sides to $\mathcal{O}(\delta^{-1})$ gives the solution

$$\delta \approx \frac{2}{R^2\sqrt{\epsilon_1}}\exp\left(-\frac{2(\epsilon_1 + \epsilon_2)}{R^2\epsilon_1(\epsilon_2 - \epsilon_1)}\right). \tag{A.20}$$

It follows that in the nanowire limit,

$$\begin{aligned}\kappa_{1\perp} &= \left(k_\parallel^2 - \epsilon_1\right)^{1/2} && \text{(A.21)}\\ &\approx \left(2\delta\sqrt{\epsilon_1}\right)^{1/2} && \text{(A.22)}\\ &\approx \frac{2}{R}\exp\left(-\frac{\epsilon_1 + \epsilon_2}{R^2\epsilon_1(\epsilon_2 - \epsilon_1)}\right). && \text{(A.23)}\end{aligned}$$

Eqs. (A.20) and (A.23) indicate that the $m = 1$ surface plasmon mode does not have a cutoff in the nanowire limit, but instead that its longitudinal wavevector approaches $\sqrt{\epsilon_1}$ exponentially, with a corresponding exponential increase in its transverse extent ($\sim 1/\kappa_{1\perp}$) and mode volume. It is therefore well-justified to say that this mode is effectively cut off, as the coupling strength to this mode becomes strongly suppressed as $R \rightarrow 0$.

Appendix B

Spontaneous emission rates near a nanowire and nanotip

B.1 Radiative and non-radiative decay rates near a nanotip

Here we derive more carefully the expressions given in Eqs. (2.45) and (2.46) for the radiative and non-radiative spontaneous emission rates near a nanotip.

To calculate the radiative rate, we consider our expression for Φ_r in Eq. (2.40) in the far-field (large v) limit, where the $K_m(qv)$ terms in Φ_r decay exponentially with v. Because of this exponential dependence at large v, to good approximation it suffices to expand the terms $\alpha_m(q), J_m(qu'), K_m(qv')$ around $q = 0$. The only non-trivial expansions occur for the terms $\alpha_m(q)$ and are given by

$$\alpha_0(q) = \frac{1}{2}\left(1-\frac{\epsilon_2}{\epsilon_1}\right) q^2 v_0^2 + \mathcal{O}(q^4), \tag{B.1}$$

$$\alpha_1(q) = \frac{1}{2}\frac{\epsilon_1-\epsilon_2}{\epsilon_1+\epsilon_2}q^2v_0^2+\mathcal{O}(q^4), \quad \cdots \tag{B.2}$$

These expansions allow for exact evaluations of the integral. It can be verified that the dipole contributions to Φ_r originate from the $m=0,1$ terms in the sum, which are readily found to be

$$\Phi_r^{(m=0)}(\mathbf{r},\mathbf{r}') \approx \frac{1}{4\pi\epsilon_0\epsilon_1}v_0^2\left(1-\frac{\epsilon_2}{\epsilon_1}\right)\frac{4(v^2-u^2)}{(u^2+v^2)^3}\ln\frac{v}{v'}+\delta\Phi(\mathbf{r}), \tag{B.3}$$

$$\Phi_r^{(m=1)}(\mathbf{r},\mathbf{r}') \approx \frac{1}{4\pi\epsilon_0\epsilon_1}\cos(\phi-\phi')\frac{\epsilon_1-\epsilon_2}{\epsilon_1+\epsilon_2}\frac{v_0^2u'}{v'}\frac{8uv}{(u^2+v^2)^3}. \tag{B.4}$$

Here $\delta\Phi$ is a complicated function, but most importantly contains no dependence on $\mathbf{r}'$. Recalling that the pseudopotentials derived above correspond to a point charge source, we can immediately obtain the potentials due to a dipole $\mathbf{p}_0e^{-i\omega t}$ at $\mathbf{r}'$ by applying the operator $(\mathbf{p}_0\cdot\nabla')$ to these expressions. In parabolic coordinates the gradient operator is given by

$$\nabla = \frac{1}{\sqrt{u^2+v^2}}\left(\hat{u}\frac{\partial}{\partial u}+\hat{v}\frac{\partial}{\partial v}\right)+\frac{1}{uv}\hat{\phi}\frac{\partial}{\partial\phi}, \tag{B.5}$$

and for a dipole located on the z-axis ($u'=0$), we find that

$$\Phi_{dip,r}^{(m=0)} \approx -\frac{1}{4\pi\epsilon_0\epsilon_1}\left(1-\frac{\epsilon_2}{\epsilon_1}\right)\frac{v_0^2}{v'^2}\frac{(\hat{v}\cdot\mathbf{r})(\mathbf{p}_0\cdot\hat{v})}{r^3}, \tag{B.6}$$

$$\Phi_{dip,r}^{(m=1)} \approx \frac{1}{4\pi\epsilon_0\epsilon_1}\frac{\epsilon_1-\epsilon_2}{\epsilon_1+\epsilon_2}\frac{v_0^2}{v'^2}\frac{(\mathbf{p}_0-\hat{v}(\mathbf{p}_0\cdot\hat{v}))\cdot\mathbf{r}}{r^3}. \tag{B.7}$$

From these expressions one can immediately identify the induced dipole moments in the nanotip,

$$\delta\mathbf{p} = -\hat{v}p_0\frac{v_0^2}{v'^2}\left(1-\frac{\epsilon_2}{\epsilon_1}\right), \quad (\mathbf{p}_0 \parallel \hat{z}) \tag{B.8}$$

$$\delta\mathbf{p} = \hat{u}p_0\frac{\epsilon_1-\epsilon_2}{\epsilon_1+\epsilon_2}\frac{v_0^2}{v'^2}, \quad (\mathbf{p}_0 \perp \hat{z}) \tag{B.9}$$

and arrive at the radiative decay rates given in Eq. (2.45).

The leading term for the non-radiative decay rate is found by calculating the divergence in the reflected field $\mathbf{E}_r(\mathbf{r}',\mathbf{r}')$ as $v'\to v_0$. The reflected field $\mathbf{E}_r = -\nabla(\mathbf{p}_0\cdot\nabla')\Phi_r$ is in general difficult to evaluate, but simplifies considerably for a dipole located on-axis ($u'=0$) due to the presence of the $J_m(qu')$ term in Φ_r, given in Eq. (2.40). The operation ∇' causes terms like $J_m(0)$ and $J'_m(0)$ to appear in $\mathbf{E}_r$, which are non-zero only when $m=0$ and $m=1$, respectively. This immediately leads to the expressions

$$\begin{aligned} \mathbf{p}_0\cdot\mathbf{E}_r(\mathbf{r}',\mathbf{r}') &= -\frac{p_0^2}{4\pi\epsilon_0\epsilon_1}\int_0^\infty dq\,\frac{q^3}{v'^2}\alpha_1(q)K_1^2(qv'), \qquad (\mathbf{p}_0\perp\hat{z}) \\ \mathbf{p}_0\cdot\mathbf{E}_r(\mathbf{r}',\mathbf{r}') &= -\frac{p_0^2}{2\pi\epsilon_0\epsilon_1}\int_0^\infty dq\,\frac{q^3}{v'^2}\alpha_0(q)K_1^2(qv'), \qquad (\mathbf{p}_0\parallel\hat{z}) \qquad \text{(B.10)} \end{aligned}$$

which were given in Eq. (2.44). Examining further the solutions to $\alpha_{0,1}$, it can easily be shown that their asymptotic expansions in the limit $qv_0\gg1$ take the form

$$\alpha_{0,1}(q)\approx\frac{1}{\pi}\frac{\epsilon_1-\epsilon_2}{\epsilon_1+\epsilon_2}e^{2qv_0}. \qquad (qv_0\gg1) \qquad \text{(B.11)}$$

At the same time, in the limit $qv'\gg1$ the behavior of $K_1^2(qv')$ is given by $K_1^2(qv')\approx(\pi/2qv')e^{-2qv'}$, and thus as $v'\to v_0$ the integrands of Eq. (B.10) exhibit very long tails due to the presence of terms $\sim e^{-2q(v'-v_0)}$ at large q. The tail is the origin of the divergence that we expect on physical grounds. Using these expansions as well as the fact that the decay rate is proportional to Im $(\mathbf{p}_0\cdot\mathbf{E})$, the integrals can be evaluated exactly and yield the non-radiative decay rates given in Eq. (2.46).

B.2 Decay rates near a nanowire: full electrodynamic calculation

In this section we derive the exact spontaneous emission rates for an atom near a nanowire by solving the full vector Maxwell's equations.

The approach is similar to that used in Chapter 2, but without resorting to the quasi-static approximation. In particular, we split up the field outside the wire (denoted region 1) into free and scattered contributions,

$$\mathbf{E}_{1,total} = \mathbf{E}_0 + \mathbf{E}_{sc}, \tag{B.12}$$

where the free field $\mathbf{E}_0$ corresponds to that of an oscillating dipole in a uniform medium of permittivity ϵ_1. The scattered field $\mathbf{E}_{sc}$ and the field $\mathbf{E}_2$ inside the wire (denoted region 2) are source-free fields that help to ensure that the necessary boundary conditions are satisfied at the wire edge. Similar definitions hold for the magnetic field H. For non-magnetic media, these fields satisfy

$$\nabla^2 \left\{ \begin{array}{c} \mathbf{E}_j \\ \mathbf{H}_j \end{array} \right\} + \frac{\omega^2}{c^2}\epsilon_j \left\{ \begin{array}{c} \mathbf{E}_j \\ \mathbf{H}_j \end{array} \right\} = 0, \tag{B.13}$$

where $j = 2, sc$ and ϵ_j is the corresponding permittivity in region j.

In our problem of interest the free field is due to an oscillating dipole $\mathbf{p}_0 e^{-i\omega t}$ located at $\mathbf{r}'$, which has a free vector potential given by

$$\mathbf{A}_0(\mathbf{r}) = -\frac{i\mu_0\omega}{4\pi}\mathbf{p}_0\frac{e^{ik_1|\mathbf{r}-\mathbf{r}'|}}{|\mathbf{r}-\mathbf{r}'|}e^{-i\omega t}. \tag{B.14}$$

From this point forward we will not explicitly write out the harmonic time dependence of all terms. We can conveniently write the free vector potential in cylindrical

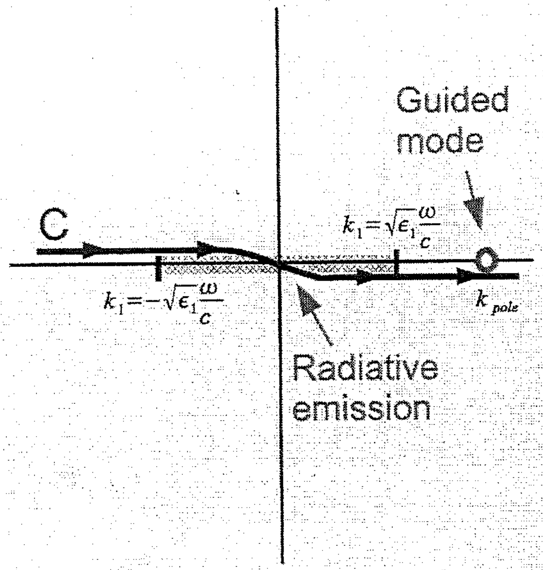

Figure B.1: Contour of integration for evaluating the integral representation of the free-space Green's function. The region in red, located between $h_\parallel = -\sqrt{\epsilon_1}\omega/c$ and $h_\parallel = \sqrt{\epsilon_1}\omega/c$, corresponds to radiative emission, while the contribution from poles (in blue) yields emission rates into guided modes.

coordinates by using the integral representation [59]

$$\frac{e^{ik_1|\mathbf{r}-\mathbf{r}'|}}{|\mathbf{r}-\mathbf{r}'|} = \frac{i}{2}\sum_{m=-\infty}^{\infty}\int_C dh_\parallel\, e^{im(\phi-\phi')+ih_\parallel(z-z')} J_m(h_{1\perp}\rho) H_m(h_{1\perp}\rho'), \tag{B.15}$$

where the contour C is shown in Fig. B.1, and $h_{i\perp}^2 \equiv \epsilon_1(\omega/c)^2 - h_\parallel^2$. From this expression one can readily find the free magnetic and electric fields using the relationships

$$\mathbf{H}_0 = \frac{1}{\mu_0}\nabla\times\mathbf{A}_0 \tag{B.16}$$

$$\mathbf{E}_0 = \frac{i}{\omega\epsilon_0\epsilon_1}\nabla\times\mathbf{H}_0. \tag{B.17}$$

For dipoles in orientations $\hat{\rho}, \hat{z}, \hat{\phi}$, respectively, the tangential components of these fields (which will be used in enforcing boundary conditions at the interface) are given by

$$
\begin{aligned}
\mathbf{H}_{0,\|}^{(\rho)} &= \frac{\omega p_0}{8\pi}\int_C dh_\| \sum_{m=-\infty}^{\infty} e^{im(\phi-\phi')+ih_\|(z-z')}\left[ih_\|\left(\frac{m^2}{xx'}J_m(x)H_m(x')+\frac{dJ_m}{dx}\frac{dH_m}{dx'}\right)\hat{\phi}\right. \\
&\quad \left.-\frac{imh_{1\perp}}{x'}J_m(x)H_m(x')\hat{z}\right], && \text{(B.18)} \\
\mathbf{E}_{0,\|}^{(\rho)} &= \frac{ip_0}{8\pi\epsilon_0\epsilon_1}\int_C dh_\| \sum_{m=-\infty}^{\infty} e^{im(\phi-\phi')+ih_\|(z-z')}\left[\left(\frac{imh_\|^2}{x}H_m'(x')J_m(x)\right.\right. \\
&\quad \left.\left.+\frac{imk_1^2}{x'}H_m(x')J_m'(x)\right)\hat{\phi}-ih_\|h_{1\perp}H_m{}'(x')J_m(x)\hat{z}\right], && \text{(B.19)} \\
\mathbf{H}_{0,\|}^{(z)} &= -\frac{\omega p_0}{8\pi}\int_C dh_\| \sum_{m=-\infty}^{\infty} e^{im(\phi-\phi')+ih_\|(z-z')}h_{1\perp}H_m(x')J_m'(x)\hat{\phi}, && \text{(B.20)} \\
\mathbf{E}_{0,\|}^{(z)} &= \frac{ip_0}{8\pi\epsilon_0\epsilon_1}\int_C dh_\| \sum_{m=-\infty}^{\infty} e^{im(\phi-\phi')+ih_\|(z-z')}\left[-\frac{mh_\|h_{1\perp}}{x}H_m(x')J_m(x)\hat{\phi}\right. \\
&\quad \left.+h_{1\perp}^2H_m(x')J_m(x)\hat{z}\right], && \text{(B.21)} \\
\mathbf{H}_{0,\|}^{(\phi)} &= \frac{\omega p_0}{8\pi}\int_C dh_\| \sum_{m=-\infty}^{\infty} e^{im(\phi-\phi')+ih_\|(z-z')}\left[\left(\frac{mh_\|}{x}J_m(x)\frac{dH_m}{dx'}\right.\right. \\
&\quad \left.\left.+\frac{mh_\|}{x'}H_m(x')\frac{dJ_m}{dx}\right)\hat{\phi}-h_{1\perp}J_m(x)\frac{dH_m}{dx'}\hat{z}\right], && \text{(B.22)} \\
\mathbf{E}_{0,\|}^{(\phi)} &= \frac{ip_0}{8\pi\epsilon_0\epsilon_1}\int_C dh_\| \sum_{m=-\infty}^{\infty} e^{im(\phi-\phi')+ih_\|(z-z')}\left[\left(\frac{h_\|^2m^2}{xx'}J_m(x)H_m(x')\right.\right. \\
&\quad \left.\left.+k_1^2J_m'(x)H_m'(x')\right)\hat{\phi}-\frac{h_\|h_{1\perp}m}{x'}H_m(x')J_m(x)\hat{z}\right]. && \text{(B.23)}
\end{aligned}
$$

Here we have defined $x = h_{1\perp}\rho$ and $x' = h_{1\perp}\rho'$.

We proceed to find the scattered fields and fields inside the wire by expanding them in a similar basis to that used for expressing the free fields. As shown in Eq. (A.4), there are only two independent components making up these fields, which we can set to be E_z and H_z. Thus, we write

$$
E_{sc,z} = \sum_{m=-\infty}^{\infty}\int_C dh_\| \, e^{im(\phi-\phi')+ih_\|(z-z')}H_m(h_{1\perp}\rho)a_m(h_\|),
$$

$$
\begin{aligned}
H_{sc,z} &= \frac{\epsilon_0\epsilon_1}{\mu_0}\sum_{m=-\infty}^{\infty}\int_C dh_\parallel\, e^{im(\phi-\phi')+ih_\parallel(z-z')} H_m(h_{1\perp}\rho) b_m(h_\parallel), \\
E_{2,z} &= \sum_{m=-\infty}^{\infty}\int_C dh_\parallel\, e^{im(\phi-\phi')+ih_\parallel(z-z')} J_m(h_{2\perp}\rho) c_m(h_\parallel), \\
H_{2,z} &= \frac{\epsilon_0\epsilon_1}{\mu_0}\sum_{m=-\infty}^{\infty}\int_C dh_\parallel\, e^{im(\phi-\phi')+ih_\parallel(z-z')} J_m(h_{2\perp}\rho) d_m(h_\parallel), \qquad \text{(B.24)}
\end{aligned}
$$

where a_m, b_m, c_m, d_m are coefficients that will be determined by enforcing the continuity of the tangential electric and magnetic fields. The other field components are related to E_z and H_z through Eq. (A.4). The continuity equations are tedious to solve, but yield

$$
\begin{aligned}
a_m^{(\rho)} = \frac{p_0 k_0^2}{8\pi\epsilon_0\zeta_m^{(\rho)}(h_\parallel)} \Bigg[& \frac{h_{1\perp}^2 h_{2\perp}^2 (h_{1\perp}^2 - h_{2\perp}^2)}{x'} h_\parallel m^2 R\sqrt{\epsilon_2} H_m(x') J_m^2(x_2) \times \\
& (H_m(x_1) J_m'(x_1) - J_m(x_1) H_m'(x_1)) \\
& + \frac{h_{1\perp}^3 h_{2\perp}^2 h_\parallel R^2 \sqrt{\epsilon_2} H_m'(x')}{\epsilon_1} (h_{1\perp}\epsilon_2 J_m(x_1) J_m'(x_2) - h_{2\perp}\epsilon_1 J_m(x_2) J_m'(x_1)) \times \\
& (h_{1\perp} H_m(x_1) J_m'(x_2) - h_{2\perp} J_m(x_2) H_m'(x_1)) \\
& - \frac{h_{1\perp}(h_{1\perp}^2 - h_{2\perp}^2)^2 h_\parallel^3 m^2 \sqrt{\epsilon_2}}{\epsilon_1} H_m(x_1) J_m(x_1) J_m^2(x_2) H_m'(x') \Bigg], \qquad \text{(B.25)}
\end{aligned}
$$

$$
\begin{aligned}
b_m^{(\rho)} = \frac{p_0 k_0^2}{8\pi\epsilon_0\zeta_m^{(\rho)}(h_\parallel)} \Bigg[& i\sqrt{\frac{\epsilon_2}{\epsilon_1}} h_{1\perp}^2 h_{2\perp}^2 (h_{1\perp}^2 - h_{2\perp}^2) h_\parallel^2 m R H_m'(x') J_m^2(x_2) \times \\
& (J_m(x_1) H_m'(x_1) - H_m(x_1) J_m'(x_1)) \\
& - \frac{i}{x'}\sqrt{\frac{\epsilon_2}{\epsilon_1}} h_{1\perp}^3 h_{2\perp}^2 m R^2 H_m(x') (h_{1\perp}\epsilon_2 H_m(x_1) J_m'(x_2) - h_{2\perp}\epsilon_1 J_m(x_2) H_m'(x_1)) \times \\
& (h_{1\perp} J_m(x_1) J_m'(x_2) - h_{2\perp} J_m(x_2) J_m'(x_1)) \\
& + \frac{i}{x'}\sqrt{\frac{\epsilon_2}{\epsilon_1}} h_{1\perp}(h_{1\perp}^2 - h_{2\perp}^2)^2 h_\parallel^2 m^3 H_m(x_1) J_m(x_1) J_m^2(x_2) H_m(x') \Bigg], \qquad \text{(B.26)}
\end{aligned}
$$

$$
a_m^{(z)} = \frac{p_0 k_0^2}{8\pi\epsilon_0\zeta_m^{(z)}(h_\parallel)} \left[i h_{1\perp}^2 x_1^2 x_2^2 H_m(x') \times \right.
$$

$$
\begin{aligned}
&(h_{1\perp} H_m(x_1) J'_m(x_2) - h_{2\perp} H'_m(x_1) J_m(x_2)) \times \\
&(h_{1\perp}\epsilon_2 J_m(x_1) J'_m(x_2) - h_{2\perp}\epsilon_1 J'_m(x_1) J_m(x_2)) \\
&-i h_{1\perp}^2 h_\parallel^2 m^2 (h_{1\perp} x_1 - h_{2\perp} x_2)^2 H_m(x_1) H_m(x') J_m(x_1) J_m^2(x_2)\Big], \qquad \text{(B.27)}
\end{aligned}
$$

$$
\begin{aligned}
a_m^{(\phi)} = {} & \frac{p_0 k_0^2}{8\pi\epsilon_0 \zeta_m^{(\phi)}(h_\parallel)} \Big[i m h_{1\perp} h_{2\perp} h_\parallel x_1 x_2 x' \epsilon_1 (h_{1\perp} x_1 - h_{2\perp} x_2) \times \\
& (J_m(x_1) H'_m(x_1) - H_m(x_1) J'_m(x_1))\, J_m^2(x_2) H'_m(x') \\
& -i h_{1\perp} h_\parallel m x_1^2 x_2^2 H_m(x')\, (h_{1\perp} H_m(x_1) J'_m(x_2) - h_{2\perp} H'_m(x_1) J_m(x_2)) \times \\
& (h_{1\perp}\epsilon_2 J_m(x_1) J'_m(x_2) - h_{2\perp}\epsilon_1 J'_m(x_1) J_m(x_2)) \\
& + i h_{1\perp} h_\parallel^3 m^3 H_m(x') H_m(x_1) J_m(x_1) J_m^2(x_2)\, (h_{1\perp} x_1 - h_{2\perp} x_2)^2 \Big], \qquad \text{(B.28)}
\end{aligned}
$$

$$
\begin{aligned}
b_m^{(\phi)} = {} & \frac{p_0 k_0^2}{8\pi\epsilon_0 \zeta_m^{(\phi)}(h_\parallel)} \Big[h_{1\perp} h_\parallel^2 m^2 \sqrt{\epsilon_1} J_m^2(x_2) (h_{1\perp} x_1 - h_{2\perp} x_2) \times \\
& \{ x' H_m(x_1) J_m(x_1) H'_m(x') (h_{1\perp} x_1 - h_{2\perp} x_2) \\
& + h_{2\perp} x_1 x_2 H_m(x') (J_m(x_1) H'_m(x_1) - H_m(x_1) J'_m(x_1)) \} \\
& - h_{1\perp} x_1^2 x_2^2 x' \sqrt{\epsilon_1} H'_m(x')\, (h_{1\perp} J_m(x_1) J'_m(x_2) - h_{2\perp} J'_m(x_1) J_m(x_2)) \times \\
& (h_{1\perp}\epsilon_2 H_m(x_1) J'_m(x_2) - h_{2\perp}\epsilon_1 H'_m(x_1) J_m(x_2)) \Big], \qquad \text{(B.29)}
\end{aligned}
$$

$$
\zeta_m^{(\rho)}(h_\parallel) = h_{1\perp}^4 h_{2\perp}^4 R^2 H_m^2(x_1) J_m^2(x_2) \sqrt{\epsilon_2}\, \Psi(h_\parallel), \qquad \text{(B.30)}
$$

$$
\zeta_m^{(z)}(h_\parallel) = h_{1\perp}^4 h_{2\perp}^4 R^4 \epsilon_1 H_m^2(x_1) J_m^2(x_2) \Psi(h_\parallel), \qquad \text{(B.31)}
$$

$$
\zeta_m^{(\phi)}(h_\parallel) = h_{1\perp}^4 h_{2\perp}^4 R^4 x' \epsilon_1 H_m^2(x_1) J_m^2(x_2) \Psi(h_\parallel), \qquad \text{(B.32)}
$$

$$
\begin{aligned}
\Psi(h_\parallel) = {} & \frac{m^2 h_\parallel^2}{R^2} \left(\frac{1}{h_{2\perp}^2} - \frac{1}{h_{1\perp}^2} \right)^2 - \left(\frac{1}{h_{2\perp}} \frac{J'_m(x_2)}{J_m(x_2)} - \frac{1}{h_{1\perp}} \frac{H'_m(x_1)}{H_m(x_1)} \right) \times \\
& \left(\frac{\epsilon_2}{h_{2\perp}} \frac{J'_m(x_2)}{J_m(x_2)} - \frac{\epsilon_1}{h_{1\perp}} \frac{H'_m(x_1)}{H_m(x_1)} \right). \qquad \text{(B.33)}
\end{aligned}
$$

Here we have defined $x_1 = h_{1\perp} R$ and $x_2 = h_{2\perp} R$, and the superscripts $(\rho), (z), (\phi)$ denote the solutions for a dipole in these orientations. The remaining coefficients

b_m, c_m, d_m that are not explicitly given do not show up in the spontaneous emission rate of the dipole and need not be considered further here.

The total spontaneous emission rate is related to the field in quadrature at the emitter position. Classically, this quantity is related to the time-averaged power delivered from the oscillating dipole to the field. The exact relationship is given by

$$\frac{\Gamma_{\text{total}}}{\Gamma_0} = 1 + \frac{6\pi\epsilon_0}{k_0^3\sqrt{\epsilon_1}} \frac{\text{Im}\left(\mathbf{p}_0 \cdot \mathbf{E}_{sc}(\mathbf{r}')\right)}{p_0^2}, \tag{B.34}$$

where Γ_0 is the spontaneous emission rate of the emitter in a uniform dielectric ϵ_1. As discussed in Chapter 2, we assume that it is related to the emission rate Γ_v in vacuum by $\Gamma_0 = \sqrt{\epsilon_1}\Gamma_v$, ignoring possible local-field corrections to this rate [61]. Using Eq. (B.24), which gives the fields along z, and Eq. (A.4), which relates the fields along z to the fields along other directions, Eq. (B.34) can readily be re-written in terms of integrals involving the coefficients a_m and b_m. For example, in the case of a radially oriented dipole,

$$\begin{aligned}\frac{\Gamma^{(\rho)}_{\text{total}}}{\Gamma_0} &= 1 + \frac{6\pi\epsilon_0}{k_0^3\sqrt{\epsilon_1}p_0}\text{Im}\left[\sum_{m=-\infty}^{\infty}\int_C dh_\parallel \frac{ih_\parallel}{h_{1\perp}} H'_m(x')a_m(h_\parallel)\right. \\ &\left. - \frac{mk_1}{h_{1\perp}x'}H_m(x')b_m(h_\parallel)\right]. \end{aligned}\tag{B.35}$$

Generally these emission rate expressions are not easily to evaluate, even approximately, except in certain limiting cases such as a small nanowire (where the quasi-static approximation holds). However, they are straightforward to solve numerically. The total emission rate can be split up into radiative, guided, and non-radiative contributions as follows. First, the radiative emission is due to the contribution to the integral in Eq. (B.35) from the region $|h_\parallel| < \sqrt{\epsilon_1}\omega/c$, where all components of the scattered field wavevector are real (see Fig. B.1). Second, the emission rate into the guided modes can be found by evaluating the contribution to Eq. (B.35) from the poles in the integrand, as shown in Fig. B.1. Because these are guided modes, their wavevectors must satisfy $|h_{\|}| > \sqrt{\epsilon_1}\omega/c$. Finally, any non-radiative emission (*e.g.*, into heating) can be found by evaluating non-resonant contributions to the integral from regions $|h_{\|}| > \sqrt{\epsilon_1}\omega/c$. If there are no inherent losses in the system ($\mathrm{Im}\,\epsilon_2 = 0$), then this contribution is zero. Generally, when losses are present, the distinction between guided emission and non-radiative emission is not perfectly well-defined, since the guided emission also decays after some propagation length, but the two can be separated by some reasonable (but nonetheless arbitrary) prescription.

Appendix C

Electromagnetic simulations using boundary element method

Our numerical implementation of the boundary element method (BEM) for electromagnetic simulations is based upon the method given in Ref. [64].

We assume that our system contains a set of known, time-harmonic source charges and currents $\rho_{\mathrm{ext}}, \mathbf{j}_{\mathrm{ext}}$ in the presence of some scattering dielectric body whose surface is denoted S (although we discuss one body here, BEM is easily generalizable to treat multiple scatterers). In the case of interest, S represents the surface of a metallic nanotip, while the external source corresponds to an oscillating point dipole $\mathbf{p}_0 e^{-i\omega t}$ at some location $\mathbf{r}'$. For simplicity we also assume that we are working with non-magnetic media, and we denote by ϵ_j $(j = 1, 2)$ the dimensionless electric permittivities outside and inside S, respectively. The underlying principle behind BEM is that the scalar and vector potentials $\phi_j(\mathbf{r})$ and $\mathbf{A}_j(\mathbf{r})$ in each region can be written (in the Lorenz gauge) in the form

$$\begin{aligned} \phi_j(\mathrm{r}) &= \frac{1}{\epsilon_0\epsilon_j}\int d\mathrm{r}'\, G_j(\mathrm{r}-\mathrm{r}')\rho_{\mathrm{ext}}(\mathrm{r}') + \frac{1}{\epsilon_0\epsilon_j}\int_S ds\, G_j(\mathrm{r}-\mathrm{s})\sigma_j(\mathrm{s}), & \text{(C.1)} \\ \mathrm{A}_j(\mathrm{r}) &= \mu_0\int d\mathrm{r}'\, G_j(\mathrm{r}-\mathrm{r}')\mathrm{j}_{\mathrm{ext}}(\mathrm{r}') + \mu_0\int_S ds\, G_j(\mathrm{r}-\mathrm{s})\mathrm{h}_j(\mathrm{s}), & \text{(C.2)} \\ G_j(\mathrm{r}) &= \frac{e^{ik_jr}}{4\pi r}, & \text{(C.3)} \end{aligned}$$

where G_j is the Green's function in a medium of uniform permittivity ϵ_j, and $k_j = \sqrt{\epsilon_j}(\omega/c)$. Physically, the equations above state that the fields in region j can be described as a result of the combination of the external sources and some effective surface charge and current distributions σ_j, h_j on S. In general, these effective distributions do not have physical significance; for example, they do not correspond to actual charges and currents, and the distributions in region 1 and region 2 are not necessarily equal (*e.g.*, $\sigma_1(\mathrm{s}) \neq \sigma_2(\mathrm{s})$). The values of σ_j, h_j are not known initially, but a set of linear integral equations for these distributions results from enforcing various boundary conditions for the scalar and vector potentials at S.

In particular, we enforce the following conditions at points $\mathrm{r}\in S$:

- Continuity of ϕ:

$$\int_S ds\ (G_1(\mathrm{r}-\mathrm{s})\sigma_1(\mathrm{s}) - G_2(\mathrm{r}-\mathrm{s})\sigma_2(\mathrm{s})) = -(\phi_{1,\mathrm{ext}}(\mathrm{r}) - \phi_{2,\mathrm{ext}}(\mathrm{r}))\,, \tag{C.4}$$

where we have defined a "free" scalar potential

$$\phi_{j,\mathrm{ext}}(\mathrm{r}) \equiv \frac{1}{\epsilon_j}\int d\mathrm{r}'\, G_j(\mathrm{r}-\mathrm{r}')\rho_{\mathrm{ext}}(\mathrm{r}'). \tag{C.5}$$

For simple forms of sources (*e.g.*, point dipoles), analytical expressions for the free potentials can be easily found. Also, it should be noted that the Green's function $G_j(\mathbf{r})$ has a divergence at $\mathbf{r} = 0$; however, this divergence is integrable so Eq. (C.4) remains well-behaved.

- Continuity of $\mathbf{A}$:

$$\int_S d\mathbf{s}\ \left(G_1(\mathbf{r}-\mathbf{s})\mathbf{h}_1(\mathbf{s}) - G_2(\mathbf{r}-\mathbf{s})\mathbf{h}_2(\mathbf{s})\right) = -\left(\mathbf{A}_{1,\mathrm{ext}}(\mathbf{r}) - \mathbf{A}_{2,\mathrm{ext}}(\mathbf{r})\right), \tag{C.6}$$

where we have defined a "free" vector potential

$$\mathbf{A}_{j,\mathrm{ext}}(\mathbf{r}) \equiv \mu_0 \int d\mathbf{r}'\, G_j(\mathbf{r}-\mathbf{r}')\mathbf{j}_{\mathrm{ext}}(\mathbf{r}'). \tag{C.7}$$

- Continuity of $\mathbf{D}_\perp$:

The normal component of the electric displacement $\mathbf{D}_\perp = \epsilon\mathbf{E}_\perp$ is given in the Lorenz gauge by $\mathbf{D}_\perp = \left(\epsilon\hat{n}_s \cdot (i\omega\mathbf{A} - \nabla\phi)\right)\hat{n}_s$. Here $\hat{n}_s$ denotes the inward-pointing (from region 1 to 2) normal vector. We first define the normal derivatives of the free Green's functions,

$$H_j \equiv \hat{n}_s \cdot \nabla_{\mathbf{r}} G_j(\mathbf{r}-\mathbf{s}). \tag{C.8}$$

Continuity of $\mathbf{D}_\perp$ can then be written in the form

$$\begin{aligned}
&-i\omega\left(\epsilon_1\hat{n}_s \cdot \mathbf{A}_{1,\mathrm{ext}} - \epsilon_2\hat{n}_s\mathbf{A}_{2,\mathrm{ext}}\right) + \left(\epsilon_1\hat{n}_s \cdot \nabla\phi_{1,\mathrm{ext}} - \epsilon_2\hat{n}_s \cdot \nabla\phi_{2,\mathrm{ext}}\right) \\
&\quad = i\omega\hat{n}_s \cdot \int_S d\mathbf{s}\ \left(\epsilon_1 G_1(\mathbf{r}-\mathbf{s})\mathbf{h}_1(\mathbf{s}) - \epsilon_2 G_2(\mathbf{r}-\mathbf{s})\mathbf{h}_2(\mathbf{s})\right) \\
&\quad - \int_S d\mathbf{s}\ \left(\epsilon_1 H_1(\mathbf{r}-\mathbf{s})\sigma_1(\mathbf{s}) - \epsilon_2 H_2(\mathbf{r}-\mathbf{s})\sigma_2(\mathbf{s})\right).
\end{aligned} \tag{C.9}$$

Like with G_j, the function $H_j(\mathbf{r})$ has an integrable divergence at $\mathbf{r} = 0$.

- Continuity of $\mathbf{H}_\parallel$:

Consider some point $\mathbf{r} \in S$, and let us define an orthonormal coordinate system u, v, w at this point such that $\hat{w}$ is normal to the interface here. Then the tangential magnetic field is related to the vector potential $\mathbf{A}$ by

$$\mathbf{H}_{\|} = \left(\frac{\partial A_w}{\partial v} - \frac{\partial A_v}{\partial w} \right) \hat{u} + \left(\frac{\partial A_u}{\partial w} - \frac{\partial A_w}{\partial u} \right) \hat{v}. \tag{C.10}$$

To facilitate numerical solutions, we would like to re-write such an expression in terms of the already-defined quantities G_j and H_j. To do this, we first note that the tangential derivative of $\mathbf{A}$, $\partial \mathbf{A}/\partial \mathbf{r}_{\|}$, is clearly continuous at the interface, and thus continuity of $\mathbf{H}_{\|}$ implies that the normal derivative of $\mathbf{A}_{\|}$, or $\partial \mathbf{A}_{\|}/\partial w$, is continuous as well. Finally, continuity of $\partial \mathbf{A}_{\|}/\partial w$ and $\partial \mathbf{A}/\partial \mathbf{r}_{\|}$ together imply that $(\hat{n}_s \cdot \nabla) \mathbf{A} - (\nabla \cdot \mathbf{A}) \cdot \hat{n}_s$ is continuous, and taking advantage of the Lorenz gauge condition, we conclude that $(\hat{n}_s \cdot \nabla) \mathbf{A} - i\omega\epsilon\mu_0\phi\hat{n}_s$ must be continuous. This can be written as

$$\begin{aligned}
&-(\hat{n}_s \cdot \nabla)(\mathbf{A}_{1,\mathrm{ext}} - \mathbf{A}_{2,\mathrm{ext}}) + i\omega\mu_0\hat{n}_s(\epsilon_1\phi_{1,\mathrm{ext}} - \epsilon_2\phi_{2,\mathrm{ext}}) = \\
&\left(\int_S ds\, H_1(\mathbf{r}-\mathbf{s})\mathbf{h}_1(\mathbf{s}) - H_2(\mathbf{r}-\mathbf{s})\mathbf{h}_2(\mathbf{s}) \right) \\
&-i\omega\mu_0\hat{n}_s \left(\int_S ds\, \epsilon_1 G_1(\mathbf{r}-\mathbf{s})\sigma_1(\mathbf{s}) - \epsilon_2 G_2(\mathbf{r}-\mathbf{s})\sigma_2(\mathbf{s}) \right).
\end{aligned} \tag{C.11}$$

Eqs. (C.4), (C.6), (C.9), and (C.11) can be written symbolically as

$$\begin{aligned}
\phi_{\mathrm{ext}} &= G_1\sigma_1 - G_2\sigma_2, \\
\mathbf{A}_{\mathrm{ext}} &= G_1\mathbf{h}_1 - G_2\mathbf{h}_2, \\
D_{\mathrm{ext}} &= \epsilon_1 H_1\sigma_1 - \epsilon_2 H_2\sigma_2 - i\omega\hat{n}_s \cdot (\epsilon_1 G_1\mathbf{h}_1 - \epsilon_2 G_2\mathbf{h}_2), \\
\alpha_{\mathrm{ext}} &= H_1\mathbf{h}_1 - H_2\mathbf{h}_2 - i\omega\mu_0\hat{n}_s(\epsilon_1 G_1\sigma_1 - \epsilon_2 G_2\sigma_2),
\end{aligned} \tag{C.12}$$

where

$$\phi_{\text{ext}} \equiv \phi_{2,\text{ext}} - \phi_{1,\text{ext}}, \tag{C.13}$$

$$\mathbf{A}_{\text{ext}} \equiv \mathbf{A}_{2,\text{ext}} - \mathbf{A}_{1,\text{ext}}, \tag{C.14}$$

$$D_{\text{ext}} \equiv i\omega\hat{n}_s \cdot \left(\epsilon_1 \mathbf{A}_{1,\text{ext}} - \epsilon_2 \mathbf{A}_{2,\text{ext}}\right) - \left(\epsilon_1 \hat{n}_s \cdot \nabla\phi_{1,\text{ext}} - \epsilon_2 \hat{n}_s \cdot \nabla\phi_{2,\text{ext}}\right), \tag{C.15}$$

$$\alpha_{\text{ext}} = \left(\hat{n}_s \cdot \nabla\right) \mathbf{A}_{\text{ext}} + i\omega\mu_0\hat{n}_s \left(\epsilon_1\phi_{1,\text{ext}} - \epsilon_2\phi_{2,\text{ext}}\right). \tag{C.16}$$

It is straightforward to invert Eq. (C.12) to get solutions for the effective charge and current distributions $\sigma_j, \mathbf{h}_j$ [64],

$$\begin{aligned}\sigma_j &= G_j^{-1} X^{-1} \left\{ D_{\text{ext}} - \epsilon_{j'}\Delta_{j'}\phi_{\text{ext}} + i\omega\hat{n}_s \cdot \Delta^{-1} \left[\left(\epsilon_1 - \epsilon_2\right) \left(\boldsymbol{\alpha} + i\mu_0\omega\hat{n}_s\epsilon_{j'}\phi_{\text{ext}}\right) \right.\right. \\ &\quad \left.\left. + \left(\epsilon_2\Delta_1 - \epsilon_1\Delta_2\right) \mathbf{A}_{\text{ext}} \right] \right\}, \end{aligned} \tag{C.17}$$

$$\mathbf{h}_j = G_j^{-1}\Delta^{-1} \left\{ \boldsymbol{\alpha} - \Delta_{j'}\mathbf{A}_{\text{ext}} + i\omega\mu_0\hat{n}_s \left(\epsilon_1 G_1 \sigma_1 - \epsilon_2 G_2 \sigma_2\right) \right\}, \tag{C.18}$$

where

$$\Delta_j \equiv H_j G_j^{-1}, \tag{C.19}$$

$$\Delta \equiv \Delta_1 - \Delta_2, \tag{C.20}$$

$$X \equiv \epsilon_1\Delta_1 - \epsilon_2\Delta_2 + \mu_0\omega^2 \left(\epsilon_1 - \epsilon_2\right)^2 \left(\hat{n}_s \cdot \Delta^{-1}\hat{n}_s\right), \tag{C.21}$$

and $j' = 1\,(2)$ when $j = 2\,(1)$.

To calculate the surface charge and current distributions numerically, if the boundary S is finite, one can mesh up the surface into a finite number of grid points, assuming that all quantities (Green's functions, surface charge distributions, etc.) are constant over a single grid point. Note that the right-hand sides of Eq. (C.18) depend only on the external sources and free Green's functions, which are already known, and with a finite mesh turn into simple products of matrices and vectors. Thus Eq. (C.18) can be numerically solved to find $\sigma_j, \mathbf{h}_j$ at each grid point. Once these distributions are known, the potentials $\phi, \mathbf{A}$ and then the fields $\mathbf{E}, \mathbf{H}$ can be calculated.

In our problem of interest, we assume that the dipole is located on the z-axis and oriented along $\hat{z}$, while the nanotip is described by a paraboloid of revolution around the z-axis. Due to the axial symmetry of the system, BEM simulations are advantageous because one only needs to calculate the unknown distributions along one dimension instead of over the entire two-dimensional surface S. At the same time, the source is a dipole oscillating at constant frequency, and thus the external charges and currents are calculated quite easily. In BEM (at least in the current formulation), it is necessary that the nanotip surface S be finite, and we implement this numerically by tapering and rounding off the nanotip far from the region of interest. In general, any termination can result in some back-reflection of the guided surface plasmons, and this results in some small oscillations of the fields due to interference with the forward-propagating surface plasmons, as barely seen, *e.g.*, in Fig. 2.6. In our simulations, the reflected amplitude is kept to within a few percent. Very fine meshes were used to ensure accuracy; in most of our simulations, for example, the spacing between points in the regions of constant nanotip radius was approximately $\lambda_{\mathrm{pl}}/400$.

Appendix D

Derivation of coupled-mode equations

In this section we derive the equations of evolution for two electromagnetically coupled systems based on Lorentz reciprocity.

First we derive the Lorentz reciprocity equation generally. Assuming non-magnetic media, suppose that $\{\mathbf{E}_1(\mathbf{r}), \mathbf{H}_1(\mathbf{r}), \epsilon_1(\mathbf{r})\}$ and $\{\mathbf{E}_2(\mathbf{r}), \mathbf{H}_2(\mathbf{r}), \epsilon_2(\mathbf{r})\}$ separately satisfy Maxwell's Equations. At this point the systems $1, 2$ and their field solutions are not necessarily related to each other at all. In the following we assume that all fields $\mathbf{E}(\mathbf{r}, t) = \mathbf{E}(\mathbf{r})e^{-i\omega t}$,$\mathbf{H}(\mathbf{r}, t) = \mathbf{H}(\mathbf{r})e^{-i\omega t}$ have harmonic time dependence. Using the vector identity

$$\nabla \cdot (\mathbf{a} \times \mathbf{b}) = \mathbf{b} \cdot (\nabla \times \mathbf{a}) - \mathbf{a} \cdot (\nabla \times \mathbf{b}), \tag{D.1}$$

and the curl relations of Maxwell's Equations we can write

$$\nabla \cdot (\mathbf{E}_1 \times \mathbf{H}_2^*) \;=\; \mathbf{H}_2^* \cdot (\nabla \times \mathbf{E}_1) - \mathbf{E}_1 \cdot (\nabla \times \mathbf{H}_2^*)$$

$$= \mathbf{H}_2^* \cdot (i\omega\mu_0 \mathbf{H}_1) - \mathbf{E}_1 \cdot (i\omega\epsilon_0\epsilon_2^* \mathbf{E}_2^*), \tag{D.2}$$

and similarly

$$\begin{aligned} \nabla \cdot (\mathbf{E}_2^* \times \mathbf{H}_1) &= \mathbf{H}_1 \cdot (\nabla \times \mathbf{E}_2^*) - \mathbf{E}_2^* \cdot (\nabla \times \mathbf{H}_1) \\ &= \mathbf{H}_1 \cdot (-i\omega\mu_0 \mathbf{H}_2^*) - \mathbf{E}_2^* \cdot (-i\omega\epsilon_0\epsilon_1 \mathbf{E}_1). \end{aligned} \tag{D.3}$$

Adding up Eqs. (D.2) and (D.3) yields the equation for Lorentz reciprocity,

$$\nabla \cdot (\mathbf{E}_1 \times \mathbf{H}_2^* + \mathbf{E}_2^* \times \mathbf{H}_1) = i\omega\epsilon_0 \mathbf{E}_1 \cdot \mathbf{E}_2^* (\epsilon_1(\mathbf{r}) - \epsilon_2^*(\mathbf{r})). \tag{D.4}$$

We now derive coupled-mode equations for two waveguides based on the Lorentz reciprocity equation above. This derivation closely follows that of Ref. [66]. We emphasize that the nature of the waveguides can be quite general, *e.g.*, they can be any type of normal dielectric or plasmonic waveguide. We let the indices $\mu, \nu = a, b$ refer to the system consisting of waveguide a without the presence of system b, and b the system consisting of waveguide b without the presence of a. We also assume that the surrounding dielectrics for systems a, b are the same, *i.e.*, $\epsilon_a(r = \infty) = \epsilon_b(r = \infty)$, and that the waveguides are co-propagating along the z-direction. It is assumed that the total electric field for the system consisting of waveguides a and b together can be written as

$$\mathbf{E}_T(\mathbf{r}) = \sum_{\nu=a,b} C_\nu(z) \mathbf{E}_\nu(\mathbf{r}), \tag{D.5}$$

with a similar expression for $\mathbf{H}$. That is, we assume that the total field can be written as a linear superposition of the unperturbed modes of systems a, b. For the case where systems a, b each have one allowed mode, the index ν refers to these unperturbed modes. In general, when a, b have $N_{a,b}$ allowed unperturbed modes, ν

is understood to be an index that covers all of these modes. We can derive exact equations of motion for $C_\nu(z)$ by using Eq. (D.4). Specifically, we will let the index $1 = T$ in Eq. (D.4) refer to the total fields $\mathbf{E}_T(\mathbf{r}), \mathbf{H}_T(\mathbf{r})$ and the dielectric profile of the combined system $\epsilon_T(\mathbf{r})$, while we will let the index $2 = \mu$ refer to any one of the allowed, unperturbed modes of systems a, b. Substituting this into Eq. (D.4) yields

$$\nabla \cdot (\mathbf{E}_T \times \mathbf{H}_\mu^* + \mathbf{E}_\mu^* \times \mathbf{H}_T) = i\omega\epsilon_0 \mathbf{E}_T \cdot \mathbf{E}_\mu^* (\epsilon_T(\mathbf{r}) - \epsilon_\mu^*(\mathbf{r})), \qquad \text{(D.6)}$$

or

$$\sum_{\nu=a,b} \nabla \cdot \left(C_\nu(z)\mathbf{E}_\nu \times \mathbf{H}_\mu^* + C_\nu(z)\mathbf{E}_\mu^* \times \mathbf{H}_\nu\right) = i\omega\epsilon_0 \sum_{\nu=a,b} C_\nu(z)\mathbf{E}_\nu \cdot \mathbf{E}_\mu^* \left(\epsilon_T(\mathbf{r}) - \epsilon_\mu^*(\mathbf{r})\right). \qquad \text{(D.7)}$$

Applying the divergence theorem to this result (and assuming that the surface terms vanish at infinity) gives

$$\begin{aligned} &\frac{\partial}{\partial z} \sum_{\nu=a,b} \int d^2\rho \left(C_\nu(z)\mathbf{E}_\nu \times \mathbf{H}_\mu^* + C_\nu(z)\mathbf{E}_\mu^* \times \mathbf{H}_\nu\right) \cdot \hat{z} = \\ &\quad i\omega\epsilon_0 \sum_{\nu=a,b} C_\nu(z) \int d^2\rho \, \mathbf{E}_\nu \cdot \mathbf{E}_\mu^* \left(\epsilon_T(\mathbf{r}) - \epsilon_\mu^*(\mathbf{r})\right). \qquad \text{(D.8)} \end{aligned}$$

The left-hand side can be further simplified,

$$\begin{aligned} LHS &= \frac{\partial}{\partial z} \sum_{\nu=a,b} \int d^2\rho \left(C_\nu(z)\mathbf{E}_\nu \times \mathbf{H}_\mu^* + C_\nu(z)\mathbf{E}_\mu^* \times \mathbf{H}_\nu\right) \cdot \hat{z} \qquad \text{(D.9)} \\ &= \sum_{\nu=a,b} \frac{dC_\nu}{dz} \left(\int d^2\rho \, (\mathbf{E}_\nu \times \mathbf{H}_\mu^* + \mathbf{E}_\mu^* \times \mathbf{H}_\nu) \cdot \hat{z}\right) \\ &\quad + C_\nu(z) \left(\frac{\partial}{\partial z} \int d^2\rho \, (\mathbf{E}_\nu \times \mathbf{H}_\mu^* + \mathbf{E}_\mu^* \times \mathbf{H}_\nu) \cdot \hat{z}\right) \qquad \text{(D.10)} \\ &= \sum_{\nu=a,b} \frac{dC_\nu}{dz} \left(\int d^2\rho \, (\mathbf{E}_\nu \times \mathbf{H}_\mu^* + \mathbf{E}_\mu^* \times \mathbf{H}_\nu) \cdot \hat{z}\right) \\ &\quad + C_\nu(z) \left(i\omega\epsilon_0 \int d^2\rho \, \mathbf{E}_\nu \cdot \mathbf{E}_\mu^* (\epsilon_\nu(\mathbf{r}) - \epsilon_\mu^*(\mathbf{r}))\right), \qquad \text{(D.11)} \end{aligned}$$

where we have applied the divergence theorem on Eq. (D.4) to get the last line.

Substituting Eq. (D.11) back into Eq. (D.8) yields a set of $N_a + N_b$ coupled, first-order differential equations that constitute the coupled-mode equations:

$$\begin{aligned} \sum_\nu \frac{dC_\nu}{dz} P_{\nu\mu}(z) &= -i\omega\epsilon_0 \sum_\nu C_\nu(z) K_{\nu\mu}(z), && \text{(D.12)} \\ P_{\nu\mu}(z) &\equiv \int d^2\rho \, (\mathbf{E}_\nu \times \mathbf{H}_\mu^* + \mathbf{E}_\mu^* \times \mathbf{H}_\nu) \cdot \hat{z}, && \text{(D.13)} \\ K_{\nu\mu}(z) &\equiv \int d^2\rho \, \mathbf{E}_\nu \cdot \mathbf{E}_\mu^* (\epsilon_\nu(\mathbf{r}) - \epsilon_T(\mathbf{r})). && \text{(D.14)} \end{aligned}$$

We emphasize that these coupled-mode equations are exact within the ansatz given by Eq. (D.5).

Appendix E

Derivation of single-photon transistor dynamics

E.1 Transformation for coherent-state input

In Secs. 4.3 and 4.4 we are interested in solving for the dynamics and field correlation functions of a two-level emitter interacting with a coherent state input. For an emitter initialized in its ground state and a right-propagating field input, the initial state can be written under the two-branch approximation in the form $|\tilde{\psi}(t \rightarrow -\infty)\rangle = D(\{\alpha_k e^{-i\nu_k t}\})|vac\rangle|g\rangle$, where the displacement operator $D(\{\alpha_k\}) \equiv \exp(\int dk\, \hat{a}^{\dagger}_{R,k}\alpha_k - \alpha^*_k \hat{a}_{R,k})$ creates a multi-mode coherent state from vacuum [107]. This property of the displacement operator motivates a state transformation given by [175]

$$|\tilde{\psi}\rangle = D\left(\{\alpha_k e^{-i\nu_k t}\}\right)|\psi\rangle, \tag{E.1}$$

so that the initial state is transformed into $|\psi(t\to-\infty)\rangle = |vac\rangle|g\rangle$. In the Heisenberg picture (and for a field initially propagating to the right), the right-going field operator transforms as $\hat{E}_R(z,t)\to\hat{E}_R(z,t)+\mathcal{E}_c(z,t)$, where the external field amplitude is $\mathcal{E}_c(z,t) = (1/\sqrt{2\pi})\int dk\,\alpha_k e^{ikz-i\nu_k t}$. The transformation thus maps the initial coherent state to a classical Rabi frequency (given by $\Omega_c = \sqrt{2\pi}g\mathcal{E}_c$) in the interaction Hamiltonian, while simultaneously mapping the initial photonic state to vacuum. The dynamics of the emitter interacting with the field modes can now be treated under the Wigner-Weisskopf approximation [107], *i.e.*, interaction with the vacuum modes gives rise to an exponential decay rate from $|e\rangle$ to $|g\rangle$ at a rate Γ. The evolution of the atomic operators consequently reduces to the usual Langevin-Bloch equations [107], which enables all properties of the atomic operators and the scattered field to be calculated. In particular, in a frame rotating at the central input field frequency ν, one finds that

$$\begin{aligned}\frac{d}{dt}\sigma_{ge} &= -\frac{\Gamma}{2}\sigma_{ge}+i\delta\sigma_{ge}-i\Omega_c\left(\sigma_{ee}-\sigma_{gg}\right)+\hat{\mathcal{F}}_{ge}(t),\\ \frac{d}{dt}\sigma_{ee} &= -\Gamma\sigma_{ee}-i\Omega_c^*\sigma_{ge}+i\Omega_c\sigma_{eg}+\hat{\mathcal{F}}_{ee}(t),\end{aligned} \tag{E.2}$$

where $\Gamma = \Gamma_{\mathrm{pl}}+\Gamma'$ is the total spontaneous emission rate (consisting of the emission rate into SPs and the emission rate Γ' into all other channels), $\delta = \nu-\omega_{eg}$, and $\hat{\mathcal{F}}_{ij}(t)$ are delta-correlated noise operators associated with the dissipation, whose specific forms are not of importance here. Note that in these equations, the dissipative term in the effective Hamiltonian of Eq. (4.1) and the quantum jump picture are now rigorously replaced by dissipation and fluctuation (*i.e.*, noise) operators that influence evolution of the atomic operators [107].

In the two-branch approximation, the Heisenberg equation of motion for the right-going field is given by

$$\left(\frac{\partial}{\partial z}+\frac{1}{v}\frac{\partial}{\partial t}\right)\hat{E}_R(z,t)=\frac{\sqrt{2\pi}ig}{v}\sigma_{ge}(t)\delta(z-z_a), \tag{E.3}$$

which can be formally integrated, giving

$$\hat{E}_R(z,t)=\hat{E}_{R,free}(z-vt)+\frac{\sqrt{2\pi}ig}{v}\sigma_{ge}\left(t-(z-z_a)/v\right)\Theta(z-z_a), \tag{E.4}$$

where $\Theta(z)$ is the step function. Similarly,

$$\hat{E}_L(z,t)=\hat{E}_{L,free}(z+vt)+\frac{\sqrt{2\pi}ig}{v}\sigma_{ge}\left(t+(z-z_a)/v\right)\Theta(z_a-z). \tag{E.5}$$

Assuming that the field initially propagates to the right, $\hat{E}_R(z,t)$ is the field transmitted past the emitter for $z>z_a$, while for $z<z_a$, $\hat{E}_L(z,t)$ is the reflected field.

E.2 Field correlations

Under the transformation given by Eq. (E.1), the first-order correlation function for the right-going field is given by

$$G_R^{(1)}(z,t)=\langle(\hat{E}_R^\dagger(z,t)+\mathcal{E}_c^*(z,t))(\hat{E}_R(z,t)+\mathcal{E}_c(z,t))\rangle, \tag{E.6}$$

which upon evaluating at $z>z_a$ yields the average transmitted intensity. Similarly, the first-order correlation function for the left-going field is

$$G_L^{(1)}(z,t)=\langle\hat{E}_L^\dagger(z,t)\hat{E}_L(z,t)\rangle. \tag{E.7}$$

To evaluate the above expressions, we proceed by substituting Eq. (E.4) and (E.5) into Eq. (E.6) and (E.7), respectively. Because the initial photonic state is vacuum following the transformation, the operators $\hat{E}_{R(L),free}$ have no effect and thus calculation of $G^{(1)}$ reduces to calculating expectation values of atomic operators, which can easily be found via the Langevin-Bloch equations. In particular, for a steady-state coherent input field, the steady-state transmitted and reflected intensities are given by

$$\begin{aligned} G_R^{(1)}(z > z_a) &= \mathcal{E}_c^2 - 2\frac{\sqrt{2\pi}g}{v}\mathcal{E}_c\mathrm{Im}\langle\sigma_{ge}\rangle + \frac{2\pi g^2}{v^2}\langle\sigma_{ee}\rangle, \\ G_L^{(1)}(z < z_a) &= \frac{2\pi g^2}{v^2}\langle\sigma_{ee}\rangle. \end{aligned} \tag{E.8}$$

It is straightforward to find the steady-state solutions for the atomic operator expectation values from Eq. (E.2),

$$\langle\sigma_{ge}\rangle = \frac{2i\Omega_c\tilde{\Gamma}}{|\tilde{\Gamma}|^2 + 8\Omega_c^2}, \tag{E.9}$$

$$\langle\sigma_{ee}\rangle = \frac{1}{2}\left(1 - \frac{|\tilde{\Gamma}|^2}{|\tilde{\Gamma}|^2 + 8\Omega_c^2}\right), \tag{E.10}$$

$$\tilde{\Gamma} \equiv \Gamma + 2i\delta. \tag{E.11}$$

Substituting these solutions into Eq. (E.8), taking the resonant case $\delta = 0$, and identifying $P = \Gamma_{\mathrm{pl}}/\Gamma'$ and $\Omega_c = \sqrt{2\pi}g\mathcal{E}_c$ yields the reflectance and transmittance values found in Eq. (4.8).

Calculation of $g^{(2)}(t)$ (see Eq. (4.9)) proceeds in a similar manner by using Eq. (E.4) to express $g^{(2)}(t)$ in terms of two-time atomic correlations. Specifically, for a stationary process, the (un-normalized) second-order correlation function for the transmitted field following the coherent-state transformation is given by

$$G_R^{(2)}(z > z_a, t) = \langle(\hat{E}_R^\dagger(0) + \mathcal{E}_c^*)(\hat{E}_R^\dagger(t) + \mathcal{E}_c^*)(\hat{E}_R(t) + \mathcal{E}_c)(\hat{E}_R(0) + \mathcal{E}_c)\rangle, \tag{E.12}$$

where the fields are all understood to be evaluated at a common point in space ($z > z_a$). For simplicity, let us take $\mathcal{E}_c$ to be real. Then, expanding out the expression above with Eq. (E.4) and simplifying, we find that

$$\begin{aligned} G_R^{(2)}(z>0,t) &= \mathcal{E}_c^4 - 4\sqrt{2\pi}\frac{g}{c}\mathcal{E}_c^3\left(\mathrm{Im}\langle\sigma_{ge}\rangle\right) \\ &\quad +4\pi\frac{g^2}{c^2}\mathcal{E}_c^2\left(\langle\sigma_{ee}\rangle + \mathrm{Re}\langle\sigma_{eg}(t)\sigma_{ge}(0)\rangle - \mathrm{Re}\langle\sigma_{ge}(t)\sigma_{ge}(0)\rangle\right) \\ &\quad -2\left(\sqrt{2\pi}\frac{g}{c}\right)^3\mathcal{E}_c\mathrm{Im}\left(\langle\sigma_{ee}(t)\sigma_{ge}(0)\rangle + \langle\sigma_{eg}(0)\sigma_{ge}(t)\sigma_{ge}(0)\rangle\right) \\ &\quad +\left(2\pi\frac{g^2}{c^2}\right)^2\langle\sigma_{eg}(0)\sigma_{ee}(t)\sigma_{ge}(0)\rangle. \end{aligned} \tag{E.13}$$

The two-time atomic correlation functions appearing above can be evaluated using the quantum regression theorem [107]. In particular, we can write the Langevin-Bloch equations (E.2) for the atomic operators in the general form

$$\frac{d}{dt}\sigma_i = M_{ij}\sigma_j + \lambda_i + \hat{\mathcal{F}}_i(t), \tag{E.14}$$

where M_{ij} and λ_i are matrices and vectors of coefficients, respectively, and $\hat{\mathcal{F}}_i$ are delta-correlated noise operators. The quantum regression theorem then states that

$$\begin{aligned} \frac{d}{dt}\langle\sigma_i(t)\sigma_k(0)\rangle &= M_{ij}\langle\sigma_j(t)\sigma_k(0)\rangle + \lambda_i\langle\sigma_k(0)\rangle, & \text{(E.15)} \\ \frac{d}{dt}\langle\sigma_k(0)\sigma_i(t)\sigma_m(0)\rangle &= M_{ij}\langle\sigma_k(0)\sigma_j(t)\sigma_m(0)\rangle + \lambda_i\langle\sigma_k(0)\sigma_m(0)\rangle. & \text{(E.16)} \end{aligned}$$

It is tedious but straightforward to solve the above differential equations via, *e.g.*, Laplace transformation, and the details are not reproduced here. For low input intensities, however, the final result is given in Eq. (4.10).

A more detailed understanding of the features in the second-order correlation function $g^{(2)}(t)$ for the transmitted field (Eq. (4.10)) can be gained from a quantum jump picture describing the system's evolution following the detection of an initial photon [111]. Specifically, the change in the wave function following detection is described by the application of a jump operator to the system, given in this case by the transmitted field operator, $\hat{E}_T = \hat{E}_{R,free} + \mathcal{E}_c + \sqrt{2\pi} i g \sigma_{ge}/v$ (cf. Eq. (E.4)). The density matrix following detection is given by $\rho_{jump} = \hat{E}_T \rho_{ss} \hat{E}_T^\dagger / \langle \hat{E}_T^\dagger \hat{E}_T \rangle_{ss}$, where ρ_{ss} is the steady-state density matrix and $\langle\rangle_{ss}$ denotes the average of quantities in steady state.

For large P, $\hat{E}_T$ is strongly influenced by its atomic component. This is responsible for, *e.g.*, the low transmittance $\mathcal{T} \approx (1+P)^{-2}$ in steady-state, as the field scattered by the emitter destructively interferes with the incoming field. Because multiple incident photons increase the transmission probability, the detection of a photon enhances the conditional probability that another photon is present in the system. In the quantum jump picture this translates into a sudden enhancement of the coherence $\langle \sigma_{ge} \rangle$ by a factor of $1+P$ over its steady-state value, $\langle \sigma_{ge} \rangle_{jump} = (1+P)\langle \sigma_{ge} \rangle_{ss} = 2i\Omega_c/\Gamma'$. The destructive interference between the incoming and scattered fields is subsequently lost, and the jump causes a sudden enhancement in the field amplitude $\langle \hat{E}_T \rangle$, as $\langle \hat{E}_T \rangle_{jump} / \langle \hat{E}_T \rangle_{ss} = 1 - P^2$. Note also that for $P > 1$ the jump results in a π-phase shift of the field relative to its equilibrium value. The initial enhancement in $\langle \hat{E}_T \rangle$ gives rise to bunching. Then, the π-phase shift and subsequent relaxation back to equilibrium causes $\langle \hat{E}_T \rangle$ to pass through zero at time $t_0 = (4 \log P)/\Gamma$, which yields the subsequent anti-bunching and reflects the cancellation of the incoming and scattered fields. For $P = 1$, this cancellation happens exactly at $t = 0$ such that $g^{(2)}(0) = 0$.

E.3 Single-photon storage

As discussed in Sec. 4.5, the optimal efficiency for storage of a single photon can be derived from time-reversal symmetry arguments and is found to be $\sim 1 - 1/P$ for large P. For the three-level emitter considered, we can derive this result explicitly by solving for the dynamics of the total wave function of the system.

Specifically, we consider the general time-dependent wave function for a system containing one excitation,

$$|\psi\rangle = \int dk \left(c_{R,k}(t)\hat{a}^{\dagger}_{R,k} + c_{L,-k}(t)\hat{a}^{\dagger}_{L,-k}\right)|g, vac\rangle + c_e(t)|e, vac\rangle + c_s(t)|s, vac\rangle. \quad \text{(E.17)}$$

For simplicity we will set the position of the emitter to be $z_a = 0$. Under the Hamiltonian given in Eq. (4.1), the state amplitudes for the field evolve (in a rotating frame) according to

$$\dot{c}_{R,k}(t) = -i\delta_k c_{R,k}(t) + igc_e(t), \quad \text{(E.18)}$$

$$\dot{c}_{L,-k}(t) = -i\delta_k c_{L,-k}(t) + igc_e(t), \quad \text{(E.19)}$$

where $\delta_k = vk - \omega_{eg}$. These equations can be formally integrated to yield

$$c_{R,k(L,-k)}(t) = c_{R,k(L,-k)}(-\infty)e^{-i\delta_k t} + ig\int_{-\infty}^{t} dt'\, c_e(t')e^{-i\delta_k(t-t')}. \quad \text{(E.20)}$$

Physically, the first term on the right-hand side can be identified with the incident single photon pulse, while the second term corresponds to the field scattered from the emitter. Eq. (E.20) can then be substituted into the equation of motion for $c_e(t)$,

$$\dot{c}_e(t) = -\frac{\Gamma'}{2}c_e(t) + i\Omega(t)c_s(t) + ig\int dk\, \left(c_{R,k}(t) + c_{L,-k}(t)\right), \quad \text{(E.21)}$$

which yields an integro-differential equation involving $c_e(t)$. In a manner analogous to the calculation of spontaneous emission rates via Wigner-Weisskopf [107], the integral over $\int dk \int dt'$ can be evaluated to yield the following equations for the atomic state amplitudes,

$$\dot{c}_e(t) = i\Omega(t)c_s(t) - \frac{\Gamma_{\text{pl}} + \Gamma'}{2}c_e(t) +$$

$$\sqrt{2\pi}ig\left(E_{free}^{(R)}(z=0,t)+E_{free}^{(L)}(z=0,t)\right), \tag{E.22}$$

$$\dot{c}_s(t) = i\Omega^*(t)c_e(t), \tag{E.23}$$

where $E_{free}^{R(L)}(z,t) = (1/\sqrt{2\pi})\langle vac|\int dk\,\hat{a}_{R(L),k}e^{ikz-i\delta_k t}|\psi(-\infty)\rangle$ are the incoming or "free" single-photon wavefunctions (in a rotating frame). Here we have identified $\Gamma_{\text{pl}} = 4\pi g^2/v$ as the spontaneous emission rate into the SP modes. Based on the time-reversal argument, it is evident that optimal storage is obtained by not having the photon incident from one direction, but rather for the photon to be split into two symmetric pulses, which are simultaneously injected into the left- and right-moving modes, *i.e.*, $E_{free}^R(0,t) = E_{free}^L(0,t)$. We can also impose a reasonable constraint that the photon storage process results in no outgoing field at the end, such that $c_{R,k(L,-k)}(\infty) = 0$, which in turn immediately implies the relationship $E_{free}^R(0,t) = E_{free}^L(0,t) = -\sqrt{2\pi}igc_e(t)/v$. Applying these constraints to Eqs. (E.22) and (E.23) yields an implicit expression for the required pulse shape $\Omega(t)$ and the following equation relating the population in state $|s\rangle$ to the incident intensity:

$$\frac{d}{dt}|c_s(t)|^2 = -v^2/(2\pi g^2)\left(\frac{d}{dt}|E_{free}^R(0,t)|^2 - \frac{\Gamma_{\text{pl}}-\Gamma'}{2}|E_{free}^R(0,t)|^2\right). \tag{E.24}$$

Assuming that the incoming field vanishes at $t=\pm\infty$, and enforcing the normalization $\int_{-\infty}^{\infty}dt|E_{free}^R(z,t)|^2 = 1/(2v)$, Eq. (E.24) can be integrated over $t=\pm\infty$ to yield $|c_s(\infty)|^2 = 1-1/P$, which physically corresponds to the probability for successful photon storage and spin flip.

Appendix F

Appendices to Chapter 5

F.1 Derivation of NLSE for photons

The Hamiltonian corresponding to the system described in Fig. 5.1 is given in a rotating frame by

$$\begin{aligned} H &= -\hbar n_z \int dz[\Delta_0 \sigma_{bb} + \Delta_p \sigma_{dd} + g\sqrt{2\pi}((\sigma_{ba} + \sigma_{dc})(\hat{E}_+ e^{ik_0 z} + \hat{E}_- e^{-ik_0 z}) + h.c.) \\ &\quad +((\Omega_+(t) e^{ik_c z} + \Omega_-(t) e^{-ik_c z})\sigma_{bc} + h.c.)], \end{aligned} \tag{F.1}$$

where $\hat{E}_\pm \equiv \hat{E}_\pm(z,t)$ are slowly-varying operators describing the quantum fields, and $\sigma_{ij} \equiv \sigma_{ij}(z,t)$ are collective, continuous operators describing the average of $|i\rangle\langle j|$ over atoms in a small but macroscopic region around z. For simplicity, we have assumed equal transition matrix elements $g_{ba} = g_{dc} = g$ between the quantum fields $\hat{E}_\pm$ and the transitions $|a\rangle$-$|b\rangle$ and $|c\rangle$-$|d\rangle$, where $g_{ij}{\sim}\langle i|r|j\rangle\sqrt{\omega_{ij}/\hbar\epsilon_0 A_{\text{eff}}}$. Note that we have also included a one-photon detuning Δ_0 between the quantum fields and transition $|a\rangle$-$|b\rangle$ (while maintaining two-photon resonance), whose purpose is to provide a group velocity dispersion or "effective mass" term in the field evolution equations. Defining slowly varying operators $\sigma_{ab} = \sigma_{ab,+}e^{ik_0 z} + \sigma_{ab,-}e^{-ik_0 z}$ and $\sigma_{cd} = \sigma_{cd,+}e^{ik_0 z} + \sigma_{cd,-}e^{-ik_0 z}$, the Maxwell-Bloch equations describing evolution of the fields under H are given by

$$\left(\frac{1}{v}\frac{\partial}{\partial t} \pm \frac{\partial}{\partial z}\right) \hat{E}_{\pm}(z,t) = \frac{\sqrt{2\pi} i g n_z}{v} \left(\sigma_{ab,\pm}(z,t) + \sigma_{cd,\pm}(z,t)\right), \tag{F.2}$$

while the usual Langevin-Bloch equations describing evolution of σ_{ij} can be derived following the methods of Refs. [113, 123, 124]. Following these references, we define polariton operators $\Psi_{\pm}$ to describe the collective excitations of field and spin-wave coherence σ_{ac} that result from coupling with the control fields, which in the relevant limit that the excitations are mostly in spin-wave form are given by $\Psi_{\pm} = g\sqrt{2\pi n_z}\hat{E}_{\pm}/\Omega_{\pm}$. To proceed further, we adiabatically eliminate the Langevin-Bloch equations for the fast-decaying atomic operators (*e.g.*, σ_{ab} and σ_{cd}), and slowly-varying operators are solved in terms of $\Psi_{\pm}$, discarding higher time derivatives in the slowly-varying limit. Plugging these results back into Eq. (F.2), and specializing to the case where $\Omega_{\pm}(t) = \Omega$, we obtain evolution equations for the polaritons alone,

$$\frac{1}{v}\partial_t \Psi + \partial_z A = -\frac{1}{v_g}\partial_t \Psi - \frac{2\pi i g^2}{v(2\Delta_p + i\Gamma)} \left(2\Psi^\dagger \Psi + A^\dagger A\right) \Psi + \text{noise}, \tag{F.3}$$

$$\frac{1}{v}\partial_t A + \partial_z \Psi = -\frac{4\pi g^2 n_z}{v(\Gamma - 2i\Delta_0)} A - \frac{2\pi i g^2}{v(2\Delta_p + i\Gamma)} \Psi^\dagger \Psi A + \text{noise}. \tag{F.4}$$

Here we have defined the symmetric and anti-symmetric combinations $\Psi = (\Psi_+ + \Psi_-)/2$ and $A = (\Psi_+ - \Psi_-)/2$, and a group velocity $v_g \approx v\Omega^2/(\pi g^2 n_z)$ under which the pulses would propagate were they not trapped. The total spontaneous emission rates Γ (which include decay into channels other than the guided fiber modes) from states $|b\rangle, |d\rangle$ are assumed to be identical for simplicity. We note that there are also noise operators, which are associated with the dissipative terms in the equations above. Because we are primarily interested in the regime where losses are not significant, the specific form of these operators is not important here. With sufficient optical depth, A can be adiabatically eliminated,

$$A \approx (2i\Delta_0 - \Gamma)v(\partial_z \Psi)/(4\pi g^2 n_z), \tag{F.5}$$

where we have assumed that the nonlinear contribution $\sim \Psi^\dagger \Psi A$ is small. Physically, this result corresponds to a pulse matching phenomenon [176] between the quantum and control fields, whereby any imbalance between Ψ_+ and Ψ_- rapidly goes to zero. Substituting the expression for A back into Eq. (F.3), and considering the relevant case where $v_g \ll v$ yields the NLSE with complex effective mass and two-body interaction strength,

$$i\partial_t \Psi = \frac{(2\Delta_0 + i\Gamma)v_g v}{4\pi g^2 n_z}\partial_z^2 \Psi + \frac{4\pi g^2 v_g}{v(\Delta_p + i\Gamma/2)}\Psi^\dagger \Psi^2 + \text{noise}. \tag{F.6}$$

Identifying $\Gamma_{1D} = 4\pi g^2/v$ and ignoring the loss terms reproduces the ideal NLSE given in Eq. (5.1).

We now consider carefully the limits under which Eq. (5.1) well approximates the complete dynamics of the field. First, one requires that the ac Stark shift of $|c\rangle$ due to the nonlinear interaction fits within the frequency range where EIT is efficient (*i.e.*, within the transparency window), which is conservatively satisfied when $n_{ph}/n_z \ll |\Delta_p|/|\Gamma - 2i\Delta_0|$. In addition, requiring that higher-order derivatives of the field be negligible compared to those appearing in Eq. (5.1) places a restriction on the maximum wavevector k_{max} of the spin-wave excitation. In the TG regime, for example, $k_{max} \sim n_{ph}$ and one consequently finds that $n_{ph}/n_z \ll \Gamma_{1D}/|2\Delta_0 + i\Gamma|$. Finally, as discussed further in Sec. F.4, one must also ensure that the loss terms in Eq. (F.6) do not cause the dissipation of too many photons, which sets a maximum allowed evolution time t_{max} for the system.

F.2 Density-density correlations in one-dimensional system of bosons

Evaluation of the density-density correlation function in the ground state is challenging even though the Hamiltonian in Eq. (5.3) is exactly solvable. However, in the regime of interest where γ is large, one can obtain an analytic expression [129] (we assume that translational invariance is present and therefore $g^{(2)}(z_1, t_1; z_2, t_2) = g^{(2)}(z_1 - z_2 = \Delta z, t_1 - t_2 = \Delta t)$),

$$\begin{aligned} g^{(2)}(\Delta z, \Delta t) \;\; = \;\; & 1 + \frac{K}{4\pi^2 n_{ph}^2} \int_{|q_1| > \pi n_{ph}} \int_{|q_2| < \pi n_{ph}} e^{it(q_1^2 - q_3^2)} \cos[(q_1 - q_2) z \sqrt{K}] \times \\ & [1 + \frac{q_1 - q_2}{\pi \tilde{g}} \int_{-\pi n_{ph}}^{\pi n_{ph}} (\frac{1}{q_3 - q_1} - \frac{1}{q_3 - q_2})], \end{aligned} \tag{F.7}$$

where $K = 1 + 4/\gamma$. Note that $g^{(2)}$ decays as t^{-1} for a range of $t > 0$.

For arbitrary interaction strength one can use the exact solution to numerically evaluate $g^{(2)}$ [129, 130, 131]. On the other hand this numerical solution [130, 131] as well as a number of other arguments [132, 177] suggests that an effective description of a one-dimensional gas of bosons, the Luttinger liquid theory, provides very good long-distance, long-time behavior. Using this theory, one can demonstrate that the density-density correlation function in the ground state exhibits a power-law decay of correlations and $2k_F$ Friedel oscillations,

$$g^{(2)}(\Delta z, \Delta t) = 1 + \frac{K}{2\pi^2 n_{ph}^2} \frac{(\Delta z)^2 - (v_g \Delta t)^2}{[(\Delta z)^2 + (v_g \Delta t)^2]^2} + \frac{B \cos(2k_F \Delta z)}{n_{ph}^2 |\Delta z + i v_g \Delta t|^{2K}} \tag{F.8}$$

where B is a non-universal constant. The interaction parameter K, or Luttinger parameter [132, 177], can be numerically extracted from the exact solution. In the limit of strong interactions, $K = 1 + 4/\gamma$ and tends to 1 in the TG regime. Here

$k_F = \pi n_{ph}$ is an emergent *Fermi* momentum.

In the case of sudden switch-on of the interaction, one can use the completeness of the Bethe-Ansatz wavefunctions and expand the initial state over this basis. Since the matrix elements of the density operator in the Bethe states are known [178], computation of the density-density correlation function starting from an arbitrary initial state can in principle be performed [179].

F.3 Expansion of the pulse

We consider the expansion of the optical pulse during stages i) and ii) introduced in Sec. 5.4. In regime i), the interaction energy of particles can be neglected in comparison with the kinetic energy as long as $\tilde{g}(t)n_{ph}$ is smaller than the kinetic energy $1/m_{\text{eff}}z_0^2$. The time t_1 at which these energies become comparable satisfies $t\propto -\log(N_{ph}^2\gamma_0)$, and thus if one chooses parameters such that $N_{ph}^2\gamma_0 > 1$ free expansion can be ignored (for large photon number one can simultaneously satisfy $\gamma_0 \ll 1$ such that the system is initially non-interacting). Regime ii), which is valid until $\gamma(t = t_c) = 1$, can be analyzed using the usual hydrodynamic equations (see, *e.g.*, Refs. [139, 140]). From the equation of motion for the flow velocity, we find $\dot{v}(t) \sim \frac{n_{ph}}{m_{\text{eff}}z_0} g(t)$, and from the conservation of particle number, $\dot{n}(t) \sim \frac{n_{ph}}{z_0} v(t)$. Assuming that the change in density at the center of the pulse is small, these equations can be integrated to yield a relative change of density $\Delta n_{ph}/n_{ph} \sim 1/\beta^2 N_{ph}^2$.

Next we consider the expansion in the strongly interacting regime. Recent work [137, 138] demonstrated that spreading of a pulse of hard core bosons enhances the "fermionic" character of the wavefunction [137]. While generally this problem requires numerical simulations, the solution turns out to be extremely simple for an initial pulse density of the form $n_{ph}(z) = n_0(1 - z^2/z_0^2)^{1/2}$, which corresponds to hard core bosons released from a parabolic potential [138]. In this case the structure of the density correlations is preserved and there is only a rescaling of length scales [138]. An explicit calculation of $g^{(2)}$ for this system is shown in Fig. 5.2. Another signature of fermionization of an expanding pulse of hard core bosons can be observed in the momentum distribution function $n(k)$ (density at wavevector k), corresponding to the Fourier transform of the first order correlation function $g^{(1)}(z, z') = \langle\psi(z)\psi^\dagger(z')\rangle$. After sufficiently long expansion it approaches a Fermi distribution [137, 138]. We emphasize that the qualitative features of our results remain valid for various shapes of the initial pulse, including Gaussian and parabolic pulses, although numerical analysis is needed to obtain precise answers.

F.4 Photon losses

In Sec. 5.4, we considered the system dynamics when the interaction parameter $\gamma(t) = \tilde{g}(t)m_{eff}/n_{ph}$ (see main text for definitions of $\tilde{g}$ and m_{eff}) has the following exponentially increasing time dependence, $\gamma(t) = \gamma_0 e^{\beta\omega_r t}$. After sufficient time, the system can enter the strongly interacting regime where $\gamma(t) \gg 1$. The maximum value $\gamma = \gamma_{max}$ achievable in our optical system is determined by dissipation of photons via linear and nonlinear losses, whose effects we now analyze more carefully. For concreteness, we will assume that the time dependence of $\gamma(t)$ is completely contained in the interaction strength $\tilde{g} = \Gamma_{1D} v_g / \Delta_p(t)$ via a time-dependent detuning

$$\Delta_p = \frac{m_{eff} \Gamma_{1D} v_g}{2 n_{ph} \gamma_0 e^{\beta \omega_F t}}. \tag{F.9}$$

It is convenient to first define a single-atom cooperativity $\eta = \Gamma_{1D}/\Gamma$, which describes the ratio of emission into the waveguide to total emission, and an optical depth $OD = \eta n_z z_0$. Here Γ is the total spontaneous emission rate of the excited states of the atom, n_z is the density of atoms coupled to the waveguide, and z_0 is the characteristic length of the system. We also recall that the nonlinear Schrodinger equation for the slowly-varying polariton operator Ψ, including losses, is given by Eq. (F.6).

The linear losses are a result of the finite bandwidth of the EIT transparency window, and their contribution to the total field evolution in Eq. (F.6) are given by

$$\frac{\partial \Psi}{\partial t} \sim \frac{\Gamma v_g}{\Gamma_{1D} n_z} \frac{\partial^2 \Psi}{\partial z^2}. \tag{F.10}$$

In the Tonks regime, the largest spatial components of the system are given by $\Delta z \sim 1/\Delta k \sim z_0/N_{ph}$, where N_{ph} is the total number of photons in the system. Then, requiring that the number of photons dissipated is small compared to the initial number of photons yields the following limit on the evolution time of the system,

$$\frac{v_g t}{z_0} \ll \frac{OD}{N_{ph}^2}. \tag{F.11}$$

As described in the main text, the dissipation rate of photons due to nonlinear losses is given in the strongly interacting regime by

$$\Gamma_{loss} \sim \frac{\Gamma}{\Delta_p} \omega_F \tag{F.12}$$

$$\sim \frac{n_{ph}^3 \gamma_0}{m_{eff}^2 \eta v_g} e^{\beta \omega_F t}. \tag{F.13}$$

The total losses are obtained by integrating $\Gamma_{loss}(t)$,

$$P_{loss} = \int_0^t dt'\,\Gamma_{loss}(t'), \tag{F.14}$$

and we require that $P_{loss} \ll 1$ so the system retains most of the photons that were initially present. Simplifying this inequality yields the following limit on t,

$$\frac{v_g t}{z_0} \ll \frac{OD}{\beta N_{ph}^2}\frac{\Gamma}{|\Delta_0|}\log\left(\frac{OD}{N_{ph}}\frac{\beta\eta}{\gamma_0}\frac{\Gamma}{|\Delta_0|}\right). \tag{F.15}$$

In addition to the limit on t imposed by losses and requiring that the majority of the initial photons are retained, there are additional requirements in order for Eq. (5.1) to be valid. In particular, one must ensure that $\Delta_p(t) \gg \Gamma$ in order for adiabatic elimination of state $|d\rangle$ to be valid, which physically corresponds to this state having no significant effect beyond its contribution to an ac Stark shift. In addition, for the adiabatic elimination of the operator A (the anti-symmetric combination of left- and right-propagating polaritons; see Eq. (F.5)) to be valid, leading up to the derivation of Eq. (5.1), one requires that

$$\frac{n_{ph}}{n_z} \ll \frac{|\Delta_p(t)|}{|\Gamma - 2i\Delta_0|}. \tag{F.16}$$

However, one can show that the limitations on t due to linear and nonlinear losses are more stringent and thus these additional inequalities will not be considered further.

Substituting the maximum time t_{max} allowed by linear and nonlinear losses back into the expression $\gamma(t) = \gamma_0 e^{\beta\omega_F t}$ and simplifying yields

$$\gamma_{max} \sim \min\left(\gamma_0 \exp\left(\frac{\beta|\Delta_0|}{\Gamma}\right), \eta\beta\frac{\Gamma}{|\Delta_0|}\frac{OD}{N_{ph}}\right), \tag{F.17}$$

where the first and second terms on the right correspond to linear and nonlinear losses, respectively (Note: defining $\zeta = \Gamma OD/|\Delta_0|N_{ph}$, the limits on t imposed by requiring

$\Delta_p \gg \Gamma$ and validity of the adiabatic elimination of A yield $\gamma_{max} \sim \eta\zeta$ and $\gamma_{max} \sim \zeta^2$, which are larger than the term $\eta\beta\zeta$ appearing in Eq. (F.17) if one reaches the strongly interacting regime). Fixing all other parameters, the value of γ_{max} can be maximized by choosing an optimal detuning $|\Delta_0|$.

Appendix G

Derivation of band structure equation for optical lattice

G.1 The KKR method

The methods for calculating the photonic band structure in an optical lattice have been discussed in detail in Refs. [155, 156, 157], and the derivation here closely follows these techniques. We assume that the lattice is made up of point-like atoms with isotropic polarizability and uniform occupation at each lattice site. The electric field in the lattice satisfies the equation

$$\left[\left(\frac{\omega^2}{c^2}+i\epsilon\right)-(\nabla\times\nabla\times)-V(\omega,\mathrm{r})\right]\mathrm{E}=0, \tag{G.1}$$

where

$$V(\omega,\mathrm{r})\equiv-(\omega/c)^2\alpha_B\sum_{\mathrm{R}}\delta(\mathrm{r}-\mathrm{R})\otimes I. \tag{G.2}$$

Here the tensor product separates spatial degrees of freedom and the polarization degrees of freedom, and the sum on R runs over all lattice sites. From this point the tensor product separating the degrees of freedom will be suppressed. α_B is a bare polarizability that we will relate to physical quantities in further discussions.

One can find the dispersion relation inside the lattice through a means similar to the KKR method in solid-state physics. Mathematically, we can write Eq. (G.1) in the form

$$\left(E - \hat{H} - \hat{V}\right)|\psi\rangle = 0. \tag{G.3}$$

We are interested in finding the eigenvalues E of the equation. The solution can be formally written in terms of the free Green's function $G_0 \equiv (E - \hat{H})^{-1}$:

$$\begin{aligned} |\psi\rangle &= G_0\hat{V}|\psi\rangle, \text{or} && \text{(G.4)} \\ \langle r|\psi\rangle &= \sum_{r_1, r_2} \langle r|G_0|r_1\rangle\langle r_1|\hat{V}|r_2\rangle\langle r_2|\psi\rangle. && \text{(G.5)} \end{aligned}$$

Suppose furthermore that $\hat{V}$ is diagonal and periodic in space, *i.e.*

$$\hat{V}(\mathbf{r}) = \sum_{\mathbf{R}} v(\mathbf{r} - \mathbf{R}), \tag{G.6}$$

where v is defined inside one unit cell and zero everywhere else. Then, we write the eigenstates $|\psi\rangle$ in the form of Bloch solutions with Bloch vector $\mathbf{k}$,

$$\begin{aligned} \psi_{\mathbf{k}}(\mathbf{r}) &= \int d\mathbf{r}_1 \sum_{\mathbf{R}} G_0(\mathbf{r} - \mathbf{r}_1, \omega(\mathbf{k}))v(\mathbf{r}_1 - \mathbf{R})\psi_{\mathbf{k}}(\mathbf{r}_1) && \text{(G.7)} \\ &= \sum_{\mathbf{R}} \int d\mathbf{r}_2 G_0(\mathbf{r} - \mathbf{r}_2 - \mathbf{R}, \omega(\mathbf{k}))v(\mathbf{r}_2)\psi_{\mathbf{k}}(\mathbf{r}_2 + \mathbf{R}), \\ &\quad \text{where } \mathbf{r}_2 = \mathbf{r}_1 - \mathbf{R}, && \text{(G.8)} \\ &= \sum_{\mathbf{R}} \int d\mathbf{r}_2 G_0(\mathbf{r} - \mathbf{r}_2 - \mathbf{R}, \omega(\mathbf{k}))v(\mathbf{r}_2)\psi_{\mathbf{k}}(\mathbf{r}_2)e^{i\mathbf{k}\cdot\mathbf{R}}, && \text{(G.9)} \end{aligned}$$

where we have used Bloch's theorem to write $\psi_{\mathrm{k}}(\mathrm{r}_2+\mathrm{R}) = \psi_{\mathrm{k}}(\mathrm{r}_2)e^{i\mathrm{k}\cdot\mathrm{R}}$ in the last line. With the potential of Eq. (G.2), the dispersion relation $\omega(\mathrm{k})$ is obtained through the determinantal condition

$$\left\| \left\{(\omega(\mathrm{k})/c)^2\alpha_B\right\}^{-1} I + \sum_R G_0(\mathrm{R},\omega(\mathrm{k}))e^{-i\mathrm{k}\cdot\mathrm{R}} \right\| = 0. \tag{G.10}$$

Use of Eq. (G.10) is made slightly more complicated by the fact that one must regularize G_0 in order to cancel the divergence at $\mathrm{r}=0$.

G.2 Regularization of Green's function

The free Green's function G_0 satisfies the equation

$$\left[\left(\frac{\omega^2}{c^2}+i\epsilon\right) - \nabla\times\nabla\times\right] G_0(\omega,\mathrm{r}-\mathrm{r}') = \delta(\mathrm{r}-\mathrm{r}')I. \tag{G.11}$$

It is straightforward to find the solutions in either momentum or real space [157]:

$$\begin{aligned}
G_0(\omega,\mathrm{p}) &= \frac{1}{k^2-p^2+i\epsilon}\Delta_{\mathrm{p}} + \frac{1}{k^2}\hat{\mathrm{p}}\hat{\mathrm{p}} && \text{(G.12)}\\
&\equiv G_0^T(\omega,\mathrm{p}) + G_0^L(\omega,\mathrm{p}), && \text{(G.13)}\\
G_0(\omega,\mathrm{r}) &= \left[-\frac{I-3\hat{\mathrm{r}}\hat{\mathrm{r}}}{4\pi k^2 r^3} - \frac{e^{ikr}}{4\pi r}\left(P(ikr)I + Q(ikr)\hat{\mathrm{r}}\hat{\mathrm{r}}\right)\right] + \\
&\quad \left[\frac{I-3\hat{\mathrm{r}}\hat{\mathrm{r}}}{4\pi k^2 r^3} + \frac{\delta(\mathrm{r})}{3k^2}I\right] && \text{(G.14)}\\
&\equiv G_0^T(\omega,\mathrm{r}) + G_0^L(\omega,\mathrm{r}), && \text{(G.15)}
\end{aligned}$$

where $k \equiv \omega/c$ and $\Delta_{\mathrm{p}} = I - \hat{\mathrm{p}}\hat{\mathrm{p}}$ is the operator that projects onto the subspace orthogonal to p. Here we have separated out the transverse (G_0^T) and longitudinal (G_0^L) components of the Green's function in momentum space. The transverse and longitudinal functions in real space are then defined as the Fourier transforms of the respective components in momentum space. The functions P and Q are defined to be

$$P(z) = 1 - z^{-1} + z^{-2}, \tag{G.16}$$

$$Q(z) = -1 + 3z^{-1} - 3z^{-2}. \tag{G.17}$$

That G_0 must be regularized can be seen by considering the problem of a single point scatterer, whose Green's function satisfies

$$\left[\left(\frac{\omega^2}{c^2} + i\epsilon\right) - V(\omega, \mathbf{r}) - \nabla \times \nabla \times\right] G(\omega, \mathbf{r} - \mathbf{r}') = \delta(\mathbf{r} - \mathbf{r}')I \quad , \tag{G.18}$$

$$V(\omega, \mathbf{r}) \equiv -(\omega/c)^2 \alpha_B \delta(\mathbf{r}) I. \tag{G.19}$$

The solution to G can be expressed in terms of G_0 through the Lippmann-Schwinger equation [35]

$$G(\omega) = G_0(\omega) + G_0(\omega)T(\omega)G_0(\omega), \tag{G.20}$$

$$T(\omega) = V(\omega) + V(\omega)G_0(\omega)V(\omega) + \cdots \tag{G.21}$$

$$= t(\omega)\delta(\mathbf{r})I, \tag{G.22}$$

where the matrix element t is easily calculated to be

$$t(\omega)I = -(\omega/c)^2 \frac{\alpha_B}{I + (\omega/c)^2 \alpha_B G_0(\omega, r = 0)}. \tag{G.23}$$

One can see that t depends on the free Green's function at $r = 0$. If G_0 is not regularized, then its divergence at $r = 0$ causes the matrix element to be zero, *i.e.*, no scattering occurs. It is evident that this unphysical result comes from the large p behavior of G_0 in momentum space, which can be modified by introducing appropriate cutoffs. Physically, the cutoffs are necessary to reconcile the treatment of scatterers idealized by point particles with the fact that Maxwell's Equations represent some macroscopic theory [157]. The cutoff parameters can be subsequently related to physical quantities related to the microscopic properties of the scatterer such as resonance frequency and linewidth.

We introduce the cutoffs [157]

$$G_0^T(\omega, \mathrm{p}) \rightarrow G_0^T(\omega, \mathrm{p}) \times \frac{\Lambda_T^2}{\Lambda_T^2 + p^2}, \tag{G.24}$$

$$G_0^L(\omega, \mathrm{p}) \rightarrow G_0^L(\omega, \mathrm{p}) \times \frac{\Lambda_L^4}{\Lambda_L^4 + p^4}, \tag{G.25}$$

where $\Lambda_T^{-1}, \Lambda_L^{-1}$ are much smaller than the length scales of interest. Thus the behavior of G_0 in real space is unaffected except near the origin. With the cutoff parameters, G_0 now becomes finite, as

$$G_0^T(\omega, r = 0) = -\left(\frac{\Lambda_T}{6\pi} + i\frac{k}{6\pi}\right) I, \tag{G.26}$$

$$G_0^L(\omega, r = 0) = \frac{\Lambda_L^3}{6\pi k^2} I. \tag{G.27}$$

The matrix element t then becomes

$$t(\omega) = -\frac{(\omega/c)^2}{\alpha_B^{-1} + \Lambda_L^3/6\pi - (\omega/c)^2\Lambda_T/6\pi - i(\omega/c)^3/6\pi} \tag{G.28}$$

$$\equiv -(\omega/c)^2\alpha_0\frac{\omega_0^2}{\omega_0^2 - \omega^2 - i(\Gamma_0\omega^3/\omega_0^2)}. \tag{G.29}$$

t evidently corresponds to the dynamic polarizability of a simple scatterer with a single resonance (*e.g.*, a two-level atom), as the bare polarizability α_B and the cutoff parameters Λ_L, Λ_T can be related to the physical quantities $\alpha_0, \omega_0, \Gamma_0$. The value of α_0 is fixed by requiring that the total scattering cross section, $\sigma_{total}(\omega) = -\mathrm{Im}\, t(\omega)/k$, be equal to the scattering cross section, $\sigma_{sc}(\omega) = |t(\omega)|^2/(6\pi)$, which ensures that any extinction in transmitted light due to the particle is due entirely to scattering. This requirement determines that $\alpha_0 = (6\pi)/(Q(\omega_0/c)^3)$, where $Q \equiv \omega_0/\Gamma_0$.

Using Eq. (G.10) and the regularized Green's function, the band structure equation can be simplified to

$$\left\| \sum_{\mathbf{R}\neq 0} e^{-i\mathbf{k}\cdot\mathbf{R}} G_0(\omega, \mathbf{R}) - t^{-1}(\omega) I \right\| = 0. \tag{G.30}$$

It is convenient to solve this determinantal condition in reciprocal space rather than real space. This conversion can easily be made by noting that

$$\frac{1}{\Omega} \sum_{\mathbf{G}} \frac{1}{(\omega/c)^2 I - |\mathbf{k}-\mathbf{G}|^2 \Delta_{\mathbf{k}-\mathbf{G}}} = \sum_{\mathbf{R}} e^{-i\mathbf{k}\cdot\mathbf{R}} G_0(\omega, \mathbf{R}). \tag{G.31}$$

Here Ω denotes the volume of a unit cell. In reciprocal space, one must again remove the divergences. Writing

$$\begin{aligned} \sum_{\mathbf{G}} \frac{1}{(\omega/c)^2 I - |\mathbf{k}-\mathbf{G}|^2 \Delta_{\mathbf{k}-\mathbf{G}}} &= \sum_{\mathbf{G}} \left[\frac{1}{(\omega/c)^2 - |\mathbf{k}-\mathbf{G}|^2} \Delta_{\mathbf{k}-\mathbf{G}} \right. \\ &\quad \left. + (\omega/c)^{-2} \left(\widehat{\mathbf{k}-\mathbf{G}}\right) \left(\widehat{\mathbf{k}-\mathbf{G}}\right) \right], \end{aligned} \tag{G.32}$$

we see that there are two divergences, which we identify as

$$\frac{1}{\Omega} \sum_{\mathbf{G}\neq 0} \frac{1}{G^2} \Delta_{\mathbf{G}} = \frac{1}{\Omega} \sum_{\mathbf{G}\neq 0} \frac{2}{3G^2} I \equiv \frac{\Lambda_T}{6\pi} I, \tag{G.33}$$

$$\frac{1}{\Omega} \sum_{\mathbf{G}} \hat{\mathbf{G}}\hat{\mathbf{G}} = \frac{1}{\Omega} \sum_{\mathbf{G}} \frac{1}{3} I \equiv \frac{\Lambda_L^3}{6\pi} I. \tag{G.34}$$

Subtracting out the divergences, one can ultimately write the equation for the dispersion relation in dimensionless form as given in Eq. (6.2).

Appendix H

Master equation for dipole-dipole interacting atoms

Here we derive a master equation for atoms interacting with each other via common electromagnetic field modes. The field modes are effectively eliminated using the Born-Markov approximation to yield an equation that describes dipole-dipole interactions of the atoms. In the following derivation we follow closely the notation and conventions of Ref. [159].

The Hamiltonian H for the entire system of atoms and field can be written in terms of an unperturbed and an atom-field interaction Hamiltonian,

$$H = H_0 + H_{\mathrm{af}}, \tag{H.1}$$

where

$$\begin{aligned} H_0 &= H_{\mathrm{atoms}} + H_{\mathrm{field}} & \text{(H.2)} \\ &= \sum_{j=1}^{N} \left(\hbar\omega_0 \sigma^j_{ee}\right) + \sum_{\mathbf{k},\mu} \hbar\omega_{\mathbf{k},\mu} \left(a^\dagger_{\mathbf{k},\mu} a_{\mathbf{k},\mu} + \frac{1}{2}\right). & \text{(H.3)} \end{aligned}$$

The atomic operators σ^j are defined as

$$\sigma^j_{ee} = \sigma^j_{eg} \cdot \sigma^j_{ge}, \tag{H.4}$$

$$\sigma^j_{ge} = \left(\sigma^j_{eg}\right)^\dagger, \tag{H.5}$$

$$\sigma^j_{eg} = \sum_{q=-1}^{1} \sigma^j_{eg}(q)\hat{\epsilon}^*_q, \tag{H.6}$$

$$\sigma^j_{eg}(q) = \sum_{m_e,m_g} \langle J_g m_g, 1q|J_e m_e\rangle |J_e m_e\rangle_j \langle J_g m_g|_j, \tag{H.7}$$

while the polarization vectors are defined as

$$\hat{\epsilon}_{\pm 1} = \mp\frac{1}{\sqrt{2}}\left(\hat{\mathrm{x}}\pm i\hat{\mathrm{y}}\right), \hat{\epsilon}_0 = \hat{\mathrm{z}}. \tag{H.8}$$

Here j is an index for the atoms, e and g denote excited and ground states, respectively, m_e and m_g the magnetic quantum numbers of the excited and ground states, and q the polarization of the transition. μ denotes the two possible polarization vectors associated with each field wave vector k. The operators $\hat{a}_{\mathrm{k},\mu}$ annihilate a photon in mode k, μ.

We now consider the evolution of the atom/field system in the interaction picture. The transformation between the full density matrix ρ_{af} in the Schrodinger picture and $\tilde{\rho}_{\mathrm{af}}$ in the interaction picture is given by

$$\tilde{\rho}_{\mathrm{af}} = e^{iH_0 t/\hbar}\rho_{\mathrm{af}}e^{-iH_0 t/\hbar}, \tag{H.9}$$

where $\tilde{\rho}_{\mathrm{af}}$ evolves according to

$$\frac{\partial\tilde{\rho}_{\mathrm{af}}}{\partial t} = \frac{1}{i\hbar}\left[\tilde{H}_{\mathrm{af}}(t), \tilde{\rho}_{\mathrm{af}}\right], \tag{H.10}$$

$$\tilde{H}_{\mathrm{af}}(t) = e^{iH_0 t/\hbar}H_{\mathrm{af}}e^{-iH_0 t/\hbar}. \tag{H.11}$$

The interaction Hamiltonian between the atoms and the field, in the interaction picture, is given by

$$\tilde{H}_{\mathrm{af}} = -\sum_{j=1}^{N}\sum_{\mathbf{k},\mu} \hbar g_k \left(\sigma^j_{eg} e^{i\omega_0 t} + h.c.\right) \cdot \left(a_{\mathbf{k},\mu}\hat{\epsilon}_{\mathbf{k},\mu} e^{i\mathbf{k}\cdot\mathbf{r}_j - i\omega_k t} + h.c.\right). \tag{H.12}$$

The atom-field coupling constant is

$$g_k = \frac{d_{eg}}{\sqrt{2J_e+1}}\sqrt{\frac{\omega_k}{2\hbar\epsilon_0 V}}, \tag{H.13}$$

where d_{eg} is the dipole transition matrix element for each atom.

We can formally integrate Eq. (H.10) once and substitute the result back into itself to obtain an integro-differential equation. We then trace out the field degrees of freedom to obtain an evolution equation for the atomic density matrix $\tilde{\rho} = \mathrm{Tr}_{\mathrm{f}}\,\tilde{\rho}_{\mathrm{af}}$ alone:

$$\frac{\partial\tilde{\rho}}{\partial t} = -\frac{1}{\hbar^2}\mathrm{Tr}_{\mathrm{f}}\int_0^t d\tau \left[\tilde{H}_{\mathrm{af}}(t), \left[\tilde{H}_{\mathrm{af}}(t-\tau), \tilde{\rho}_{\mathrm{af}}(t-\tau)\right]\right]. \tag{H.14}$$

To make the above equation more useful, we make the Born-Markov approximation, replacing $\tilde{\rho}_{\mathrm{af}}(t-\tau)$ with $\tilde{\rho}(t)\otimes|0\rangle\langle 0|$. Physically, this amounts to assuming that correlations in the field are negligible and that the field can always be approximated by a vacuum state, and that the correlation time of the atom-field system is much shorter than any atomic time scales. We can then consistently also extend the time integral to infinity, such that

$$\frac{\partial\tilde{\rho}}{\partial t} \approx -\frac{1}{\hbar^2}\mathrm{Tr}_{\mathrm{f}}\int_0^\infty d\tau \left[\tilde{H}_{\mathrm{af}}(t), \left[\tilde{H}_{\mathrm{af}}(t-\tau), \tilde{\rho}(t)\otimes|0\rangle\langle 0|\right]\right]. \tag{H.15}$$

Explicitly writing out $\tilde{H}_{\mathrm{af}}(t)$ and $\tilde{H}_{\mathrm{af}}(t')$, where $t' = t-\tau$, gives

$$\tilde{H}_{\mathrm{af}}(t) \;=\; -\sum_{j,\mathbf{k},\mu} \hbar g_k \left(\sigma^j_{eg} e^{i\omega_0 t} + \sigma^j_{ge} e^{-i\omega_0 t}\right)\cdot$$

$$
\left(a_{\mathbf{k},\mu}\hat{\epsilon}_{\mathbf{k},\mu}e^{i\mathbf{k}\cdot\mathbf{r}_j-i\omega_k t}+a^{\dagger}_{\mathbf{k},\mu}\hat{\epsilon}^{*}_{\mathbf{k},\mu}e^{-i\mathbf{k}\cdot\mathbf{r}_j+i\omega_k t}\right), \tag{H.16}
$$

$$
\begin{aligned}
\tilde{H}_{\mathrm{af}}(t') &= -\sum_{j',\mathbf{k}',\mu'}\hbar g_{k'}\left(\sigma^{j'}_{eg}e^{i\omega_0 t'}+\sigma^{j'}_{ge}e^{-i\omega_0 t'}\right)\cdot \\
&\quad \left(a_{\mathbf{k}',\mu'}\hat{\epsilon}_{\mathbf{k}',\mu'}e^{i\mathbf{k}'\cdot\mathbf{r}_{j'}-i\omega_{k'}t'}+a^{\dagger}_{\mathbf{k}',\mu'}\hat{\epsilon}^{*}_{\mathbf{k}',\mu'}e^{-i\mathbf{k}'\cdot\mathbf{r}_{j'}+i\omega_{k'}t'}\right).
\end{aligned} \tag{H.17}
$$

When we substitute the expansions above into Eq. (H.15) and perform the trace, the only non-zero terms will be those associated with $a_{\mathbf{k},\mu}a^{\dagger}_{\mathbf{k}',\mu'}|0\rangle\langle 0|$, $a^{\dagger}_{\mathbf{k},\mu}|0\rangle\langle 0|a_{\mathbf{k}',\mu'}$, $a^{\dagger}_{\mathbf{k}',\mu'}|0\rangle\langle 0|a_{\mathbf{k},\mu}$, and $|0\rangle\langle 0|a_{\mathbf{k}',\mu'}a^{\dagger}_{\mathbf{k},\mu}$, where $\mathbf{k}=\mathbf{k}'$ and $\mu=\mu'$. Making these simplifications and replacing the sum on k by an integral gives

$$
\begin{aligned}
\frac{\partial\tilde{\rho}}{\partial t} &= -\frac{V}{(2\pi c)^3}\int_0^{\infty}d\omega_k\,\omega_k^2\sum_{j,j',\mu}g_k^2\int_0^{\infty}d\tau \\
&\quad \Big[e^{ikr_{jj'}-i(\omega_k-\omega_0)\tau}\left(\sigma^{j}_{eg}\cdot\hat{\epsilon}_{\mathbf{k},\mu}\right)\left(\sigma^{j'}_{ge}\cdot\hat{\epsilon}^{*}_{\mathbf{k},\mu}\right)\tilde{\rho}(t) \\
&\quad +e^{ikr_{jj'}-i(\omega_k+\omega_0)\tau}\left(\sigma^{j}_{ge}\cdot\hat{\epsilon}_{\mathbf{k},\mu}\right)\left(\sigma^{j'}_{eg}\cdot\hat{\epsilon}^{*}_{\mathbf{k},\mu}\right)\tilde{\rho}(t) \\
&\quad -e^{-ikr_{jj'}+i(\omega_k+\omega_0)\tau}\left(\sigma^{j}_{eg}\cdot\hat{\epsilon}^{*}_{\mathbf{k},\mu}\right)\tilde{\rho}(t)\left(\sigma^{j'}_{ge}\cdot\hat{\epsilon}_{\mathbf{k},\mu}\right) \\
&\quad -e^{-ikr_{jj'}+i(\omega_k-\omega_0)\tau}\left(\sigma^{j'}_{ge}\cdot\hat{\epsilon}^{*}_{\mathbf{k},\mu}\right)\tilde{\rho}(t)\left(\sigma^{j}_{ge}\cdot\hat{\epsilon}_{\mathbf{k},\mu}\right)+h.c.\Big].
\end{aligned} \tag{H.18}
$$

Here we have omitted all fast-oscillating (or energy non-conserving) terms such as $\sigma^{j}_{ge}\sigma^{j'}_{ge}e^{-2i\omega_0 t}$, and have also defined $\mathbf{r}_{jj'}=\mathbf{r}_j-\mathbf{r}_{j'}$.

The time integral can be evaluated using the formula

$$
\int_0^{\infty}d\tau\,e^{-i(\omega_k\mp\omega_0)\tau}=\pi\delta(\omega_0\mp\omega_k)\pm i\mathcal{P}\frac{1}{\omega_0\mp\omega_k}, \tag{H.19}
$$

where $\mathcal{P}$ denotes the principal value, while the angular integral is straightforward but tedious to evaluate. One then finds that

$$
\begin{aligned}
\frac{\partial\tilde{\rho}}{\partial t} &= \frac{1}{i\hbar}\left(H_{\mathrm{eff}}\tilde{\rho}-\tilde{\rho}H^{\dagger}_{\mathrm{eff}}\right)+\mathcal{L}[\tilde{\rho}], && \text{(H.20)} \\
H_{\mathrm{eff}} &= -i\frac{\hbar\Gamma_0}{2}\sum_{j=1}^{N}\sigma^{j}_{ee}-\frac{\hbar\Gamma_0}{2}\sum_{j\neq j'}\sigma^{j}_{eg}\cdot\left[i\alpha(k_0\mathbf{r}_{jj'})+\beta(k_0\mathbf{r}_{jj'})\right]\cdot\sigma^{j'}_{ge}, && \text{(H.21)}
\end{aligned}
$$

$$\mathcal{L}[\tilde{\rho}] \;=\; \Gamma_0 \sum_{j\neq j'} \sigma^{j}_{ge} \cdot \tilde{\rho}\alpha(\mathrm{r}_{jj'}) \cdot \sigma^{j'}_{eg}, \tag{H.22}$$

where $\Gamma_0 = k_0^3 d_{eg}^2/[3\pi\epsilon_0\hbar(2J_e+1)]$ is the spontaneous emission rate of a single atom.

The tensors α and β are given by

$$\alpha(\rho) \;=\; \frac{3}{2}(I-\hat{\rho}\hat{\rho})\frac{\sin\rho}{\rho} + \frac{3}{2}(I-3\hat{\rho}\hat{\rho})\left(\frac{\cos\rho}{\rho^2} - \frac{\sin\rho}{\rho^3}\right), \tag{H.23}$$

$$\beta(\rho) \;=\; \frac{3}{2}(I-\hat{\rho}\hat{\rho})\frac{\cos\rho}{\rho} - \frac{3}{2}(I-3\hat{\rho}\hat{\rho})\left(\frac{\sin\rho}{\rho^2} + \frac{\cos\rho}{\rho^3}\right). \tag{H.24}$$

Appendix I

Roughness and temperature-dependent surface plasmon propagation losses

This appendix contains details of the calculations presented in Sec. 2.6 of SP propagation losses as functions of surface roughness and temperature.

I.1 Radiative scattering

Suppose that in the presence of roughness, the first-order scattered field E_z is given by Eq. (2.63). Using the expressions derived in Eq. (2.3) for the unperturbed, incident SP field, and letting $k_{\|}$ denote the unperturbed SP wavevector, the total (incident plus scattered) fields to first order in p are given by

$$\mathrm{E}_1^{\text{total}} = \left(\frac{ik_{\|}k_{1\perp}}{k_1^2} b_1 H_0'(k_{1\perp}\rho) e^{ik_{\|}z} + p \int_{-\infty}^{\infty} dh_{\|} \, \frac{ih_{\|}h_{1\perp}}{k_1^2} H_0'(h_{1\perp}\rho) e^{ih_{\|}z} A(h_{\|}) \right) \hat{\rho}$$

$$\begin{aligned}
& + \left(\frac{k_{1\perp}^2}{k_1^2} b_1 H_0(k_{1\perp}\rho) e^{ik_\parallel z} + p \int_{-\infty}^{\infty} dh_\parallel \, \frac{h_{1\perp}^2}{k_1^2} H_0(h_{1\perp}\rho) e^{ih_\parallel z} A(h_\parallel) \right) \hat{z} \\
\mathrm{E}_2^{\mathrm{total}} &= \left(\frac{ik_\parallel k_{2\perp}}{k_2^2} b_2 J_0'(k_{2\perp}\rho) e^{ik_\parallel z} + p \int_{-\infty}^{\infty} dh_\parallel \, \frac{ih_\parallel h_{2\perp}}{k_2^2} J_0'(h_{2\perp}\rho) e^{ih_\parallel z} B(h_\parallel) \right) \hat{\rho} \\
& + \left(\frac{k_{2\perp}^2}{k_2^2} b_2 J_0(k_{2\perp}\rho) e^{ik_\parallel z} + p \int_{-\infty}^{\infty} dh_\parallel \, \frac{h_{2\perp}^2}{k_2^2} J_0(h_{2\perp}\rho) e^{ih_\parallel z} B(h_\parallel) \right) \hat{z} \\
H_{1,\phi}^{\mathrm{total}} &= \frac{1}{\omega\mu_0} \left[ik_{1\perp} b_1 H_0'(k_{1\perp}\rho) e^{ik_\parallel z} + p \int_{-\infty}^{\infty} dh_\parallel \, ih_{1\perp} H_0'(h_{1\perp}\rho) e^{ih_\parallel z} A(h_\parallel) \right] \\
H_{2,\phi}^{\mathrm{total}} &= \frac{1}{\omega\mu_0} \left[ik_{2\perp} J_0'(k_{2\perp}\rho) b_2 e^{ik_\parallel z} + p \int_{-\infty}^{\infty} dh_\parallel \, ih_{2\perp} J_0'(h_{2\perp}\rho) e^{ih_\parallel z} B(h_\parallel) \right]. \qquad \text{(I.1)}
\end{aligned}$$

The boundary condition equations in Eq. (2.64) can be solved by plugging in the fields above, carefully expanding the equations as a power series in p, and then solving for each order of p, utilizing the expansions

$$\begin{aligned}
\hat{t} &= \hat{z} + p\frac{d\zeta}{dz}\hat{\rho} + \mathcal{O}(p^2), \\
F_{i,m}(k_{i\perp}\rho_0) &= F_{i,m}(k_{i\perp}R) + p\zeta k_{i\perp} F_{i,m}'(k_{i\perp}R) + \mathcal{O}(p^2), \\
F_{i,m}(h_{i\perp}\rho_0) &= F_{i,m}(h_{i\perp}R) + p\zeta h_{i\perp} F_{i,m}'(h_{i\perp}R) + \mathcal{O}(p^2), \qquad \text{(I.2)}
\end{aligned}$$

where $F_{1,m}(x) = H_m(x)$ and $F_{2,m}(x) = J_m(x)$. The resulting $\mathcal{O}(p^0)$ equations are trivially satisfied by the SP fields of a smooth nanowire, while the $\mathcal{O}(p)$ equations are found to be

$$\begin{aligned}
& \int_{-\infty}^{\infty} dh_\parallel \left[\frac{h_{1\perp}^2}{k_1^2} H_0(h_{1\perp}R) A(h_\parallel) - \frac{h_{2\perp}^2}{k_2^2} J_0(h_{2\perp}R) B(h_\parallel) \right] e^{ih_\parallel z} = \\
& \quad \left[\frac{k_{2\perp}^3}{k_2^2} b_2 \zeta(z) J_0'(k_{2\perp}R) - \frac{k_{1\perp}^3}{k_1^2} b_1 \zeta(z) H_0'(k_{1\perp}R) + \frac{ik_\parallel k_{2\perp}}{k_2^2} b_2 \frac{d\zeta}{dz} J_0'(k_{2\perp}R) \right. \\
& \quad \left. - \frac{ik_\parallel k_{1\perp}}{k_1^2} b_1 \frac{d\zeta}{dz} H_0'(k_{1\perp}R) \right] e^{ik_\parallel z} \\
& \int_{-\infty}^{\infty} dh_\parallel \left[h_{1\perp} H_0'(h_{1\perp}R) A(h_\parallel) - h_{2\perp} J_0'(h_{2\perp}R) B(h_\parallel) \right] e^{ih_\parallel z} = \\
& \quad \left[k_{2\perp}^2 b_2 \zeta(z) J_0''(k_{2\perp}R) - k_{1\perp}^2 b_1 \zeta(z) H_0''(k_{1\perp}R) \right] e^{ik_\parallel z}. \qquad \text{(I.3)}
\end{aligned}$$

Here we assume that the metal inherently has no losses, *i.e.*, $\mathrm{Im}\,\epsilon_2 = 0$, such that $k_\parallel$ is purely real. Then, by plugging in the Fourier transform of $\zeta(z)$ given in Eq. (2.65), the equations above become purely algebraic. It is tedious but straightforward to show that the solutions are given by Eq. (2.66), with the coefficients $f(h_\parallel)$ and $g(h_\parallel)$ defined via

$$\begin{aligned}
f(h_\parallel) &= \frac{h_{2\perp} N J_0(h_{2\perp}R) - k_2^2 M(h_\parallel) J_0'(h_{2\perp}R)}{H_0(h_{1\perp}R)J_0'(h_{2\perp}R)h_{1\perp}k_2^2 - H_0'(h_{1\perp}R)J_0(h_{2\perp}R)h_{2\perp}k_1^2}, \\
g(h_\parallel) &= \frac{h_{1\perp} N H_0(h_{1\perp}R) - k_1^2 M(h_\parallel) H_0'(h_{1\perp}R)}{H_0(h_{1\perp}R)J_0'(h_{2\perp}R)h_{1\perp}k_2^2 - H_0'(h_{1\perp}R)J_0(h_{2\perp}R)h_{2\perp}k_1^2}, \\
M(h_\parallel) &= \left(\frac{k_{1\perp}^3}{k_1^2} - \frac{k_\parallel k_{1\perp}(h_\parallel - k_\parallel)}{k_1^2}\right) b_1 H_0'(k_{1\perp}R) \\
&\quad - \left(\frac{k_{2\perp}^3}{k_2^2} - \frac{k_\parallel k_{2\perp}(h_\parallel - k_\parallel)}{k_2^2}\right) b_2 J_0'(k_{2\perp}R), \\
N &= b_1 k_{1\perp}^2 H_0''(k_{1\perp}R) - b_2 k_{2\perp}^2 J_0''(k_{2\perp}R).
\end{aligned} \tag{I.4}$$

To evaluate the expression for $\Gamma_{\mathrm{rad,rough}}$ in Eq. (2.73), we first normalize the fields such that the denominator takes the value $\hbar\omega/4L$. For concreteness, we assume that the conducting nanowire exhibits a Drude-like behavior and that we are operating well below the plasma frequency, such that $\epsilon_2(\omega) = 1 - \omega_p^2/\omega^2 \approx -\omega_p^2/\omega^2$. In this case the dispersive term in the denominator is positive and given by $\frac{d}{d\omega}(\omega\epsilon_2(\omega)) \approx |\epsilon_2(\omega)|$. In the nanowire limit, normalization of the integral is straightforward and yields a coefficient $b_1 \approx \sqrt{\hbar\omega k_0^4 \epsilon_1^2 R^2/\epsilon_0 \tilde{V} \tilde{C}^4 L}$. Here $\tilde{V}$ is a dimensionless parameter given by

$$\tilde{V} = \frac{8\epsilon_1^2}{\pi C^2}\left(\frac{K_1^2(C)}{|\epsilon_2| I_1^2(C)} \int_0^C dx\, x\left(I_1^2(x) + I_0^2(x)\right) + \frac{1}{\epsilon_1}\int_C^\infty dx\, x\left(K_1^2(x) + K_0^2(x)\right)\right). \tag{I.5}$$

Then, using the relationships $k_\parallel \approx C/R$, $k_{i\perp} \approx iC/R$ one can calculate the leading terms of $f(h_\parallel)$ as $R \to 0$,

$$f(h_\parallel) \approx \frac{h_{2\perp} b_1 (C/R)^2 \phi}{-2ik_1^2 h_{2\perp}/\pi h_{1\perp} R}, \tag{I.6}$$

where we have defined $\phi \equiv (b_2/b_1)J_0''(iC) - H_0''(iC)$. In the equation above we have explicitly given the leading terms of the numerator and denominator of $f(h_\parallel)$. The ratio b_1/b_2 is given in Eq. (2.4), which in the nanowire limit results in the simplification of ϕ given in Eq. (2.75).

We now consider the limits of validity of our perturbative approach to calculating radiative scattering, specifically considering the expansions made in Eq. (I.2) that are necessary for the perturbative method used here. The first of these expansions requires that $|d\zeta/dz| \ll 1$, which can be re-written as a condition on the slope, $s \ll 1$. Physically this requirement states that the typical length of a rough patch be much larger than its typical height. The second line of Eq. (I.2) requires that $|k_{i\perp}\zeta| \ll 1$. In the nanowire regime this requirement is equivalent to $\delta \ll \lambda_{\mathrm{pl}}$, which states that the height of a rough patch must be much smaller than the SP wavelength. Finally, the third line of Eq. (I.2) requires $|h_{i\perp}\zeta| \ll 1$, within the range of $h_{i\perp}$ that are appreciably scattered into. From Eqs. (2.66) and (2.68), we see that the relevant range for the parallel component of the wavevector is given by $k_\parallel - 1/a \lesssim h_\parallel \lesssim k_\parallel + 1/a$, and thus the largest relevant transverse wavevector is $|h_{i\perp,\mathrm{max}}| \sim \max_{-1\leq\theta\leq 1} \left|\sqrt{\epsilon_i(\omega/c)^2 - (k_\parallel + \theta/a)^2}\right|$. In the nanowire regime, $k_\parallel \approx C/R$, there are two limiting cases. The first is when the correlation length a is much larger than R, $a \gg R$, in which case $|h_{i\perp,\mathrm{max}}| \sim C/R$ and $|h_{i\perp}\zeta| \ll 1$ reduces to $\delta \ll \lambda_{\mathrm{pl}}$. In the other limiting case, $R \gg a$, one finds that $|h_{i\perp,\mathrm{max}}| \sim 1/a$ and the corresponding requirement is given by $s \ll 1$.

I.2 Non-radiative scattering

The elements of the matrices M_i and vectors v_i appearing in the matrix integral equation of Eq. (2.85) in the presence of surface roughness are given by

$$
\begin{aligned}
M_0(h) &= \begin{pmatrix} \tilde{K}_m(hR) & -\tilde{I}_m(hR) \\ h\epsilon_1\tilde{K}'_m(hR) & -h\epsilon_2\tilde{I}'_m(hR) \end{pmatrix}, \\
M_1(h,q) &= \begin{pmatrix} q\tilde{K}'_m(qR) & -q\tilde{I}'_m(qR) \\ M_1^{21}(h,q) & M_2^{22}(h,q) \end{pmatrix} e^{i(h-q)z'}, \\
M_1^{21}(h,q) &= \epsilon_1(q^2\tilde{K}''_m(qR) + q(h-q)\tilde{K}_m(qR)), \\
M_2^{22}(h,q) &= -\epsilon_2(q^2\tilde{I}''_m(qR) + q(h-q)\tilde{I}_m(qR)), \\
M_2(h,q,q') &= \begin{pmatrix} \frac{q^2}{2}\tilde{K}''_m(qR) & -\frac{q^2}{2}\tilde{I}''_m(qR) \\ M_2^{21}(h,q,q') & M_2^{22}(h,q,q') \end{pmatrix} e^{i(h-q)z'}, \\
M_2^{21}(h,q,q') &= \epsilon_1\left(\frac{q^3}{2}\tilde{K}'''_m(qR) + \left(q^2 + \frac{qq'}{2}\right)(h-q-q')\tilde{K}'_m(qR)\right), \\
M_2^{22}(h,q,q') &= -\epsilon_2\left(\frac{q^3}{2}\tilde{I}'''_m(qR) + \left(q^2 + \frac{qq'}{2}\right)(h-q-q')\tilde{I}'_m(qR)\right), \\
\mathrm{v}_0(h) &= -\begin{pmatrix} \tilde{I}_m(hR) \\ h\tilde{I}'_m(hR) \end{pmatrix} \tilde{K}_m(h\rho'), \\
\mathrm{v}_1(h,q) &= -\begin{pmatrix} q\tilde{I}'_m(qR) \\ q^2\tilde{I}''_m(qR) + q(h-q)\tilde{I}_m(qR) \end{pmatrix} \tilde{K}_m(q\rho')e^{i(h-q)z'}, \\
\mathrm{v}_2(h,q,q') &= -\begin{pmatrix} \frac{q^2}{2}\tilde{I}''_m(qR) \\ v_2^2(h,q,q') \end{pmatrix} \tilde{K}_m(q\rho')e^{i(h-q)z'}, \\
v_2^2(h,q,q') &= \frac{q^3}{2}\tilde{I}'''_m(qR) + \left(q^2 + \frac{qq'}{2}\right)(h-q-q')\tilde{I}'_m(qR).
\end{aligned}
\tag{I.7}
$$

I.3 Temperature-dependent electron-phonon scattering

I.3.1 Derivation of electron-phonon interaction Hamiltonian

First, we recall that the phonon Hamiltonian and the displacement operator $\hat{R}_n$ of ion n are given by

$$\begin{aligned} H_{ph} &= \sum_{\mathbf{q}} \hbar\omega_{\mathbf{q}} \hat{a}^{\dagger}_{\mathbf{q}} \hat{a}_{\mathbf{q}}, && \text{(I.8)} \\ \hat{R}_n &= \frac{1}{\sqrt{N}} \sum_{\mathbf{q}} e^{i\mathbf{q}\cdot\mathbf{R}_n} \hat{\epsilon}_{\mathbf{q}} \sqrt{\frac{2\hbar}{M\omega_{\mathbf{q}}}} (a_{\mathbf{q}} + a^{\dagger}_{-\mathbf{q}}). && \text{(I.9)} \end{aligned}$$

Here, $\hbar\omega_{\mathbf{q}}$ and $\hat{\epsilon}_{\mathbf{q}}$ are the energy and polarization of phonon mode $\mathbf{q}$, M is the ion mass, N is the total number of ions, and $\hat{a}_{\mathbf{q}}$ is the annihilation operator for mode $\mathbf{q}$. The subscript $\mathbf{q}$ appearing in the summations above and in $\omega_{\mathbf{q}}, \hat{a}_{\mathbf{q}}$ are understood to cover the polarization degrees of freedom as well. The electron-phonon Hamiltonian to lowest order is obtained by expanding the electron-ion interaction Hamiltonian,

$$H_{el-ion} = \int d\mathbf{r} \sum_{n\sigma} \hat{\psi}^{\dagger}_{\sigma}(\mathbf{r}) \hat{\psi}_{\sigma}(\mathbf{r}) V_0(\mathbf{r} - \mathbf{R}_n), \tag{I.10}$$

to first order around the ion equilibrium positions $\mathbf{R}^{(0)}_n$. Here $\hat{\psi}_{\sigma}(\mathbf{r})$ annihilates an electron of spin σ at position $\mathbf{r}$. Performing this expansion, and simultaneously expressing the operator $\hat{\psi}_{\sigma}(\mathbf{r}) = (1/\sqrt{N}) \sum_{\mathbf{k}\sigma} \hat{c}_{\mathbf{k}\sigma} \phi_{\mathbf{k}}(\mathbf{r})$ in terms of the Bloch functions $\phi_{\mathbf{k}}$ and their annihilation operators $\hat{c}_{\mathbf{k}\sigma}$, one arrives at

$$H_{el-ph} = \frac{1}{N} \int d\mathbf{r} \sum_{n\mathbf{k}\mathbf{k}'\sigma} \hat{c}^{\dagger}_{\mathbf{k}'\sigma} \hat{c}_{\mathbf{k}\sigma} \phi^{*}_{\mathbf{k}'}(\mathbf{r}) \phi_{\mathbf{k}}(\mathbf{r}) \left(\nabla_{\mathbf{R}_n} V_0\right) \cdot \hat{R}_n \big|_{\mathbf{R}_n = \mathbf{R}^{(0)}_n}. \tag{I.11}$$

One can simplify the above expression by utilizing Bloch's Theorem to apply a shift to the states $\phi^*_{\mathbf{k}'}$ and $\phi_{\mathbf{k}}$,

$$\begin{aligned} H_{el-ph} &= \frac{1}{N}\sum_{n\mathbf{k}\mathbf{k}'\mathbf{q}\sigma}\sqrt{\frac{2\hbar}{MN\omega_{\mathbf{q}}}}\left(\hat{a}^\dagger_{\mathbf{q}}+\hat{a}_{-\mathbf{q}}\right)\hat{c}^\dagger_{\mathbf{k}'\sigma}\hat{c}_{\mathbf{k}\sigma}e^{i(\mathbf{q}-\mathbf{k}+\mathbf{k}')\cdot\mathbf{R}^{(0)}_n}\times \\ &\quad \int d\mathbf{r}\,\phi^*_{\mathbf{k}'}(\mathbf{r}-\mathbf{R}^{(0)}_n)\left(\hat{\epsilon}_{\mathbf{q}}\cdot\nabla_{\mathbf{R}_n}V_0\right)\big|_{\mathbf{R}_n=\mathbf{R}^{(0)}_n}\phi_{\mathbf{k}}(\mathbf{r}-\mathbf{R}^{(0)}_n) \qquad \text{(I.12)} \\ &= \sum_{\mathbf{k}\mathbf{q}\mathbf{G}\sigma}\sqrt{\frac{2\hbar}{MN\omega_{\mathbf{q}}}}\left(\mathbf{Q}_{\mathbf{k}+\mathbf{q}+\mathbf{G},\mathbf{k}}\cdot\hat{\epsilon}_{\mathbf{q}}\right)\hat{c}^\dagger_{\mathbf{k}+\mathbf{q}+\mathbf{G},\sigma}\left(\hat{a}_{\mathbf{q}}+\hat{a}^\dagger_{-\mathbf{q}}\right)\hat{c}_{\mathbf{k}\sigma}, \qquad \text{(I.13)} \end{aligned}$$

where G is a reciprocal lattice vector and

$$\mathbf{Q}_{\mathbf{k}'\mathbf{k}} \equiv \langle\phi_{\mathbf{k}'}|\nabla_{\mathbf{R}}V_0(\mathbf{r}-\mathbf{R})|_{\mathbf{R}=0}|\phi_{\mathbf{k}}\rangle. \qquad \text{(I.14)}$$

For simplicity we will consider only normal scattering events, where only the $\mathbf{G}=0$ term contributes, and ignore umklapp processes, which leads to the electron-phonon interaction Hamiltonian given in Eq. (2.98).

I.3.2 Derivation of electron-field Hamiltonian

The electron-field interaction Hamiltonian is given in first quantized form by

$$H_{el-field} = \frac{e}{2m}\sum_j \hat{\mathbf{p}}_j\cdot\mathbf{A}(\mathbf{r}_j)+\mathbf{A}(\mathbf{r}_j)\cdot\hat{\mathbf{p}}_j, \qquad \text{(I.15)}$$

where $\hat{\mathbf{p}}_j$ is the canonical momentum operator of electron j, and A is the vector potential. In the following we will assume the electrons are interacting with a uniform classical plane-wave field,

$$\mathbf{E} = \mathbf{E}_0\left(e^{i\mathbf{h}\cdot\mathbf{r}-i\omega t}+c.c.\right). \qquad \text{(I.16)}$$

In this case, the interaction Hamiltonian becomes

$$H_{el-field} = \frac{e\hbar}{2m}\frac{\mathbf{E}_0}{i\omega}\cdot\left(\sum_j\frac{\nabla_j}{i}e^{i\mathbf{h}\cdot\mathbf{r}_j}+e^{i\mathbf{h}\cdot\mathbf{r}_j}\frac{\nabla_j}{i}\right)e^{-i\omega t}+h.c. \qquad \text{(I.17)}$$

$$\equiv \frac{e\mathbf{E}_0}{i\omega}\hat{\mathbf{v}}(\mathbf{h})e^{-i\omega t} + h.c., \tag{I.18}$$

where we have defined

$$\hat{\mathbf{v}}(\mathbf{h}) \equiv \frac{\hbar}{2im}\left(\sum_j \nabla_j e^{i\mathbf{h}\cdot\mathbf{r}_j} + e^{i\mathbf{h}\cdot\mathbf{r}_j}\nabla_j\right). \tag{I.19}$$

We can simplify the interaction Hamiltonian somewhat by considering the action of the operator

$$\hat{\mathbf{v}}_{\mathbf{h}} \equiv \frac{\hbar}{2im}\left(\nabla e^{i\mathbf{h}\cdot\mathbf{r}} + e^{i\mathbf{h}\cdot\mathbf{r}}\nabla\right) \tag{I.20}$$

on any Bloch state $\phi_{\mathbf{k}-\mathbf{h}/2}$. We first write $\phi_{\mathbf{k}-\mathbf{h}/2}(\mathbf{r}) = e^{i(\mathbf{k}-\mathbf{h}/2)\cdot\mathbf{r}}u_{\mathbf{k}-\mathbf{h}/2}(\mathbf{r})$ in terms of a plane wave and a periodic function u that has the same periodicity as the underlying lattice. Then

$$\hat{\mathbf{v}}_{\mathbf{h}}\phi_{\mathbf{k}-\mathbf{h}/2} = \frac{\hbar}{im}e^{i(\mathbf{k}+\mathbf{h}/2)\cdot\mathbf{r}}\left(i\mathbf{k}u_{\mathbf{k}-\mathbf{h}/2} + \nabla u_{\mathbf{k}-\mathbf{h}/2}\right). \tag{I.21}$$

It can be seen that the matrix element

$$\begin{aligned}
\langle\mathbf{k}'|\hat{\mathbf{v}}_{\mathbf{h}}|\mathbf{k}-\mathbf{h}/2\rangle &= \int d\mathbf{r}\,\phi^*_{\mathbf{k}'}(\mathbf{r})\hat{\mathbf{v}}_{\mathbf{h}}\phi_{\mathbf{k}-\mathbf{h}/2}(\mathbf{r}) && \text{(I.22)}\\
&= \int d\mathbf{r}\,\frac{\hbar}{im}e^{i(\mathbf{k}-\mathbf{k}'+\mathbf{h}/2)\cdot\mathbf{r}}u^*_{\mathbf{k}'}(\mathbf{r})\,\times\\
&\qquad \left(i\mathbf{k}u_{\mathbf{k}-\mathbf{h}/2}(\mathbf{r}) + \nabla u_{\mathbf{k}-\mathbf{h}/2}(\mathbf{r})\right) && \text{(I.23)}
\end{aligned}$$

vanishes unless $\mathbf{k}' = \mathbf{k} + \mathbf{h}/2$, since the periodic functions u have non-vanishing Fourier components only at reciprocal lattice vectors $\mathbf{G}$. Furthermore, assuming that the functions $u_{\mathbf{k}\pm\mathbf{h}/2}(\mathbf{r})$ are just small perturbations to the function $u_{\mathbf{k}}(\mathbf{r})$, to lowest order we can make the replacements $u_{\mathbf{k}\pm\mathbf{h}/2} \approx u_{\mathbf{k}}$ in the equation above. In making this assumption, we also implicitly assume that only intraband electronic transitions occur. Now,

$$\langle\mathbf{k}+\mathbf{h}/2|\hat{\mathbf{v}}_{\mathbf{h}}|\mathbf{k}-\mathbf{h}/2\rangle \approx \frac{\hbar}{im}\int d\mathbf{r}\,u^*_{\mathbf{k}}(\mathbf{r})\left(i\mathbf{k}u_{\mathbf{k}}(\mathbf{r}) + \nabla u_{\mathbf{k}}(\mathbf{r})\right) \tag{I.24}$$

$$\equiv \mathrm{v}_{\mathbf{k}}, \tag{I.25}$$

where $\mathrm{v}_{\mathbf{k}} \approx \nabla_{\mathbf{k}} \mathcal{E}(\mathrm{k})/\hbar$ is the electron velocity in state **k**. With these simplifications, the electron-field Hamiltonian in second quantized form immediately follows, as given in Eq. (2.100).